Experimental investigation of Ce-115 and related compounds in high magnetic fields

Sanu Mishra

Sanu Mishra. Experimental investigation of Ce-115 and related compounds in high magnetic fields. Strongly Correlated Electrons [cond-mat.str-el]. Université Grenoble Alpes [2020-..], 2021. English. NNT : 2021GRALY026 . tel-03497769

THÈSE

Pour obtenir le grade de

DOCTEUR DE L'UNIVERSITE GRENOBLE ALPES

Spécialité : **Physique de la Matière Condensée et du Rayonnement**

Arrêté ministériel : 25 mai 2016

Présentée par

Sanu MISHRA

Thèse dirigée par **Dr. Ilya SHEIKIN, Directeur de recherche, Laboratoire National des Champs Magnétiques Intenses (LNCMI – CNRS), Grenoble**

et codirigée par **Albin DE MUER, Maître de conférences, Universite Grenoble-Alpes et LNCMI-CNRS, Grenoble**

préparée au sein du **Laboratoire National des Champs Magnétiques Intenses - Centre national de la recherche scientifique (LNCMI - CNRS)**
dans **l'École Doctorale Physique**

Etude expérimentale des composés Ce-115 et apparentés sous champs magnétiques intenses

Experimental investigation of Ce-115 and related compounds in high magnetic fields

Thèse soutenue publiquement le **24 mars 2021**,
devant le jury composé de :

Monsieur THIERRY KLEIN
PROFESSEUR DES UNIVERSITES, Universite Grenoble Alpes et Institut Néel - CNRS, (Président)
Monsieur JOACHIM WOSNITZA
PROFESSEUR, Technische Universität Dresden et Hochfeld Magnetlabor Helmholtz-Zentrum Dresden-Rossendorf (HLD HZDR), (Rapporteur)
Monsieur DAI AOKI
PROFESSEUR, ICC-IMR, Tohoku University, (Rapporteur)
Madame ALIX MCCOLLAM
PROFESSEUR ASSISTANT, High Field Magnet Laboratory (HFML), Radboud Universiteit Nijmegen, (Examinatrice)
Monsieur HISATOMO HARIMA
PROFESSEUR, Department of Physics, Graduate School of Science, Kobe University, (Examinateur)

Abstract

The heavy fermion compound $CeRhIn_5$ offers an ideal playground to investigate the rich physics of strongly correlated electron systems. It can be readily tuned to a quantum critical point by hydrostatic pressure, chemical doping, and magnetic fields. While the pressure-induced quantum critical point is long accepted to be of the Kondo-breakdown type, the one induced by the magnetic field at $B_c \approx 50$ T was suggested to be of the spin-density-wave type. This assumption is based on the observation of additional de Haas–van Alphen frequencies deep inside the antiferromagnetic state, above $B^* = 30$ T, where a novel phase of enhanced in-plane electronic anisotropy emerges. These additional frequencies were interpreted as a signature of an abrupt Fermi-surface reconstruction due to the field-induced itineracy of the f electrons at B^*.

Our comprehensive angular-dependent de Haas–van Alphen study of $CeRhIn_5$ and its non-f reference compound $LaRhIn_5$ establishes the localized character of the f electrons inside and outside of the antiferromagnetic phase. This rules out any significant field-induced Fermi-surface reconstruction, particularly across B^*. We suggest the field-induced quantum criticality in $CeRhIn_5$ does not conform with the established theoretical models.

A part of the thesis is dedicated to understanding the origin of the elusive state above B^*. Our observation of a distinct specific-heat anomaly at B^* suggests it to be a real phase transition, probably weakly first-order. Further, our ultrasound study for a field applied at 2° from the c axis revealed anomalies at B^* in all the symmetry-breaking ultrasonic modes, suggesting additional broken symmetries. Similar anomalies of the opposite sign were observed at the well-established metamagnetic transition at $B_m \simeq 20$ T. In conjunction with the observation of both anomalies strictly within the antiferromagnetic state, this suggests that the transition at B^* corresponds to a field-induced change of the magnetic structure from commensurate to incommensurate. Finally, the angular-dependent behavior of the anomaly at B^*, contradictory to the previously reported transport studies on microfabricated samples of $CeRhIn_5$, emphasize the crucial role of the uniaxial strain inherently present in the latter.

Our de Haas–van Alphen measurements on the related heavy fermion superconductor $CeCoIn_5$ revealed anomalous quantum oscillations between 20 and 24 T, where some of the effective masses also show an unusual field-dependence. Similarly, our magnetoresistance measurements revealed a clear anomaly at 23 T, further suggesting that a field-induced instability occurs in $CeCoIn_5$ at this field.

The final part of the thesis is dedicated to growing high-quality single crystals of the Ce-218 family. The samples of Ce_2CoIn_8 were grown of sufficiently high quality to show quantum oscillations for the first time. The Fermi surface is found to be qualitatively similar to $CeCoIn_5$, but with larger orbits. Some of the effective masses are found to be strongly enhanced.

Key Words :

High magnetic field
Specific heat
$CeRhIn_5$
Fermi surface
Ultrasound velocity
$CeCoIn_5$

Abstract in French

Le composé à fermions lourds $CeRhIn_5$ constitue un terrain de jeu idéal pour étudier la riche physique des systèmes à électrons fortement corrélés. Il peut facilement être pousser à travers un point critique quantique par pression hydrostatique, dopage chimique et champ magnétique. Alors que le point critique quantique induit par la pression est communément reconnu être de type $\ll$ suppression de Kondo $\gg$, celui induit par champ magnétique à $B_c = 50$ T est suggéré être de type $\ll$ onde de densité de spin $\gg$. Cette hypothèse est basée sur l'observation de fréquences de Haas-van Alphen supplémentaires au cœur de l'état antiferromagnétique au-dessus de $B^* = 30$ T, où une nouvelle phase de forte anisotropie électronique dans le plan apparait. Ces nouvelles fréquences ont été interprétées comme la signature d'une soudaine reconstruction de la surface de Fermi due à l'itinérance des électrons f induite par le champ à B^*. Nos études détaillées de la dépendance angulaire de l'effet Haas-van Alphen sur $CeRhIn_5$ et son composé de référence sans électrons f, $LaRhIn_5$, établissent le caractère localisé des électrons f de part et d'autre du point critique quantique antiferromagnétique. Ceci élimine toute possibilité de reconstruction de surface de Fermi sous champ, notamment de part et d'autre B^*. Nous suggérons que le comportement critique quantique induit sous champ dans $CeRhIn_5$ n'est pas conforme avec les modèles théoriques existants.

Une partie de cette thèse est dédiée à la compréhension de l'origine de ce mystérieux état au-dessus de B^*. Notre observation d'une claire anomalie de chaleur spécifique à B^* suggère qu'il s'agit d'une réelle transition de phase, probablement faiblement du 1^{er} ordre. Par ailleurs, nos études d'ultrasons pour un champ appliqué à 2° de l'axe c montrent des anomalies à B^* dans tous les modes acoustiques qui brisent la symétrie, suggérant des ruptures de symétrie supplémentaires. Des anomalies similaires mais de signe opposé ont été observées à la transition méta$-$magnétique bien connue à $B_m = 20$ T. Comme par ailleurs, les deux anomalies ne surviennent que dans l'état antiferromagnétique, la transition à B^* semble correspondre à une modification induite sous champ de la structure magnétique d'un état commensurable à un état incommensurable. Finalement, en contradiction avec les précédentes études de transport sur des microéchantillons de $CeRhIn_5$, le comportement angulaire de l'anomalie à B^* souligne le rôle crucial de la contrainte uni-axiale intrinsèquement présente dans ces derniers.

Nos mesures de Haas-van Alphen sur le supraconducteur à fermions lourds apparenté $CeCoIn_5$ montrent des oscillations quantiques anormales entre 20 et 24 T, là ou certaines masses effectives montrent également une dépendance en champ inhabituelle. De façon similaire, nos mesures de magnétorésistance montrent une nette anomalie à 23 T, suggérant qu'une instabilité induite sous champ survient dans $CeCoIn_5$ à ce champ.

La partie finale de cette thèse est dédiée à la croissance de monocristaux de haute qualité de la famille Ce$-$218. Les échantillons de Ce_2CoIn_8 obtenus sont de suffisamment haute qualité pour observer des oscillations quantiques pour la premiére fois. La surface de Fermi semble être qualitativement similaire à celle de $CeCoIn_5$, mais avec des orbites plus grandes. Certaines des masses effectives sont particulièrement élevées.

Mots Clés :

champ magnétique intense
chaleur spécifique
$CeRhIn_5$
surface de Fermi
vitesse de l'ultrason
$CeCoIn_5$

Acknowledgments

I would like to acknowledge the continuous and unending support of a number of people without whom this work would not have been possible.

Firstly, I would like to thank Ilya Sheikin, my PhD supervisor. Ilya has been an exceptional mentor and has provided me with excellent guidance. Starting from researching relevant scientific literature to honing my experimental and scientific writing skills, Ilya has assisted and trained me throughout. I would also like to thank my PhD co-supervisor and office mate Albin DeMeur. We worked together on specific heat experiments and developed a new probe for high field measurements, with which we were finally able to obtain really nice results. I also thank Albin for all the informative discussions we had, both scientific as well as others.

I would like to thank the members, referees and president of my PhD defense committee. I thank Prof. Joachim Wosnita and Prof. Dai Aoki for accepting to be the referees for my thesis. I thank them for carefully evaluating my PhD thesis and providing valuable and comprehensive reports on it. I would like to thank Prof. Thierry Klein for presiding over my PhD defense jury and for writing a comprehensive final report after the defense. I would like to thank Prof. Hisatomo Harima and Prof. Alix McCollam for accepting to be the jury members for my defense and for their interesting questions and comments. I thank all the members of the jury for their inputs and suggestions for improving this thesis. I would also like to thank the members of my thesis follow up committee, Dr. Claudine Lacroix and Dr. Pierre Rodiere, for their valuable suggestions and continuously monitoring the progress of this thesis.

All my collaborators, both here in Grenoble as well as abroad, have extensively assisted me during this work. I would like to start by first thanking our collaborators in HLD-HZDR Dresden, where I frequently visited to perform the pulsed field measurements. I would like to thank Tobias Förster, our local contact at HLD for the dHvA measurements in pulsed magnetic fields. I would like to thank Denis Gorbunov, our local contact at HLD Dresden for ultrasound measurements in pulsed fields. Together with Denis, we performed comprehensive ultrasound measurements over the last two and half year. Next, I would like to thank our close collaborators at HLD, Jacob Hornung and Johannes Klotz. Together, we worked on many projects and performed a number of experiments, both at HLD Dresden on their superconducting magnet as well as here at LNCMI Grenoble on the resistive magnet. I would also like to thank David LeBoeuf and Daniel Campbell, our collaborators and local contact for ultrasound measurement in Grenoble. I thank Matthias Raba, our group member, for his support and contributions. I thank Prof. Dai Aoki for inviting me to Oarai, Japan for a two month stay as a visiting young researcher at ICC-IMR, Tohoku university. It turned out to be a fun and productive visit. Not only I learned to grow high quality single crystals but also, I traveled a lot and experienced the Japanese culture and way of life. I thank Prof. H. Harima, our collaborator at Kobe university, for performing band structure calculations for the various heavy fermion systems we worked on as well as his insights into understanding our experimental results. I would also like to thank M. B. Lepetit, C. Simon, R. Settai, Y. Nemoto, Y. Tokunaga and S. Zherlitsyn for fruitful scientific discussions. I thank all my collaborators for their inputs and suggestions in the preparation of the three manuscripts we wrote so far based on part of this PhD thesis, all of which are now published in reputed journals.

I sincerely thank all the LNCMI staff for assisting and supporting me during the course of my thesis. I thank our laboratory secretaries for helping me with the administrative processes. I am also thankful to the engineering and cryogenic teams, operators for the resistive magnet, cleaning staff and all the other labmates who have assisted me whenever I needed. I am thankful to all

my friends for continuously supporting me over the course of the last three and a half years. I especially thank my flatmates Hemant and Sumit for the memorable time we had.

Finally, I am grateful to my parents and family for their constant support. It is their unhinged confidence in me that has finally resulted into this fruitful scientific work.

Contents

Chapter 1

Introduction

1.1 A brief review of electronic systems

1.1.1 General introduction

The physical properties of an electronic system are driven by the behavior of its electrons. Be it a metal, a semi-conductor, or a strongly-correlated-electron system, each owe its unique physical properties to a distinct electronic behaviour resulting from the interaction of its electrons with their environment, i.e., the ionic lattice and the rest of the electrons.

For instance, a free electron can attain arbitrary energy due to the absence of an environment to interact with and alter its character. But when present in an atom, it can only acquire a discrete energy of the atomic orbital it occupies. Subsequently, when atoms are clustered together into a lattice to form a matter, the electrons tend to behave in a distinct manner as a result of the electron-lattice and electron-electron interactions.

In a matter such as a metal, the electrons are bundled together into groups known as 'energy bands', that are separated from other energy bands by an energy gap. The electrons in the most 'energetic' group, the conduction band, are responsible for the macroscopic properties, such as the electrical conductivity, thermal conductivity, heat capacity, magnetic susceptibility, electrodynamics, etc.

Such properties solely dependent on the conduction electrons, wandering through the lattice, can be understood within a simple 'free-electron model' or the Drude-Sommerfeld model [1, 2, 3]. This model treats the conduction electrons in a metal as an ensemble of free electrons neglecting electron-lattice interactions. The electronic wave-function is represented by a plane wave extending throughout the lattice, analogous to the itineracy of the conduction electrons. However, this model can not explain other classes of matter, such as semiconductors, insulators, semi-metals or even some metallic properties, such as Hall effect and magnetoresistance, in which the electron-lattice interactions cannot be ignored.

Therefore, came to the rescue, a 'nearly free model' that laid to the foundations of the band-theory of solids. This theory comprehensively took into account the interactions between the conduction electrons and the ionic lattice. Within this theory, the periodic lattice potential modulates the free electron wave-function leading to the formation of energy bands and band gaps, unlike the continuous parabolic energy dispersion relation of the free electron model. With the ideas of energy bands and energy gaps, the physics arising due to electron-lattice interactions could be comprehensively accounted for to explain systems like semi-conductors and insulators.

1.1.2 Strongly correlated electron systems

In a certain special class of electronic systems, the electron-lattice interactions are much weaker than the interactions amongst the electrons themselves that play the most dominant role in shaping the overall macroscopic properties. These interactions amongst the electrons are referred to as correlations. Such materials are known as strongly correlated electron systems (SCES). These strong electronic correlations lead to exotic physical properties, such as long-range magnetic order, unconventional superconductivity, and heavy-fermion state. Since they possess such exotic and novel states of matter, SCES are also colloquially referred to as Quantum Materials.

Usually, strongly correlated electron systems are intermetallic compounds containing elements with partially filled *d* or *f* orbitals. The spatial confinement of these orbitals leads to an increased electronic repulsion causing stronger correlations. Most materials containing transition metals (*d* orbital electrons) are either magnetic or superconducting, depending on the electronic shell in which *d* electrons lie [4].

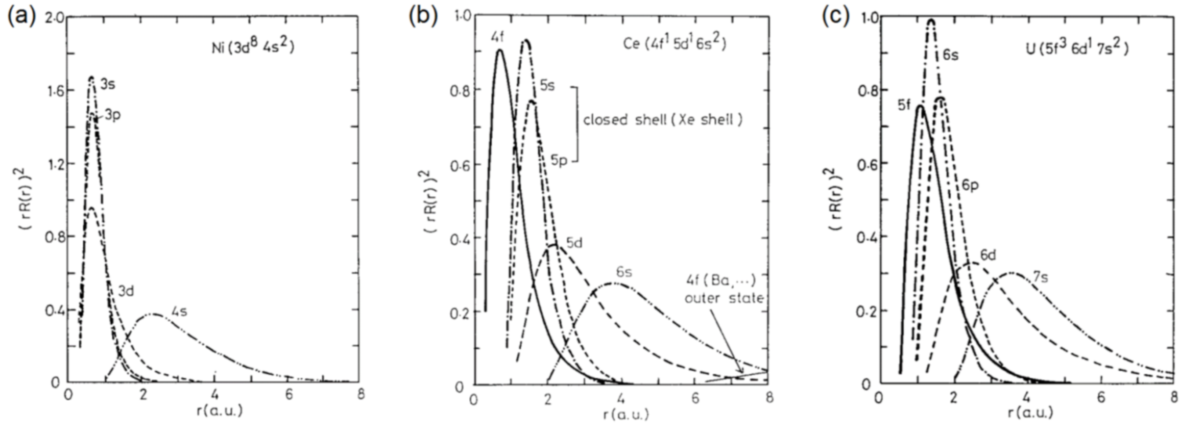

Figure 1.1: Spatial distribution of charge densities in $3d$, $4f$ and $5f$ orbitals, taken from Ref. [5]

Strongly correlated electron systems with elements containing $4f$ or $5f$ electrons house rich physics due to special character of these electrons [5, 6, 7, 8, 9]. Due to the huge positive nuclear charge, the f-orbital is pulled inside the ionic core rendering it localized, much more than the d orbitals as is evident from the spatial distribution of electric charge in $3d$, $5f$ and $4f$ orbitals shown in Fig. 1.1. Further, the large spin-orbit coupling in f-orbitals combines the spin (S) and angular momentum (L) of the f-states into a state of definite total angular momentum J. The interaction of large spin degrees of freedom of the f orbitals with conduction electron degree of freedom can lead to a remarkable physics, such as a non-magnetic delocalized character to the f orbitals. Therefore, intermetallic systems with elements like cerium and uranium reside in a crossover region between the localized and itinerant character and form an exotic class of strongly correlated electron materials.

It is pertinent to comprehensively take into account the electronic correlation effects to understand the overall macroscopic properties of strongly correlated electron systems. In this regard, several extensive theories were developed treating such systems as a many-body ensemble of electrons. While these theories have been able to successfully explain many-body effects to a certain degree, a comprehensive model accounting for the electronic correlations in entirety is still lacking. In the following section, I will discuss the theoretical attempts to capture the many-body effects in SCES.

1.1.3 Theoretical approaches to many-body effects in SCES

Initial attempts to describe electron-electron repulsion were inspired from the semi-empirical methods aimed at describing many-electron atoms, where the modified atomic energy levels were obtained by including empirical parameters to Bohr's model [10]. Later on, more formal methods were devised to tackle the complicated many-body problem. There are essentially two pathways. The first is a computational approach from the first principles - the so called *ab-initio* method, and the other is an analytic one - the model Hamiltonian approach.

***ab-initio* methods:** The *ab-initio* methods started in 1926 with the Schrodinger equation that gave motivation to the so called mean-field approach. In such an approach, the mean-field approximation is implied, i.e., a particle in a many-body system experiences an effective potential (V_{eff}) created by the rest of the particles.

In 1927, D. Hartree came up with his self-consistent field method to approximate wavefunctions of atoms and ions [11]. Within this method, the time-independent Schrodinger equation (non-relativistic approximation) for each particle, taking V_{eff} created by the rest of the particles, was solved self-consistently by an iterative method running on an Ansatz/seed solution. Although, the method was theoretically sound, it didn't respect the anti-symmetry of the wave-function (Pauli principle), a consequence of quantum statistics. Therefore, it failed to account for the exchange interactions associated with the anti-symmetry, which was later corrected by Fock and Slater in their renewed Hartree-Fock method [12, 13]. Although, the Hartree-Foch method was successful in explaining many-body effects in a number of systems, in many other systems, certain deviations still arose from the mean-field approximation. The deviations were collectively termed as correlations.

These 'correlations' have in parts contributions from the *Coulomb correlations* and from the *Fermi correlations.* The Fermi correlation is basically the contribution arising from the electronic exchange interaction, and was accounted for in the Hartree-Fock method. However, the Hartree-Foch method failed to account for the Coulomb correlations.

Later, several approaches were developed to account for the Coulomb correlation effects due to the electronic repulsion. These are known as the post Hartree-Fock methods. In this regard, a huge advancement was made with the development of the Hohenberg-Kohn theorem that led to uniquely defining a system's wave-function by its charge density ρ. This laid to the foundation of the highly successful density functional theory (DFT). A differential equation, referred to as the Kohn-Sham equation, is derived by the variation of energy functional $\mathrm{E}[\rho]$ depending on the local electronic charge density $\rho = \rho(r)$.

$$E[\rho] = T[\rho] + \int \rho(\mathbf{r}) V_{ext}(\mathbf{r}) d^3r + \int \frac{\rho(\mathbf{r})\rho(\mathbf{r'})}{\mathbf{r - r'}} d^3r d^3r' + E_{xc}[\rho] \tag{1.1}$$

Here $T[\rho]$ is the kinetic energy, V_{ext} is the external potential acting on the electrons, the third term is the Hartree-term for Coulomb interaction between electrons, and $E_{xc}[\rho]$ is the so-called exchange or correlation term. The Kohn-Sham equation for single electron wave functions are solved in an effective potential V_{eff} self consistently just like in the Hartree-Fock method. Simply put, the DFT is a direct generalization of the Hartree-Fock approach. The DFT approach would be exact if the explicit form of $E_{xc}[\rho]$ was known, but it is not the case. However, approximations like the local density approximation (LDA) and its spin counterpart, the local spin density approximation (LSDA) for exchange correlation energy have been highly successful in the DFT methods. Using these approximations, the DFT has been successfully applied to describe electronic properties of atoms, molecules and solids, where correlations are not too strong.

By 1989, it was realized that the problem can be further simplified by considering a large number of nearest neighbors, and then can be solved for any strength of the Coulomb repulsion as the spatial fluctuations can be neglected, leaving only time dependent on-site fluctuations [14, 15]. This laid the foundations of the dynamical mean-field theory (DMFT), which mapped lattice models to an effective impurity problem with correlated electrons experiencing a mean-field, which, this time, is dynamic, i.e., time or energy dependent. Dynamical mean-field methods clearly represent a new advance in the many-body physics, but they are still unable to capture numerous many-body effects in strongly correlated electron systems, such as the divergent behavior of the effective masses. This is why the generalization of DMFT to account for real materials is an active area of research. The above considerations demonstrate that *ab-initio* methods alone, in principle, cannot provide sufficient insights in the physics of the strongly-correlated electron systems because of their computational complexity and the unknowns involved.

Model Hamiltonian approach: The model Hamiltonian approach simplifies the full many-body Hamiltonian to take into account only the relevant degrees of freedom, i.e., the valence electron orbitals near the Fermi level. New insights have been achieved through model assumptions and simplification of initial many-body Hamiltonian. For example, one of the simplest models of correlated electrons, the Hubbard-Hamiltonian, simplifies the many-body problem by simply accounting for the interplay between electron hopping (t_{ij}) and local on-site repulsion U. But the model Hamiltonian approach can be used only for a limited number of simpler systems.

Quasiparticle approach: The much needed breakthrough to explain the behavior of strongly correlated electron systems came with a complimentary approach, the so-called quasiparticle approach. This approach replaced the many-body interacting particle ensemble by long-lasting excitations, interacting with each other, above a certain vacuum ground state. These excitations are referred to as the quasiparticles. The quasiparticle approach laid down the foundations of the renowned Landau theory of quasiparticles or the Landau Fermi-liquid theory.

1.1.4 Landau Fermi-liquid theory

The impleading problem to understand many-body interactions in a matter at low temperatures, that had been a bone of contention, was resolved to a great extent by the renowned Fermi-liquid (FL) theory. This theory was a significant advancement over established models for simpler systems, such as metals, where the electronic interactions are negligible. Simple statistical models, such as the Drude-model, that treated electrons in metals as a gas of non-interacting classical particles, and the Sommerfeld-model that treated metals as an ensemble of fermions, successfully explained metallic properties such as

1. a well defined Fermi surface [16],
2. the temperature dependence of the specific heat $C \propto \gamma T$,
3. the temperature dependence of the susceptibility $X_{para}(T) \simeq$ constant,
4. Wiedemann–Franz law i.e., $\kappa/\sigma \propto T$, where κ and σ are the thermal and electrical conductivities, respectively.

Since only non-interacting fermions are involved, these models are also referred to as the Fermi-gas models. However, these models are not useful when complex many-body interactions, such as the electron-electron interactions, become significant, like in SCES. Therefore, in an attempt to overcome the shortcomings of the Fermi-gas model, Landau proposed a revamp to the Fermi-gas model to account for electronic correlation effects in his Fermi-Liquid (FL) theory.

In his theory, Landau treated interacting electronic system's low energy excitations as quasiparticles. These quasiparticles are analogous to non-interacting fermions of the Fermi-gas model with the same spin, charge, momentum but have their dynamical properties, such as mass and magnetic moment modified or renormalized to take into account the interaction with other fermions. The quasiparticles have an associated finite lifetime, τ, such that $\hbar/\tau = k_BT$. The renormalization of quasiparticle effective masses is given by

$$m^* = m_0 \left(1 + \frac{F_l}{3}\right), \tag{1.2}$$

where F_l is the Landau renormalization parameter and m_0 is the free electron mass. In some strongly correlated electron systems, such as the so-called heavy fermions, m^* is huge and can be as large as 1000 m_0. The quasiparticle mass enhancement leads to a large density of states (DOS) at the Fermi level given as

$$N(\epsilon_F) = \frac{m^* k_F}{\pi^2 \hbar^2} \tag{1.3}$$

where k_F is the Fermi vector.

The quasiparticle mass and DOS renormalization enhances the electronic contribution to the specific heat as

$$C = \frac{\pi^2 k_B^2 N(\epsilon_F)}{3}\, T. \tag{1.4}$$

From equation 1.4, it is evident that qualitatively the behaviour of a Fermi-liquid is similar to a Fermi-gas, and is only renormalized according to the electron-electron interaction. Therefore, the ground state of the Fermi-gas model can be adiabatically transformed to the ground state of the Fermi-liquid model if the interaction is slowly turned on.

Furthermore, an important experimental indicator of the Fermi-liquid state is the resistivity, ρ, which scales as T^2 and has contributions from the inelastic electron-electron and umklapp scattering. It is written as

$$\rho = \rho_0 + AT^2. \tag{1.5}$$

Instability of the Fermi-liquid states were shown to lead to exotic phases in strongly correlated electron systems. The Pomeranchuk instability of the Fermi liquid towards a nematic phase is one of the prominent examples.

1.2 Heavy fermions

Heavy fermions (HF) are a special class of materials within the strongly correlated electron systems. HFs contain a rare-earth or actinide element with a partially filled f orbital. They are named as such because of the extremely enhanced quasiparticle effective masses, reaching up to 1000 times the bare electron mass in some cases.

In the HF systems, electrons in the f orbital of rare-earth elements like cerium and uranium lead to peculiar properties. It is the interplay of the f electron and conduction electrons internal degrees of freedom like spin, charge, and orbital moment, that exhibit exotic phenomena. This interplay makes heavy fermion systems extremely sensitive to small variations of external parameters, such as temperature, pressure, or magnetic field. The ground state in these systems is governed by two competing interactions, namely the Kondo interaction and the Ruderman–Kittel–Kasuya–Yosida (RKKY) interaction. In the following sections, I will discuss these two interactions in detail.

1.2.1 Kondo interaction

In an attempt to resolve the long puzzling low-temperature resistivity minima observed in several metals [see. Fig. 1.2], Jun Kondo proposed the idea of Kondo interaction [17, 18, 19, 20].

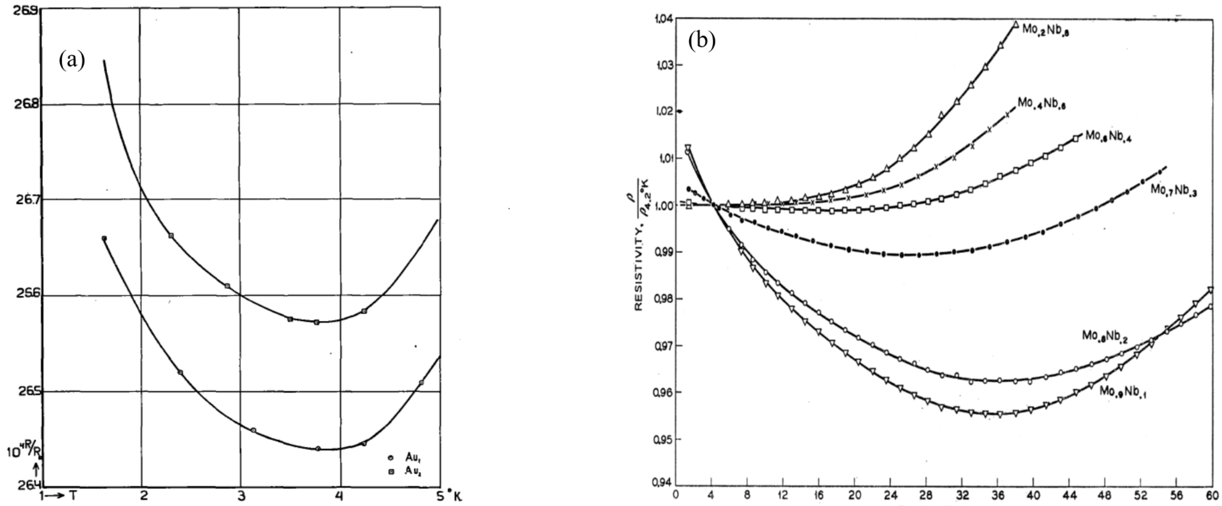

Figure 1.2: Resistivity minimum observed in (a) Gold Ref [17] and (b) $Mo_{1-x}Nb_x$ alloy Ref [19].

By 1960's, it was realized that the observed resistivity minima was due to dilution of metal with scant amount of magnetic impurities. When a magnetic impurity is placed in a sea of conduction electrons, an exchange coupling occurs between the localized magnetic moment of the magnetic impurity $\vec{S}$ and the conduction electrons spin $\vec{\sigma}$ of the host metal, given by

$$J\vec{S}.\vec{\sigma}, \tag{1.6}$$

where J is the effective strength of the exchange interaction. For $J < 0$, the exchange interaction tends to align the conduction electron spin in a direction opposite to that of magnetic impurity spin (antiferromagnetic coupling). Kondo considered this interaction of magnetic impurity and conduction electrons by including a higher order logarithmic scattering contribution due to spin-flip of the magnetic moment as

$$J^2 N(\epsilon) \log |\epsilon_F - \epsilon_k| \tag{1.7}$$

where ϵ_k is the energy of an electron, ϵ_F is the Fermi energy and $N(\epsilon)$ is the density of states at the Fermi level. This logarithmic contribution becomes significant for the electron energies close to the Fermi energy at finite temperatures i.e., $\epsilon_F - \epsilon_k \simeq k_B T$.

$$J^2 N(\epsilon) \log (k_B T) \tag{1.8}$$

This additional scattering term leads to an anomalous increase in resistivity with decreasing temperatures.

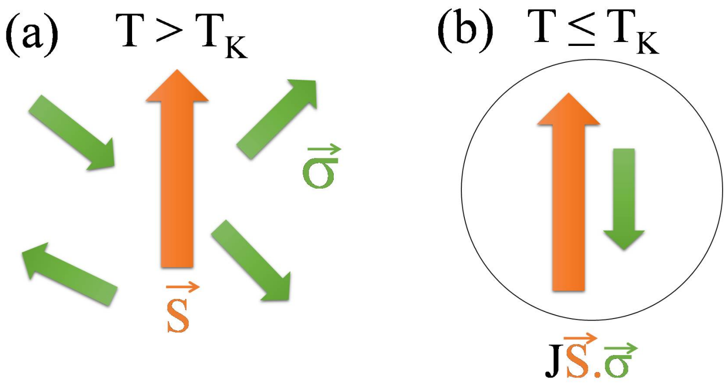

Figure 1.3: Formation of a Kondo singlet at low temperatures. (a) At $T \geq T_K$, local moment in a sea of conduction electrons. (b) Kondo singlet formed at $T \leq T_K$.

A schematic representation of the Kondo effect is shown in figure 1.3. At high temperatures, the impurity spin is only weakly coupled to the conduction electron, but at lower temperatures, the localized impurity moment is gradually screened out by the conduction electrons due to the AF coupling, resulting into a non-magnetic Kondo singlet [21].

The temperature below which the Kondo interaction takes prominence is characteristic of the system and is known as the Kondo temperature, T_K.

$$T_K \simeq \frac{1}{N(\epsilon)} e^{-1/JN(\epsilon)} \tag{1.9}$$

The Kondo temperature corresponds to the binding energy of a Kondo singlet. As Kondo interaction starts taking prominence, a local single impurity Kondo effect occurs and $\log T$ scattering term begins to contribute to the resistivity with decreasing temperatures until a maximum in resistivity is reached at $T = T_{coh}$ as indicated by the dashed line in Fig. 1.4. At T_{coh}, individual Kondo singlets develop coherence leading to a composite and coherent non-magnetic state. Therefore, at temperatures below T_{coh}, the resistivity drops sharply with decreasing temperature as shown in figure 1.4. Similarly, other physical properties are also affected as the localized moments are gradually screened. For example the Curie susceptibility ($\chi \propto 1/T$) of the localized moments changes to paramagnetic susceptibility at low temperatures ($\chi \propto 1/T_K$).

In heavy fermion systems, the lattice sites are occupied by ions containing f electrons acting as localized moments in a sea of conduction electrons. Such an arrangement is known as the Kondo lattice [23, 24]. Here, the Kondo interaction results in formation of an ensemble of local Kondo singlets which hybridize with the conduction band resulting into flatted hybridized bands separated by an energy gap close to the Fermi-level, as shown in Fig. 1.5 (a),(b),(c).

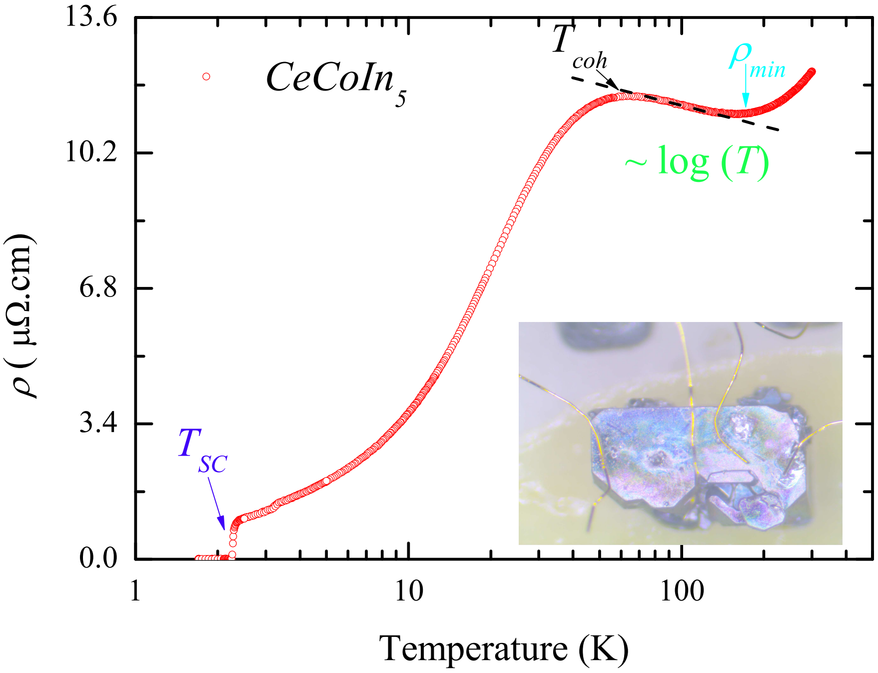

Figure 1.4: Kondo effect in the heavy fermion superconductor CeCoIn$_5$. Resistance of CeCoIn$_5$ showing the resistivity minima ρ_{min} at $T \sim 200\ K$, a $\log T$ increase below ρ_{min} upto the Kondo coherence temperature T$_{coh} \sim 50\ K$, and a superconducting transition at $T_{SC} = 2.3\ K$

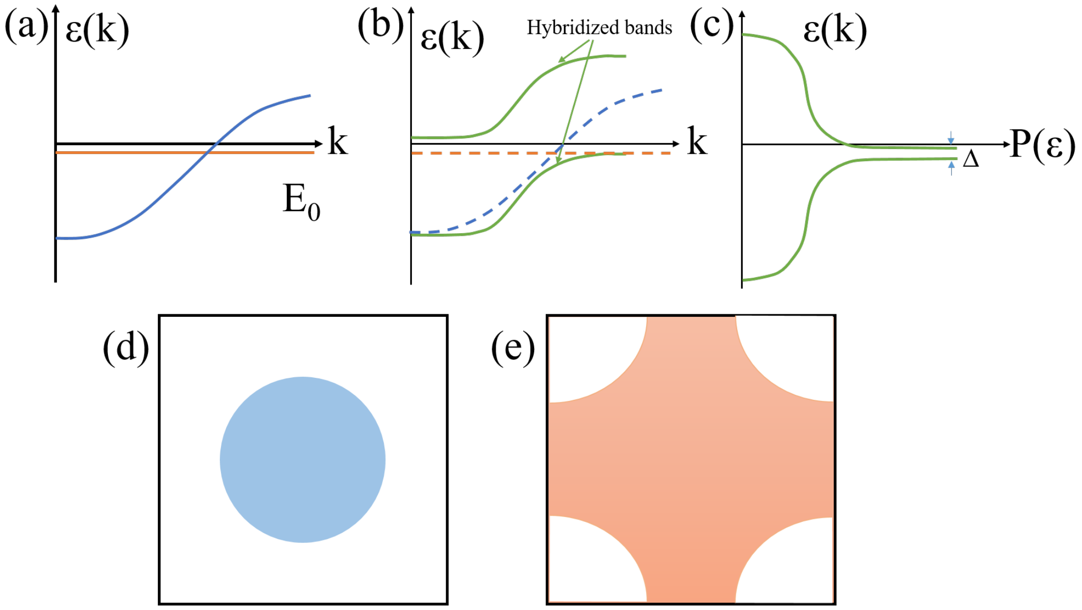

Figure 1.5: Lattice Kondo effect in a heavy fermion system. (a) The energy dispersion relation for the conduction band (in blue) and the localised moment (orange). (b) resulting flattened heavy band (green) as Kondo singlets hybridize with the conduction band (c) Density of states of hybridized bands separated by a band gap Δ. Fermi surface corresponding to (d) localized and (e) hybridized states. Adapted from Ref. [22]

These hybridized bands have renormalized/enhanced quasiparticle effective masses, which in turn renormalize the dynamical physical properties as discussed in the Fermi-liquid theory. The hybridized state is referred to as the heavy-fermion state due to heavy effective masses of the quasiparticle involved. Furthermore, in the heavy fermion state, the Fermi surface grows [25, 26] due to the additional contribution coming from the f electrons compared to the non-hybridized/localized state, where only the conduction electrons forms the Fermi surface (Fig. 1.5(d),(e).)

Therefore, in f-electron systems, the Kondo interaction favours a non-magnetic heavy-fermion ground state. Next, I will discuss the RKKY interaction.

1.2.2 Ruderman Kittel Kasuya Yosida interaction

As discussed in the previous section, due to the Kondo effect, a localized moment in a sea of conduction electrons is effectively screened out by a cloud of conduction electrons coupled anti-ferromagnetically to it. The reorganization of the conduction electrons at the localized moment alters the remaining of the conduction electron sea with a nearly periodic modulation damping sinusoidally, known as the Freidel oscillations, as shown in Fig. 1.6.

In an atomic arrangement, such as the Kondo lattice, the localized moments positioned at the lattice sites can interact with each other indirectly through the Friedal oscillations of the conduction electrons. This indirect exchange between the localized moments is known as the RKKY interaction.

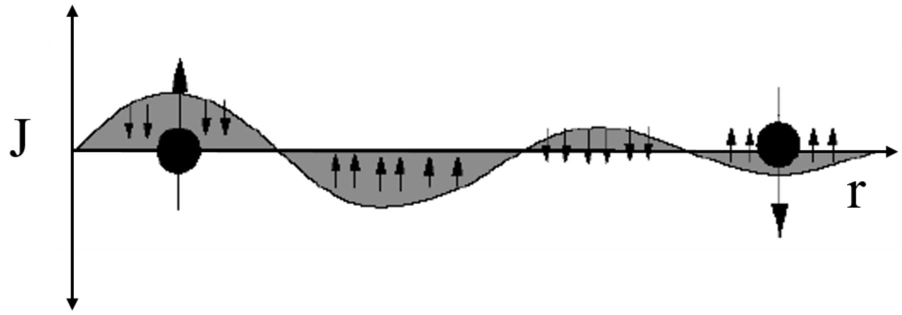

Figure 1.6: Indirect exchange between localized moments due to the Friedel oscillations of the conduction electrons

The effective strength of the RKKY interaction damps sinusoidally with the Fermi wave vector $2k_F$ [27], given as

$$J(r) \propto J^2 N(\epsilon) F(2k_F r), \tag{1.10}$$

where

$$F(x) = \frac{xcosx - sinx}{x^4} \tag{1.11}$$

The RKKY interaction ($T_{RKKY} \propto J^2 N(\epsilon)$) tends to align the localized moments in ferromagnetic or anti-ferromagnetic order depending on the moment of the localized ions, k_F and lattice parameters (i.e. position of the localized f ions). Therefore, the RKKY interaction favours a magnetic ground state.

1.2.3 Doniach phase diagram

From the discussion in the preceding sections it is clear that the Kondo and the RKKY interactions favour ground states of opposing nature, i.e., non-magnetic and magnetic, respectively. Therefore, the competition of the two interactions becomes crucial in determination of the overall physical properties of Kondo lattices or heavy fermion systems. This competition was beautifully summarized in 1977 by S. Doniach in his famous Doniach phase diagram [24], shown in figure 1.7.

This diagram depicts the competition between the energy scales corresponding to the Kondo ($T_K \simeq N(\epsilon)^{-1} e^{-1/JN(\epsilon)}$) and the RKKY ($T_{RKKY} \propto J^2 N(\epsilon)$) interactions as a function of strength of the exchange/coupling constant and DOS at the Fermi level.

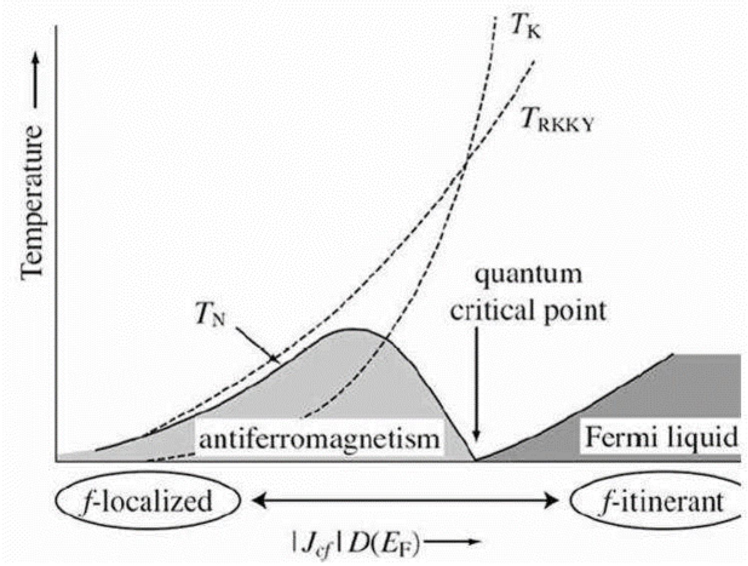

Figure 1.7: Doniach phase diagram from Ref. [24]. The x axis represents the strength of the exchange/coupling constant times DOS at the Fermi level. The y axis represents the energy scale in terms of temperature

The RKKY interaction dominates for weak exchange coupling, i.e., $JN(\epsilon)$ less than a critical value $J_cN(\epsilon)$, resulting into a magnetic ground state. For strong exchange coupling, i.e., $JN(\epsilon) > J_cN(\epsilon)$, the Kondo effect dominates, resulting in the formation of coherent Kondo singlets at low temperatures, i.e., the non-magnetic Fermi-liquid state. A continuous variation of $JN(\epsilon)$ from weak to strong coupling regime changes the ground state of the Kondo lattice system from magnetically ordered to a non-magnetic Fermi-liquid state that occurs through a continuous or second-order phase transition at $J = J_c$. Such a continuous phase transition at the absolute zero temperature is known as a quantum phase transition and occurs at the quantum critical point $(0\ K, J_cN(\epsilon))$(see fig. 1.8). Experimentally, the QCP can be achieved by tuning the exchange coupling constant using a non-thermal parameter such as pressure, magnetic fields, uniaxial-stress, or chemical substitution.

In the vicinity of a quantum phase transition, novel exotic states of matter arise. Next, I shall discuss the exotic physics that arises near a QCP.

1.2.4 Quantum criticality

In the Kondo lattice systems, a quantum phase transition (QPT) usually separates an ordered state from a disordered one, such as a magnetically-ordered state from a magnetically-disordered state.

Generally, a continuous phase transition is identified with a finite order parameter in the ordered state that vanishes across the transition into the disordered state. As $T \to T_c$, the system approaches classical criticality and thermal fluctuations of the order parameter grow in the vicinity of the critical point and become long-ranged and diverging at a classical critical point, i.e, $T = T_c$. The green shaded region in Fig. 1.8 depicts the growing thermal fluctuations of the order parameter at the classical order-disorder transition boundary as classical criticality is approached.

On the other hand, for temperatures significantly smaller than T_c, thermal fluctuations ($\sim k_BT$) become comparable/smaller than quantum fluctuations arising due to the Heisenberg uncertainty principle given by

$$\Delta E = \hbar\omega \sim \frac{\hbar}{\tau_c}, \tag{1.12}$$

where τ_c is the decay time scale associated with quantum fluctuations.

As $T \to 0$, quantum fluctuations dominate over thermal fluctuations, $\hbar\omega > k_BT$, and, thereby, become the driving force of the associated quantum phase transition [28, 29]. At $T = 0$, the critical

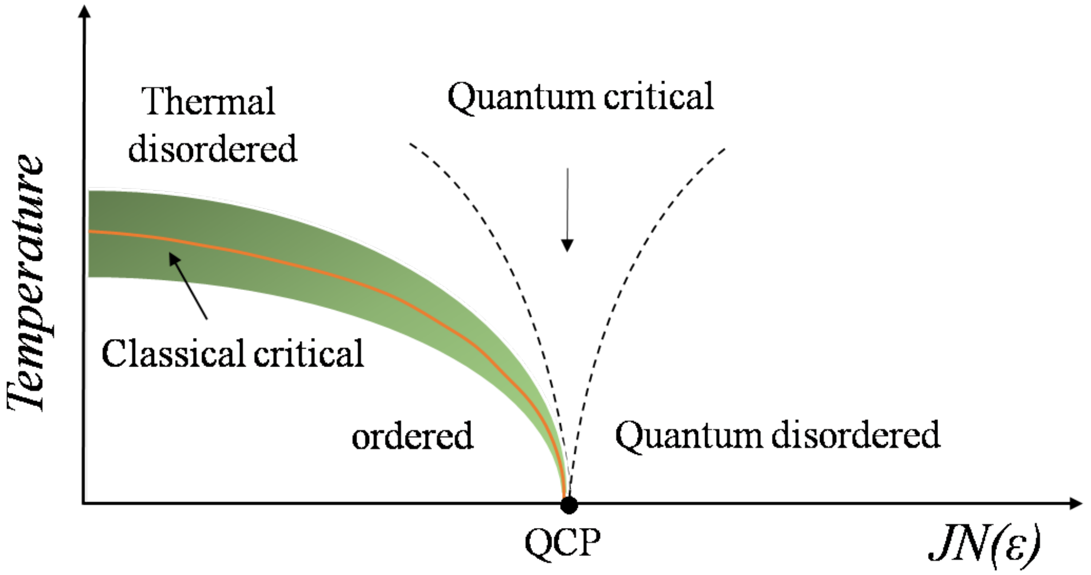

Figure 1.8: Phase diagram for a strongly correlated electron system showing a QPT. The black dotted line depicts the quantum critical region. The orange solid line depicts a classical phase transition and corresponding thermal fluctuations are shown by the green shaded region (see text for details).

value of the non-thermal tuning parameter where quantum fluctuations diverge is known as the quantum critical point (QCP) [30, 31, 32, 33, 34].

The region of enhanced quantum fluctuations or the 'zero point motion' in the vicinity of the QCP is known as the quantum critical region. This region houses rich exotic physics in form of a quantum matter. For instance, the interaction of quantum fluctuations with Fermi-liquid quasiparticles leads to a deviation from the Fermi-liquid behavior to a non-Fermi liquid behaviour [35, 36] observed in various physical properties, such as

1. Resistivity : $\rho(T) = \rho_0 + AT^n$ where $1 < n < 1.5$,
2. Specific heat : $C \propto -lnT$
3. Susceptibility : $\chi \sim \chi_0\,(1 - c(T/T_0))$.

Moreover, in very clean samples, unconventional superconductivity has been observed near the QCP [37, 38]. Several other exotic novel phases, like electron-nematic state [39, 40, 41, 42, 43], have also been observed in the vicinity of the QCP. The possibility to explore such rich quantum states of matter makes QCP's a central topic of research in modern condensed matter physics. Another related problem is to understand how enhanced quantum fluctuations lead to exotic novel phases. In this regard, heavy fermion systems are an ideal playground to study quantum criticality. As illustrated in Doniach phase diagram, heavy fermion systems can be conveniently driven across a QCP. And for this purpose, magnetic field, in particular, is a rather convenient/clean parameter for investigation, as it can be varied continuously to tune the same system across the QCP to different quantum states.

Before moving to investigations of heavy fermions, I shall discuss theoretical models dealing with the physics close to a QCP. While there is some consensus in this regard, a generalized understanding is still elusive.

Types of Antiferromagnteic QCPs

Currently, the physics close to a QCP separating an antiferromagnetic state from the heavy Fermi-liquid/Kondo state is understood by classifying the QCPs into two different classes. The first one is the local or Kondo-breakdown type, and the second one is the spin density-wave type QCP.

1. Local or Kondo-breakdown type QCP

The local or Kondo-breakdown type QCP refers to a quantum criticality scenario, in which the paramagnetic Fermi-liquid state abruptly *breaks down* when a system crosses the QCP and enters into the antiferromagnetic state [30, 44, 45, 46].

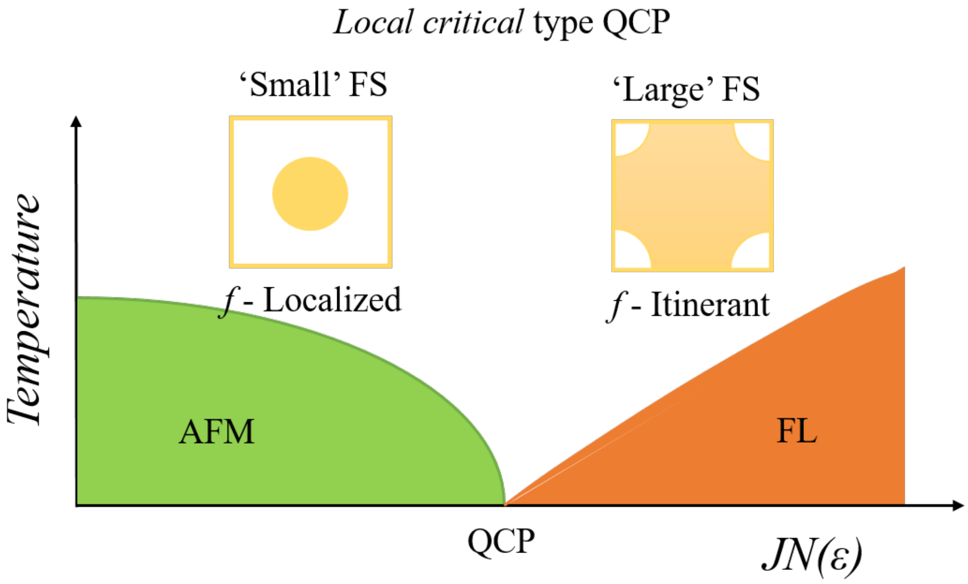

Figure 1.9: Local or Kondo-breakdown type quantum critical point. The Fermi surface and the f electron character change abruptly across the QCP.

The Kondo state breakdown is accompanied by a change in nature of the f electrons. From being itinerant in the Fermi liquid state due to hybridization with the conduction electrons, the f electrons decouple from the conduction band and become localized at the ionic sites upon entering the magnetically ordered state. As a consequence of localization, the f electrons cease to contribute to the Fermi surface leading to an abrupt reconstruction of the Fermi surface, i.e., from a 'large Fermi surface' corresponding to itinerant f electrons to a 'small Fermi surface' corresponding to localized f electrons. Furthermore, at the Kondo breakdown type QCP, the effective masses of quasiparticles diverge everywhere on the Fermi surface. A schematic phase diagram for the Kondo-breakdown type QCP is shown in Fig. 1.9.

2. Spin Density Wave (SDW) type QCP

The SDW type QCP refers to a quantum criticality scenario, in which the transition from the heavy Fermi-liquid state to the antiferromagnetic magnetic state does not break the heavy quasiparticles abruptly, which remain intact upon crossing the QCP.

Across a SDW-type QCP, the f electrons remain itinerant and the Fermi surface largely unchanged. Fluctuations of the antiferromagnetic order parameter take prominence close to this QCP. The f itinerant antiferromagnetic phase in the vicinity of such a QCP is described in terms of a spin-density-wave order of the heavy quasiparticles of the paramagnetic state. The theoretical description is based on itinerant spin-fluctuation theory [47, 48, 49, 29, 50]. In this scenario, the effective masses diverge only on certain portions of the Fermi surface connected by the antiferromagnetic wave vector, i.e, the so-called hot-spots. The effective masses of quasiparticles on the rest of the Fermi surface remain unchanged. A schematic phase diagram for the SDW type QCP is shown in Fig. 1.10.

Since the Fermi surfaces with itinerant and localized f electrons possess different size and morphology, the two types of quantum critical points can be easily distinguished experimentally by performing Fermi surface studies across QCP. Similarly, the variation of effective masses across the QCP can also help in distinguishing the type of QCP. To this effect, Fermi surface studies based on

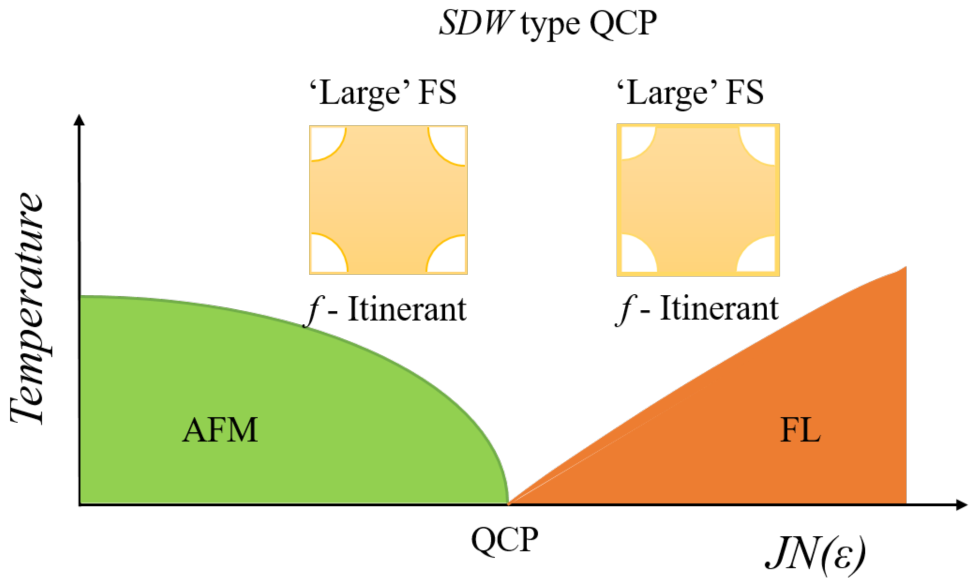

Figure 1.10: Spin density wave type quantum critical point. The Fermi surface and f electron character remain unchanged across the QCP.

quantum oscillations have proved to be of extreme importance [51, 52, 53]. As will be discussed in detail in the following sections, using quantum oscillations, the morphology of complicated Fermi surfaces, the quasiparticle effective masses, and several other important parameters such as the scattering length and the mean free path can be determined.

1.3 Probes to investigate heavy fermions

Several experimental probes are generally used to investigate various aspects of heavy fermions. Here I discuss the various probes used during this thesis.

1.3.1 Fermi surface studies and quantum oscillations

In the simplest of terms, quantum oscillations are periodic oscillations of the electronic density of states at the Fermi-level in magnetic fields. Quantum oscillations, therefore, naturally manifest themselves in every physical property that is directly or indirectly linked to the electronic density of the states at the Fermi level, like resistivity, magnetization, elastic constants, etc.

Landau quantization and the Onsager relation

Quantum oscillations are a direct consequence of the quantization of electronic energy levels in an applied magnetic field, and can be directly deduced from the electron motion in a magnetic field using a semi-classical approach and the Bohr-Sommerfeld quantization of the electron orbit [54] [55].

Motion of an electron in magnetic-field

For an electron moving in an uniform magnetic field (B), the equation of motion in the semi-classical approach can be simply written as the rate of the change of momentum ($\hbar\dot{k}$) due to the Lorentz force

$$\hbar\dot{k} = -ev_F(k) \times B \tag{1.13}$$

Here, e is the electronic charge, k is the wavevector representing the electron and v_F is the Fermi velocity deduced from the energy dispersion $(\epsilon - k)$ relation as

$$v_F(k) = \frac{1}{\hbar}\,\frac{\partial\epsilon(k)}{\partial k} \tag{1.14}$$

The Lorentz force acts perpendicular to the electron motion and does zero work on it. Therefore, the electron energy ϵ remains constant even as k changes with time as it traverses a trajectory in a magnetic field. Also, from eq. 1.14, v_F is the gradient of constant energy surfaces, and, since $\dot{k}$ is perpendicular to v_F, this implies that $\dot{k}$ must be tangential to the constant energy surface. Further, $\dot{k}$ is also perpendicular to B. Therefore, it follows that the end of the k vector traces out an orbit, which is the intersection of constant ϵ surface and a plane normal to B. This trajectory of electron motion can be obtained by integrating the equation 1.13 with respect to time

$$\hbar(k - k_0) = -e(R - R_0) \times B, \tag{1.15}$$

where R is the position vector of the electron in real space. Eq 1.15 implies that projection of the classical trajectory on to a plane normal to B is a scaled version of its trajectory in the k space with a 90° tilt, as shown in Fig. 1.11(a) and (b).

The electron traces this orbit periodically with an angular cyclotron frequency, ω_c, which can be calculated by substituting v_F from eq. 1.14 into eq. 1.13 as

$$\begin{aligned} dt &= \frac{\hbar^2}{e(grad_k(\epsilon \times B))}dk \\ &= \frac{\hbar^2}{eB}\frac{dk}{(\frac{\Delta\epsilon}{\Delta k'_n})} \\ &= \frac{\hbar^2}{eB}\frac{dk.\Delta k'_n}{\Delta\epsilon} \end{aligned} \tag{1.16}$$

Here, $k^{'}$ is the component of k normal to B and κ is the component parallel to B. $\Delta k^{'}$ is the change of the normal component $k^{'}$ over a time Δt. Δk is the change from one constant energy surface at $\epsilon(k)$ to another constant energy surface at $\epsilon + \Delta\epsilon(k + \Delta k)$. $dk.\Delta k'_n$ corresponds to an area element ΔS_n traced over a time dt [see fig. 1.11(c)].

Integrating eq. 1.16 over the whole orbit gives the time period $T = 2\pi/\omega_c$

$$\omega_c = \frac{2\pi eB}{\hbar^2}/(\frac{\partial S}{\partial\epsilon})_\kappa \tag{1.17}$$

Now, according to the Bohr-Sommerfeld quantization rule the resulting semi-classical orbit is quantized 1.18 as following

$$\oint p.dq = (r + \gamma)2\pi\hbar \tag{1.18}$$

In our case, the canonical momentum is $p = \hbar k - eA$, where A is the vector potential defined as $B = \nabla \times A$, and the canonical position is $q = R'$, where R' is the projection of the real space orbit on the plane perpendicular to B. Therefore, substituting these two in eq. 1.18, we have

$$\oint(\hbar k - eA).dR' = (r + \gamma)2\pi\hbar \tag{1.19}$$

From eq. 1.13, substituting $\hbar k = e\,(R \times B)$

$$\oint(R \times B).dR' - \oint A.dR' = (r + \gamma)\frac{2\pi\hbar}{e} \tag{1.20}$$

Using Stokes theorem $\oint A.dR' = \int_S(\nabla \times A)dS = \int_S B.dS$, we have

$$B.\oint(R \times dR') - \int_S B.dS = (r + \gamma)\frac{2\pi\hbar}{e} \tag{1.21}$$

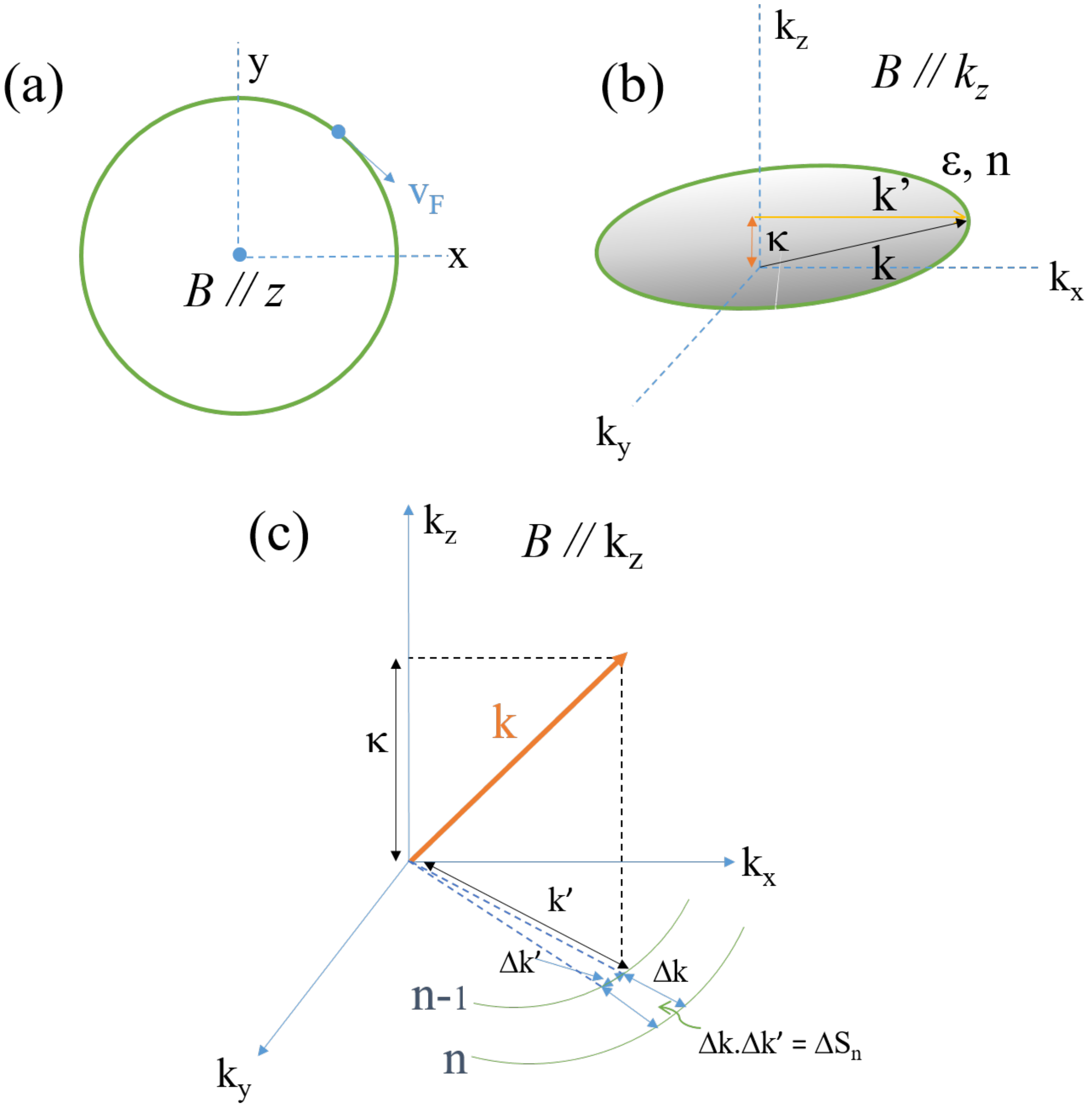

Figure 1.11: Motion of an electron in a plane perpendicular to the magnetic field in an orbit in (a) real space and (b) corresponding motion in k-space, which is a scaled version of the orbit in real space with a 90° tilt, as discussed in the text. (c) area ΔS_n between $n-1^{th}$ and n^{th} levels traced by the electron at a fixed κ.

Now, $\oint (R \times dR') = 2a$, where a is the area of the orbit in real space. Therefore, we have

$$B.2a - \int_S B.dS = (r+\gamma)\frac{2\pi\hbar}{e} \tag{1.22}$$

$\int_S B.dS = B.a$ is simply the magnetic flux ϕ through the orbit, which gives

$$\begin{aligned} 2\phi - \phi &= (r+\gamma)\frac{2\pi\hbar}{e} \\ &= (r+\gamma)\frac{2\pi\hbar}{e} \qquad (1.23) \end{aligned}$$

Equation 1.23 implies that the motion of an electron in a magnetic field is quantized into orbits in real space such that the magnetic flux through these orbits is a multiple of the universal quantum of flux $(2\pi\hbar)/e$.

This quantization of the electron orbit can be obtained in the reciprocal or k space by a simple transformation, using equation 1.13, which can be rewritten as

$$\frac{dr}{dt} = \frac{\hbar}{eB}\left(\frac{dk}{dt}\right) \tag{1.24}$$

For a infinitesimally small change of position over a time Δt, $dr/dt = \Delta r/\Delta t$.

$$\begin{aligned} \Delta r &= \frac{\hbar}{eB}\Delta k \qquad (1.25) \\ a_n &= \left(\frac{\hbar}{eB}\right)^2 S_n, \qquad (1.26) \end{aligned}$$

where a_n is the area in real space and S_n is the area in k space.

$$\begin{aligned} \phi_n &= B.a_n \qquad (1.27) \\ &= B.\left(\frac{\hbar}{eB}\right)^2 S_n \qquad (1.28) \\ &= \left(\frac{\hbar}{e}\right)^2 \frac{1}{B} S_n \qquad (1.29) \end{aligned}$$

Using eq. 1.23, we obtain the renowned Onsager relation for the electron orbit quantization in k-space as

$$S_n = (n+\gamma)\frac{2\pi e}{\hbar} B \tag{1.30}$$

The above equation implies that in k-space, for a fixed quantum number n and a magnetic field B, the electrons move in an orbit of a fixed area $S_n = S_{\epsilon,\kappa}$ on a particular constant energy surface. The section of the plane normal to the magnetic field taken at a certain κ (component of k parallel to field) on a constant energy surface determines ϵ of S_n area orbit for that particular constant energy surface, as shown in Fig. 1.12(a). Variation of κ (implying k) will give such plane sections of area S_n on different constant energy surfaces. These plane sections, lying on discrete constant energy surfaces, can be visualized as a tube of the cross section area S_n and co-axial with the field direction, as shown in Fig. 1.12(b).

Similarly, for the fixed field B, such tubes with different cross-sections can be visualized for different quantum numbers. This family of tubes is referred to as the Landau tubes. These Landau tubes are just an extension of Landau levels, which, at a fixed κ, can be visualized as discrete energy levels lying on successive Landau tubes. To sum up, the Onsager relation states that the permitted electronic states in k-space lie on Landau tubes.

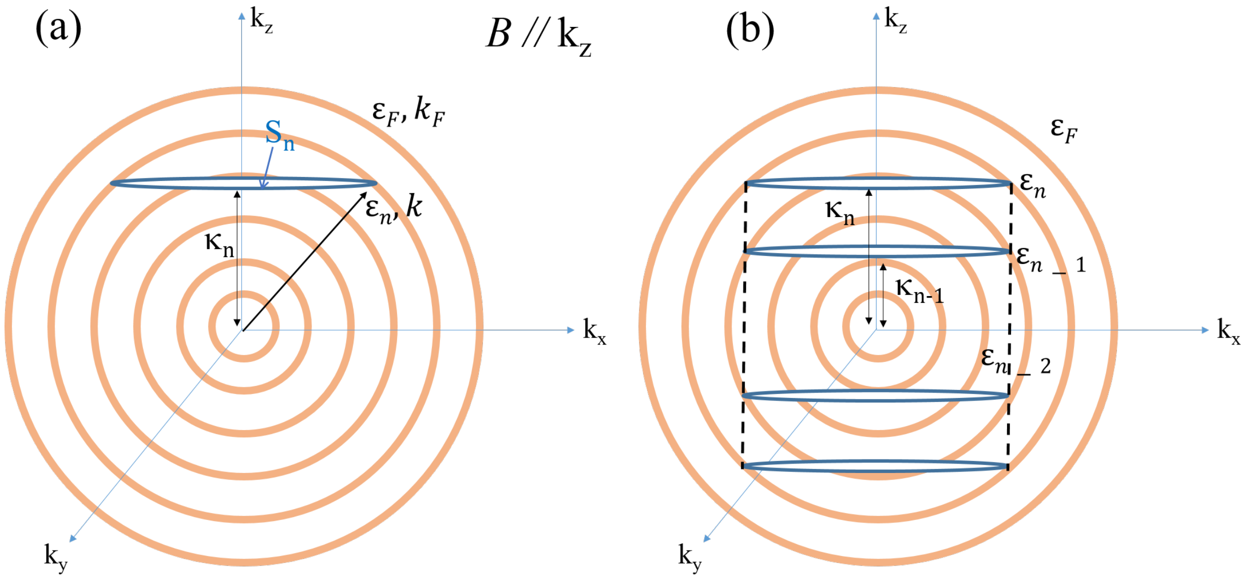

Figure 1.12: Simplified visualization of a Landau tube in k-space for a free electron gas. (a) A section of an orbit of area S_n taken at $\kappa = \kappa_n$ on the constant energy surface ϵ_n. (b) Similar sections of area S_n at different $\kappa's$ on different energy surfaces. A tube of the area S_n can be visualized along the black dotted lines.

Landau tubes for a Free electron gas

For the free electron gas, the Landau tubes are coaxial cylinders parallel to magnetic field, as shown in Fig. 1.13. The constant energy surface for the free electron gas is a sphere in k-space given as

$$\epsilon = \frac{\hbar^2 k^2}{2m_0} \tag{1.31}$$

where $k^2 = k_x^2 + k_y^2 + k_z^2$ is the square of the Fermi wave vector. Now, for the simple case of magnetic field along the k_z direction, $k_z = \kappa$. The intersection of constant energy sphere with a plane section at κ will be a circle of the area $S_n = \pi(k_x^2 + k_y^2)$. The free electron energy can then be written as

$$\epsilon = \frac{\hbar^2}{2m_0}\left(\frac{S_n}{\pi} + \kappa^2\right) \tag{1.32}$$

Using the Onsager relation for S_n, we get

$$\epsilon = (n + 1/2)\,\beta_0 B + \frac{\hbar^2 \kappa^2}{2m_0}, \tag{1.33}$$

where $\beta_0 = e\hbar/m_0 c$. Substituting $\epsilon(k)$ from eq. 1.31 into eq. 1.33, we obtain the equation for Landau tubes as

$$\frac{\hbar^2}{2m_0}(k_x^2 + k_y^2) = (n + 1/2)\beta_0 H \tag{1.34}$$

The energy difference between two neighbouring Landau levels, i.e., at a given κ and for the successive quantum numbers n and $n+1$ can be obtained from Onsager relation and eq. 1.17 as

$$\begin{aligned} (\Delta\epsilon)_{\Delta n=1} &= \left(\frac{\partial\epsilon}{\partial S}\right)_{\kappa} (\Delta S)_{\Delta n=1} \\ &= \frac{2\pi e B}{\hbar}\left(\frac{\partial\epsilon}{\partial S}\right)_{\kappa} \\ &= \hbar\omega_c && (1.35) \\ &= \beta B, && (1.36) \end{aligned}$$

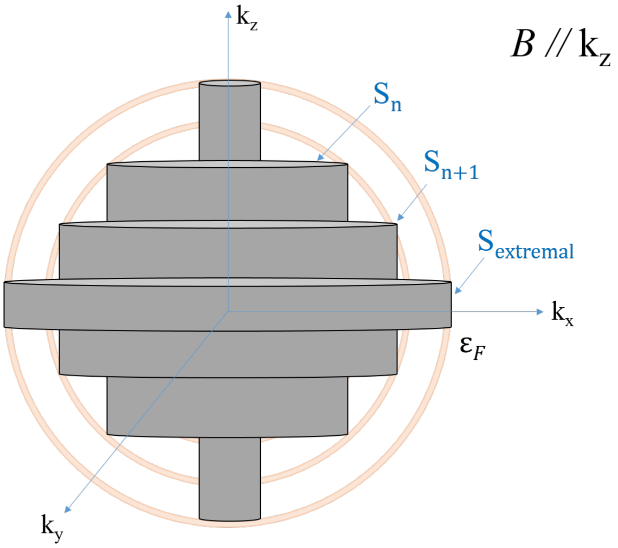

Figure 1.13: Landau tubes as a set of coaxial cylinders parallel to B for a free electron gas.

where $\beta = \frac{e\hbar}{m}$, and $m = \frac{\hbar^2}{2\pi}\left(\frac{\partial S}{\partial \epsilon}\right)_\kappa$ is the cyclotron mass.

Quantum oscillations

The Onsager relation states that for a fixed κ and n, the cross-section of a Landau tube S_n is proportional to the applied magnetic field B. At the Fermi surface, the cross-section of the Landau tube is equal to the extremal cross-section of the Fermi surface (S_{ext}) perpendicular to the magnetic field direction.

Therefore, if n^{th} Landau tube at a magnetic field B_n coincides with the Fermi surface, i.e., $S_n = S_{ext}$, then we have

$$\frac{S_n}{B_n} = (n+\gamma)\frac{2\pi e}{\hbar} \tag{1.37}$$

Now with increasing magnetic field, the area of Landau tubes will increase such that at a higher field B_{n+1}, the n^{th} tube will cross the Fermi surface, while its immediate neighbor, the $(n-1)^{st}$ Landau tube, will coincide with the Fermi surface, i.e., $S_{n-1} = S_{ext}$. Thus we have

$$\frac{S_{n+1}}{B_{n+1}} = \frac{2\pi e}{\hbar}(n+1+\gamma) \tag{1.38}$$

Since at the Fermi level, $S_n = S_{n-1} = S_{ext}$, subtracting the above two equations, we get

$$\begin{aligned} S_{ext}\left(\frac{1}{B_{n+1}} - \frac{1}{B_n}\right) &= \frac{2\pi e}{\hbar} \\ \left(\frac{1}{B_n} - \frac{1}{B_{n+1}}\right) &= \frac{2\pi e}{\hbar S_{ext}} \\ \Delta\left(\frac{1}{B}\right) &= \frac{2\pi e}{\hbar S_{ext}} \qquad (1.39) \end{aligned}$$

This implies that equal increments in $1/B$ will produce orbits of the same size, S_{ext}. In other words, the occurrence of the Fermi surface extremal orbit (frequency) is periodic in $1/B$. In terms of the occupancy of the electronic states, according to the Fermi function, only the states below the Fermi level are occupied. Thus, with increasing magnetic field, as each Landau tube crosses the Fermi level ϵ_F, it will empty the electronic density onto the neighboring Landau tube just below ϵ_F. Therefore, the passage of consecutive Landau levels across the Fermi surface will cause a discontinuity in the density of states at the Fermi level with a periodic occurrence at $\Delta(1/B)$ intervals. These periodic variation of the density of state at the Fermi level is known as the quantum oscillations. The corresponding frequency F is given by the Onsager relation as

$$F = \frac{\hbar S_{ext}}{2\pi e} \tag{1.40}$$

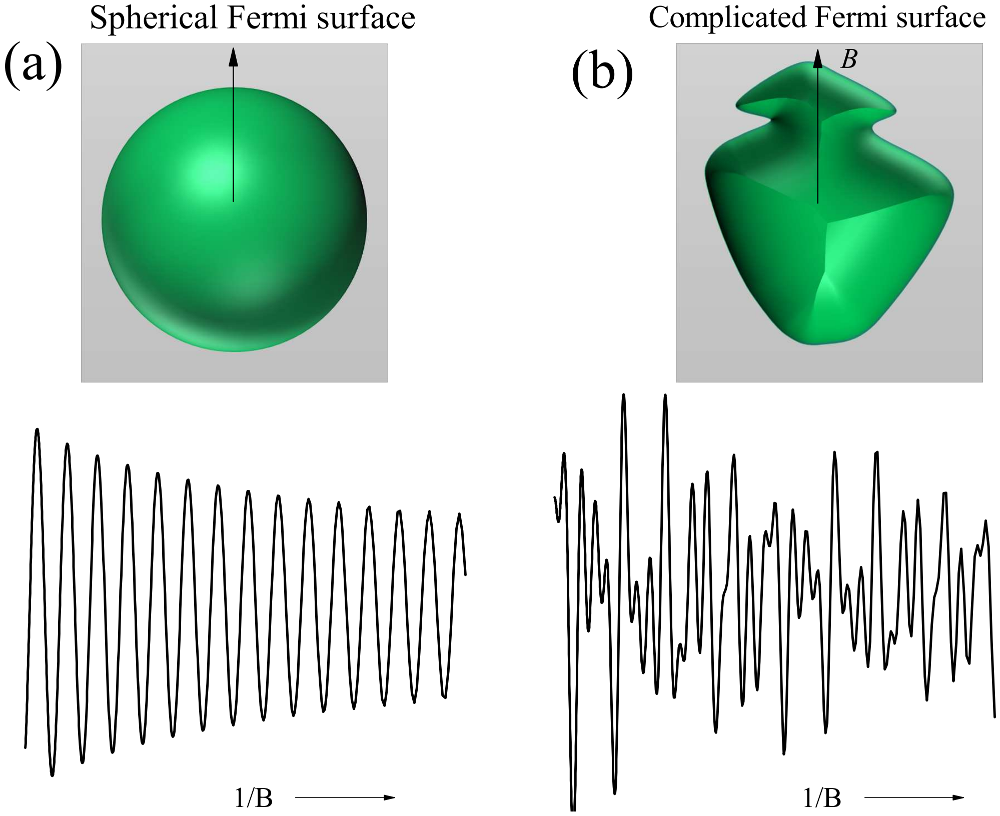

Figure 1.14: Quantum oscillations as a function of $1/B$ corresponding to (a) a spherical Fermi surface comprises of only one frequency (b) while a complicated Fermi surface (real system) comprises a superposition of multiple frequencies (the oscillations shown are not exact for FS but only a representation).

For a spherical Fermi surface, there is only one extremal orbit and, therefore, its quantum oscillations have only one frequency [see Fig. 1.14(a)]. For real systems, the Fermi surface is often more complicated due to the presence of multiple bands, and more than one extremal orbit are possible in the direction perpendicular to the field. Therefore, quantum oscillations observed for such a Fermi surface will be a superposition of several frequencies, as shown in Fig. 1.14(b).

Each frequency of quantum oscillations is directly proportional to an extremal cross-section of the Fermi surface perpendicular to the applied magnetic field. Therefore, a Fermi surface can be mapped exactly by measuring quantum oscillation as a function of the of magnetic field orientations, as shown in Fig. 1.15. As evident from Fig. 1.15(a) and (c), for spherical Fermi surface, the only quantum oscillation frequency remains unchanged for any orientation of the magnetic field. On the other hand, cylindrical Fermi surface, such as shown in Fig. 1.15(b), the single quantum oscillation frequency smoothly evolves with the field orientation, as shown in Fig. 1.15(c). Anisotropic Fermi surfaces usually have more than one frequency.

Every physical property dependent on the electronic density of states at the Fermi level, such as resistivity, magnetization and elastic constants (where electron-phonon coupling leads to QOs), inherently show quantum oscillations when measured as a function of the magnetic field. Therefore, by measuring such physical properties, the morphology of complex Fermi surfaces can be experimentally mapped.

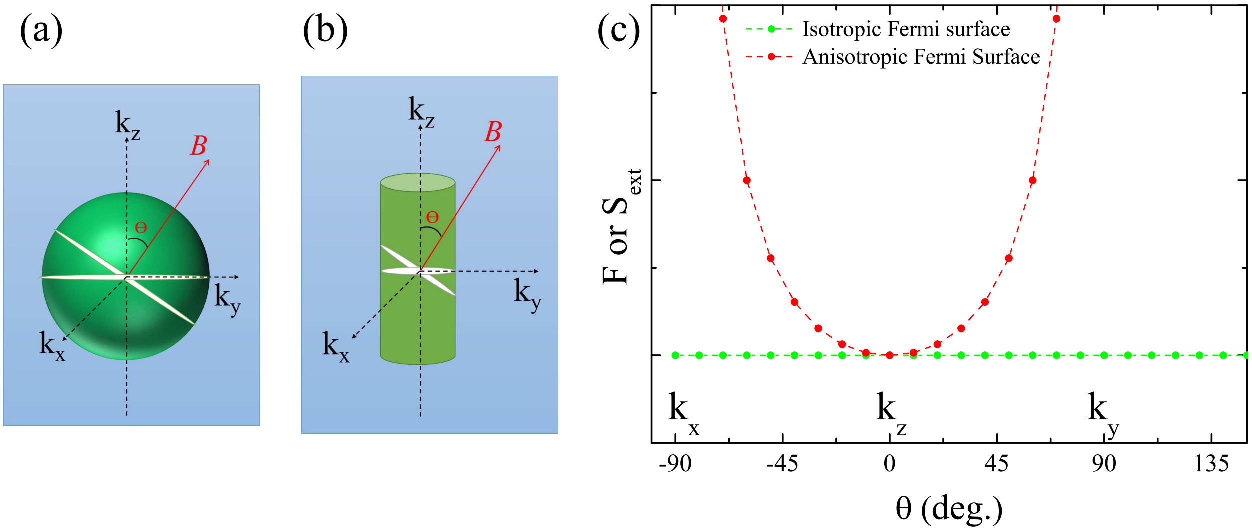

Figure 1.15: Fermi Surface topology of (a) a spherical and (b) a cylindrical Fermi surface determined through the angular variation extremal orbit in a direction perpendicular to magnetic field.

The de Haas-van Alphen effect

As discussed in the previous section, Landau quantization leads to quantum oscillations of the electronic density of states at the Fermi level that are reflected in most of the physical properties. The Quantum oscillations observed in magnetization, are known as the de Haas-van Alphen (dHvA) effect. The dHvA oscillations are described by the famous Liftshitz-Kosevich (LK) [56, 57] formula (eq. 1.44). The LK formula can be conveniently deduced from fundamental thermodynamics (see Ref. [54] for details). Magnetization, being a thermodynamic quantity, can be deduced from the thermodynamic potential Ω of a system defined as

$$\Omega = F - N\zeta, \tag{1.41}$$

where ζ is the chemical potential, N is the number of electrons, $F = E - TS$ is the free energy, E is the internal energy and S is the entropy of the system.

The vector magnetic moment can then be obtained as the derivative of Ω at constant ζ

$$\vec{M} = -\left(grad_B \Omega\right)_\zeta \tag{1.42}$$

Individually, the components of magnetization parallel, $M_\parallel$, and perpendicular, $M_\perp$, to B are obtained as

$$\begin{aligned} M_\parallel &= -(\partial\Omega/\partial B)_\zeta \\ M_\perp &= -\frac{1}{B}\left(\partial\Omega/\partial\theta\right)_{\zeta,B}. \end{aligned} \tag{1.43}$$

Here, θ is the angle specifying the direction of field in the plane in which Ω varies the most rapidly with the direction of field.

Lifshitz-Kosevich formula

The LK formula gives the oscillatory part of the magnetization (M_{osc}). Basically, M_{osc} comprises of a summation of dHvA oscillations corresponding to all the extremal cross-sections of the Fermi surface as well as their harmonics.

$$M_{osc} = \sum_r \sum_i \frac{(-1)^r}{r^{3/2}} A_i \; sin\left(\frac{2\pi r F_i}{B} + \beta_i\right) \tag{1.44}$$

Here, the summation running over i adds the dHvA oscillations F_i corresponding to the i^{th} extremal orbit of the Fermi surface. The summation running over r encompasses higher harmonics of the fundamental dHvA oscillations frequencies, F_i's. β_i is the phase shift. A_i is the amplitude of the i^th oscillation given as

$$A_i = \frac{e^{5/2} V F_i B^{1/2}}{(2\hbar)^{1/2}\pi^{5/2} m} \left|\frac{\partial^2 S_i}{\partial \kappa^2}\right|^{-1/2} R_T R_D R_S, \tag{1.45}$$

where V is the volume of the sample, and $\left|\frac{\partial^2 S_i}{\partial \kappa^2}\right|$ is the curvature factor that refers to the change of the cross-section area around the extremal orbit along the direction of the field. Therefore, while for a cylindrical Fermi surface, $\left|\frac{\partial^2 S_i}{\partial \kappa^2}\right|$ is small, leading to quantum oscillations with large amplitude, $\left|\frac{\partial^2 S_i}{\partial \kappa^2}\right|$ is large for a pancake like Fermi surface, resulting in smaller oscillations amplitude.

The multipliers R_T, R_D and R_S are known as the reduction factors, and are responsible for damping the amplitude of dHvA oscillations. R_T is the temperature reduction factor, R_D is the Dingle reduction factor and R_S is the spin damping factor. Each of these factors will be independently discussed in the following sections.

1. Temperature reduction factor (R_T)

The temperature reduction factor, R_T, refers to the effect of a finite temperature in smearing the amplitude of quantum oscillations and is given as

$$\begin{aligned} R_T &= \frac{\pi\lambda}{\sinh(\pi\lambda)} & (1.46)\\ &= \frac{2\pi^2 r k_B T/\beta B}{\sinh(2\pi^2 r k_B T/\beta B)}. & (1.47)\end{aligned}$$

Here $\lambda = 2\pi r k_B T/\beta B$ is the amplitude smearing factor, where $\beta = \frac{e\hbar}{m^*}$, with m^* being the quasiparticle effective mass renormalized by electron-electron and electron-phonon interactions.

For $\lambda = 2\pi r k_B T/\beta B \ll 1$,

$$R_T \approx 1$$

This implies that for $m^* \simeq m_0$, R_T approaches unity at low temperatures and high fields. Also, R_T is almost temperature independent at low temperatures. On the other hand, for $\lambda = 2\pi r k_B T/\beta B \gg 1$,

$$R_T = \frac{4\pi^2 r k_B T}{\beta B} e^{-2\pi^2 r k_B T/\beta B},$$

implying that for enhanced effective masses, the temperature reduction factor exponentially damps the dHvA amplitude even at low temperatures.

The temperature reduction factor with relevant parameters can be written in a simplified form as

$$R_T = \frac{\alpha r m^* T/B}{\sinh(\alpha r m^* T/B)} \tag{1.48}$$

where $\alpha = \frac{2\pi^2 k_B}{e\hbar} \simeq 14.69\ T/K$

The temperature dependence of the reduction factor R_T for different effective masses m^* (ranging from $1-100\ m_0$) is shown in Fig. 1.16. It is evident, that high magnetic fields and low temperatures are necessary to observe quantum oscillations corresponding to higher effective masses. For instance, in a commercially available superconducting magnet reaching upto moderate fields, say 18 T, quantum oscillations corresponding to very small effective masses, $m^* \simeq 1-2\ m_0$, can be easily observed at ^{4}He temperatures, while atleast ^{3}He temperatures are necessary to observe oscillations for $m^* \simeq 10\ m_0$ [Fig. 1.16(a)]. Even lower temperatures are needed, such as in the range of a dilution refrigerator temperature or lower, to observe quantum oscillations corresponding to still higher effective masses, i.e., $m^* \simeq 100\ m_0$. In a resistive or hybrid magnetic reaching upto higher fields, say 40 T, these quantum oscillations can be observed at higher temperatures as shown in Fig. 1.16 (b).

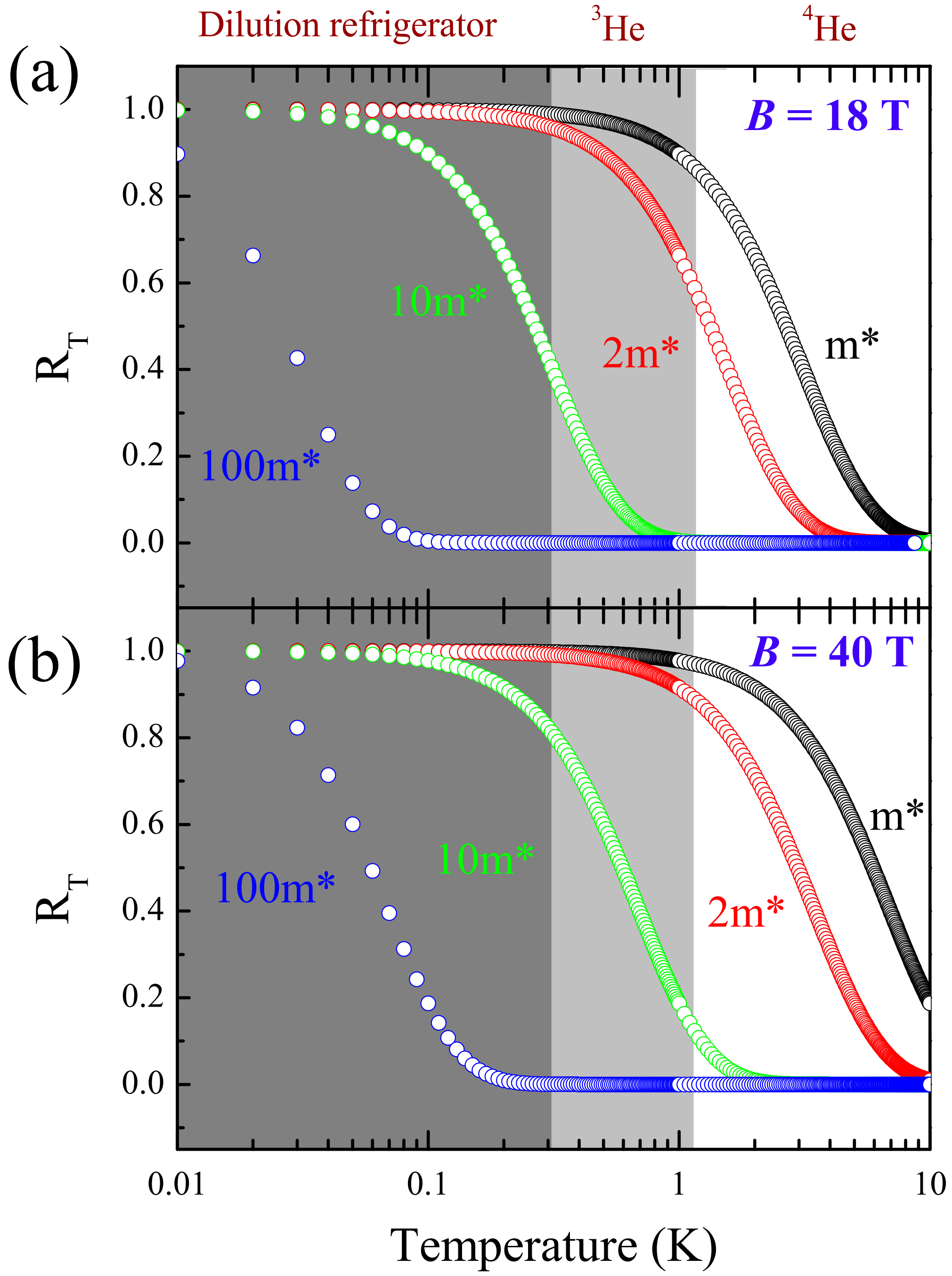

Figure 1.16: Temperature reduction factor to the dHvA amplitudes with different effective masses as a function of the temperature at two different magnetic fields (a) $B = 18$ T and (b) 40 T.

Effective masses

The effective masses corresponding to the dHvA oscillations can be experimentally determined as a consequence of the temperature reduction factor, since

$$A(T) = A_0 \; R_T \tag{1.49}$$

where $A(T)$ is the dHvA amplitude at temperature T and A_0 is the amplitude at the lowest temperature. A fit based on eq. 1.48 to the temperature dependence of dHvA amplitudes gives the effective mass as a fitting parameter.

2. Dingle reduction factor (R_D)

The Dingle reduction factor refers to the effect of scattering on the dHvA amplitude. Due to the scattering of electrons, either because of impurities or otherwise, there is an associated finite relaxation time, τ. As a result, the Landau levels are broadened according to the uncertainty principle. And the 'Dingle' reduction factor R_D due to the level broadening is given as

$$\begin{aligned} R_D &= exp(-\frac{2\pi^2 r k_B T_D}{\beta B}) \\ &= exp(-\frac{2\pi^2 r k_B T_D m^*}{e\hbar B}) \\ &= exp(-\frac{\alpha r m^* T_D}{B}), \end{aligned} \tag{1.50}$$

where $T_D = \frac{\hbar}{2\pi k_B}\frac{1}{\tau}$ is known as the Dingle temperature.

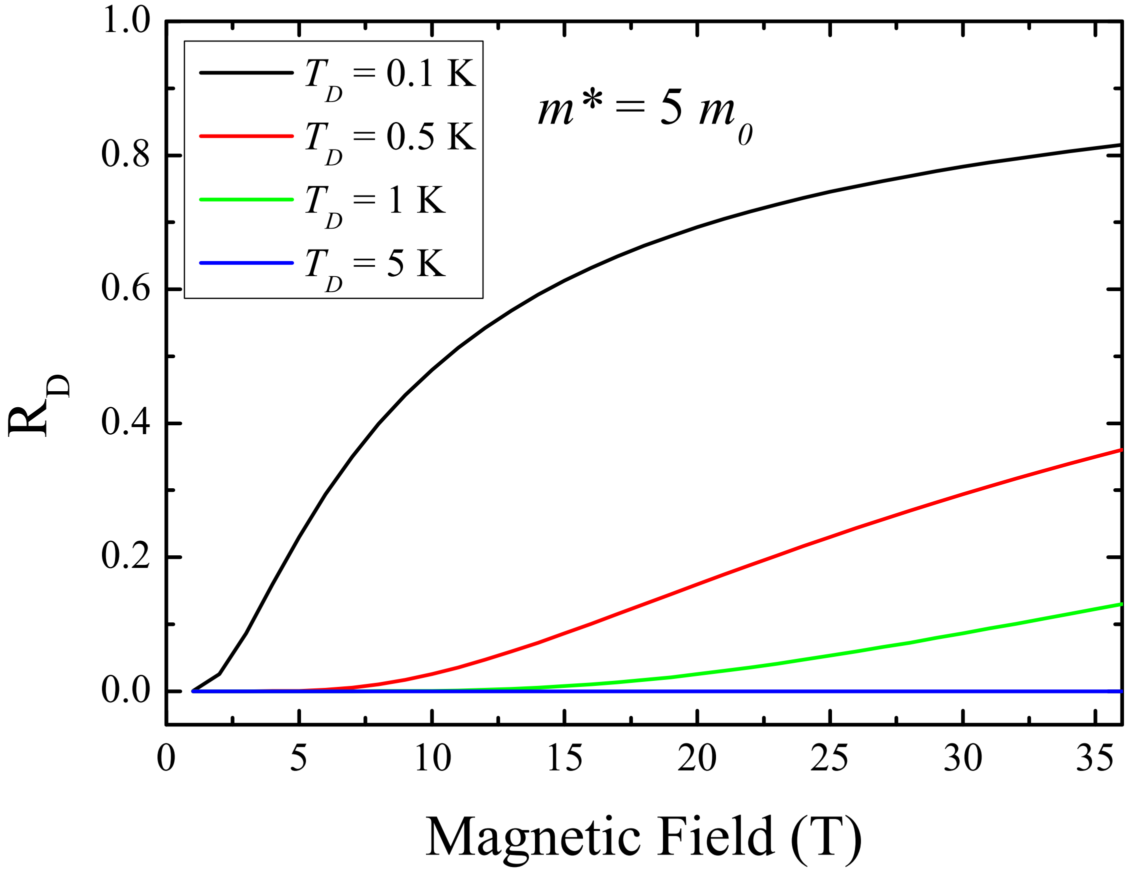

Figure 1.17: Dingle reduction factor as a function of magnetic field for a dHvA frequency with $m^* = 5m_0$ at a few different Dingle temperatures.

The Dingle reduction factor as a function of magnetic field for an orbit with $m^* = 5m_0$ at a few different Dingle temperatures is shown in Fig. 1.17. It is evident that the amplitude of dHvA oscillations at a constant field is diminished with increasing the Dingle temperature, i.e., increasing electronic scattering. This implies that the Dingle temperature has an effect on the dHvA amplitude equivalent to an increased temperature, $T_{eq} = T + T_D$. In this regard, the Dingle temperature becomes a rather important parameter to infer the quality of the sample depending on impurity scattering. It is pertinent to have samples with T_D as small as possible to observe quantum oscillations. Further, higher fields are needed to observe quantum oscillations in 'dirtier', samples, i.e. with a higher T_D.

Experimentally, the Dingle temperature of an orbit can be determined from the magnetic field dependance of its dHvA amplitude. Using eq. 1.45 and eq. 1.50, we have

$$A_i \propto B^{1/2} \frac{m^*T/B}{sinh(\alpha r m^* T/B)} exp(-\frac{\alpha r m^* T_D}{B}) \tag{1.51}$$

At a fixed temperature T, for an orbit with the effective mass m^*, the dHvA amplitude will be

$$A_i \propto B^{-1/2} \frac{exp\,(-\alpha r m^* T_D/B)}{sinh(\alpha r m^* T/B)} \tag{1.52}$$

Eq. 1.52 can be rewritten in the so-called Dingle plot [see Fig. 1.18] form as

$$ln \left[A(B) B^{1/2} sinh \left(\frac{\alpha m^* T}{B} \right) \right] = -\alpha m^* T_D \frac{1}{B} + const. \tag{1.53}$$

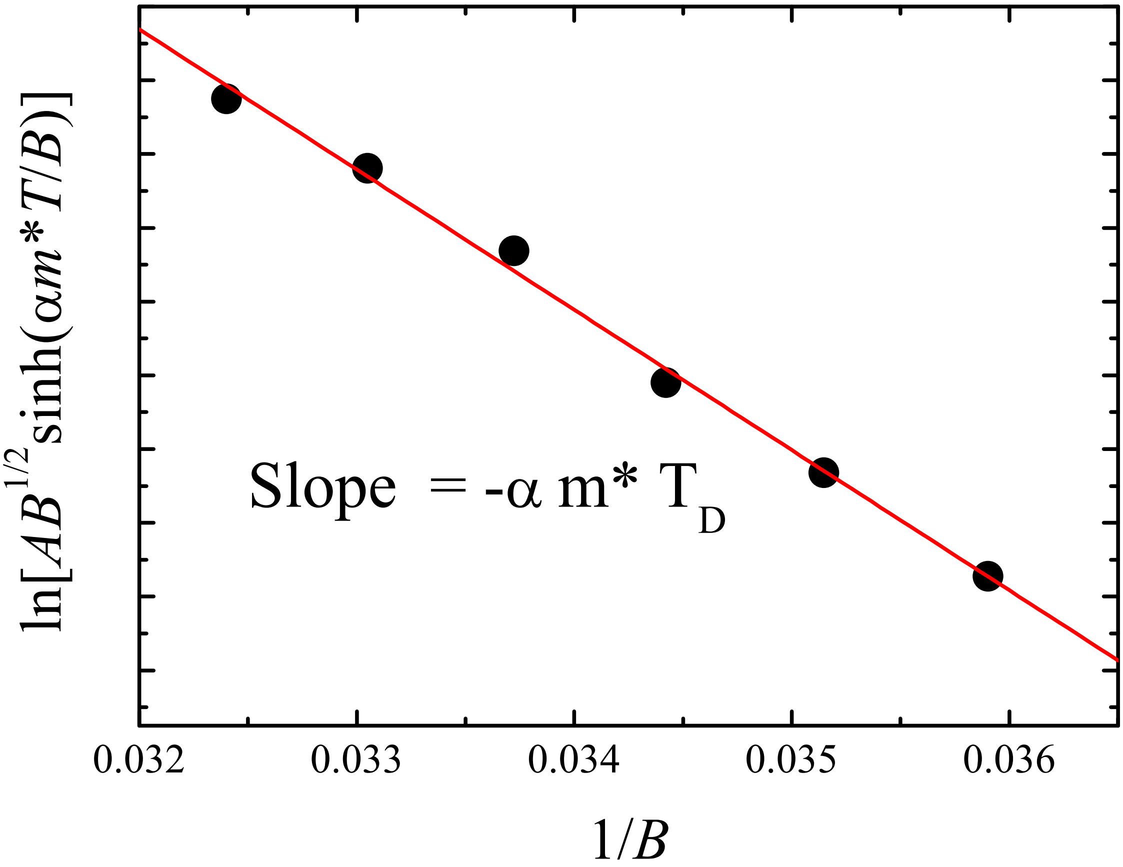

Figure 1.18: The evolution of dHvA amplitude with magnetic field plotted as the so-called 'Dingle plot'.

The Dingle temperature can then be determined from the slope of 'Dingle-plot' as

$$T_D = \frac{slope}{-\alpha m^*} \tag{1.54}$$

Apart from the indication of the sample quality, the electronic mean free path, $l = v_F\tau = \frac{\hbar k_F}{m^*}$ corresponding to individual orbits can also be deduced from the Dingle temperatures

$$l = \frac{\hbar r^2 k_F}{2\pi k_B m^* T_D}. \tag{1.55}$$

Since $S_{ext} = \pi k_F^2$, using Onsager relation, the mean-free path can be re-written as

$$l = \frac{\hbar^2}{2\pi k_B m^* T_D}\sqrt{\frac{2e}{\hbar}F} \tag{1.56}$$

The Dingle reduction factor is not renormalized by the many-body interactions.

3. Spin reduction factor R_S

The final reduction factor of the dHvA amplitude is the spin reduction factor R_S [58]. In an applied magnetic field, the spin degeneracy of the energy levels is lifted as

$$\epsilon \pm \frac{1}{2}\Delta\epsilon, \tag{1.57}$$

where $\epsilon = \frac{1}{2}g\beta_0 H$ with $\beta_0 = \frac{e\hbar}{m_0 c} = 2\mu_B$ (μ_B is the Bohr magneton). g is the Lande spin splitting factor, taken as 2 for free electron.

This splitting of an energy level is equivalent to a phase difference ($\phi = \frac{\Delta\epsilon}{\beta H}$) between the oscillations arising from the spin-up and spin-down electrons. Such a phase difference leads to a reduction of the dHvA amplitude. The overall amplitude of the oscillations will a superposition of amplitudes from spin-up and spin-down multiplied by the spin reduction factor, which, for r^{th} harmonic can be written as

$$\begin{aligned} R_S &= \cos(r\pi\phi/2) \\ &= \cos(r\pi\Delta\epsilon/\beta H) \\ &= \cos(r\pi g(m^*/m_0)/2) \\ &= \cos(r\pi S) \end{aligned}$$

The dHvA amplitude vanishes when the contributions from the two spins cancel each other. This is known as spin zero. The value of g can be determined from spin zero positions.

Apart from the above mentioned reduction factors, the sample and field inhomogeneity also lead to reduction of the dHvA amplitude.

Conditions for dHvA oscillations

Different reduction factors impose certain conditions that must be fulfilled to observe dHvA oscillations. These conditions are listed below.

1. Low temperature and high fields: At a finite temperature T, due to the thermal excitations $k_B T$, quasiparticles in states just below the Fermi-level are excited to states just above the Fermi level. This leads to the broadening of the density of states at the Fermi level. Unlike at $T = 0$, as a particular Landau level crosses the Fermi surface, the quasiparticles do not move abruptly to the Landau level just inside the Fermi surface, but rather gradually as the the Fermi level is broadened. Thus, for a discontinuity in electronic density of states to occur at the Fermi level, the temperature broadening $k_B T$ of the Fermi level must be much smaller than the distance between two consecutive Landau levels $\hbar\omega_c$, i.e.,

$$k_B T \ll \hbar\omega_c \tag{1.58}$$

which can be re-written as

$$\frac{B}{T} = \frac{m^* k_B}{\hbar e} \tag{1.59}$$

2. High quality samples: To observe quantum oscillations, the electron should be able to perform at least one cyclotron motion during the relaxation time, i.e., $\omega_c\tau > 2\pi$. This imposes a restriction on impurity scattering and, thereby, on the sample quality as

$$\tau > \frac{2\pi m^*}{eB} \tag{1.60}$$

In summary, the dHvA effect provides significant information about the electronic states in the vicinity of the Fermi energy. Information such as the Fermi surface morphology, effective masses are extremely useful to study quantum critical phenomenon on heavy fermion systems.

1.3.2 Heat capacity

Heat capacity is a direct thermodynamic response (ΔT) of a system to a supplied energy (ΔQ) and is given as

$$C = \lim_{\Delta T \to 0} \frac{\Delta Q}{\Delta T} \tag{1.61}$$

It is a classical probe to measure excited states of a system in a relevant temperature or energy range.

In a metal, the electronic contribution ($C_e = \gamma T$) to heat capacity becomes significant only at low temperatures where the lattice (phonon) vibrations start freezing and the phonoic contribution ($C_{ph} = \beta T^3$) becomes very small. If a magnetically ordered state occurs in the system, an additional magnetic contribution C_{mag} is added to the heat capacity as

$$C = C_e + C_{ph} + C_{mag} \tag{1.62}$$

The magnetic contribution is usually approximated using various models accounting for magnon and spin density wave terms.

In the electronic contribution $C_e = \gamma T$, γ is known as the Sommerfeld coefficient given by

$$\gamma = \frac{\pi^2}{2}\frac{N_0 k_B^2}{\epsilon_F} \tag{1.63}$$

Since the Fermi energy is inversely proportional to the mass of the particles, we have

$$\gamma \propto m \tag{1.64}$$

Therefore, the Sommerfeld coefficient is a direct indicator of the thermal effective masses of quaiparticles. Particularly, for heavy fermions, huge effective masses, which cannot be observed through quantum oscillations (due to the limitations discussed in previous sections), can be accounted for through the Sommerfeld coefficient. Therefore, γ, is an extremely important indication of the strong electronic correlations.

Furthermore, heat capacity measurements can act as a complimentary probe to establish if the Fermi surface is thoroughly determined through quantum oscillations or parts of it are missed, by comparing the sum of effective masses of individual orbits obtained through quantum oscillations with the thermal effective mass deduced from γ.

The most significant use of heat capacity is to experimentally identify and characterize thermodynamic phase transitions. Thermodynamic transitions involve an entropy change (for an ordered-disorder transition) or a latent heat change, which appears as a distinct feature in heat capacity. Therefore, heat capacity is often used as a classical probe to not only detect thermodynamic phase transitions, but also to establish order of the phase transition. A first-order thermodynamic phase transition manifests itself as a sharp δ-function like anomaly due to the involvement of the latent heat, while a second-order transition manifests itself as a distinct λ-like feature, as shown in Fig. 1.19.

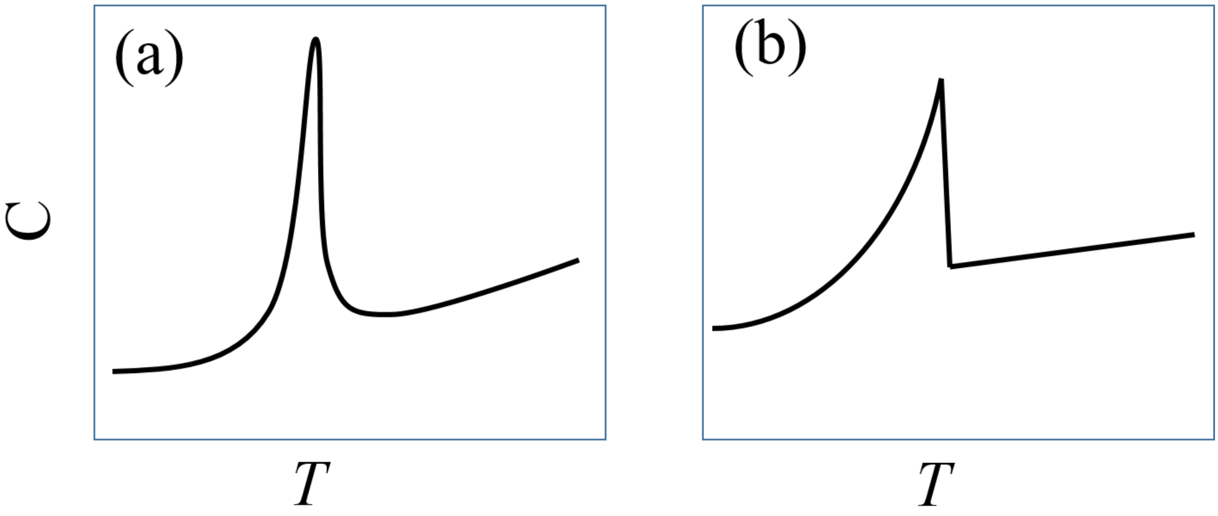

Figure 1.19: Schematic representation of (a) a first-order transition as a δ-like feature and (b) a second-order transition as a λ-like feature in specific heat.

1.3.3 Elastic constants

Similar to heat capacity, elastic modulus of a material is also a thermodynamic quantity. But, instead of supplied heat, elastic constants are a response to applied strains and can be obtained as the second-derivative of the free energy of a system, i.e.,

$$c = \frac{d^2F}{de} \tag{1.65}$$

where c is the elastic constant, F is the free energy of the system, and e is the applied strain.

Usually, the electronic character of a system is coupled, up to a certain degree, to the crystal lattice due to electron-phonon coupling. In cases where this coupling is strong enough, the electronic properties can be detected as a lattice response using dilatometric probes.

The remarkable aspect of the elastic response is that, a thermodynamic phase transition appears as a sharp, distinct anomaly in relevant elastic constants due to the strain-order parameter coupling. Therefore, the symmetries of an order-parameter associated with a phase transition can be determined. Furthermore, complex phase transitions that break only certain symmetries of the underlying electronic-magnetic structure, such as the electronic-nematic or exotic metamagnetic transitions, can also be studied as structural, magnetic, etc. degrees of freedom couple to specific elastic constants. Therefore, probing elastic properties is a vital tool to investigate intricate aspects of unknown phase transitions in heavy fermion systems.

Before moving to a discussion on how to investigate heavy fermion physics using elastic properties, I shall briefly discuss elastic constants of a tetragonal lattice, in which numerous heavy fermion materials crystallize. Further, I shall also discuss how an elastic constant or a combination of them can be measured using characteristic elastic waves.

Elastic constants for a tetragonal lattice

The elastic stiffness constants or simply elastic constants of a crystal lattice can be obtained from its response to elastic waves using the Hooke's law;

$$\sigma = ce, \tag{1.66}$$

where σ is the stress, c is the elastic stiffness constant, and e is the elastic strain.

According to the Hooke's law, the strain-stress relation for a cubic lattice is written as

$$\begin{array}{lcccccccccccc}
X_x & = & C_{11}e_{xx} & + & C_{12}e_{yy} & + & C_{13}e_{zz} & + & C_{14}e_{yz} & + & C_{15}e_{zx} & + & C_{16}e_{xy} \\
Y_y & = & C_{21}e_{xx} & + & C_{22}e_{yy} & + & C_{23}e_{zz} & + & C_{24}e_{yz} & + & C_{25}e_{zx} & + & C_{26}e_{xy} \\
Z_z & = & C_{31}e_{xx} & + & C_{32}e_{yy} & + & C_{33}e_{zz} & + & C_{34}e_{yz} & + & C_{35}e_{zx} & + & C_{36}e_{xy} \\
Y_z & = & C_{41}e_{xx} & + & C_{42}e_{yy} & + & C_{43}e_{zz} & + & C_{44}e_{yz} & + & C_{45}e_{zx} & + & C_{46}e_{xy} \\
Z_x & = & C_{51}e_{xx} & + & C_{52}e_{yy} & + & C_{53}e_{zz} & + & C_{54}e_{yz} & + & C_{55}e_{zx} & + & C_{56}e_{xy} \\
X_y & = & C_{61}e_{xx} & + & C_{62}e_{yy} & + & C_{63}e_{zz} & + & C_{64}e_{yz} & + & C_{65}e_{zx} & + & C_{66}e_{xy}
\end{array}$$

Here the quantities on left hand side are stresses, in which the capital letter denotes the direction of the force, and the subscript denotes the normal to the plane to which the force is applied. For an elementary cube, there are six independent stress component denoted by $X_x, Y_y, Z_z, Y_z, Z_x, X_y$.

The infinitesimal elastic change in length along the direction of applied stress is the elastic deformation or strain denoted by $\epsilon_{\alpha\beta}$, where $\alpha, \beta = x, y, z$ such that the displacement along the x, y, and z direction are u, v, and w, respectively. Therefore, we have the strain components defined in terms of elastic deformations as

$$\begin{aligned}
e_{xx} \equiv \epsilon_{xx} &= \frac{\partial u}{\partial x} \\
e_{yy} \equiv \epsilon_{yy} &= \frac{\partial v}{\partial y} \\
e_{zz} \equiv \epsilon_{zz} &= \frac{\partial w}{\partial z} \\
e_{xy} \equiv \epsilon_{yx} + \epsilon_{xy} &= \frac{\partial u}{\partial y} + \frac{\partial v}{\partial x} \\
e_{yz} \equiv \epsilon_{zy} + \epsilon_{yz} &= \frac{\partial v}{\partial z} + \frac{\partial w}{\partial y} \\
e_{zx} \equiv \epsilon_{zx} + \epsilon_{xz} &= \frac{\partial u}{\partial z} + \frac{\partial w}{\partial x}
\end{aligned} \tag{1.67}$$

Finally, the 36 quantities, $C_{i,j}$ (where $i, j = 1, 2, 3, 4, 5, 6$) are known as the elastic stiffness constants or moduli of elasticity and are inverse of elastic compliances or elastic constants.

For a particular lattice system, the elastic stiffness constants can be written as a tensor of rank 3. The $C_{i,j}$ are symmetrical, and thus the number of independent $C_{i,j}$ decrease from 36 to 21.

The number of $C_{i,j}$ is further reduced depending on the symmetries of the concerned crystal structure. For a cubic crystal symmetry, there are only 3 independent elastic stiffness constants, namely, C_{11}, C_{12}, C_{44} which can be written in a matrix form as

$$\begin{pmatrix} X_x \\ Y_y \\ Z_z \\ Y_z \\ Z_x \\ X_y \end{pmatrix} = \begin{pmatrix} C_{11} & C_{12} & C_{12} & 0 & 0 & 0 \\ C_{12} & C_{11} & C_{12} & 0 & 0 & 0 \\ C_{12} & C_{12} & C_{11} & 0 & 0 & 0 \\ 0 & 0 & 0 & C_{44} & 0 & 0 \\ 0 & 0 & 0 & 0 & C_{44} & 0 \\ 0 & 0 & 0 & 0 & 0 & C_{44} \end{pmatrix} \times \begin{pmatrix} e_{xx} \\ e_{yy} \\ e_{zz} \\ e_{yz} \\ e_{zx} \\ e_{xy} \end{pmatrix} \tag{1.68}$$

All the cerium-based heavy fermions belonging to the 115 and 218 families crystallize into a tetragonal crystal structure. Unlike the cubic lattice, a tetragonal crystal has 6 independent elastic stiffness constants namely, $C_{11}, C_{12}, C_{13}, C_{33}, C_{44}, C_{66}$ and can be written in a matrix form as

$$\begin{pmatrix} X_x \\ Y_y \\ Z_z \\ Y_z \\ Z_x \\ X_y \end{pmatrix} = \begin{pmatrix} C_{11} & C_{12} & C_{13} & 0 & 0 & 0 \\ C_{12} & C_{11} & C_{13} & 0 & 0 & 0 \\ C_{13} & C_{13} & C_{33} & 0 & 0 & 0 \\ 0 & 0 & 0 & C_{44} & 0 & 0 \\ 0 & 0 & 0 & 0 & C_{44} & 0 \\ 0 & 0 & 0 & 0 & 0 & C_{66} \end{pmatrix} \times \begin{pmatrix} e_{xx} \\ e_{yy} \\ e_{zz} \\ e_{yz} \\ e_{zx} \\ e_{xy} \end{pmatrix} \tag{1.69}$$

These elastic stiffness constants can be probed independently or as a combination using elastic waves that induce elastic deformations in the lattice.

Let us assume that an elastic wave, such as an ultrasonic wave, induces a displacement 'u' along the x-direction. Then, the equation of motion in the x-direction can be written as

$$\rho\frac{\partial^2 u}{\partial t^2} = \frac{\partial X_x}{\partial x} + \frac{\partial X_y}{\partial y} + \frac{\partial X_z}{\partial z} \tag{1.70}$$

where ρ is the density and u is the displacement along the x-direction. Using eq. 1.69, we have

$$\begin{aligned}
\rho\frac{\partial^2 u}{\partial t^2} &= C_{11}\frac{\partial\epsilon_{xx}}{\partial x} + C_{12}\frac{\partial\epsilon_{yy}}{\partial x} + C_{13}\frac{\partial\epsilon_{zz}}{\partial x} + C_{66}\frac{\partial\epsilon_{xy}}{\partial y} + C_{44}\frac{\partial\epsilon_{zx}}{\partial z} \\
&= C_{11}\frac{\partial^2 u}{\partial x^2} + C_{12}\frac{\partial^2 v}{\partial x\partial y} + C_{13}\frac{\partial^2 w}{\partial x\partial z} + C_{66}\left(\frac{\partial^2 u}{\partial y^2} + \frac{\partial^2 w}{\partial x\partial y}\right) + C_{44}\left(\frac{\partial^2 u}{\partial z^2} + \frac{\partial^2 w}{\partial z\partial x}\right) \\
&= C_{11}\frac{\partial^2 u}{\partial x^2} + C_{66}\frac{\partial^2 u}{\partial y^2} + C_{44}\frac{\partial^2 u}{\partial z^2} + (C_{12} + C_{66})\frac{\partial^2 v}{\partial x\partial y} + (C_{13} + C_{44})\frac{\partial^2 w}{\partial x\partial z} \qquad (1.71)
\end{aligned}$$

Similar equations of motion can be written for displacement v along the y direction

$$\begin{aligned}
\rho\frac{\partial^2 v}{\partial t^2} &= \frac{\partial Y_x}{\partial x} + \frac{\partial Y_y}{\partial y} + \frac{\partial Y_z}{\partial z} \\
&= C_{66}\frac{\partial e_{xy}}{\partial x} + \frac{\partial(C_{12}e_{xx} + C_{11}e_{yy} + C_{13}e_{zz})}{\partial y} + C_{44}\frac{\partial e_{yz}}{\partial z} \\
&= C_{66}\frac{\partial(\epsilon_{yx} + \epsilon_{xy})}{\partial x} + \frac{\partial(C_{12}e_{xx} + C_{11}e_{yy} + C_{13}e_{zz})}{\partial y} + C_{44}\frac{\partial(\epsilon_{zy} + \epsilon_{yz})}{\partial z} \\
&= C_{66}\left(\frac{\partial^2 u}{\partial y\partial x} + \frac{\partial^2 v}{\partial x^2}\right) + C_{12}\frac{\partial u^2}{\partial x\partial y} + C_{11}\frac{\partial v^2}{\partial y^2} + C_{13}\frac{\partial w^2}{\partial y\partial z} + C_{44}\frac{\partial^2 v}{\partial z^2} + C_{44}\frac{\partial^2 w}{\partial z\partial y} \\
&= C_{66}\frac{\partial^2 v}{\partial x^2} + C_{11}\frac{\partial v^2}{\partial y^2} + C_{44}\frac{\partial^2 v}{\partial z^2} + (C_{12} + C_{66})\frac{\partial^2 u}{\partial x\partial y} + (C_{13} + C_{44})\frac{\partial^2 w}{\partial z\partial y} \qquad (1.72)
\end{aligned}$$

and displacement w along the z direction, respectively.

$$\begin{aligned}
\rho\frac{\partial^2 w}{\partial t^2} &= \frac{\partial Z_x}{\partial x} + \frac{\partial Z_y}{\partial y} + \frac{\partial Z_z}{\partial z} \\
&= C_{44}\frac{\partial e_{zx}}{\partial x} + C_{44}\frac{\partial e_{yz}}{\partial y} + \frac{\partial(C_{13}e_{xx} + C_{13}e_{yy} + C_{33}e_{zz})}{\partial z} \\
&= C_{44}\frac{\partial(\epsilon_{zx} + \epsilon_{xz})}{\partial x} + C_{44}\frac{\partial(\epsilon_{zy} + \epsilon_{yz})}{\partial y} + \frac{\partial(C_{13}\epsilon_{xx} + C_{13}\epsilon_{yy} + C_{33}\epsilon_{zz})}{\partial z} \\
&= C_{44}\frac{\partial(\epsilon_{zx} + \epsilon_{xz})}{\partial x} + C_{44}\frac{\partial(\epsilon_{zy} + \epsilon_{yz})}{\partial y} + \frac{\partial(C_{13}\frac{\partial u}{\partial x} + C_{13}\frac{\partial v}{\partial y} + C_{33}\frac{\partial w}{\partial z})}{\partial z} \\
&= C_{44}\frac{\partial(\frac{\partial u}{\partial z} + \frac{\partial w}{\partial x})}{\partial x} + C_{44}\frac{\partial(\frac{\partial v}{\partial z} + \frac{\partial w}{\partial y})}{\partial y} + \frac{\partial(C_{13}\frac{\partial u}{\partial x} + C_{13}\frac{\partial v}{\partial y} + C_{33}\frac{\partial w}{\partial z})}{\partial z} \\
&= C_{44}\left(\frac{\partial^2 w}{\partial x^2} + \frac{\partial w^2}{\partial y^2}\right) + C_{33}\frac{\partial^2 w}{\partial z^2} + (C_{13} + C_{44})\left(\frac{\partial^2 u}{\partial x\partial z} + \frac{\partial^2 v}{\partial y\partial z}\right)
\end{aligned} \tag{1.73}$$

Wave-equations of the form such as in eqn. 1.71, 1.72, and 1.73 can then be solved to obtain elastic constants in terms of the wave velocities for propagation in the high symmetry directions for longitudinal or transverse particle motion as

$$C_{i,j} = \rho c_s^2 \tag{1.74}$$

where c_s is the wave velocity.

Elastic constants in different ultrasonic modes

1. Propagation along the [100] direction

For propagation along the [100] direction, there are 3 possible ultrasonic modes, one longitudinal and two transverse modes.

In the longitudinal mode, the particle displacement u is along the direction of the propagation, i.e., [100] or x direction, and can be written as

$$u = u_0 \exp \iota(Kx - \omega t), \tag{1.75}$$

where $K = 2\pi/\lambda$ is the wavevector in the direction of the propagation, and ω is the frequency. Therefore, the wave velocity is $c_s = \omega/K$.

Now, substituting eq. 1.75 into eq. 1.71, we get

$$\begin{aligned} \rho\omega^2 &= C_{11}K^2 \\ c_s &= \sqrt{\frac{C_{11}}{\rho}} \end{aligned} \tag{1.76}$$

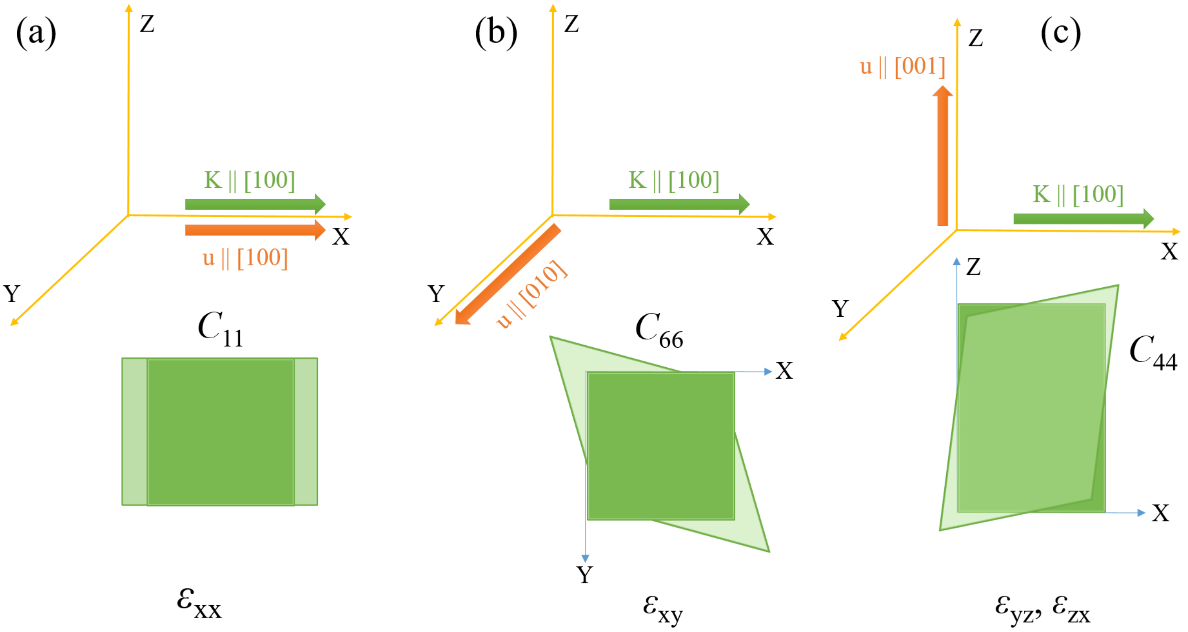

Figure 1.20: Elastic wave propagating along the [100] direction induces elastic deformations given by (a) C_{11} for the longitudinal mode (b) C_{66} for the transverse in-plane mode and (c) C_{44} for the transverse out of plane mode. For each deformation, the associated deformation/strain is also mentioned.

In the transverse or shear mode, the particle motion is perpendicular to the direction of the propagation. Therefore, the particle displacement can be either along the [010] or y direction or along the [001] or z direction.

The particle displacement v along the y direction can be written as

$$v = v_0 \exp \iota(Kx - \omega t) \tag{1.77}$$

and substituting eq. 1.77 into eq. 1.72 gives

$$\begin{aligned} \rho\omega^2 &= C_{66}K^2 \\ c_s &= \sqrt{\frac{C_{66}}{\rho}} \end{aligned} \tag{1.78}$$

Similarly, the particle displacement w along the z direction can be written as

$$w = w_0 \exp \iota(Kx - \omega t) \tag{1.79}$$

and substituting eq. 1.79 into eq. 1.73 gives

$$\begin{aligned} \rho\omega^2 &= C_{44}K^2 \\ c_s &= \sqrt{\frac{C_{44}}{\rho}} \end{aligned} \tag{1.80}$$

The results for all the 3 modes for the propagation along the [100] direction are summarized in Fig. 1.20. It is evident that the elastic wave velocity for the longitudinal mode is a direct measure of the C_{11} elastic stiffness constant (see Fig. 1.20(a)). On the other hand, the elastic wave velocity for the transverse mode in the tetragonal basal plane gives the C_{66} elastic stiffness constant (Fig. 1.20(b)), while for the transverse mode out of the basal plane it gives the C_{44} elastic stiffness constant(Fig. 1.20(c)). C_{11} corresponds to lattice expansion/contraction along the [100] direction, whereas C_{44} and C_{66} are symmetry breaking modes and can potentially be sensitive to monoclinic and orthorhombic/rhombohedral lattice distortions, respectively.

Since in the tetragonal crystal symmetry, the directions [100] and [010] are equivalent, the propagation along the [010] direction gives exactly the same elastic constants as those for the propagation along the [100] direction.

2. Propagation along the [110] direction

Similar to the [100] direction, in case of the propagation along the [110] direction, there are also 3 possible ultrasonic modes, one longitudinal and two transverse modes.

For the particle motion in the tetragonal basal plane, the particle displacements in the direction of propagation, i.e., [110], can be written as a linear combination of propagations along [100] and [010]. Therefore, the two components of the particle displacement are

$$\begin{aligned} u &= u_0 \exp[\iota(K_x x + K_y y - \omega t)] \\ v &= v_0 \exp[\iota(K_x x + K_y y - \omega t)] \end{aligned} \tag{1.81}$$

Now, substituting eq. 1.81 into eq. 1.71 and eq. 1.72 gives

$$\begin{aligned} -\rho\omega^2 u &= -C_{11}K_x^2 u - C_{66}K_y^2 u - (C_{12} + C_{66})K_x K_y v \\ -\rho\omega^2 v &= -C_{66}K_x^2 v - C_{11}K_y^2 v - (C_{12} + C_{66})K_x K_y u \end{aligned} \tag{1.82}$$

The set of equations 1.82 can be solved simultaneously by equating the determinant to zero. Using $K_x = K_y = K/\sqrt{2}$, we have

$$\begin{vmatrix} \rho\omega^2 - \frac{(C_{11}+C_{66})K^2}{2} & -\frac{(C_{12}+C_{66})K^2}{2} \\ -\frac{(C_{12}+C_{66})K^2}{2} & \rho\omega^2 - \frac{(C_{11}+C_{66})K^2}{2} \end{vmatrix} = 0 \tag{1.83}$$

$$\left(\rho\omega^2 - \frac{(C_{11}+C_{66})K^2}{2}\right)^2 - \left(\frac{(C_{11}+C_{66})K^2}{2}\right)^2 = 0 \tag{1.84}$$

$$\left[\left(\rho\omega^2 - \frac{(C_{11}+C_{66})K^2}{2} - \frac{(C_{11}+C_{66})K^2}{2}\right)\right]\left[\left(\rho\omega^2 - \frac{(C_{11}+C_{66})K^2}{2} + \frac{(C_{11}+C_{66})K^2}{2}\right)\right] = 0 \tag{1.85}$$

Therefore, we get two solutions for the wave velocity. Either

$$\rho\omega^2 = \frac{1}{2}\left(C_{11} + C_{12} + 2C_{66}\right)K^2 \tag{1.86}$$

$$c_s = \sqrt{\frac{1}{2\rho}\left(C_{11} + C_{12} + 2C_{66}\right)} \tag{1.87}$$

which is the case for the longitudinal mode, i.e., the particle motion along [110] or

$$\begin{aligned} \rho\omega^2 &= \frac{1}{2}\left(C_{11} - C_{12}\right)K^2 \\ c_s &= \sqrt{\frac{1}{2\rho}\left(C_{11} - C_{12}\right)} \qquad (1.88) \end{aligned}$$

which is the case for the transverse mode in the tetragonal basal plane, i.e, the particle motion along $[1\bar{1}0]$.

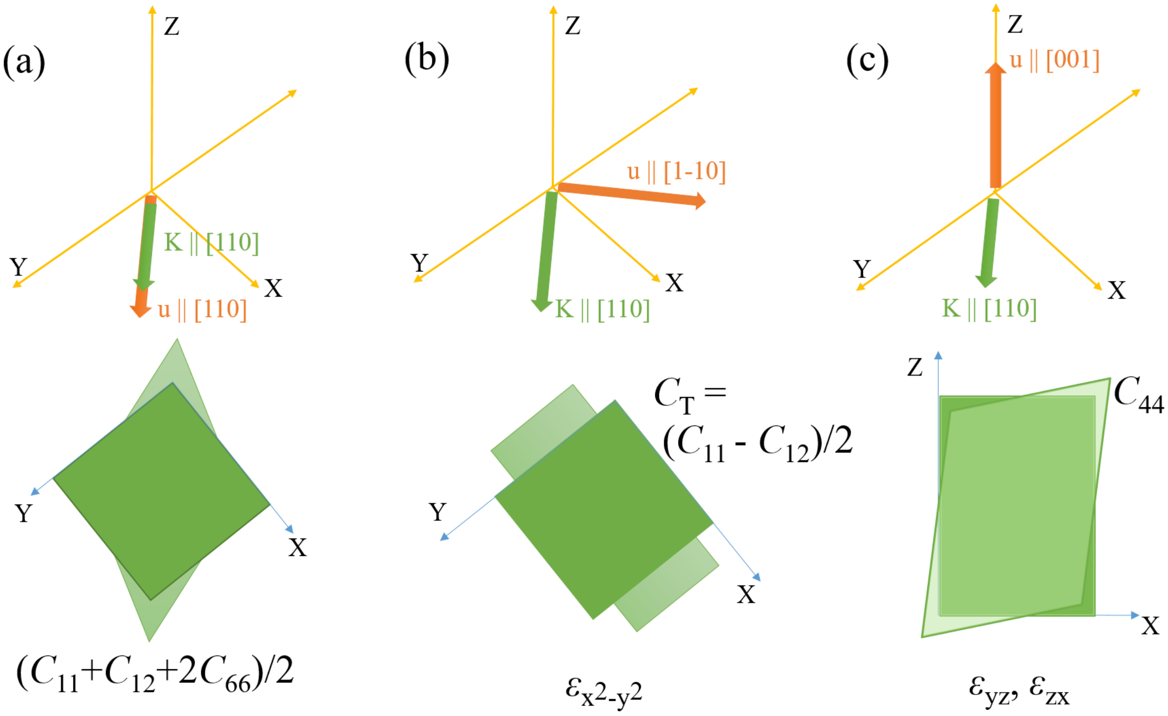

Figure 1.21: Elastic wave propagating along the [110] direction induces elastic deformations given by (a) $(C_{11} + C_{12} + 2C_{66})/2$ for the longitudinal mode (b) $(C_{11} - C_{12})/2$ for the transverse in-plane mode and (c) C_{44} for the transverse out of plane mode. For each deformation, the associated deformation/strain is also mentioned.

For the out of plane transverse mode, i.e., for the particle motion w along the [001] direction, we have

$$w = w_0 \exp[\iota(K_x x + K_y y - \omega t)] \tag{1.89}$$

Substituting eq. 1.89 into eq. 1.73, we get

$$\begin{aligned} \rho\omega^2 &= C_{44}(K_x^2 + K_y^2) \\ c_s &= \sqrt{\frac{C_{44}}{\rho}} \qquad (1.90) \end{aligned}$$

The results for all the 3 modes for the propagation along the [110] direction are summarized in Fig. 1.21. The elastic wave velocity in the longitudinal mode gives a combination of the elastic constants C_{11}, C_{12}, C_{66}. On the other hand, the elastic wave velocity for the transverse mode in the tetragonal basal plane gives the combination $(C_{11} - C_{12})/2$ (Fig. 1.21(b)), while for the transverse mode out of the basal plane it gives the elastic stiffness constant C_{44} (Fig. 1.21(c)).

3. Propagation along the [001] direction

For the elastic wave propagating along the [001] or z-direction, there are two possible modes, one longitudinal and one transverse mode.

The transverse mode is equivalent to the out of plane transverse mode for the propagation along [100] and [110] directions, and, therefore, the velocity gives the elastic constant C_{44}.

In the longitudinal mode, the particle motion is along the [001] or z direction, and is given as

$$w = w_0 \exp^{\iota(Kz - \omega t)} \tag{1.91}$$

Now, substituting eq. 1.91 into 1.73

$$\begin{aligned} \rho\omega^2 &= C_{33}K^2 \\ c_s &= \sqrt{\frac{C_{33}}{\rho}} \end{aligned} \tag{1.92}$$

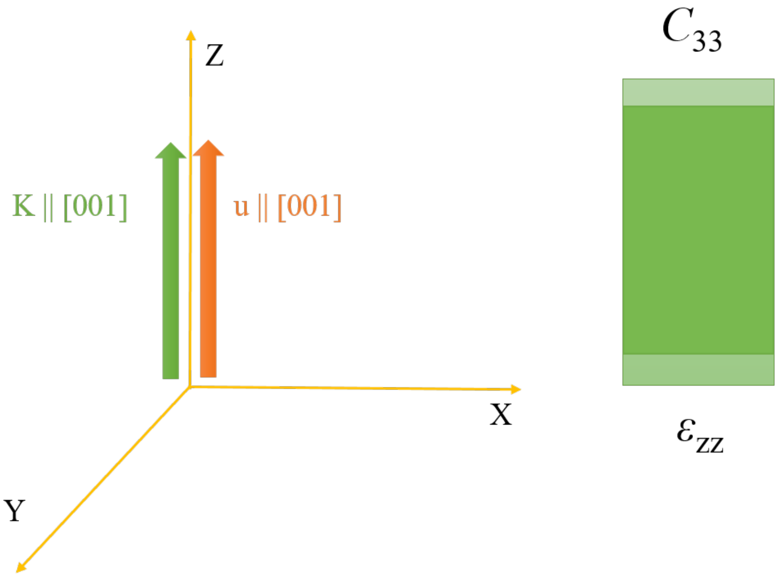

Figure 1.22: Longitudinal elastic wave propagating along the [001] direction induces an elastic deformation given by C_{33}. The associated deformation/strain is ϵ_{zz}.

Therefore, the velocity of the longitudinal elastic wave propagating in the [001] direction directly gives the elastic stiffness constant C_{33}, and the corresponding deformation is shown in Fig. 1.22.

Finally, the effective elastic stiffness constants corresponding to different ultrasonic modes for a tetragonal lattice can be summarized in the Table 1.1.

These elastic constants obtained from different elastic modes can help in determining the symmetry of the order parameter of a transition which is a vital information in understanding its origin.

Elastic Stiffness Constants Table			
Ultrasonic Mode	Propagation Direction ($\vec{k}$)	Polarization Direction ($\vec{u}$)	Effective Elastic Stiffness Constant
Longitudinal	[100]	[100]	C_{11}
Transverse	[100]	[010]	C_{66}
Transverse	[100]	[001]	C_{44}
Longitudinal	[110]	[110]	$(C_{11}+C_{12}+2C_{66})/2$
Transverse	[110]	[1-10]	$(C_{11}-C_{12})/2$
Transverse	[110]	[001]	C_{44}
Longitudinal	[001]	[001]	C_{33}

Table 1.1: Effective elastic stiffness constants obtained for different ultrasonic modes in a tetragonal lattice. The first column mentions the longitudinal transverse nature of the ultrasonic mode. The second and third columns depicts the directions of propagation and polarization, receptively. The corresponding elastic constant are listed in the fourth column.

1.3.4 Magnetization

Similar to heat capacity and elastic constants, magnetization is also a thermodynamic response of a system and can be defined as the derivative of the free energy (F) with respect to magnetic field at constant temperature, volume and chemical potential

$$M = \left(\frac{dF}{dB}\right)_{T,V,N}. \tag{1.93}$$

Magnetization gives a measure of the magnetic moment of a bulk system and, therefore, is an extremely useful probe to detect changes in the magnetic structure. In several Kondo lattice systems, a sharp change in magnetization occurs at a first-order field-induced metamagnetic transition and, therefore, magnetization can act as the ultimate probe to distinguish it from other thermodynamic phase transitions which is an extremely important information in pursuit of identifying the nature and origin of unknown phase transitions.

1.3.5 Resistivity

Resistivity of metallic systems has long been regarded as an impeccable probe in experimental physics. In metals, resistivity scales as T^2 at low temperatures due to the electron-electron scattering

$$\rho = \rho_0 + AT^2 \tag{1.94}$$

In Kondo lattice system, it gives a direct indication of heavy Fermi liquid state through an enhanced A coefficient which is related to the Sommerfeld coefficient as $A \propto \gamma^2$. Further, Kondo coherence appears as a maximum in resistivity. In the vicinity of a QCP, non-Fermi liquid behavior can be detected as deviations from the T^2 scaling, as well as a superconducting state as zero resistivity. Also, electronic phase transitions can be detected as sharp anomalies in resistivity as a function of magnetic field (magnetoresistance) and temperature. Moreover, quantum oscillations can also be detected in resistivity (known as Shubnikov-de Haas effect) to perform Fermi surface studies.

Chapter 2

Experimental Techniques

During the course of this thesis, various sensitive and high-resolution experimental techniques were used to investigate different aspects of heavy-fermion systems discussed in Chapter 1. All the measurements were performed at the two high-field facilities of the European Magnetic Field Laboratory (EMFL), namely, the LNCMI-G in Grenoble, France and the HLD-HZDR in Dresden, Germany. Also, a part of this thesis was dedicated to growing high-quality single crytals of heavy fermions at the IMR, Tohoku university, Japan. Therefore, a separate section will be devoted to self-flux growing technique in a later chapter.

2.1 dHvA effect using torque method

The magnetic torque method is widely used for measuring de Haas-van Alphen effect. As the name suggests, this method is based on measuring the magnetic torque that a material experiences in magnetic fields.

A sample placed in a homogeneous magnetic field experiences a magnetic torque $\vec{\tau}$ due to the interaction of its bulk magnetic moment $\vec{M}V$ with the external magnetic field $\vec{B}$. As a consequence, quantum oscillations in magnetization (the dHvA effect) are directly reflected in magnetic torque.

$$\begin{aligned} \vec{\tau} &= \vec{M}V \times \vec{B} \\ |\,\vec{\tau}\,| &= M_{\perp}VB \end{aligned} \tag{2.1}$$

If the external magnetic field is inhomogeneous, the sample also experiences a force $\vec{F} = -\nabla(\vec{M}.\vec{B})$ given by the gradient of the potential energy associated with magnetic moment. Therefore, to keep the force negligibly small, the sample should be very small and must be placed at the field center.

In a conventional torque method in static fields, a non-magnetic cantilever made of copper Beryllium (CuBe) is used as sample holder. The sample is glued on top of it, as shown in Fig. 2.1. The cantilever also acts as the upper plate of a capacitor with its bottom plate attached to the sample holder platform. In applied magnetic fields, the cantilever bends due to the torque on the sample, thereby changing capacitance between the two plates. For a small bending, the variation of the capacitance is proportional to the torque, while for large bending, a non-linear correction has to be applied to calculate the torque as follows

At zero field, the capacitance between the cantilever and the ground plate separated by d_0 is

$$C_0 = \frac{\epsilon A}{d_0} \tag{2.2}$$

where A is the area of the cantilever and ϵ is permittivity. In a magnetic field, if the cantilever bends by Δd due to the torque, then the capacitance is given by

$$C = \frac{\epsilon A}{d_0 + \Delta d} \tag{2.3}$$

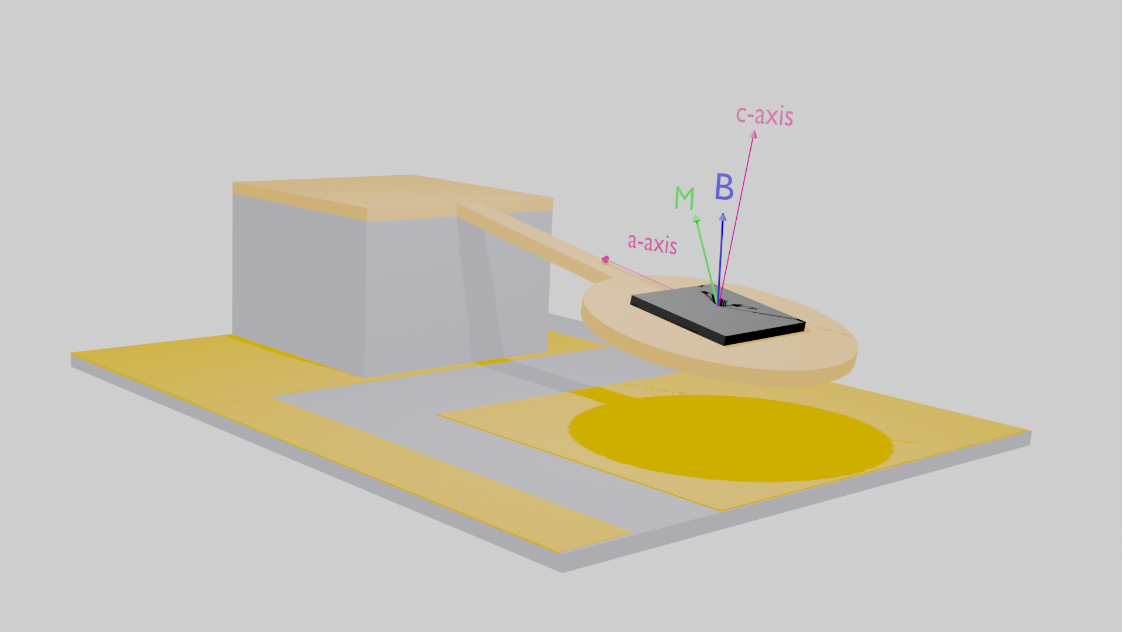

Figure 2.1: A setup for the torque method. A sample (black slab) is glued on top of a metallic cantilever (yellow), which is bent towards the ground plate due to a magnetic torque on the sample in applied magnetic fields.

The change in capacitance ΔC is

$$\begin{aligned}\Delta C = C - C_0 &= \frac{\epsilon A}{d_0 + \Delta d} - \frac{\epsilon A}{d_0} \\ &= C_0 \left(- \frac{\Delta d}{d_0 + \Delta d} \right) \qquad (2.4)\end{aligned}$$

The direction of bending depends on the direction of the torque, as shown in Fig. 2.2. At zero field, the cantilever is at equilibrium position [Fig. 2.2(a)]. If the torque is out of the plane, then the cantilever bends away from the ground plate, i.e., Δd is positive [Fig. 2.2(a)], while for torque into the plane the cantilever bends towards the ground plate, i.e., Δd is negative. Therefore, depending on the direction of bending, the change in capacitance is different for the same amount of bending Δd.

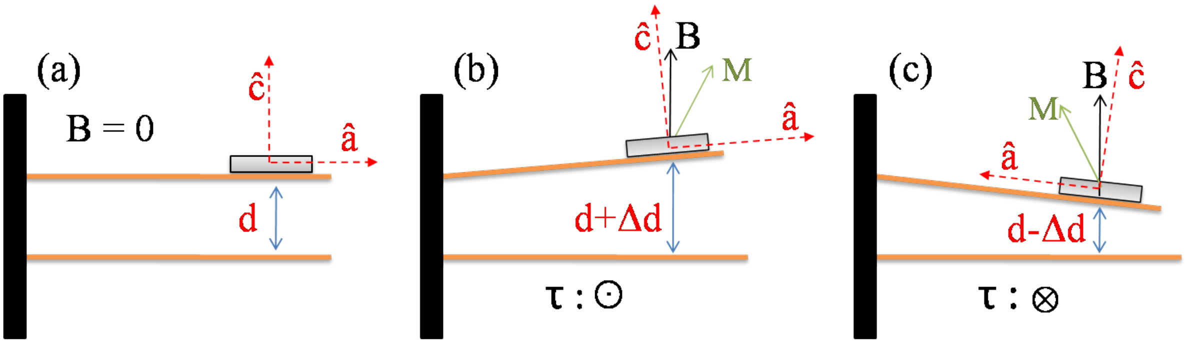

Figure 2.2: Cantilever is (a) in equilibrium position at zero magnetic field, (b) bent away from the ground plate due to an out-of-plane torque, (c) bent towards the ground plate due to an into-the-plane torque.

$$\left| \frac{\Delta d}{d - \Delta d} \right| > \left| \frac{\Delta d}{d + \Delta d} \right| . \qquad (2.5)$$

ΔC is larger when the cantilever bends towards the ground plate and, hence, the measurement is more sensitive in this case [Fig. 2.2(c)].

The magnetic torque can be calculated by measuring ΔC as

$$\begin{aligned} \Delta C &= C_0 \left(\frac{\tau}{d+\tau} \right), \\ \tau &\propto \left(-\frac{\Delta C / C_0}{1 - \Delta C / C_0} \right). \end{aligned} \tag{2.6}$$

For a small deflection of the cantilever $\Delta C / C_0 << 1$, $\tau \propto \Delta C$.

C_0 is typically ≤ 1 pF in our setup where the cantilever and ground plate are separated by 100 μm. The capacitance is measured using a precision capacitance bridge. For this purpose, either a single standalone instrument, like the high precision capacitance bridge from Andeen-Hagerling, can be used, or a precision capacitance bridge (Wein bridge) driven by an independent oscillator (an ultra-low distortion function generator) can be used. In the latter case, the output signal from the capacitance bridge is read using a lock-in amplifier. A high sensitivity, typically $\sim 10^{-5}$ pF, was achieved using a precision capacitance bridge.

In pulsed magnetic field, the torque method is slightly altered. Due to the extremely small duration of pulses (typically ≤ 150 ms), the torque is measured using commercially available piezoresistive microcantilevers with large eigenfrequency suitable for such transient measurements. A sample is mounted at the end of the piezoresistive cantilever. The torque on the sample is detected as a change in the resistance. Even small change is resistance is precisely detected using a wheatstone bridge whose output voltage is first amplified using a preamplifier and then recorded by a transient recorder [59]. Metallic cantilevers are not suitable in pulsed fields due to the eddy current heating.

For a material with an isotropic Fermi surface, the magnetization direction is always along the applied field, i.e., $M \parallel H$ and therefore, $\vec{\tau} = 0$, rendering the torque method unsuitable. For materials with anisotropic Fermi surfaces, the magnetization has a component orthogonal to the magnetic field ($\vec{M_\perp}$). The component of this torque about any particular axis perpendicular to H is

$$\vec{\tau} = -\frac{1}{F}\frac{\partial F}{\partial \theta} M_{\parallel} B V \tag{2.7}$$

Here F is the dHvA frequency, θ is an angle specifying the direction of field in the plane normal to the chosen axis and $M_{\parallel}$ is the parallel component of M containing the oscillatory part of magnetization M_{osc} given by Lifshitz-Kosevich formula. The torque, therefore, contains an oscillatory part as well.

Another disadvantage of the torque method is that the torque vanishes for fields along crystallographic symmetry axes as $\partial F / \partial \theta = 0$. But this fact is used as an advantage for very precise alignment of the sample with the field as shown in Fig. 2.3. Upon approaching angles closer to the symmetry axis [001], the torque becomes smaller and vanishes for field precisely along [001].

Data analysis

Depending on the magnetic anisotropy the overall torque signal can contain a predominant non-oscillatory contribution that has to be subtracted to obtain raw dHvA oscillations.

In an anisotropic material, the magnetic response also occurs in a direction other than that of the applied field and, therefore, magnetization is given as

$$\vec{M} = \bar{\chi} \vec{B}, \tag{2.8}$$

where $\bar{\chi}$ is the magnetic susceptibility tensor, which has an isotropic contribution χ_i and an anisotropic contribution χ_a. For example, in materials with a tetragonal crystal structure, the susceptibility tensor can be written as

$$\bar{\chi} = \begin{pmatrix} \chi_i & 0 & 0 \\ 0 & \chi_i & 0 \\ 0 & 0 & \chi_i + \chi_a \end{pmatrix} \tag{2.9}$$

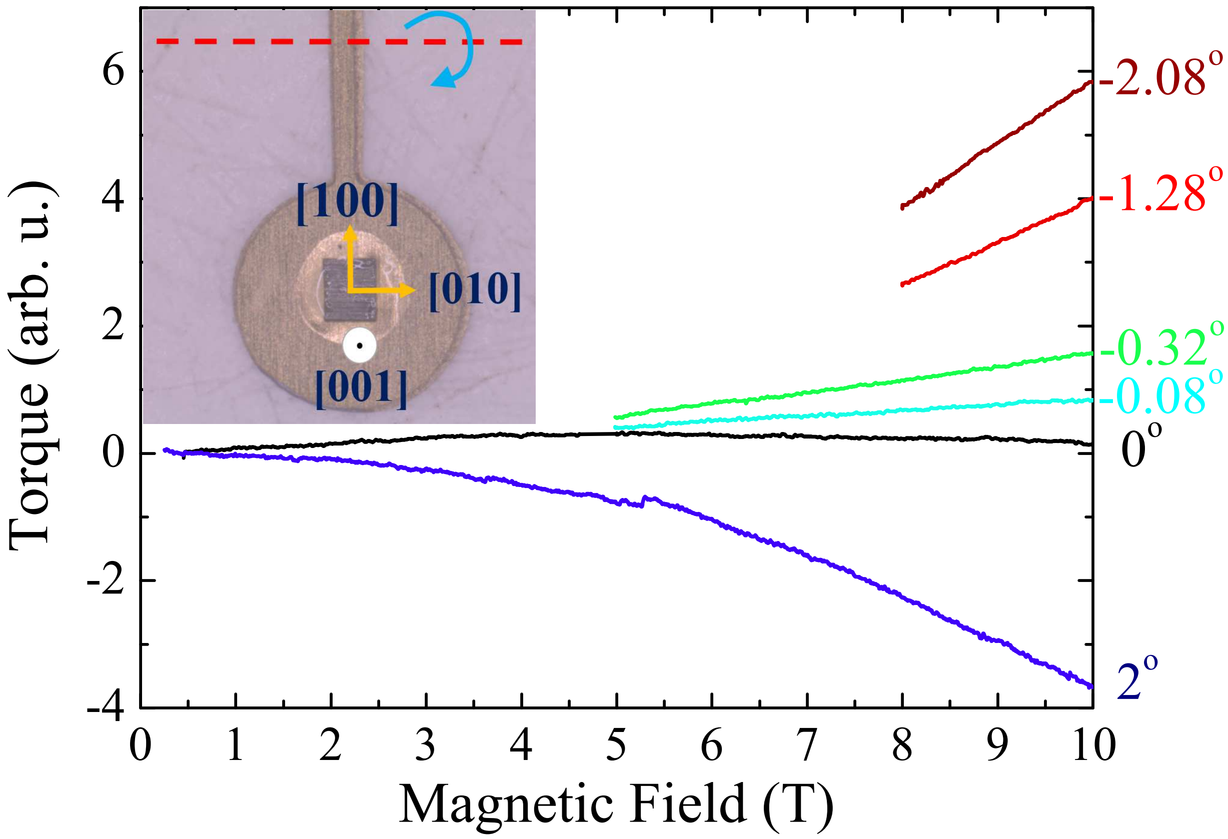

Figure 2.3: Alignment of the symmetry axis of the sample along the field direction in toque method. The picture in the inset shows a sample mounted on a metallic cantilever.

For a magnetic field applied out of the tetragonal basal plane, at an angle θ from the c axis, the magnetization $\vec{M}$ can be written as

$$\vec{M} = \begin{pmatrix} \chi_i & 0 & 0 \\ 0 & \chi_i & 0 \\ 0 & 0 & \chi_i + \chi_a \end{pmatrix} \begin{pmatrix} 0 \\ -B\sin\theta \\ B\cos\theta \end{pmatrix} = \begin{pmatrix} 0 \\ -\chi_i B\sin\theta \\ (\chi_i + \chi_a)B\cos\theta \end{pmatrix} \tag{2.10}$$

Using eq. 2.1 the torque $\vec{\tau}$ will be

$$\vec{\tau} = \begin{pmatrix} 0 \\ -\chi_i B\sin\theta \\ (\chi_i + \chi_a)B\cos\theta \end{pmatrix} \times \begin{pmatrix} 0 \\ -B\sin\theta \\ B\cos\theta \end{pmatrix} = \begin{pmatrix} \chi_a\,(B)^2\cos\theta\sin\theta \\ 0 \\ 0 \end{pmatrix} \tag{2.11}$$

Therefore, the magnetic torque is non-zero only in magnetically anisotropic material, and is proportional to B^2

$$\mid \vec{\tau} \mid = V\chi_a B^2 \cos\theta\sin\theta \tag{2.12}$$

The non-oscillatory background torque can be orders of magnitude higher than the oscillatory part of the torque in materials with strong magnetic anisotropy such as in some heavy fermions. This background torque needs to be subtracted from the overall torque signal with an appropriate polynomial fit. Moreover, in certain cases, the overall torque signal might contain special features, like a metamagnetic transition and therefore, will require unique consideration rather than just a simple polynomial background subtraction. In case the dHvA oscillations comprise of low dHvA frequencies, the background must be subtracted in such a way that the low dHvA frequencies are not affected.

After subtracting the non-oscillatory background, the remaining oscillatory torque signal is analyzed to extract the dHvA frequencies and their amplitudes. This can be done by performing a

Fourier transform on the signal that converts a signal in time domain to its counterpart in frequency domain, i.e., $f(t) \to F(k)$.

$$F(k) = \int_{-\infty}^{\infty} f(t)e^{-2\pi\iota kt} \tag{2.13}$$

Since our torque signal is not a continuous but a discrete data set, instead of Fourier transform, we compute the discrete Fourier transform (DFT) defined for a sequence x_n of length N as

$$F(k) = \sum_{n=0}^{N-1} x_n e^{-\left(\frac{2\pi\iota}{N}kn\right)} \tag{2.14}$$

where $k = 0, ...N-1$.

The DFT is performed by using a shrewd mathematical algorithm known as the Fast Fourier transform (FFT) [60]. Generally, DFT is performed on data collected at equal interval Δt so that the indexes can be easily converted into time $t = n\Delta t$, and frequency as

$$f(k) = \frac{k}{N\Delta t}. \tag{2.15}$$

The frequency resolution is then given by

$$\Delta f = f(k) - f(k-1) = \frac{1}{N\Delta t} \tag{2.16}$$

The maximum frequency, or the folding frequency is

$$f_{max} = \frac{f_k}{2} = \frac{N}{2}\Delta f = \frac{1}{2\Delta t} \tag{2.17}$$

As explained in the previous chapter, quantum oscillation are periodic in $\frac{1}{B}$, therefore we perform FFT on the oscillatory torque as a function of inverse magnetic field, i.e., $\tilde{\tau}$ vs $\frac{1}{B}$. The first step is to interpolate the $\tilde{\tau}$ vs $\frac{1}{B}$ data set to convert the data into equally spaced intervals in $\frac{1}{B}$ for DFT. For a magnetic field range from B_{min} to B_{max} and N_{int} interpolation points, in analogy to Δt, the interval between two data points here is

$$\begin{aligned} \Delta\left(\frac{1}{B}\right) &= \frac{1}{N_{int}-1}\left(\frac{1}{B_{min}} - \frac{1}{B_{max}}\right) \\ &= \frac{1}{N_{int}-1}\frac{B_{max}-B_{min}}{B_{max}B_{min}} \end{aligned} \tag{2.18}$$

The frequency resolution is then given by

$$\Delta F = \frac{N_{int}-1}{N_{int}}\frac{B_{max}-B_{min}}{B_{max}B_{min}} \tag{2.19}$$

and the maximum frequency is

$$F_{max} = \frac{N_{int}-1}{2}\frac{B_{max}-B_{min}}{B_{max}B_{min}} \tag{2.20}$$

Therefore, the maximum dHvA frequency depends only on the inverse field interval determined by selected field range and the number of interpolation points. On the other hand, the frequency resolution depends on the total number of points, and can be improved by padding the interpolated data with zeros up to a total number of points N_{tot}. The improved frequency resolutions will then be

$$\Delta F = \frac{N_{int}-1}{N_{tot}}\frac{B_{max}-B_{min}}{B_{max}B_{min}} \tag{2.21}$$

Finally, to reduce the FFT spectral leakage, a correction window function is applied to the original data. For this purpose, a cosine sum window known as the Hamming window, was used, mathematically defined as

$$w[n] = \sum_{k=0}^{K}(-1)^k a_k cos\left(\frac{2\pi kn}{N}\right), \quad where \quad 0 \le n \le N \tag{2.22}$$

While data analysis softwares like Origin, have in-built functions to perform FFT analysis, I used a dedicated MATLAB code written by Johannes Klotz.

2.2 Heat capacity techniques

Experimentally, heat capacity is obtained by measuring the thermal response of a sample to supplied heat. The idea is to thermally isolate the sample from the environment and connect it to the thermal-bath only via one known thermally conducting channel, i.e., a weak thermal link of thermal conductance κ, as shown in the schematic figure 2.4.

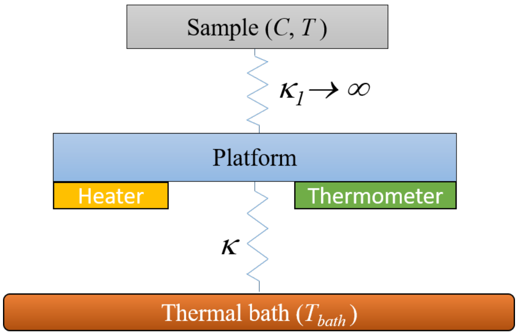

Figure 2.4: Schematic of a basic setup for measuring specific heat. Sample is placed on a platform with a heater and a thermometer. The whole assembly is weakly coupled to the thermal bath.

The specific heat, C, can then be determined by measuring the relaxation time, τ, for the sample to exponentially relax to the thermal bath as

$$\begin{aligned} T &= T_{bath} + A\exp(-\frac{\kappa t}{C}) \\ C &\propto \kappa\tau \end{aligned} \tag{2.23}$$

where T is the sample temperature and T_{bath} is the bath temperature.

To perform such a measurement, we need a heater to supply the heat directly to the sample, a thermometer to measure the sample temperature in real time, and another thermometer to be used as a reference thermometer for the thermal bath. The thermometer requirements are meticulously met by using a commercially available Cernox (ceramic silicon oxynitride) chip [61, 62] generally used as a highly sensitive low-temperature thermometer. The Cernox chip is composed of a thin sensing film (of conducting ZrN and non-conducting ZrO) with negative temperature coefficient deposited on a shappire substrate.

During this work, two different experimental techniques were used to measure specific heat. The thermal-relaxation technique was used at constant magnetic fields while sweeping temperature and the AC-calorimetric technique was used at a constant temperature while sweeping magnetic field.

2.2.1 Thermal relaxation

In the thermal relaxation method, a single bare Cernox chip (CX-1030), such as shown in Fig. 2.5(a), was used as both the sample heater and the thermometer and the platform. The sample is glued on the back side of the chip [Fig. 2.5(b)]. The chip is connected to the thermal bath via a weak thermal link provided by four thin phosphor bronze wires [see Fig. 2.5(c)]. The wires also provide a mechanical support to the chip, and are used as current leads. The Cernox chip is simultaneously used as both the sample heater and the thermometer to measure the sample temperature in real time.

Calibration of the Cernox chip : The resistance of the Cernox chip, R_C, is calibrated in-situ against the reference thermometer of the thermal bath. To this end, small currents of a few μAs are supplied to the Cernox chip and the signal is read using a DC multimeter, at a constant bath temperature, T_{bath}. The chip resistance at $T_{bath} = 2.5\ K$ for a few different supplied powers P is shown in Fig. 2.6(a). A linear extrapolation of R_C at small excitations gives the intercept, i.e,

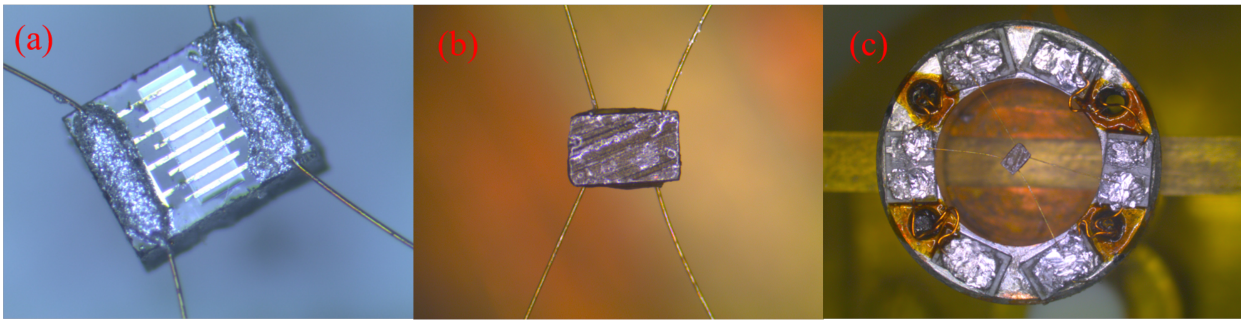

Figure 2.5: Setup to measure specific heat using thermal-relaxation technique, (a) bare Cernox chip, (b) sample glued on the back side of the Cernox chip shown in (a), (c) Cernox chip connected to the thermal bath with four wires.

the chip resistance R_{C0} at zero power. For $P = 0$, the chip and sample temperature is the same as the thermal-bath temperature, i.e., $T = T_{bath}$. Therefore, the chip resistance, R_C, at a given temperature can be obtained using the reference thermometer of the thermal-bath.

A similar process is repeated at several different bath temperatures to obtain corresponding R_{C0}'s. Once R_{C0}'s are known at a few different temperatures, we fit $\ln R_{C0}$ vs $\ln T$ with an appropriate polynomials fit such as one defined in eq. 2.24

$$\ln T = \Sigma a_n X^n \tag{2.24}$$

In this equation, $X \in [-1, 1]$ is a normalized variable deduced for each $\ln R_{C0}$ using their averaged value $< \ln R_{C0} >$ at different bath temperatures and the standard deviation σ and is defined as $X = (\ln R_{C0} - < \ln R_{C0} >)/\sigma$. This polynomial fit to $\ln R_{C0}$ vs $\ln T$ is basically the calibration curve for the Cernox chip as shown in Fig. 2.6(b).

The thermal conductance of the weak thermal link is also calibrated in-situ using the chip calibration. In this regard, a pair of points is used from among the last three points (say, (P_n, R_n), (P_{n-1}, R_{n-1}), (P_{n-2}, R_{n-1})) at high excitation power to obtain κ at a particular T_{bath} as

$$\kappa = \frac{\Delta P}{\Delta T} \tag{2.25}$$

Fig. 2.6(c) shows κ/T as a function of temperature. It is more or less constant and only weakly temperature-dependent, implying that, in a first order approximation κ is linear in temperature. From the calibration, we obtain $\kappa/T \simeq 4 \times 10^{-7}\ W/K^2$ for the 50 μm and $\kappa/T \simeq 1 \times 10^{-7}\ W/K^2$ for the 25 μm thick phosphor bronze wires of the calorimeter. Also, κ is essentially independent of the magnetic field, as was verified from measurement in magnetic fields (see. Fig. 2.6(d)). The bath thermometer used is field calibrated.

Relaxation: Thermal-relaxation is performed independent of the calibration. Initially, without any applied excitation to the chip the sample is in equilibrium with the thermal bath, i.e., $T = T_{bath}$.

Then a constant heating current I_1 is continuously supplied to the system. The sample heats up and undergoes 'up-relaxation', i.e., an exponential decrease of the chip voltage (and R_C as well), and saturates at a higher temperature that is $2 \times T_{bath}$. The heating current is then decreased to a smaller I_2, and, therefore, the sample undergoes 'down-relaxation', i.e., an exponential increase of the chip resistance to another saturation value as shown in Fig. 2.7. The specific heat can be calculated from either the 'up' or 'down' relaxation as following

For a power $P = I^2 R$ supplied to the sample, the heat equation can be written as

$$R_C I^2 dt = [C + C_{addenda}] dT + \int_{T_b}^{T} \kappa(T')\ dT'\ dt. \tag{2.26}$$

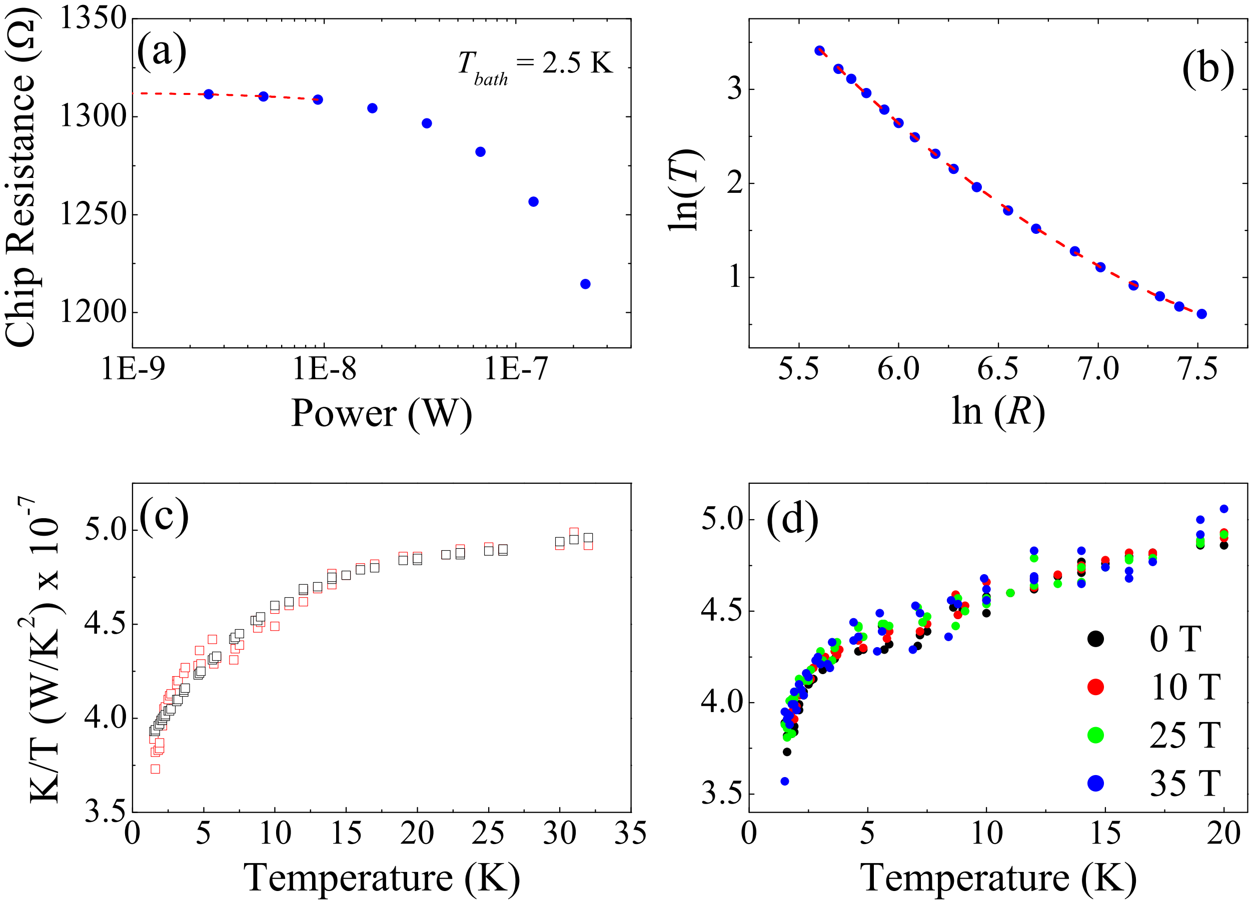

Figure 2.6: In situ calibration of Cernox chip. (a) chip resistances at a few different excitation power. (b) calibration curve obtained for the Cernox chip (c) thermal conductance of phosphor bronze wire at different bath temperature calculated using the chip calibration.

Here C is the specific heat of the sample and $C_{addenda}$ is the additional contribution to the total heat capacity of the system from the addenda comprising of the Cernox chip, the Apiezon grease, and the wires.

The chip resistance corresponding to the saturated temperature T_∞ is R_∞. Also, at saturation, $dT = 0$. Therefore, eq. 2.26 becomes

$$R_\infty I^2 dt = 0 + \int_{T_b}^{T_\infty} \kappa(T')dT' \; dt. \tag{2.27}$$

Subtracting eq. 2.27 from eq. 2.26, we get

$$\begin{aligned}(R_C - R_\infty) &= [C + C_{addenda}]dT + \int_{T}^{T_\infty} \kappa dT' \; dt, \\ C + C_{addenda} &= \frac{(R_C - R_\infty)I^2 + \int_{T_\infty}^{T} \kappa(T')dT'}{dT/dt}. \end{aligned} \tag{2.28}$$

From the above equation, it is evident that specific heat of the system can be determined if we know the sample temperature, the thermal conductance κ in the relevant temperature range, and the chip resistance R_C and R_∞.

This technique provides an accuracy of 1%. Also, its sensitivity of 10^{-3} is ideal to detect even very small changes in specific heat. Further details of this technique are given elsewhere [63].

The addenda contribution to the specific heat must be subtracted from the total specific heat of the system in order to obtain the absolute specific heat of the sample. To this end, the addenda,

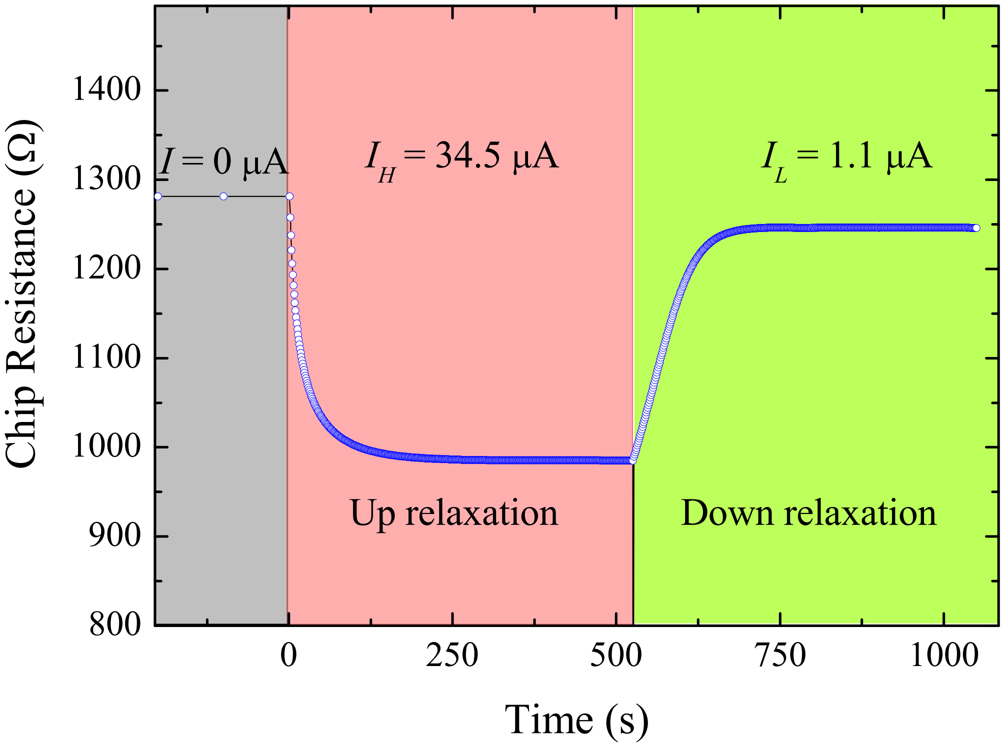

Figure 2.7: Up and down relaxation of the sample corresponding to the high and low currents, respectively at a bath temperature $T_{bath} = 2.5$ K

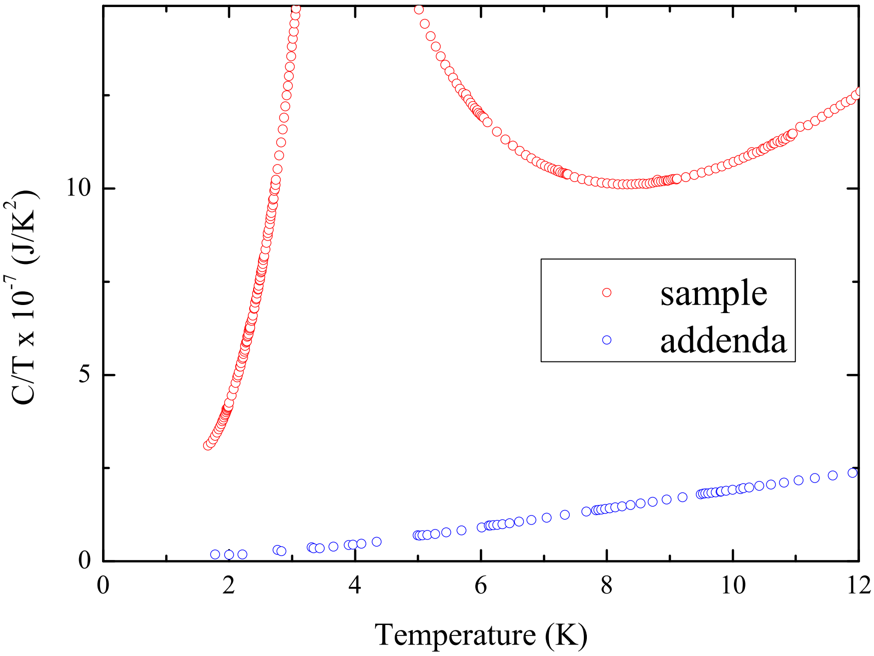

Figure 2.8: A typical addenda contribution (blue open circles) to the total specific heat of a system i.e. sample + addenda (red open circles).

i.e., the heat capacity of the system without sample, is first measured as a function of temperature in zero field. The addenda is later subtracted from all the curves obtained with a mounted sample. The addenda contribution to heat capacity is independent of magnetic fields. A typical addenda contribution to the total specific heat is shown in Fig. 2.8

2.2.2 AC calorimetry

The AC calorimetric method is highly useful in detecting very small changes in the specific heat as a function of an external parameter such as magnetic field. For example, a weakly first-order field-induced transition not apparent in the thermal-relaxation specific heat method, can be detected distinctly by the AC calorimetric technique. In the thermal-relaxation method, a nearly temperature-independent field-induced phase transition cannot be observed in temperature sweeps at constant fields. Therefore, in such a situation AC calorimetry is helpful as it allows measuring specific heat as a function of field at a constant temperature.

The AC calorimetry was first developed by Sullivan and Seidel [64] in 1968. Since then, there have been numerous improvements of this technique.

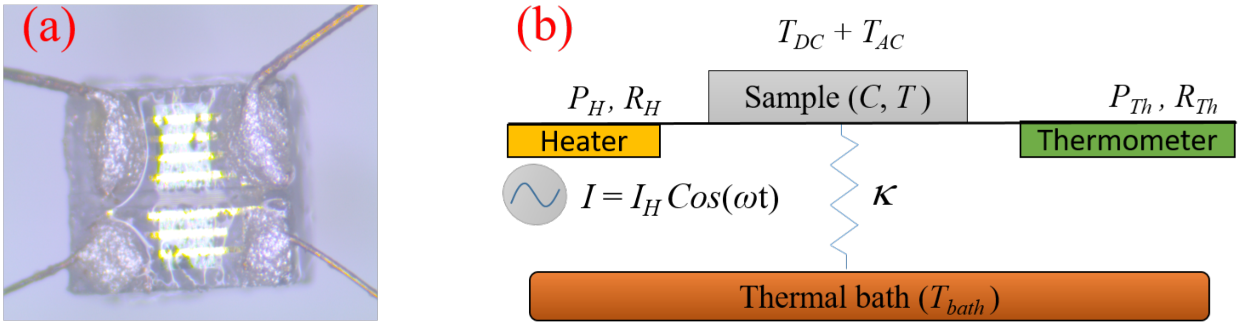

Figure 2.9: (a) Cernox chip cut into two parts to make the heater and thermometer independent. (b) Basic setup for AC calorimetry. The heater is supplied with AC excitation and thermometer with DC.

Unlike the thermal relaxation technique, in the AC calorimetry, the heater and the thermometer are separated, as shown in Fig. 2.9(a). The heater part of the Cernox chip of the resistance R_H is excited by a small AC current $I_H cos(\omega_H t)$ of a few μA at an appropriate excitation frequency ($\omega_H = 2\pi f$), chosen according to a particular system characteristics. A schematic diagram of an AC calorimeter is shown in Fig. 2.9(b). The sample temperature is measured using the thermometer part of the chip excited by a small DC current of a few μA. The AC power $I_H^2 R_H cos^2(\omega_H t)$ generated by the heater has two effects. First, it increases the sample temperature above the thermal bath temperature T_{bath}. Second, it induces an oscillatory thermal response T_{AC} with the sample temperature T oscillating at twice the excitation frequency [64, 65] i.e $\omega = 2\omega_H$ [see Fig. 2.10(a)]. The resulting sample temperature is thus given by:

$$T = T_{bath} + T_{DC} + T_{AC} \tag{2.29}$$

Here T_{DC} is an inevitable effect arising from self-heating of the heater and the thermometer due to supplied excitations. T_{DC} is the excess in sample temperature T with respect to the thermal bath temperature. It depends on the average power generated by the heater, $P_H = I_H^2 R_H/2$, and the thermometer, P_{Th}, as well as the thermal conductance κ between the system and the thermal bath, i.e., $T_{DC} = (P_{Th} + P_H)/\kappa$.

The heat capacity of the system, C, is obtained from the oscillatory thermal response as

$$\begin{aligned} T_{AC} &= \frac{P_H}{\kappa + \iota\omega C} \\ &= \frac{P_H \kappa}{\kappa^2 + \omega^2 C^2} - \iota \frac{\omega C P_H}{\kappa^2 + \omega^2 C^2} \end{aligned} \tag{2.30}$$

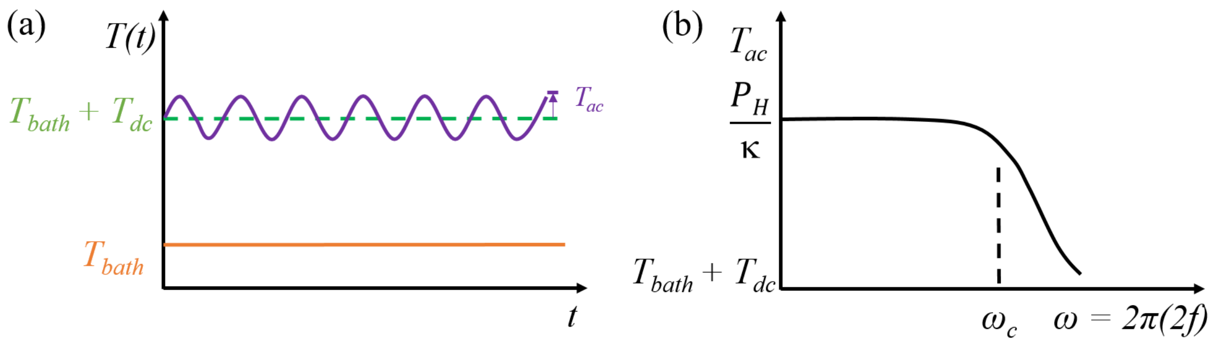

Figure 2.10: (a) Schematic illustration of temperature oscillations T_{ac} in the sample with an additional heating T_{DC} above the bath temperature T_{bath}. (b) Variation of the amplitude of temperature oscillations T_{ac} with the oscillation frequency ω.

Both the real and the imaginary terms of the complex Eq. 2.30 depend on P_H, κ, C, ω. However, the phase, θ, between the two terms provides a more direct measure of the heat capacity of the system, independent of P_H as

$$\tan\theta = \frac{C\omega}{\kappa} \tag{2.31}$$

In the first-order approximation, κ is proportional to the temperature, and is independent of the magnetic field. Therefore, at a constant excitation frequency,

$$\tan\theta \propto \frac{C}{T} \tag{2.32}$$

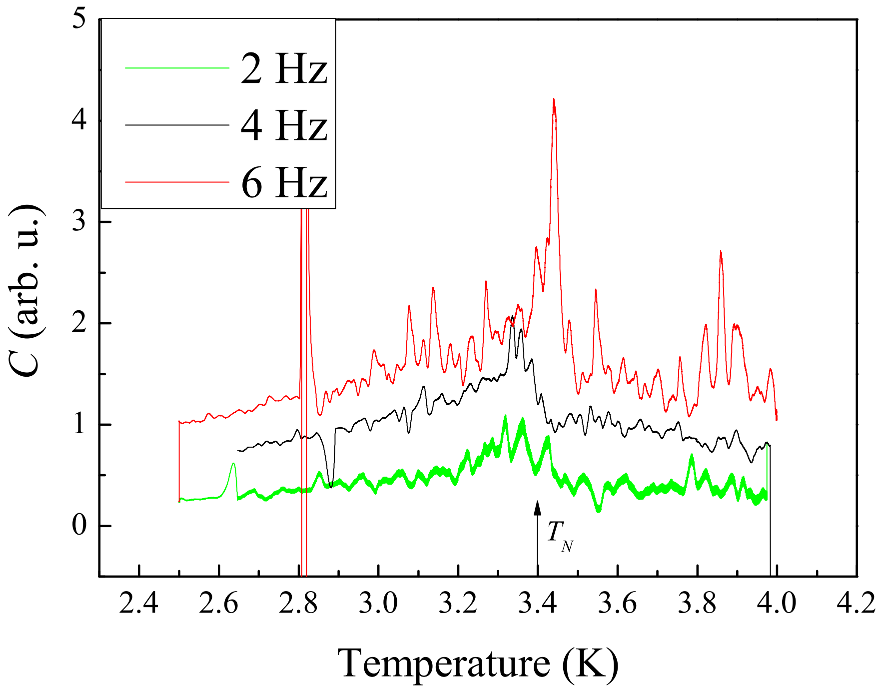

Figure 2.11: Specific heat obtained using AC technique at different excitation frequencies.

Selection of excitation frequency: Using eq. 2.30, the amplitude of sample temperature oscillations can be written as

$$\mid T_{AC} \mid = \frac{P_H}{\sqrt{\kappa^2 + \omega^2 C^2}} \tag{2.33}$$

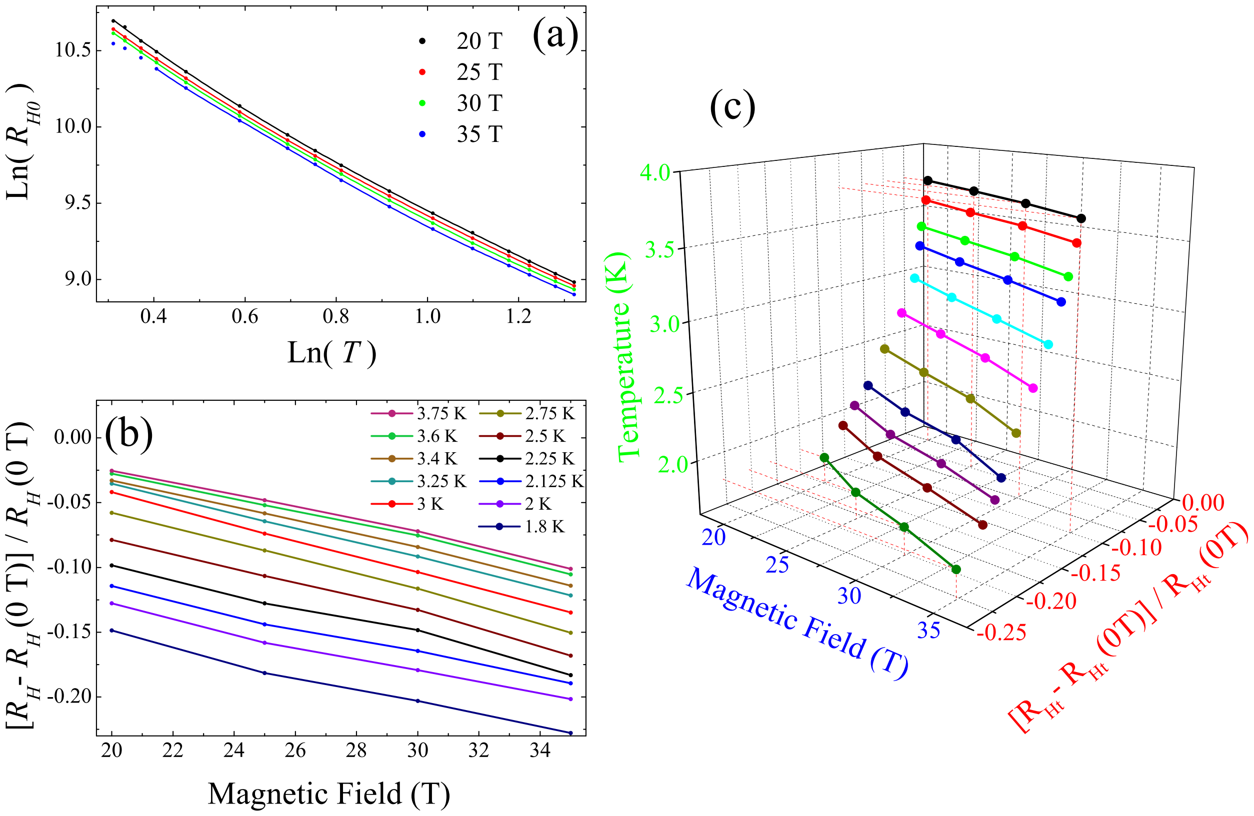

Figure 2.12: Heater calibration (a) calibration curves at 4 different fields. (b) variation in heater resistance with magnetic field at different bath temperatures (c) 3-D surface plot of (b)

$| T_{AC} |= P_H/\kappa$ for $\kappa \gg \omega C$. The sample is strongly coupled to the thermal bath and the sample temperature oscillates with the maximum amplitude $T_{AC} = T_{DC} = P_H/\kappa$. Such a configuration is insensitive to specific heat of the system.

$| T_{AC} |= P_H/\omega C$ for $\kappa \ll \omega C$. At very large excitation frequency, the thermal relaxation are to slow to follow the driving heating power and therefore, T_{AC} is very small. In this case the sample temperature is $T = T_{bath} + T_{DC}$. The sample temperature oscillations $T_{AC} = P_H/C\omega$ are 90° out-of-phase with respect to the heater power P_H.

$| T_{AC} |= P_H/\sqrt{2}\kappa$ for $\omega = \kappa/C$. $\omega = \kappa/C$ is the cutoff frequency separating the above two extremal cases.

For the technique to be most sensitive to the specific heat of the sample, we judiciously choose an excitation frequency close to ω_c (as shown in Fig. 2.10(b)) depending on the particulars of the system under study. We try to select an excitation frequency such that not only the amplitude of temperature oscillations T_{AC} are big enough to determine the specific heat sensitively but are also negligible compared to the bath temperature. In our experiments $T_{AC} \sim\ 10 - 100\ mK$. Experimentally, $\omega_c = \kappa/C$ can be chosen by tuning to an excitation frequency for which the phase is $\theta = 45°$. A suitable excitation frequency close to ω_c can be chosen by performing measurement with the sample at a few different excitation frequencies and look for the maximum sensitivity as shown in Fig. 2.11.

Heater calibration: To precisely determine the sample temperature, the resistance of the Cernox heater is calibrated with respect to the reference thermometer of the thermal bath. To take into account the self-heating effects, i.e, T_{DC}, the heater resistance at zero excitation, R_{H0}, is obtained by a linear extrapolation of the heater resistances R_H at a few different small excitations. At zero self heating, the heater temperature is the same as the bath temperature. R_{H0} is determined at a few different bath temperatures to obtain calibration curve i.e., $\ln R_{H0}$ vs ln_T as shown in Fig.

2.12(a). The above process is then repeated to precisely calibrate the heater in magnetic fields using the field calibrated reference thermometer of the thermal bath. We determined R_{H0} values at four different magnetic fields (20 T, 25 T, 30 T and 35 T) at several different temperatures in the range of interest, i.e., from 1.3 K to 4 K. This way, calibration curves, i.e., R_{H0} vs T, are obtained at the above mentioned magnetic fields, as shown in Fig. 2.12(b) and Fig. 2.12(c).

Finally, using these calibration curves with appropriate polynomial fits, the sample temperature in a magnetic field is precisely determined. Due to the magnetoresistance of the heater and the thermometer, there is a very small variation, less than 1%, of the sample temperature in magnetic fields. For the AC specific heat measurements, the sample temperature, T, indicated in the later chapters is the value averaged over the relevant field interval.

2.3 Elastic response using ultrasound velocity

The elastic stiffness constants are obtained by measuring the velocity of ultrasonic elastic waves through a single crystalline sample. We measured the ultrasound velocity and elastic attenuation using either a frequency-sensitive or a phase- sensitive detection pulse-echo technique.

The pulse-echo method

In this method, we used piezoelectric transducers to generate and detect longitudinal and transverse acoustic waves. The measurement can be performed in either a reflection mode [see Fig. 2.13(a)], where a single transducer, attached to a flat surface of the sample, acts as both the ultrasonic generator and the detector, or in a transmission mode [see Fig. 2.13(b) and (c)], in which the generator and the detector are separate, and glued at the opposite parallel faces of the sample.

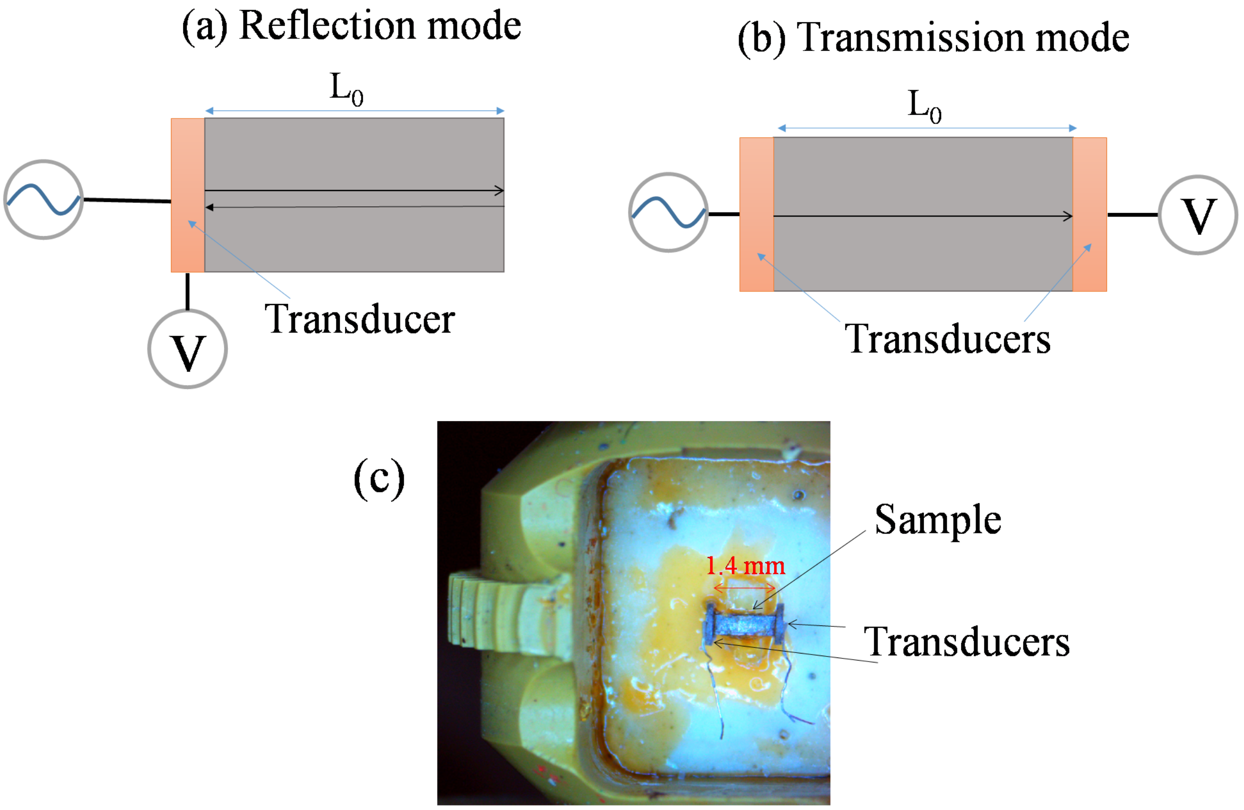

Figure 2.13: Schematic setup of the pulse-echo method for ultrasound velocity and attenuation measurement in the (a) reflection and (b) the transmission modes. (c) Actual sample-transducer assembly in the transmission mode.

An ultrasonic pulse generated by the generator transducer propagates through the sample. A part of the pulse is directly transmitted to the detector, while the rest is reflected back into the sample from the boundary. Pulses reaching the detector after multiple reflections at the opposite boundaries of the sample results in different echoes, which diminishes at each additional reflection. The velocity and the attenuation of the ultrasound pulse are determined through these echoes received at the detector. Each transit through the sample length (L_0) gives a phase shift $\phi = KL_0$ with respect to the original pulse signal, where $K = \omega/c_s$. The phase shift in the n^{th} echo is

1. $\phi_n = 2nKL_0$: for the reflection mode
2. $\phi_n = (2n+1)KL_0$: for the transmission mode

To measure the ultrasound velocity, a particular echo is selected (say n^{th} echo in the transmission mode). Then, the phase shift with respect to the reference signal is

$$\begin{aligned}\phi_n &= KL_0(2n+1)\\ &= \frac{\omega}{c_s}L_0(2n+1),\end{aligned} \tag{2.34}$$

Differentiating eq. 2.34 gives

$$\frac{d\phi_n}{\phi_n} = \frac{d\omega}{\omega} - \frac{dc_s}{c_s} + \frac{dL_0}{L_0} \tag{2.35}$$

Usually, the thermal expansion of the sample due to the temperature change, or the magnetostriction due to magnetic field can be neglected in comparison to the velocity changes, i.e., $dL_0/L_0 \approx 0$

2.3.1 Frequency sensitive or phase-locked method

In the frequency sensitive detection, the phase is kept constant, i.e., $d\phi = 0$. Therefore, the change in frequency is directly proportional to the change of the velocity.

$$\frac{d\omega}{\omega} = \frac{dc_s}{c_s} \tag{2.36}$$

The change of the velocity is measured by tracing the change of the frequency using a feedback loop that keeps the phase constant by changing the frequency.

The attenuation α of the ultrasound pulse amplitude can be obtained from an exponential fit of the consecutive echoes A_1 at x_1 and A_2 at x_2 with a complex parameter $K_r + \iota\alpha$ as

$$\begin{aligned}A_1(x_1) &= A_0 e^{\iota K_r x_1 - \alpha x_1}\\ A_2(x_2) &= A_0 e^{\iota K_r x_2 - \alpha x_2}.\end{aligned} \tag{2.37}$$

Subtracting the above two equation, we get

$$\alpha = \frac{1}{x_2 - x_1}\ln\left(\frac{A_1}{A_2}\right), \tag{2.38}$$

or in units of db/cm

$$\alpha = \frac{20}{x_2 - x_1}\log_{10}\left(\frac{A_1}{A_2}\right) \tag{2.39}$$

Generally, we select either the 1^{st} or the 2^{nd} echo, and monitor its variation as a function of temperature or magnetic field to measure the ultrasound velocity and attenuation. The relative accuracy of this method is $\frac{\Delta v}{v} \sim 10^{-6}$. The absolute velocity can be determined for the n^{th} echo in transmission mode as

$$v = L_0\frac{2n+1}{t}. \tag{2.40}$$

where t is the time taken between the generation of an ultrasound pulse and the detection of its n^{th} echo. In the $\mathrm{CeRhIn_5}$ samples of lengths between 1.5 - 2.5 mm, the typical values of absolute sound velocities measured at 4.2 K were 2000-4000 m/s. For the various modes, ultrasound frequencies were 30-200 MHz.

A schematic of the setup for the frequency-sensitive pulse-echo technique is shown in Fig. 2.14. A voltage divider divides the signal generated by the frequency generator (RF gen.) and gives the signal for the sample and for the reference (Hybrid). The output signal from the sample is multiplied with a signal from the hybrid in one of the mixers, while in the other one it is multiplied with a $\pi/2$ shifted signal also from the hybrid. The outputs from the two mixers are read using the gated integrator (GI) or boxcar averager.

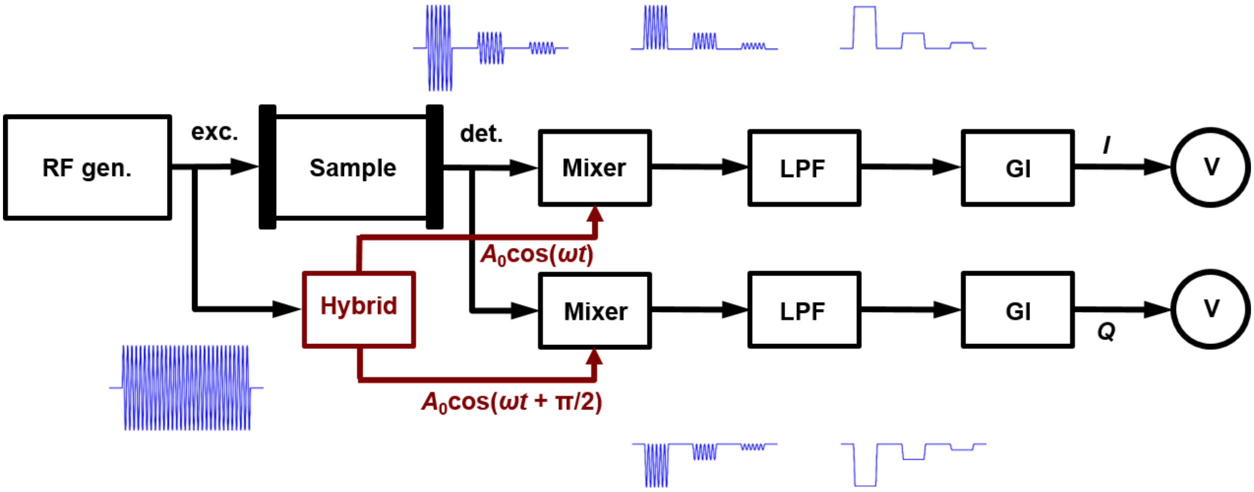

Figure 2.14: Schematic of the setup for a frequency-sensitive pulse-echo technique by Ref. [66].

2.3.2 Phase sensitive or frequency-locked method

Due to the extremely small duration ($\leq$150 ms) of the pulses in pulsed magnetic fields, the feedback loop is too slow to track the frequency change as a function of the magnetic field. Therefore, an alternate method is used to measure the ultrasound velocity and the attenuation. Instead of the phase shift, the frequency is held constant. The change of the velocity is then directly proportional to the change of the phase, which is determined by a comparative method numerically.

In this method, the overall signal during the pulse is divided into a fixed number of segments (10000) depending on the repetition rate (50 kHz or 20 μs) of the ultrasonic pulse. Each recorded segment contains a raw signal composed of echos coming from the sample. The amplitude and the phase were obtained through data analysis of the measured raw sine wave signal coming from the sample. For the data analysis, a phase comparator was used, between the reference signal and the signal from the sample [see Fig. 2.15]. The phase comparator gives two outputs, an in-phase signal I and a signal Q, phase separated from I, by $\pi/2$.

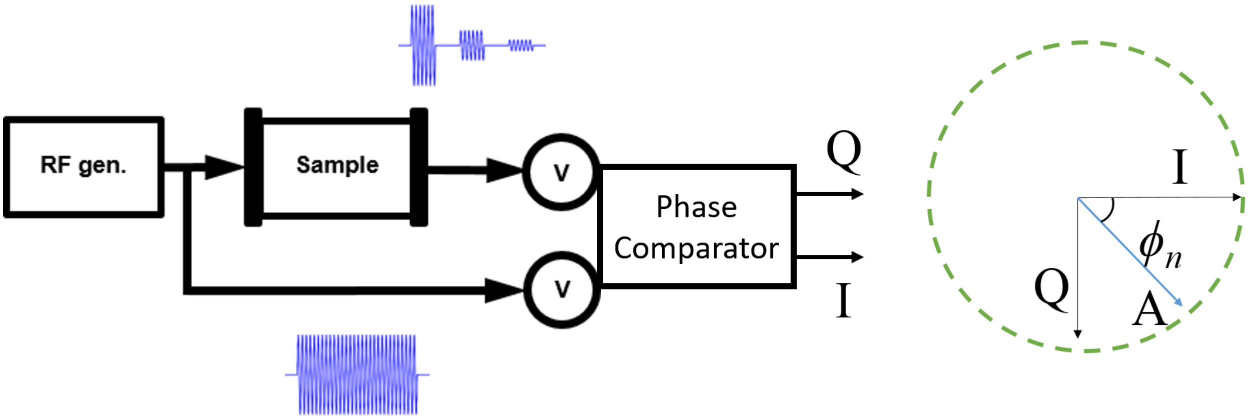

Figure 2.15: Schematic of the setup for a phase-sensitive pulse-echo technique by Ref. [66]. The phase and amplitude are numerically calculated from the orthogonal outputs I and Q from the phase comparator.

The phase and the amplitude can then be calculated as

$$tan(\phi_n) = \frac{Q_n}{I_n}, \tag{2.41}$$

$$A_n = \sqrt{I_n^2 + Q_n^2} \tag{2.42}$$

2.4 Longitudinal magnetization using Faraday balance

As discussed in section 1.1, the torque method for dHvA oscillations gives only a measure of the magnetization component perpendicular to magnetic field. The magnetization component parallel to the field, i.e., longitudinal magnetization is measured using an alternate capacitive technique based on the Faraday balance principle [67]. In this technique, a sample of the magnetization M is placed on a mobile CuBe platform exposed to a fixed magnetic field gradient dB/dz produced by a ferromagnetic Nickel piece which is also used as the ground plate of the capacitor as shown in Fig. 2.16

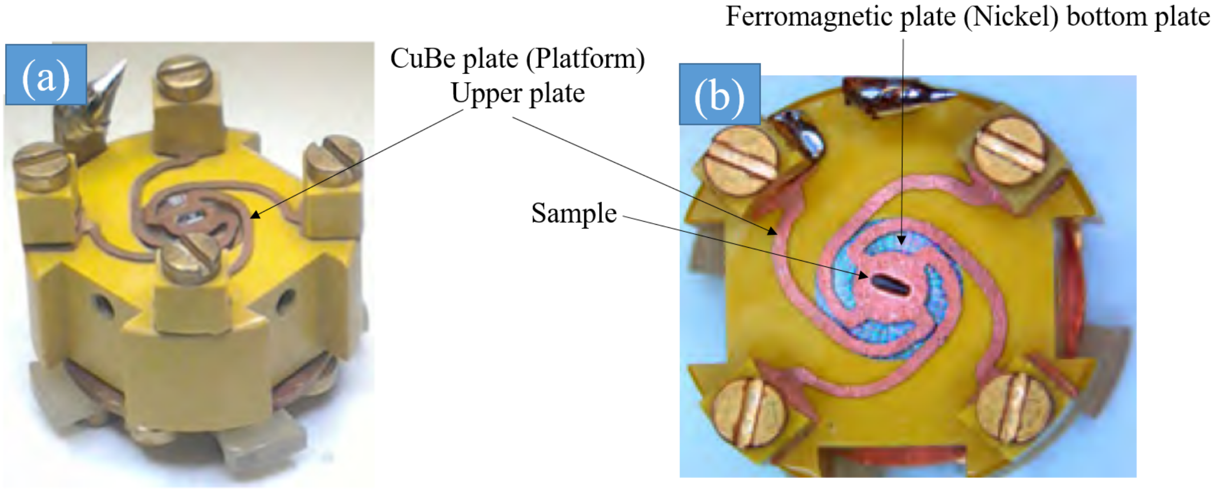

Figure 2.16: Faraday balance for measuring longitudinal magnetization

The mobile CuBe platform is displaced by a force $\vec{F}$ acting on the sample along the direction of the field gradient

$$\vec{F} = -\vec{M}\frac{d\vec{B}}{dz} \tag{2.43}$$

Similar to the torque method, the sample displacement is measured as the change of the capacitance using a high precision capacitance bridge from Andeen-Hagerling. The sensitivity of this method is 10^{-7} emu.

2.5 Magnetoresistance using four-point method

Magnetoresistance measurements were performed on both bulk samples as well as microstructured devices of heavy fermion systems. The microstructured devices were fabricated at HLD/MPI Dresden using focussed ion beam (FIB).

Magnetoresistance measurements were performed using a standard *four-point* resistivity method in a dilution fridge in static fields. The measurements were performed with a very small ac excitation current of the order of $10 - 100$ μA and the output signal was amplified using pre-amplifier and transformers and detected using a lock-in amplifier. The sensitivity of the measurement is $5m\Omega$.

Chapter 3

$CeRhIn_5$

Rare-earth-based materials are now widely recognized as an ideal playground for exploration of the fascinating physics that develops around a quantum critical point (QCP), a second-order phase transition at zero temperature [68, 44, 69]. In Ce-based compounds, such a QCP can be induced by hydrostatic pressure, chemical doping, or magnetic field, where it typically separates a magnetically ordered from a nonmagnetic ground state. Therefore, from the experimental point of view, Ce-based heavy-fermion materials are particularly suitable systems to investigate. Further, in these compounds, relatively small energy scales allow the tuning of the electronic correlations by using accessible pressures and magnetic fields leading to novel exotic states such as unconventional superconductivity, electronic-nematicity and/or other unusual states in the vicinity of a QCP.

Among the many Ce-based heavy fermions, the so-called 'Ce-115' heavy fermion systems, discovered only two decades back, have attracted particular attention. The observation rich physics in form of magnetism, unconventional superconductivity, NFL behaviour, pressure and field-induced quantum critical points among many other exotic phenomena, have established the Ce-115 family ($CeRhIn_5$, $CeCoIn_5$ and $CeIrIn_5$) as the poster child of heavy fermion physics. However, in-spite of a vast number of studies, several aspects of these compounds still remain poorly understood. This thesis is an attempt to understand such unresolved aspects in the two compounds, $CeRhIn_5$ and $CeCoIn_5$. This particular chapter is dedicated to $CeRhIn_5$ and the subsequent chapter is focused on the compound $CeCoIn_5$.

Finally, the 2D-like compounds in the Ce-115 heavy fermion family can be systematically extended to their 3D-like analogs forming the so called 'Ce-218' heavy fermion family. Although, the members of the Ce-218 family are qualitatively similar to their corresponding 2D analogs in Ce-115s family, the energy scales associated with physical properties such as T_c (for SC state), T_N (for AFM state), T_{coh} (for Kondo effect) are significantly modified. Therefore, the final chapter is dedicated to growth and characterization of Ce-218 compounds, especially Ce_2CoIn_8.

3.1 Introduction

Similar to all the members of Ce-115 heavy fermion family, $CeRhIn_5$ also crystallizes into a tetragonal $HoCoGa_5$ structure (space group $P4/mmm$) with lattice parameter $a = 4.652$ Åand $c = 7.542$ Å. At ambient pressure and zero magnetic field, it undergoes an antiferromagnetic (AFM) transition at $T_N = 3.8$ K. The electronic specific heat coefficient, $\gamma \approx 400$ mJ/K^{2}mol, makes $CeRhIn_5$ a moderate heavy-fermion material [70, 71, 72]. In the AFM state, the electronic contribution is $\gamma_0 \sim 56$ mJ/K^{2}mol [73].

3.1.1 Pressure as tuning parameter

In 2000, Hegger et al. detected a pressure-induced superconducting state in $CeRhIn_5$ at pressures above 16.3 kbar, with a maximum transition temperature $T_c \sim 2.2$ K at P = 21 kbar [70] [see Fig. 3.1]. Since then, $CeRhIn_5$ has taken the center stage as a prototypical material to investigate heavy fermion physics. The appearance of pressure-induced superconductivity qualitatively conformed with the Doniach picture and the widely accepted view that superconductivity in AFM heavy fermions is mediated by spin fluctuations near the AFM QCP [37].

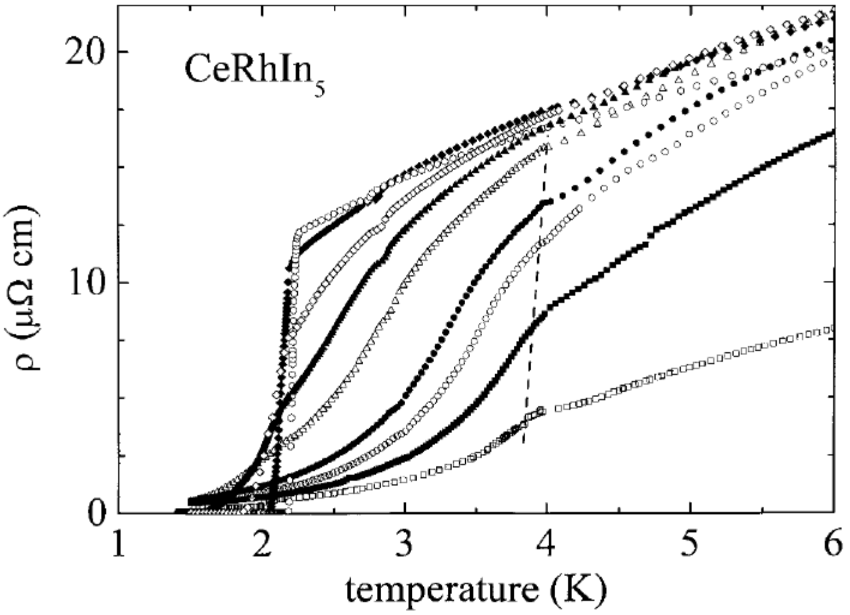

Figure 3.1: Pressure induced superconductivity in CeRhIn$_5$. Adapted from Ref. [70]

Before CeRhIn$_5$, the cubic heavy fermion compound CeIn$_3$ and tetragonal CePd$_2$Si$_2$ also showed pressure-induced superconducting phase near the AFM QCP but with a smooth suppression of the AFM state [37]. However, in CeRhIn$_5$, Hegger et al. detected an abrupt disappearance of antiferromagnetism and appearance of superconductivity at a critical pressure P_c between 14.5 and 16.3 kbar. Therefore, the transition from AFM to SC state was attributed to be first-ordered. Also, the initial transition temperature T_c of the pressure induced superconducting state in CeRhIn$_5$ was roughly 10 times that of CeIn$_3$, which was thought to be due to its unique electronic structure.

The tetragonal CeRhIn$_5$ is composed of planes of CeIn$_3$ with intermediate layers of RhIn$_2$ sandwiched in between. In an analogy with the high-temperature cuprate superconductors, the structure can be viewed as a stack of alternating layers of conducting CeIn$_3$ and insulating RhIn$_2$ along the c axis [74] [see fig. 3.2(a)]. It was suggested that the quasi-two-dimensional configuration of the CeIn$_3$ layers is at the heart of the unusual pressure dependence of CeRhIn$_5$.

Subsequently, a number of studies were carried out to understand the electronic and magnetic structure of CeRhIn$_5$. In this regard, a ^{115}In nuclear quadrupolar resonance (NQR) study revealed that in the AFM state, a magnetic moment $\mu_{Ce} \sim$ 0.1 - 0.2 μ_B is localised at cerium site with a spiral modulation that is incommensurate with the lattice [75]. Further, based on several neutron diffraction studies, it was established that in the AFM phase, the Ce moments are antiferromagnetically aligned within the CeIn$_3$ planes [see fig. 3.2(a), (b)] and the Ce moments spiral transversely along the c axis with the incommensurate propagation vector $\mathbf{Q} = (0.5, 0.5, 0.297)$ [76]. Along this spiral, the twist of magnetic moments is approximately 107° per CeIn$_3$ layer and is apparently related to the intervening RhIn$_2$ layer [76] [see fig. 3.2(c)]. The quasi-2D structure of CeRhIn$_5$ was indicated by the NQR study and later established by the anisotropic Fermi surfaces observed in a dHvA study [77]. Several dHvA experiments unambiguously suggest that the f electrons of CeRhIn$_5$ are localized at ambient pressure [78, 79].

More careful studies on cleaner samples revealed that superconductivity evolves rather smoothly and at pressures lower than 16 kbar [80]. Also, the region of coexistence of AFM and SC was found to exist in a wider pressure range. Furthermore, a dHvA study exploring the evolution of the Fermi surface with pressure revealed that the onset of superconductivity is accompanied by a simultaneous build up of a heavy fermion state (i.e. enhancement of effective masses) upto 2.1 GPa, however the Fermi surface remained unchanged [81]. Taking a cue from the drastic increase

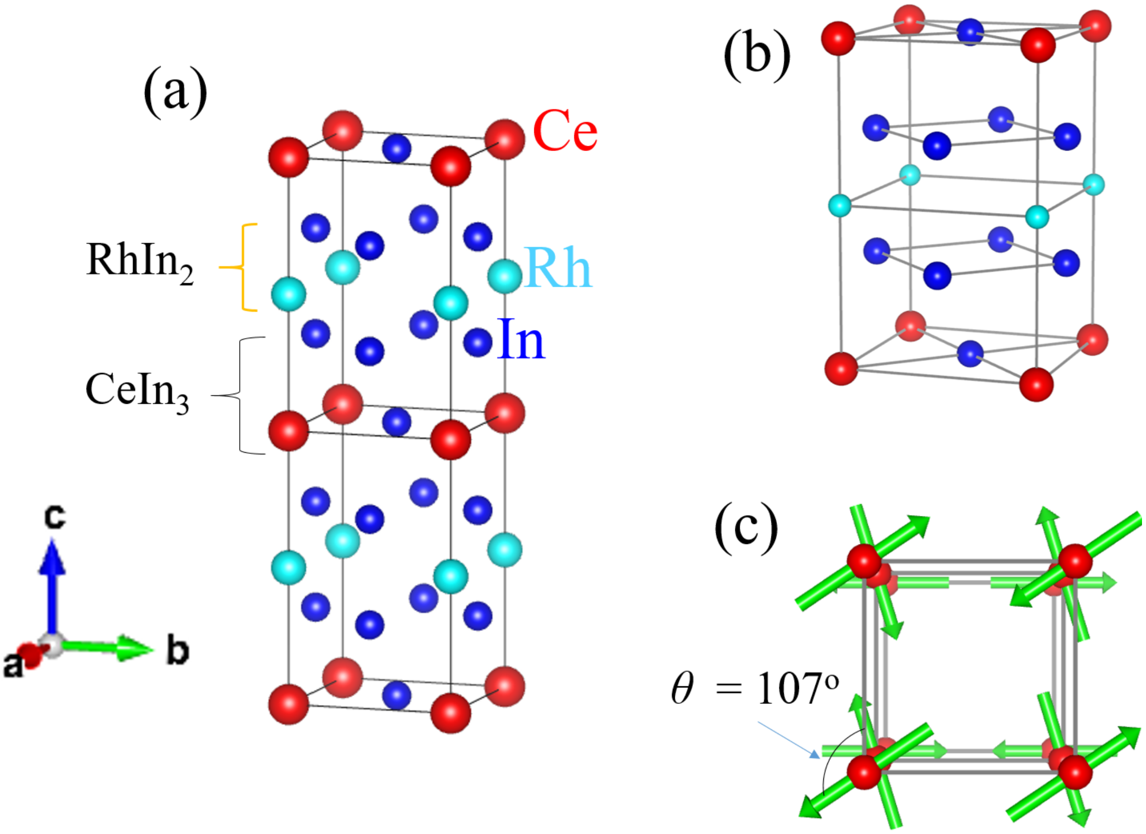

Figure 3.2: Crystal structure of $CeRhIn_5$. (a) alternating layers of $CeIn_3$ and $RhIn_2$ stacked along the c axis. (b) unit cell of $CeRhIn_5$ (c) transverse view from c direction showing a tilt of $\theta = 107^\circ$ between Ce moments on consecutive $CeIn_3$ layers.

of the effective masses with pressure on the two quasi-cylindrical Fermi surfaces, H. Shishido et al. carried forward their study to still higher pressures. In 2005, in their highly influential paper, H. Shishido et al. reported a divergent behavior of the effective masses at 2.35 GPa accompanied by a drastic change of the Fermi surface [82]. As the critical pressure $P_c = 2.35$ GPa is reached, all the dHvA frequencies observed at $P = 0$ increase discontinuously signaling an abrupt Fermi surface reconstruction as a consequence of the f electron delocalization [82] [Fig. 3.3(a)]. In addition, the effective masses diverge at P_c [Fig. 3.3(b)]. These observations are consistent with local critical or Kondo-breakdown type QCP. The pressure-induced QCP in CeRhIn$_5$ is now considered to be a textbook example of the Kondo-breakdown type QCP.

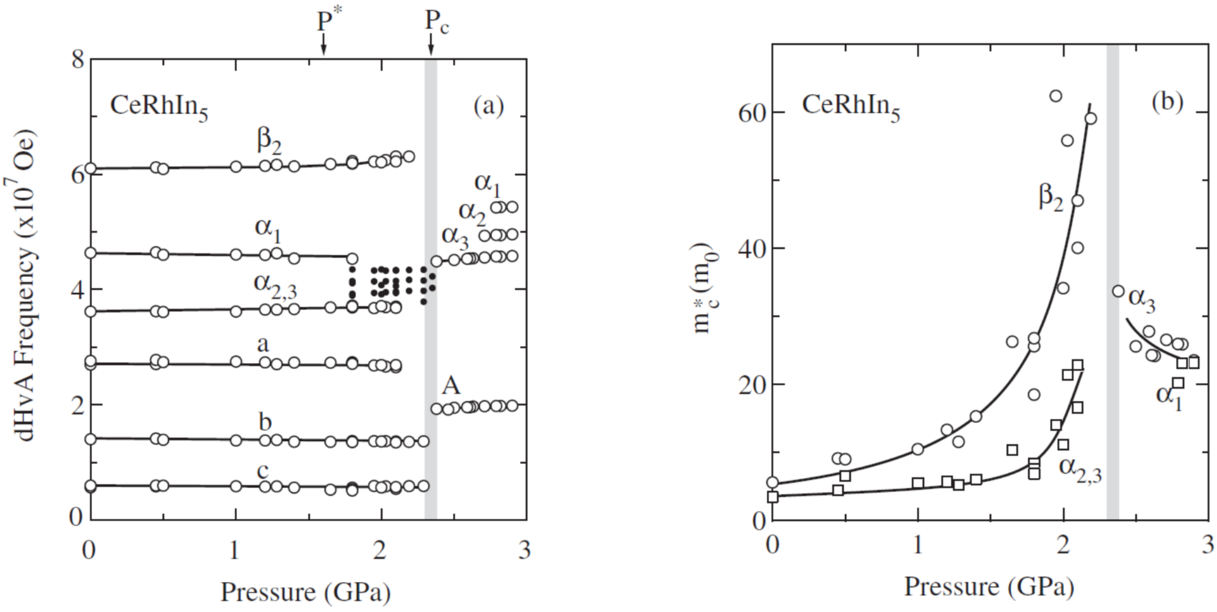

Figure 3.3: Pressure-induced QCP in CeRhIn$_5$, adapted from Ref [82]. (a) An abrupt change of dHvA frequencies at $P_c = 2.3$ GPa and (b) the corresponding divergence of the effective masses of $\alpha_{2,3}$ and β_2 orbits.

In 2006, a startling observation was made by an AC magnetic susceptibly study in the form of coexistence of SC and AFM in CeRhIn$_5$ at ambient pressure. Instead of being pressure-induced, superconductivity was observed at ambient pressure with a $T_c \approx 90$ mK [83]. The T$_c$ increased significantly above 10 kbar, exactly where T$_N$ starts decreasing rapidly [see fig. 3.4(a)]. This competitive coexistence of superconductivity and antiferromagnetism attracted a lot of attention with a combination of two different tuning parameters such as pressure-field and pressure-substitution studies.

In parallel, studies were also directed at understanding the role of helical magnetic structure as a factor for stabilizing the superconducting state. Up to 8.6 kbar, the magnetic structure remains unchanged with $\mathbf{Q} = (0.5, 0.5, 0.297)$. At 10 kbar, however, a sudden change in the magnetic structure occurs with $\mathbf{Q} = (0.5, 0.5, 0.396)$ [84], although, the magnetic transition temperature remains the same. This change of the magnetic modulation may be the outcome of a change in the electronic character of this material at 9 kbar where SC and AFM compete. The change of $\mathbf{Q}$ in the pressure range from 8.6 to 10 kbar signifies a change in the rotation angle of the spiral spin structure from 107° to 142.6°, as shown in fig. 3.4(b).

3.1.2 Chemical pressure or substitution as tuning parameter

Several attempts have also been made to study the QCP and coexistence of SC and AFM states by either diluting or increasing the concentration of different ions.

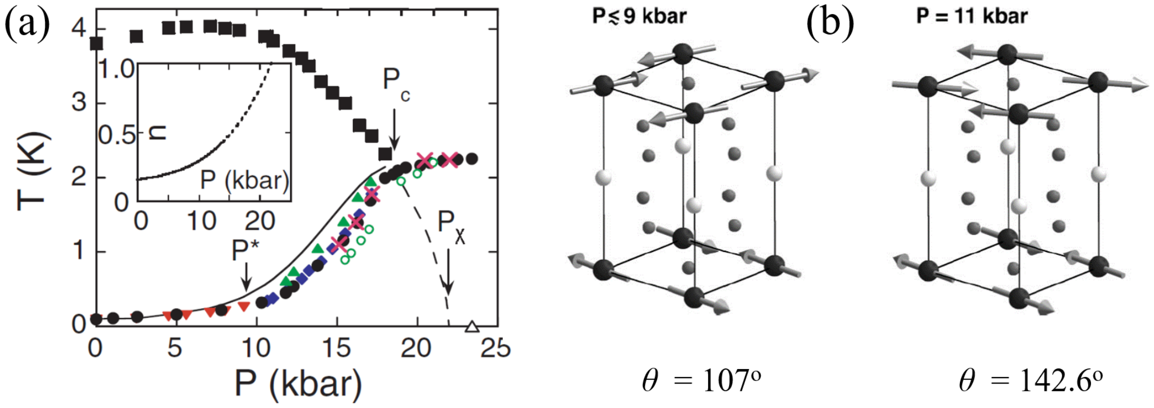

Figure 3.4: Competitive coexistence of the AFM and SC state in CeRhIn$_5$ with pressure, adapted from Ref [83]. (b) Pressure induced change of the magnetic structure [84]

CeRh$_{1-x}$Co$_x$In$_5$

When Rh is substituted with Co, the incommensurate AFM order with $\mathbf{Q} = (0.5, 0.5, 0.297)$ of pure CeRhIn$_5$ is weakly suppressed for small dopings. For intermediate Co concentrations a commensurate AFM with $\mathbf{Q_c} = (0.5, 0.5, 0.5)$ and an incommensurate AFM structure with $\mathbf{Q_I} = (0.5, 0.5, 0.42)$ evolves that coexists with SC state [85, 86] [see Fig. 3.5(a)]. This suggests that $\mathbf{Q_c}$ and $\mathbf{Q_I}$ modulations are significantly enhanced in the intermediate x range, and may be connected with the evolution of the superconductivity.

Upon substituting Rh by Co, a discontinuous change of the dHvA frequencies was observed in CeRh$_{1-x}$Co$_x$In$_5$ [87]. However, the FS reconstruction does not occur at the critical concentration $x_c \approx 0.8$, where the AFM order is suppressed, but deep inside the AFM state, at $x \simeq 0.4$, where the AFM order alters its character and superconductivity emerges. Furthermore, the effective masses do not diverge anywhere. Thus, the doping-induced QCP appears to be of the SDW type.

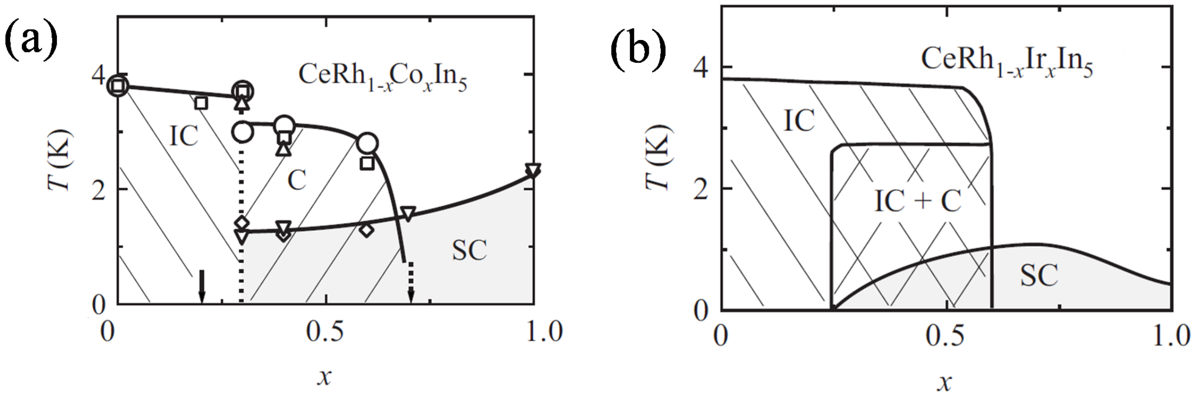

Figure 3.5: Temperature-concentration phase diagram for (a) CeRh$_{1-x}$Co$_x$In$_5$, adapted from ref. [86] and (b) CeRh$_{1-x}$Ir$_x$In$_5$ adapted from ref. [88, 85]. The region of coexistence contains 3 distinct states, namely SC, AFM IC and AFM C

CeRh$_{1-x}$Ir$_x$In$_5$

When Rh is substituted with Ir, the superconducting region was observed over a broad range of dopings $0.3 \leq x_{Ir} \leq 1$. Also, the region of coexistence of SC and AFM is from $x_{Ir} = 0.3$ to $x_{Ir} = 0.6$ [89, 90]. Under pressure, the broad superconducting dome splits into two distinct SC phases. The one coexisting with AFM state has a higher T$_c$ [91, 92]. The region of coexistence of SC and AFM revealed the coexistence of two distinct antiferromagnetic structures, as shown in Fig. 3.5(b). One of them is the incommensurate helical structure with $\mathbf{Q} = (0.5, 0.5, 0.297)$, of pure CeRhIn$_5$, while the other one is a commensurate structure with $\mathbf{Q} = (0.5, 0.5, 0.5)$ that appears below T$_{Nc}$ = 2.7 K. The appearance of the commensurate AFM order was suggested to be responsible for superconductivity [88].

La$_x$Ce$_{1-x}$RhIn$_5$

The substitution of a non-4f ion La in place of Ce leaves f electrons localized, but shifts the $P-T$ phase diagram further into the magnetic side [93, 79]. The pressure-induced superconducting state still persists upon dilute doping of Ce with a non-magnetic (non-4f) La[93]. Upon a 10% substitution, T$_N$ is suppressed from 3.8 K to 2.7 K with the same staggered moment of Ce = 0.38 μ_B [94, 93].

CeRhIn$_{4.84}$Sn$_{0.16}$

Similar to La$_x$Ce$_{1-x}$RhIn$_5$, in Sn-doped CeRhIn$_5$ i.e., CeRhIn$_{4.84}$Sn$_{0.16}$, the T$_N$ is suppressed from 3.8 K to 2.7 K. However, the P-T phase diagram shifts towards the Kondo state [93] similar to the case of Rh substitution by Co or Ir.

3.1.3 Magnetic field as tuning parameter

The behavior of CeRhIn$_5$ in magnetic field is unique. Magnetic field applied in the basal plane of the tetragonal crystal structure induces two additional magnetic transitions [see Fig. 3.6(a) and (b)], observed in specific heat [73], thermal expansion, and magnetostriction measurements [95]. The one at low temperatures is a first-order metamagnetic transition. It occurs at $B_m \sim 2$ T at low temperatures [78, 73, 95]. The transition corresponds to a change of the magnetic structure from the ambient pressure and zero field incommensurate helicoidal phase $\mathbf{Q} = (1/2, 1/2, 0.297)$ [76] to a commensurate collinear square-wave ('up-up-down-down' configuration) with the propagation vector $\mathbf{Q} = (1/2, 1/2, 1/4)$ [96, 97, 98]. A schematic diagram of such a field-induced change of the magnetic structure is shown in Fig. 3.7.

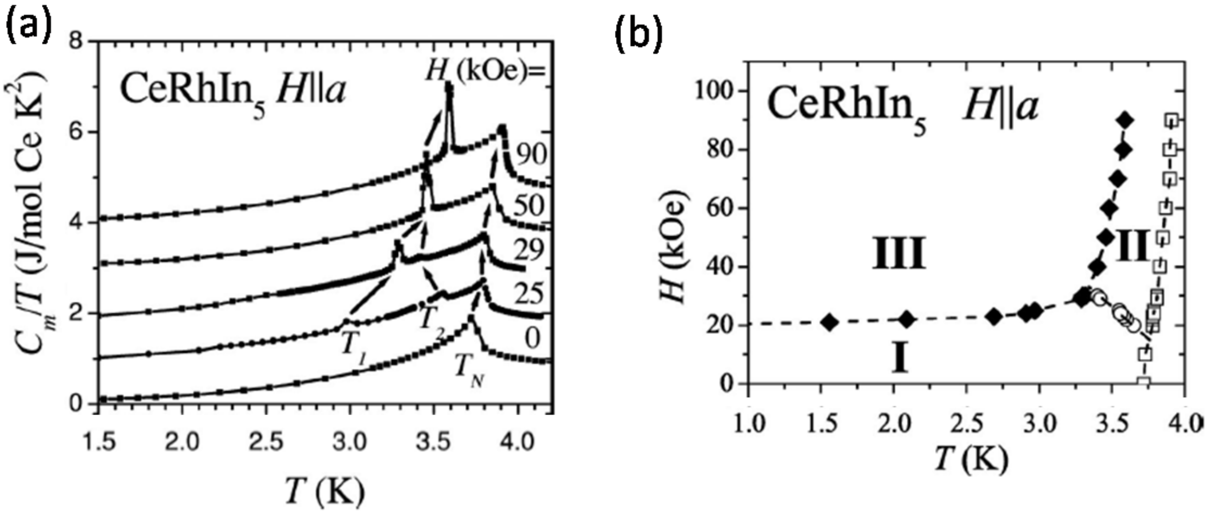

Figure 3.6: Magnetic field induced phase transitions in CeRhIn$_5$ for field applied along the a axis (left) and the corresponding phase diagram (right). Solid symbols represent first-order and open symbols represents second-order transition. Adapted from Ref [73]

In the 'up-up-down-down'-type structure, the magnetic moments still lie within the basal plane, but are now aligned perpendicular to the applied field direction [96, 97]. When the magnetic field is tilted away from the basal plane, this metamagnetic transition field B_m increases, and initially follows a $1/\cos(\alpha)$ dependence, where α is the angle from the basal plane towards the c axis [78]. At

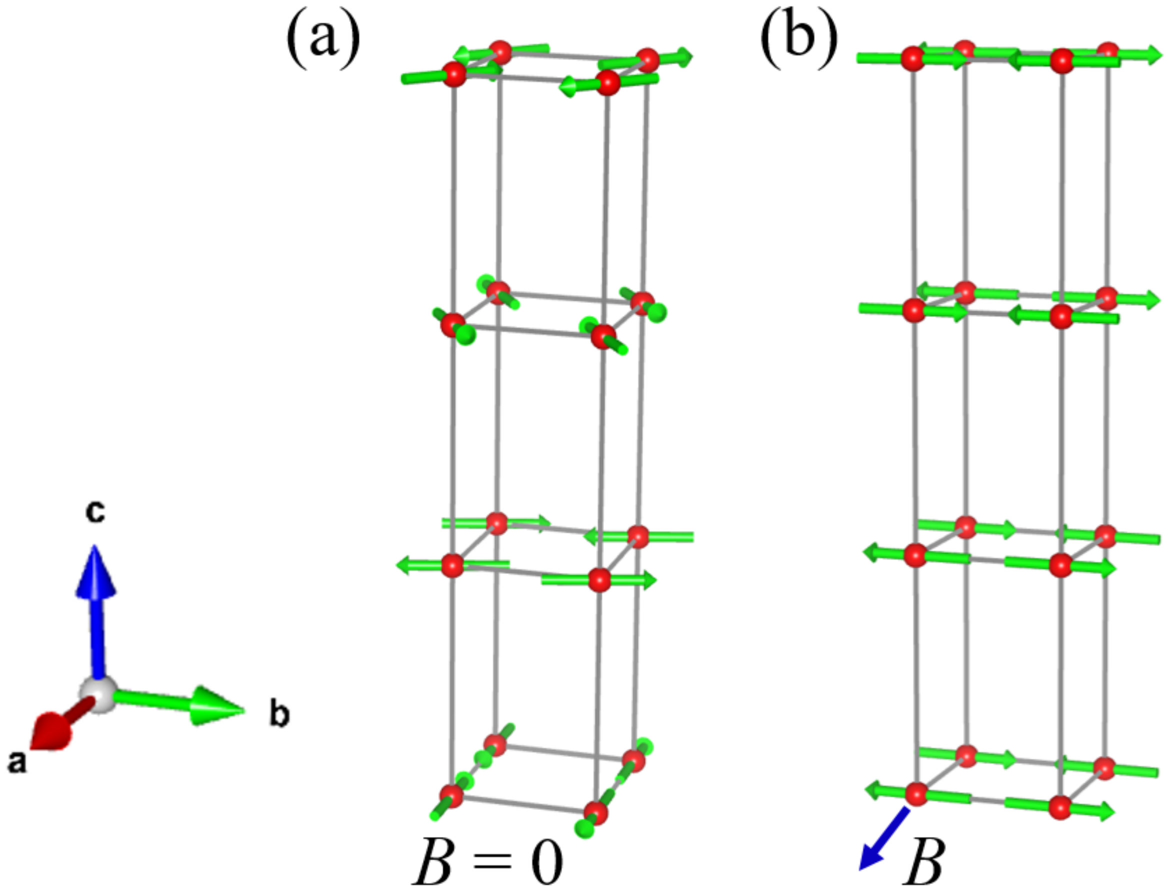

Figure 3.7: A schematic illustration of the (a) helical incommensurate magnetic structure in $CeRhIn_5$ at ambient pressure and zero field and (b) the commensurate collinear “up-up-down-down” field-induced magnetic structure for $B \geq 2$ T along the a axis.

larger angles $\alpha \geq 75°$, B_m deviates from this dependence to lower values. It occurs slightly above 20 T when the field is applied at $\theta = 2°$ from the c axis, the lowest angle at which we observed the corresponding anomaly.

The higher temperature transition is second order. This transition occurs in a narrow temperature range. The exact magnetic structure throughout this temperature-field range is still not clear. According to the initial report, this transition corresponds to a small change of the ordered moment, while the propagation vector remains the same as in zero magnetic field [96]. However, a more recent report suggests that this phase corresponds to the incommensurate elliptical helix with strongly modulated magnetic moments and temperature-dependent propagation vector $\mathbf{Q} = (1/2, 1/2, l(T))$ [97].

A field-induced QCP was reported to occur at the critical magnetic field, B_c, of about 50 T along both the c and a axes [99, 100], as shown in Fig. 3.8. The critical field of the AFM suppression is surprisingly high considering the AFM ordering transition temperature $T_N = 3.8$ K. Furthermore, in a strongly anisotropic material like $CeRhIn_5$, almost the same critical field for the two principal crystallographic directions is also surprising. It must be noted, however, that this experiment was performed in pulsed fields using an AC calorimetry in which the two low field-induced transitions were not detected.

The interest in $CeRhIn_5$ was renewed with the observation of a *new feature* at a magnetic field $B^* \approx 30$ T applied along or close to the c axis. This high-field feature was observed deep within the AFM state. It separates the high-field phase of $CeRhIn_5$ from the well-studied low-field phase. So far, this feature has been detected in several measurements at a field around 30 T or B^* (from

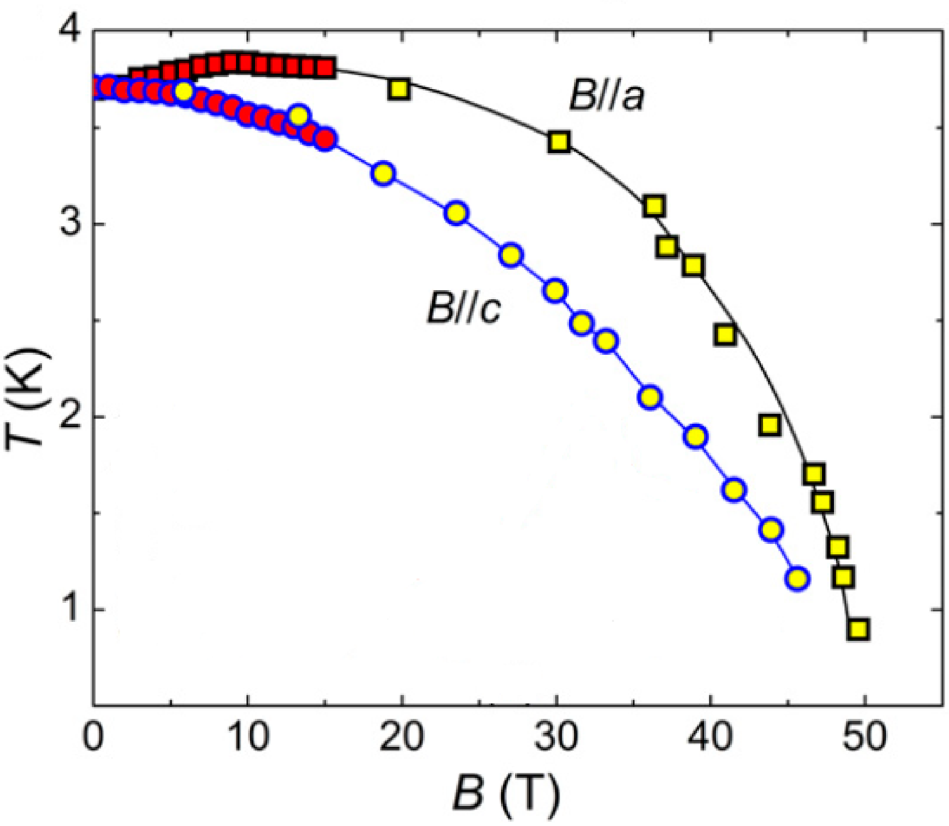

Figure 3.8: Magnetic field induced quantum critical point in CeRhIn$_5$ at 50 T. Adapted from ref [99].

now on) [99, 101, 102, 43, 103, 104, 105]. Various interpretations were put forward to explain the nature or origin of this feature and the high-field state above it. Now I shall discuss these studies and their interpretations one by one.

This feature was first detected as an anomaly in hall resistivity ρ_{xy}, at B^*, as shown in Fig. 3.9(b) [99]. The feature at $B_m = 18$ T corresponds to the 2 T metamagnetic transition from incommensurate to commensurate structure for a field orientation of a few degrees away from the c axis. In the same paper, dHvA measurements in high magnetic fields also revealed an unusual physics at B^*. Although, there was no direct indication of any anomaly at B^* in the raw torque signal, quantum oscillations, however, revealed an emergence of new dHvA frequencies in fields above B^*. The newly observed orbits above B^* are α_2, α_1, and β_1 as shown in Fig. 3.9(a). The appearance of these new dHvA frequencies was interpreted as a field-induced Fermi-surface reconstruction above 30 T, where the Fermi-surface changes from *small* to *large*, and the f electrons change their character from localized to itinerant.

This implies that the field-induced QCP is of the SDW type, as shown in Fig. 3.9(c). The latter result is very surprising given that magnetic fields are generally expected to localize $4f$ electrons. Moreover, contrary to pressure- and doping-induced QCPs, the low-field dHvA frequencies do not change at B^*, which seriously questions the validity of the FS reconstruction scenario. This inconsistency motivated us to re-examine the FS of CeRhIn$_5$ at high magnetic fields.

From there on, efforts were naturally made to unravel the high-field physics of CeRhIn$_5$. In this regard, magnetoresistance measurement have been particularly employed. CeRhIn$_5$ is a highly conductive metal, as evident by the in-plane and out-of-plane resisivities of a few $\mu\Omega$cm. Therefore, direction-dependent resistivity measurements under high magnetic fields were carried out on microstructured devices of CeRhIn$_5$ fabricated using focused ion beam (FIB).

In the magnetoresistance measurements on FIB devices of CeRhIn$_5$, Moll et al. detected a sharp increase in the in-plane resistivity at B^*, which then gradually decreases at higher fields up to a minimum at the critical field for AFM the suppression at B_c, while the out-of-plane resistivity

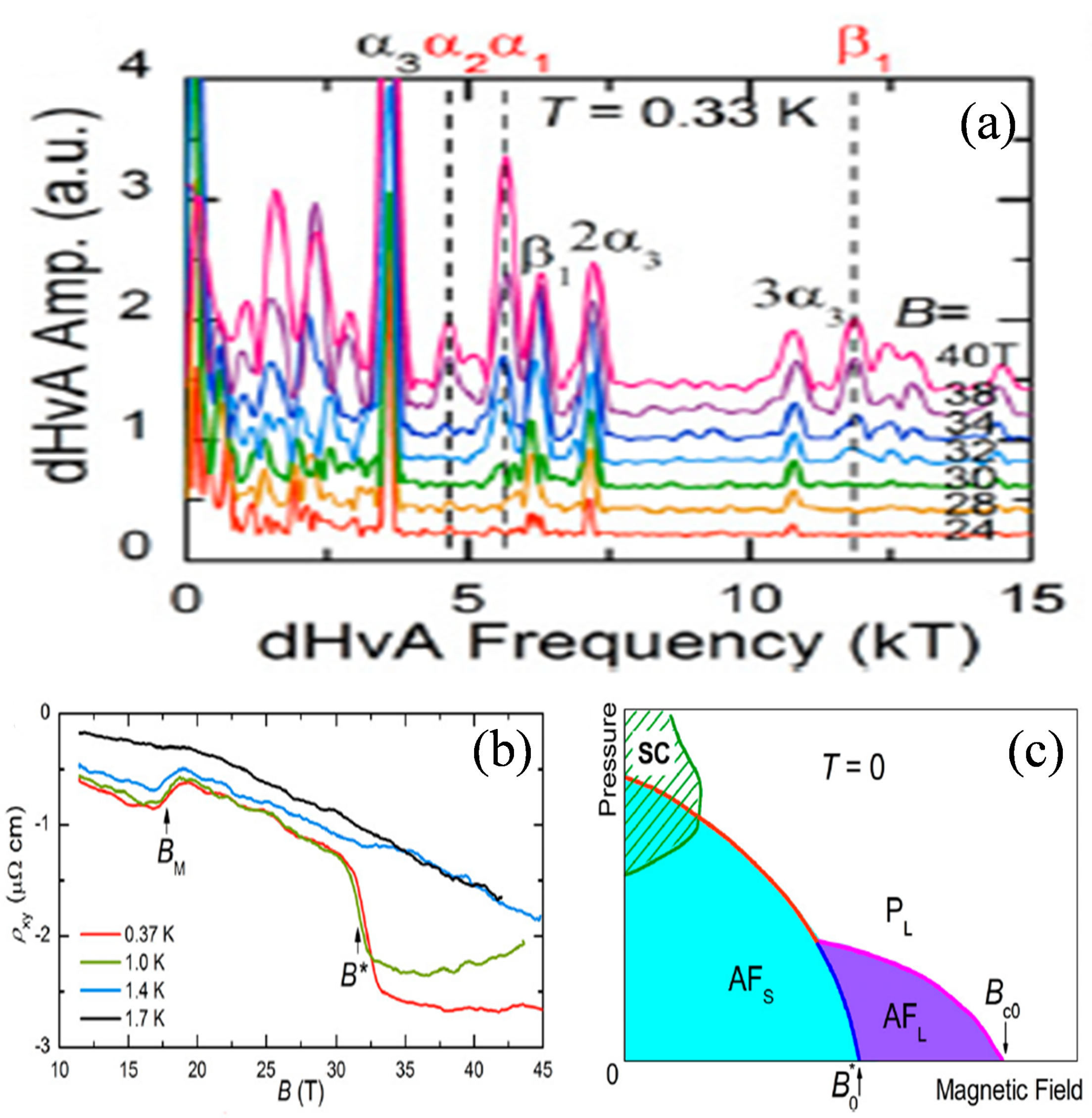

Figure 3.9: Field induced Fermi surface reconstruction at B^* depicting (a) an emergence of new dHvA frequencies, (b) a sharp anomaly in the hall resistivity, (c) the $T - B$ phase diagram of the SDW type QCP with delocalization of the f electrons, which occurs inside the AFM phase at B^*. Adapted from ref. [99].

remained featureless, as shown in Fig. 3.10(a). The feature at B^* showed a huge hysteresis associated with a reminiscent or memory-dependent state generally seen for a first-order transition. Further, a non-linear electrical transport revealed increasing conductivity with current bias. Based on these observations, the feature at B^* was interpreted as a first-order transition into a density wave (DW) state [101].

The magnetic field, at which the feature occurs, has a relatively weak dependence on the angle θ of the field from the c axis. The feature was observed at 27 T for $\theta \sim 0°$, and it exists up to $\theta \sim 60°$ at 34 T. However, the size of the step showed a non-monotonous angular dependence with a maximum at 20° [fig. 3.10(b)]. The suggested $T - B$ phase diagram depicting the field-induced density wave state is shown in Fig. 3.10(c). It must be noted that the size of the hysteresis was found to be sample dependent, and it decreases for larger sample. The FIB fabricated samples are strained, especially the thinner ones, as they are glued onto a substrate. Therefore, the effect of strain on the observed magnetoresistance feature at 30 T in FIB fabricated CeRhIn$_5$ samples cannot be ruled out.

The question of hysteresis was carefully considered by Ronning et al. in a more recent magne-

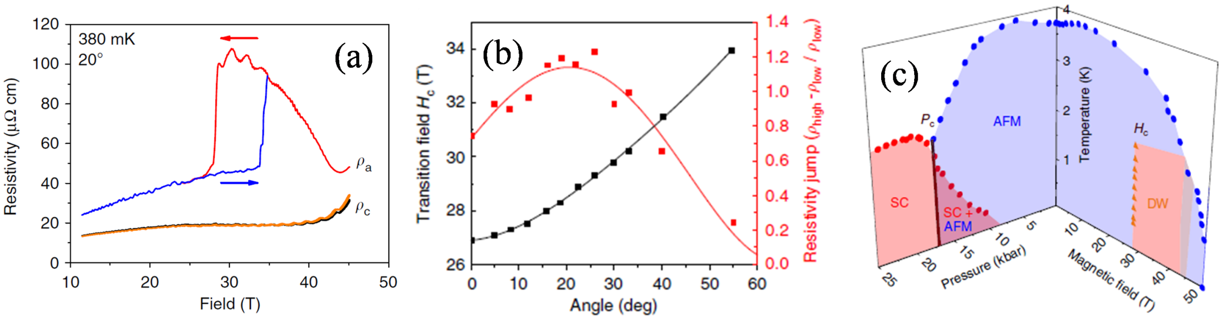

Figure 3.10: Magnetoresistance in FIB fabricated microstructures of CeRhIn$_5$, adapted from Ref. [101]. (a) The anomaly in the in-plane resistivity with a huge hysteresis. (b) Angle dependence of the size and the position of the anomaly. (c) Suggested $T-B$ phase diagram with high field DW state.

toresistance study on FIB fabricated devices of special geometry[43]. One FIB fabricated device probed the resistivity in the basal plane along the two orthogonal directions [110] and [1$\bar{1}$0], and a second FIB device proved the resistivity along the symmetry-inequivalent orthogonal directions [100] and [010]. The magnetoresistance of each device showed a resistive anomaly for fields at $\sim 20°$ from the c axis around $B^* \sim 28$ T, signaling the entry into the high-field phase. At the same time, a substantial asymmetry between the two orthogonal in-plane resistance bars emerged (red, blue traces in Fig. 3.11(a)).

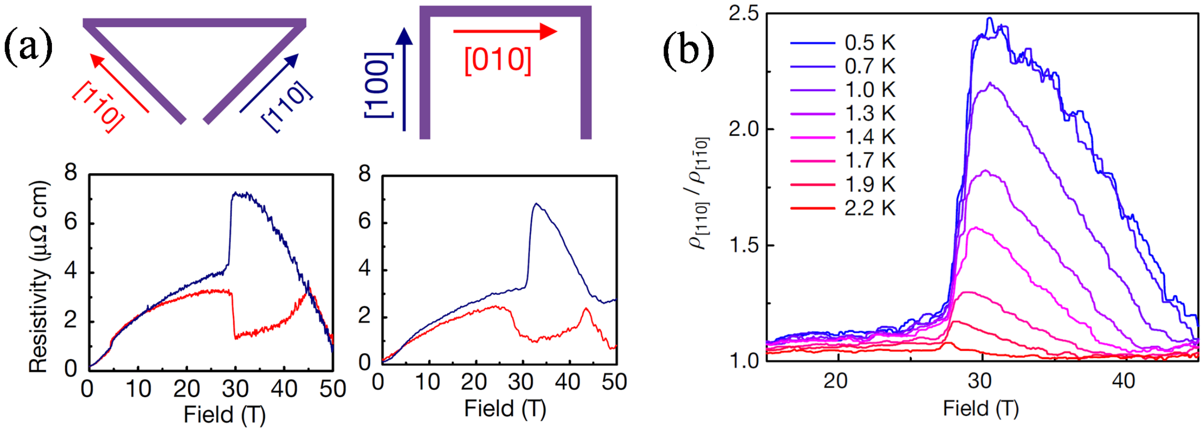

Figure 3.11: (a) In-plane electronic anisotropy in CeRhIn$_5$ at field applied at 20° from the c axis for two FIB devices probing the orthogonal symmetry inequivalent channels [110], [1$\bar{1}$0] and [100], [010]. Adapted from Ref.[43]. (b) Temperature dependence of the magnetoresistance anomaly at B^*.

The most striking observation was the appearance of a strong in-plane resistivity anisotropy ($\rho_{\|}/\rho_{\perp}$) in this high-field phase beyond B^*. The in-plane anisotropy at B^* was observed to be the most pronounced for $\theta = 20°$. The anisotropy successively decreases at higher fields and becomes isotropic at the AFM phase boundary in accordance with the previous report [101] [see Fig. 3.11(a) and (b)].

The presence or absence of a hysteresis was studied by the gradual closing of resistivity anisotropy in the current channels along [110] and [1$\bar{1}$0] directions with the orientation of magnetic field θ from the c axis at $B = 35$ T. At $\theta = 20°$ the anisotropy is maximum, and it decreases to zero on approaching $\theta = 0°$. The up and down angle sweeps are identical indicating no hysteresis [see Fig. 3.12]. The vanishing of the hysteresis at $B \parallel c$ was then argued as incompatible with density waves. Furthermore, the non-linear conductivity was found to decrease with increasing electric bias contrary to the report by Moll et al.

Therefore, based on these new observations, Ronning et al. suggested an alternate interpretation

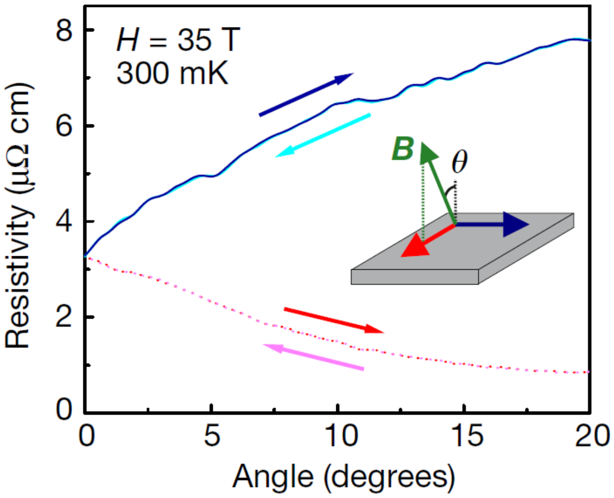

Figure 3.12: The high-field in-plane electronic anisotropy as a function of the angles θ from the c toward the a axis. Arrows indicate the direction of rotation of sample in field. Adapted from Ref.[43].

of the high-field state. They attributed the in-plane resistivity anisotropy at $B^* \approx 30$ T to the in-plane symmetry breaking of the underlying electronic structure from C_4 to C_2. The feature at B^* corresponds to a transition into a state of lower symmetry similar to an electronic-nematic phase [43, 103]. The electronic-nematic phase interpretation is based on the necessity of a finite in-plane field component to give rise to the anisotropy through the directional alignment of the nematic domains.

The electronic-nematic state due to the in-plane symmetry breaking is accompanied by a small lattice distortion $\frac{\Delta L}{L} \leq 2 \times 10^{-6}$ for a magnetic field applied at $\theta = 11^\circ$ from the c axis [43]. Later on, a high-resolution dilatometry study was performed to carefully understand the response of the lattice to this new phase at B^* [103]. They observed no hysteresis and a broad transition and therefore, suggested it to be a crossover rather than a real thermodynamic transition. This was a plausible scenario as thermodynamic probes, such as magnetic torque, specific heat, and magnetization, also failed to detect a direct anomaly of the new phase at B^*. A small expansion in the a-axis magnetostriction was observed [see Fig. 3.13] that was explained as breaking of the in-plane tetragonal symmetry C_4 due to a finite in-plane field component. The broken C_4 symmetry of the underlying lattice marks the onset of the nematic order. The in-plane lattice expansion was interpreted as an enhanced hybridization between Ce $4f$ and the in-plane In (i.e. In(1)) conduction electrons at fields above B^*. This interpretation is in accordance with the field-induced itineracy of the f electrons and the robust Kondo coupling in high fields, previously suggested [99].

Recently, a high-field NMR study was carried out to better understand the microscopic origin of the high-field phase by measuring the ^{115}In NMR spectra at the two inequivalent indium sites, namely, In(1) and In(2) [104]. The main finding of this study was based on the simulation of the experimental NMR spectra over the whole field range, below and above B^*, with the same low-field nuclear quadrupolar parameters except for decreased formal In(1) and In(2) Knight shifts ΔK at fields above $B^* = 31$ T. A detectable local structural distortion or a significant change of the magnetic structure at B^*, was therefore, ruled out. The decrease of the formal In(1) and In(2) Knight shifts above B^* was interpreted as a decrease of the internal fields at these sites and thus a decrease of the bulk magnetization. Therefore, in absence of change of the magnetic structure, the decrease in ΔK was interpreted as a decrease of the ordered moment μ_{Ce} and therefore, a decrease of the hyperfine, coupling which can be explained by an increased Kondo screening due to the hybridization of the f and conduction electron.

Independent of the simulation of the experimental NMR data and its interpretation, based on the observation of a characteristic ‘double horn’ spectral distribution pattern, it was concluded that the magnetic structure above B^* is incommensurate with a similar, if not identical $\mathbf{Q} =$

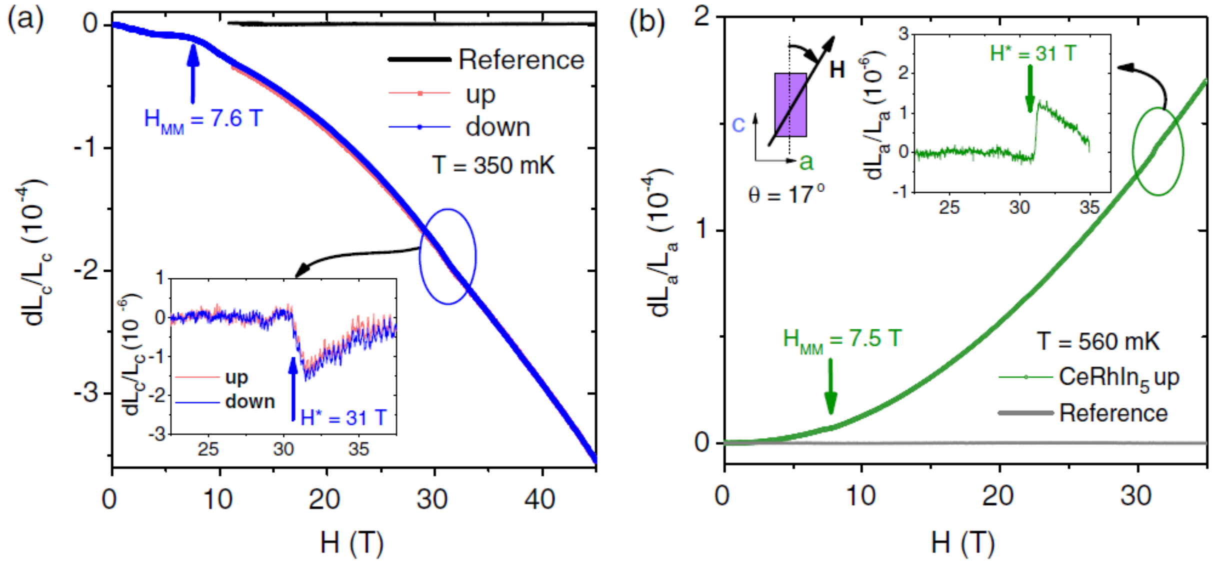

Figure 3.13: Magnetostriction along the (a) c axis and (b) a axis in CeRhIn$_5$ for a field applied at $\theta = 17°$ from the c axis. Adapted from ref [103]

$(0.5, 0.5, 0.297)$.

Lastly, recent high-field ultrasound velocity measurement revealed a sharp anomaly in the transverse elastic constant $C_T = \frac{C_{11}-C_{12}}{2}$ at B^* [105]. It was interpreted in terms of crystal symmetry breaking resulting into quadrupolar ordering. This work conform with the so far accepted picture of the enhanced c-f hybridization and the Fermi surface reconstruction.

In spite of the various interpretations discussed above, the exact origin and nature of this new phase is still under debate. It is still unclear whether the anomaly corresponds to a real thermodynamic phase transition or a crossover. Therefore, the high-field phase in CeRhIn$_5$ calls for further more careful studies.

In this chapter of my thesis, we challenge some of the above discussed interpretations based on our recent high-field results in CeRhIn$_5$. Based on our specific heat measurements, we will settle the debate of anomaly at B^* being a real transition rather than a crossover. Most important, we will challenge the idea of the field-induced Fermi-surface reconstruction and the SDW-type QCP by showing a continuous localization of the f electrons up to 70 T. Our results effectively negate the so far accepted picture of the field-enhanced $c-f$ hybridization or Kondo coupling and field-induced itinerancy of the f electrons. Moreover, we will show that the story of the magic angle of 20°, where the electronic anisotropy was observed to be strongest, is not compatible with bulk single crystalline samples. Our ultrasound velocity results will show that decreasing the in-plane field component increases the size of the feature at B^*, which goes against the now accepted picture of the electronic-nematic phase, in which a finite in-plane field component align the nematic domains along a certain direction with the maximum of nematic susceptibility at $\theta = 20°$. We will show that the high-field phase is not an absolute in-plane phenomenon, but poses a 3-D characteristics. Based on our results, we will put forward a new, more evolved, yet simpler hypothesis for the high-field phase. We discuss the high-field transition at B^* as a field-induced change of the magnetic structure. To truly confirm the nematic character of the high-field phase in bulk samples, we suggest magnetoresistance measurements on bulk single crystalline samples, so that strain effects are rendered ineffective (if such an experiment is possible). Finally, our ultrasound results on bulk CeRhIn$_5$ in contrast with magnetoresistance study on FIB fabricated devices, opens up a discussion around the possibility of strain as a tuning parameter for electronic correlations in CeRhIn$_5$.

3.2 dHvA effect in high magnetic fields

3.2.1 Abstract

We report a comprehensive de Haas-van Alphen (dHvA) study of the heavy-fermion material CeRhIn$_5$ in magnetic fields up to 70 T. Several dHvA frequencies gradually emerge at high fields as a result of magnetic breakdown. Among them is the thermodynamically important β_1 branch, which has not been observed so far. Comparison of our angular-dependent dHvA spectra with those of the non-4f compound LaRhIn$_5$ and with band-structure calculations evidences that the Ce 4f electrons in CeRhIn$_5$ remain localized over the whole field range. This rules out any significant Fermi-surface reconstruction, either at the suggested nematic phase transition at $B^* \approx$ 30 T or at the putative quantum critical point at $B_c \simeq$ 50 T. Our results rather demonstrate the robustness of the Fermi surface and the localized nature of the 4f electrons in- and outside of the antiferromagnetic phase.

3.2.2 Introduction

In spite of numerous experimental investigations of strongly correlated electron systems in the vicinity of a QCP, the details of what drives the QCP remain the subject of much theoretical debate. As mentioned in the previous chapter, there are currently two fundamentally different theoretical models, which attempt to describe the physics of antiferromagnetic (AFM) QCPs in heavy-fermion (HF) materials. The models can be distinguished by whether the Ce 4f electrons are localized or itinerant on the either side of a QCP. Here, “itinerant” means that the f electrons are fully hybridized with the conduction electrons, and, therefore, contribute to the Fermi surface (FS). The first type of QCP, referred to as a spin-density-wave (SDW) QCP [29, 50], assumes the f electrons to be itinerant on both sides of a QCP. In this case, if delocalization of f electrons occurs, it occurs inside the magnetic phase. The second type of QCP, known as a Kondo-breakdown QCP [44, 106, 30, 107, 108], suggests that a transition from itinerant to localized 4f electrons occurs precisely at the QCP. Furthermore, the effective masses of the conduction quasiparticles are expected to diverge upon approaching this type of QCP.

Since the FSs with itinerant and localized f electrons possess different size and morphology, the two cases can be easily distinguished experimentally by performing quantum-oscillation measurements, such as the de Haas–van Alphen (dHvA) effect. A comparison of the experimental angular-dependent dHvA spectra with results of band-structure calculations, both for localized and itinerant 4f electrons, allows us to distinguish between both scenarios. For Ce-based compounds, a comparison can also be made using experimental results obtained on La-based analogs, which serve as f-localized references, since the electronic structures of Ce and La differ by only one f electron.

The heavy fermion compound CeRhIn$_5$ can play a crucial role in expanding our understanding of quantum critical points. The antiferromagnetic ground state in CeRhIn$_5$ can be tuned to a QCP by pressure [70, 109, 110, 111], chemical substitution [89, 112, 113], and magnetic field [99, 100]. The pressure-induced QCP in CeRhIn$_5$ is now considered as a textbook example of the Kondo-breakdown type. Several dHvA experiments evidence that the f electrons of CeRhIn$_5$ are localized at ambient pressure [78, 79], although some of the theoretically predicted dHvA frequencies were not experimentally observed [78]. As the critical pressure for the suppression of antiferromagnetism, $P_c = 2.3$ GPa, is reached, all dHvA frequencies observed at $P < P_c$ change discontinuously, signaling an abrupt FS reconstruction as a consequence of the f-electron delocalization [82]. In addition, the effective masses diverge at P_c, further supporting the Kondo-breakdown scenario. A similar discontinuous change of the dHvA frequencies was observed upon substituting Rh by Co in CeRh$_{1-x}$Co$_x$In$_5$ [87]. However, the FS reconstruction does not occur at the critical concentration $x_c \approx 0.8$, where the AFM order is suppressed, but deep inside the AFM state, at $x \simeq 0.4$, where the AFM order alters its character and superconductivity emerges to coexist with antiferromagnetism. Furthermore, the effective masses do not diverge here. Thus, the substitution-induced QCP appears to be of the SDW type.

Recently, a field-induced QCP was reported to occur at the critical field $B_c \simeq 50$ T applied both along the c and a axis [99, 100]. Furthermore, an electronic-nematic phase transition was observed at B^*, and attributed to an in-plane symmetry breaking [43, 103]. Finally, as discussed previously, Jiao et al. [99, 102] reported the emergence of additional dHvA frequencies at $B^* \approx 30$ T, which was interpreted as a field-induced FS reconstruction associated with the f-electron delocalization and therefore, suggesting the field-induced Fermi surface to be of the SDW-type [see Fig. 3.9]. This result is surprising given that magnetic fields are generally expected to localize f electrons. This motivated us to thoroughly re-examine the FSs of CeRhIn$_5$ at high magnetic fields through a comprehensive angular-dependent dHvA study. To definitely establish the character of f electron in CeRhIn$_5$ in high magnetic fields, we also performed angular-dependent dHvA effect measurement in its f-localized references compound LaRhIn$_5$, also in high fields, to compare the Fermi-surfaces of the two compounds.

3.2.3 Band-structure calculations

In order to address the question of whether the f electrons in CeRhIn$_5$ are itinerant or localized at high magnetic fields, band-structure calculations were performed for both CeRhIn$_5$ with itinerant f electrons and LaRhIn$_5$ [1]. Band-structure calculations were carried out using a full potential linearized augmented plane wave (FLAPW) method with the local density approximation (LDA) for the exchange correlation potential. For the LDA, the formula proposed by Gunnarsson and Lundqvist [114] was used. For the band-structure calculations, the program codes TSPACE and KANSAI were used.

The space group of CeRhIn$_5$ is $P4/mmm$ (# 123, D^1_{4h}). The lattice parameters used for the calculation are $a = 4.6521$ Å and $c = 7.5404$ Å [115]. These parameters are similar to those previously reported [70, 116, 74, 117]. In $P4/mmm$, the 1a (0.0, 0.0, 0.0) and 1b site (0.0, 0.0, 0.5) are occupied by Ce and Rh ions, respectively. Indium ions occupy the 1c (0.5, 0.5, 0) and 4i site (0.0, 0.5, 0.3068). In the calculation for LaRhIn$_5$, the Ce ion was just replaced by the La ion, because this is a non-4f reference material.

In the FLAPW method, the scalar relativistic effect [118] is considered for all electrons and the spin-orbit coupling is included self-consistently for all valence electrons as a second variational procedure. The muffin-tin (MT) sphere radii are set as $0.3543a$ for Ce and La, and $0.32806a$ for Rh and In. Here, a is the lattice constant for the a axis. Core electrons (Xe core minus $5s^25p^6$ for Ce and La, Kr core minus $4p^6$ for Rh, Kr core for In) are calculated inside the MT sphere in each self-consistent step. $5s^25p^6$ electrons on Ce and La, $4p^6$ on Rh, and $4d^{10}$ on In ions are calculated as valence electrons by using the second energy window. The LAPW basis functions are truncated at $|\mathbf{k} + \mathbf{G}_i| \leq 4.85\ (2\pi/a)$, corresponding to 771 LAPW functions at the Γ point. 225 sampling points uniformly distributed in the irreducible 1/16th of the Brillouin zone (BZ) (2048 points in the full BZ) were used for potential convergence and the final band structure. The fermi surfaces calculated from these band structure calculations is shown in Fig. 3.14.

Similar calculations were previously performed for CeCoIn$_5$ [119, 78] and CeIrIn$_5$ [120] with itinerant f electrons, and provided an excellent agreement with experimental results. The calculated FSs, shown in Fig. 3.14, closely resemble those reported previously [121, 78, 122, 99]. Although there are similarities between the FSs with localized and itinerant f electrons, several significant morphological differences between the two scenarios are apparent. The topologies of the quasi-two-dimensional (2D) FS sheets originating from band 15 and giving rise to the α orbits are almost identical. Only the orbit size is different. There is, however, an additional three-dimensional (3D) FS sheet in the itinerant scenario. The FS sheets originating from band 13 are considerably different in the localized and itinerant cases. The complicated cross-like sheet giving rise to the ε orbits in the localized case is replaced by two small ellipsoidal pockets in the itinerant scenario. The most essential difference, however, is the morphology of the FS sheets originating from the electron band 14. In the localized case, a quasi-2D sheet gives rise to the orbits β_1 (belly) and β_2 (neck). In the itinerant scenario, on the contrary, this sheet is more 3D with a larger β_1 orbit that is present over

---

[1] These calculations were performed by H. Harima, Kobe university, Japan.

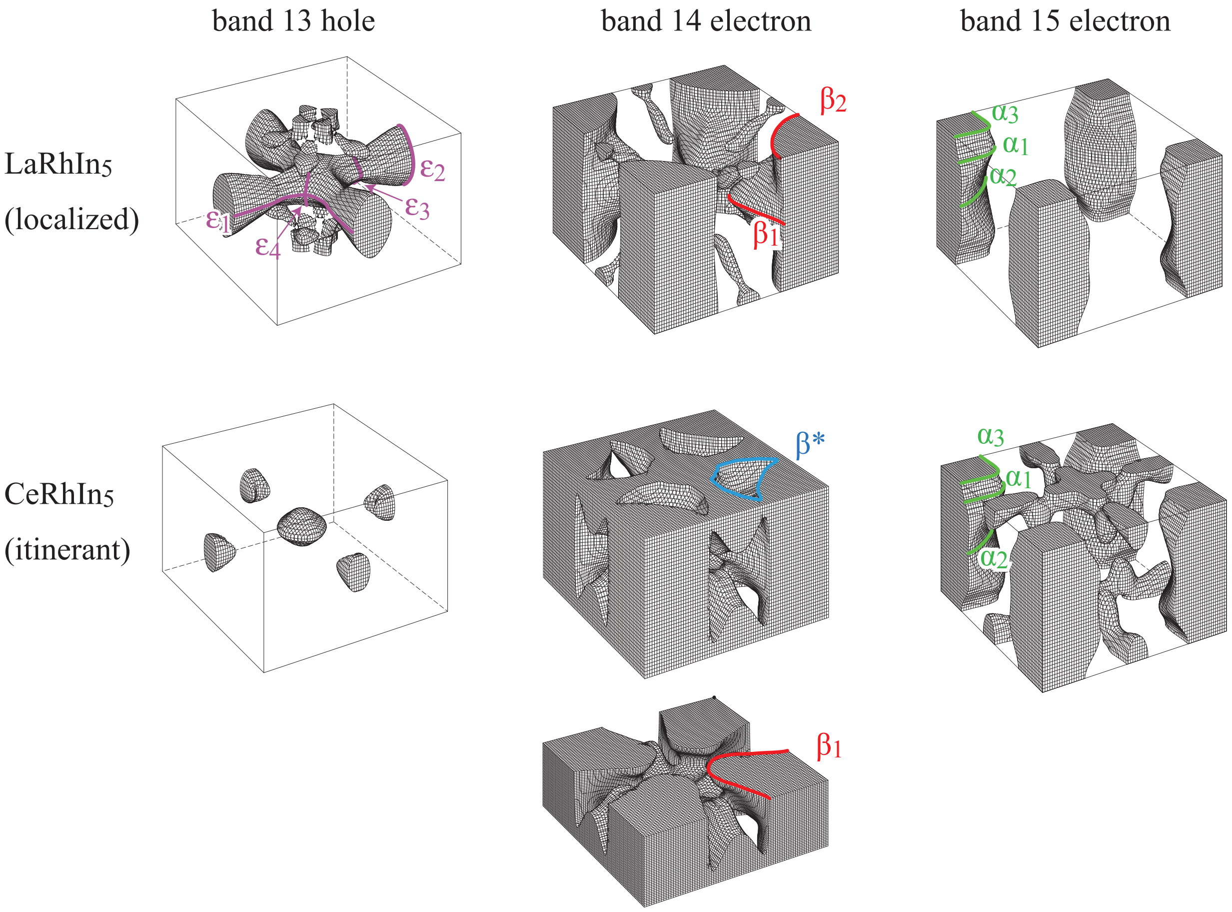

Figure 3.14: Calculated FSs with localized (top) and itinerant (bottom) f electrons. Solid lines indicate some extremal cross-sections discussed in the text.

a more limited angular range, and an entirely missing neck orbit β_2. The latter is replaced by a much smaller hole orbit β^*, which exists at very small angles only. This difference alone is sufficient to decide which of the calculated FSs yields a better agreement with the experimental results.

3.2.4 Experimental methods

For our dHvA experiments, high-quality (residual resistivity ratio $\rho_{RT}/\rho_0 \sim 300$) single crystals of CeRhIn$_5$ grown by the In self-flux method were used, details of which are given elsewhere [78]. The dHvA experiments were performed using magnetic-torque methods in both static (up to 36 T) and pulsed (up to 70 T) magnetic fields. The former were performed in a dilution refrigerator ($T_{base} \sim$ 30 mK) equipped with a low-temperature rotator using a metallic capacitive cantilever. The latter were done in a ^{3}He cryostat ($T_{base} \sim$ 620 mK) using a piezoresistive microcantilever. When using a rotator, the sample was first carefully aligned on the cantilever with respect to the rotation axis. The whole setup was then mounted in the rotator of the dilution refrigerator probe at a small negative angle. The sample was then rotated in field in small steps until the background torque vanished. Since magnetic torque vanishes when a magnetic field is applied along a symmetry axis, this orientation was taken as the reference, i.e., field parallel to the c axis. The estimated error in the angle determination is less than 0.1°. Once the reference orientation was found, the sample was always rotated in the same direction to avoid hysteresis.

3.2.5 Field-dependence of the first-order phase transition from incommensurate to commensurate magnetic structure

At ambient pressure and zero magnetic field, the magnetically ordered ground state of CeRhIn$_5$ is an incommensurate helicoidal phase characterized by the propagation vector $\mathbf{Q} = (1/2, 1/2, 0.297)$ [76]. The magnetic moments on the cerium ions are aligned antiferromagnetically in the tetragonal basal plane and spiral transversely along the c axis [76, 123]. When the magnetic field is applied in the basal plane, a first-order phase transition occurs at $B_m \simeq 2$ T at low temperatures [78, 73, 95]. The transition corresponds to a change of the magnetic structure to a commensurate sine-wave structure with the propagation vector $\mathbf{Q} = (1/2, 1/2, 1/4)$ [96, 97, 98]. The magnetic moments are still in the basal plane, but now aligned perpendicular to the applied field direction [96, 97]. When the magnetic field is tilted away from the basal plane, the transition field B_m increases, and initially follows a $1/\cos(\alpha)$ dependence, where α is the angle from the basal plane towards the c axis [78].

In magnetic-torque measurements, the transition manifests itself by a clear anomaly, as shown in Fig. 3.15(a). B_m deviates from the $1/\cos(\alpha)$ dependence at higher angles [see Fig. 3.15(b)]. It occurs slightly above 20 T when the field is applied at $\theta = 2°$, the lowest angle at which we observed the corresponding anomaly.

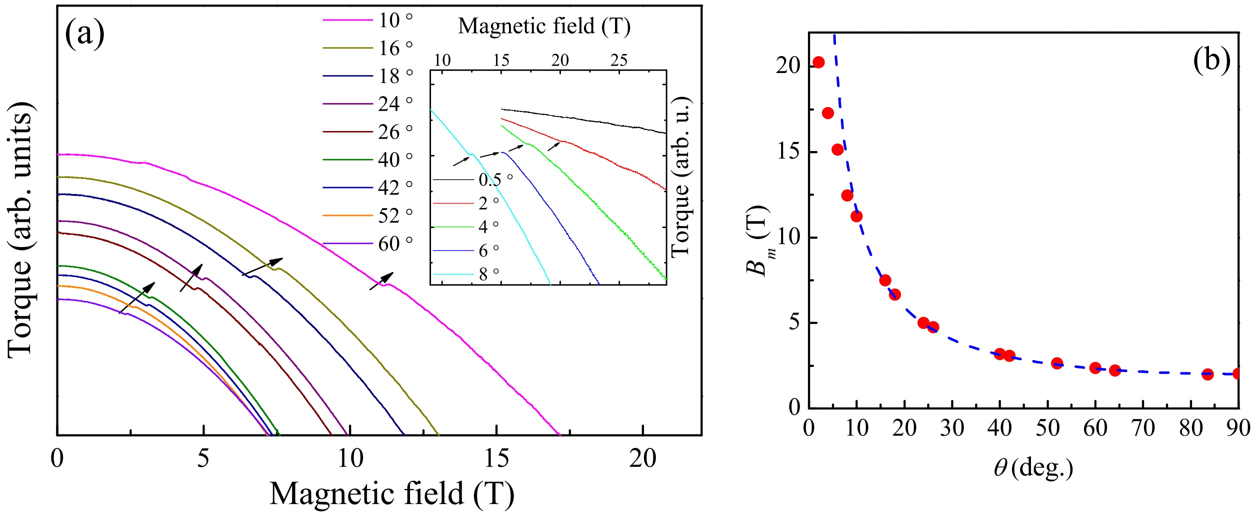

Figure 3.15: First-order metamagnetic transition in CeRhIn$_5$. Black arrows in (a) indicate the metamagnetic transition in the raw torque signal at various field orientations, θ. (b) Angular dependence of the metamagnetic transition field B_m. The dashed line represents $B_m^a/\cos(\alpha) = B_m^a/\sin(\theta)$, where $B_m^a = 2$ T is the transition field along the a axis, and α is the angle from a to the c axis.

All the static-field measurements reported here were performed at fields higher than B_m, i.e., in the commensurate phase with $\mathbf{Q} = (1/2, 1/2, 1/4)$. This implies that the magnetic Brillouin zone is smaller than its paramagnetic counterpart. As a consequence, the topology of the Fermi surface in the antiferromagnetic state is modified with respect to the paramagnetic phase, for which the band-structure calculations are performed. This might be approximated by a band-folding procedure where the paramagnetic Fermi surface is folded into the smaller Brillouin zone based on a large magnetic unit cell. In the particular case of CeRhIn$_5$, the reduction of the Brillouin zone hardly affects the Fermi surface sheet originating from band 15. On the other hand, the sheet originating from band 14, especially the largest β_1 orbit is strongly affected. This orbit can only be observed via magnetic breakdown.

3.2.6 dHvA oscillations in CeRhIn$_5$ and LaRhIn$_5$

Figure 3.16 shows the oscillatory torque after subtracting a non-oscillating background and the corresponding fast-Fourier transforms (FFTs) in CeRhIn$_5$ for several magnetic-field orientations

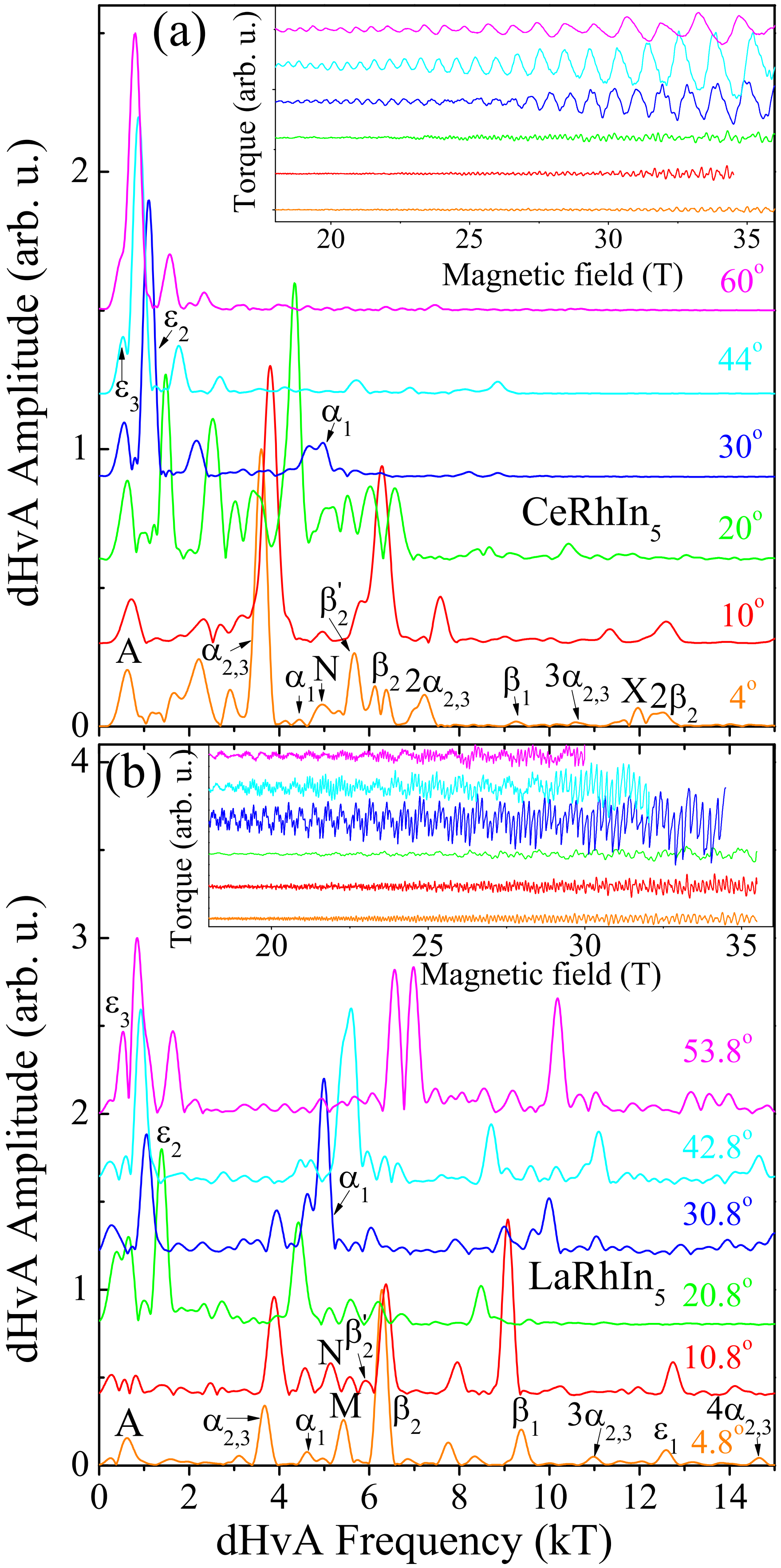

Figure 3.16: Fourier spectra of the dHvA oscillations (shown in the inset) of CeRhIn$_5$ for magnetic field applied at various angles, θ, from the c towards the a axis at T = 30 mK. The FFTs are performed over the field interval from B_{min} = 29 T to B_{max} = 36 T, except at 10° where it is 29 - 34.5 T (see the inset) due to experimental constraints. (b) Shows an equivalent figure of FFTs for the dHvA oscillations (shown in the inset) of LaRhIn$_5$ for magnetic field applied at various angles, θ, from the c towards the a axis at T = 50 mK. The FFTs in (b) are also performed over the same $1/B$ interval, $\Delta(1/B) \approx 0.028$ T^{-1}, with B_{min} adjusted with respect to the available B_{max} (see the inset) due to experimental constraints. The curves are shifted vertically for clarity. All FFTs are normalized to the strongest dHvA spectral peak.

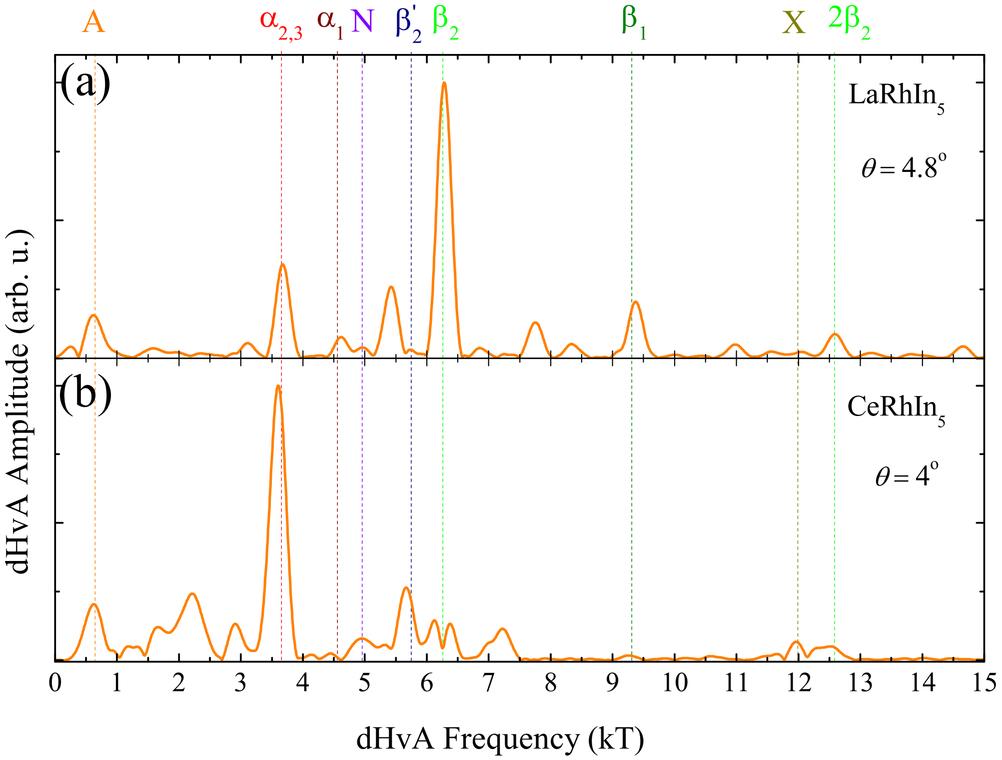

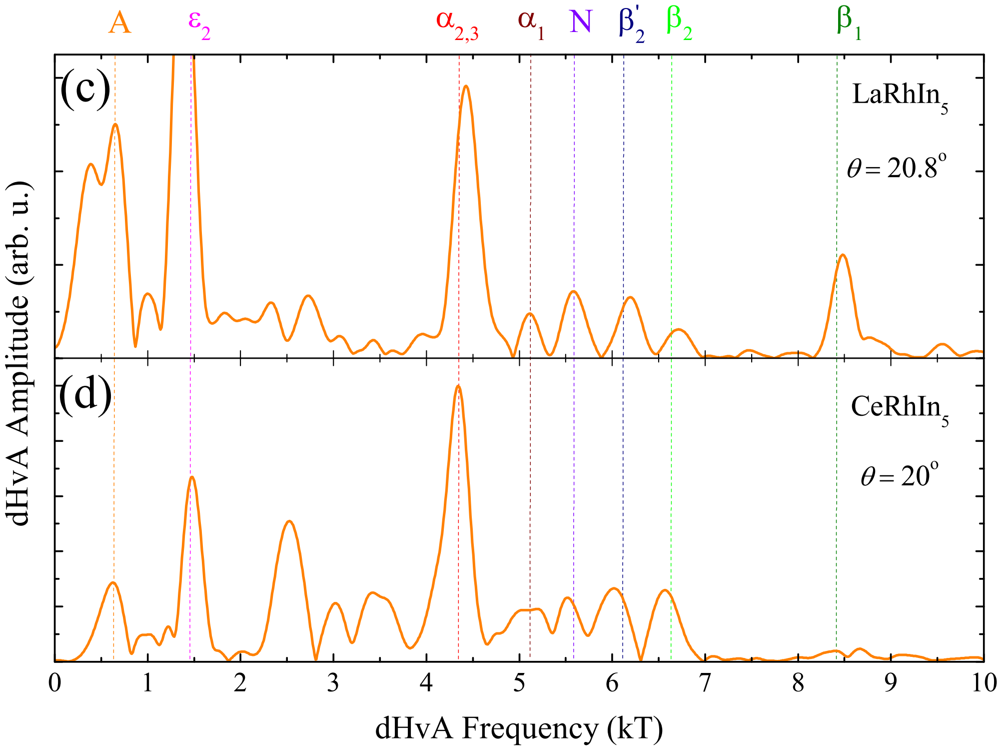

Figure 3.17: Comparison of the high field FFT spectra of the dHvA oscillations in LaRhIn$_5$ [(a) and (c)] and CeRhIn$_5$ [(b) and (d)] with magnetic applied at two close angles of 4.8° (a) and 4° (b), and 20.8° (c) and 20° (d).

θ, where θ is the angle from the c towards the a axis. The FFTs are performed over a field interval mostly above B^* with high-enough resolution to distinguish various dHvA frequencies. We observed all dHvA frequencies detected in previous low- [121, 78, 79] and high-field [99, 102, 103] measurements. In addition, we observed a new, previously undetected, dHvA frequency β_1, whose origin will be discussed later in more detail. Figure 3.16(b) shows the the corresponding oscillatory torque after subtracting a non-oscillating background and the FFTs in LaRhIn$_5$ for several magnetic-field orientations. We observed all the fundamental dHvA frequencies, namely α_i and β_i, predicted by the band-structure calculations. These frequencies were also observed in previous measurements in fields up to 13 T [78]. In addition to these fundamental frequencies, several additional frequencies, such as N, M, and β_2', gradually emerge at high fields, as shown in Fig. 3.21. These frequencies were not observed in previous lower field measurements [78]. This suggests that they originate from magnetic breakdown orbits. Almost all of the frequencies observed in CeRhIn$_5$ are also observed in LaRhIn$_5$ as shown in Fig. 3.17. Remarkably, the frequencies N, and β_2', were also observed to emerge at high fields in CeRhIn$_5$, as shown in Fig. 3.17 and discussed in section 3.2.8. Next we compare the experimentally obtained angular dependance of the dHvA frequencies in CeRhIn$_5$ with the band-structure calculations for both localized [Fig. 3.18(a)] and itinerant [Fig. 3.18(b)] f electrons. For this comparison, the dHvA frequencies were extracted from FFTs, such as shown in Fig. 3.16, performed over the field range 29 - 36 T [2] (B_{avg} = 32.12 T [3]). There is excellent agreement between the experimentally observed branches $\alpha_{2,3}$, α_1, β_2, and β_1 and their counterparts calculated for localized f electrons [Fig. 3.18(a)]. These branches originate from the quasi-2D FS sheets from bands 14 and 15. The experimentally observed branches ε_2 and ε_3 also agree very well with the f-localized calculations. These branches originate from the cross-like FS sheet from band 13. The branch X is observed only at small angles close to the c axis, and it does not seem to correspond to any calculated extremal area. Neither do the branches β_2' and N correspond to any calculated branch. These frequencies will be discussed later in more detail. On the other hand, there is a clear disagreement of the experimental data with band-structure calculations assuming itinerant f electrons [Fig. 3.18(b)]. The most significant signature of this disagreement is the presence of the β_2 branch, which is supposed to be completely absent in the itinerant scenario. This branch was also observed in previous high-field dHvA [99, 102] and magnetostriction [103] measurements. In measurements under high pressure, this frequency disappears above P_c, where the f electrons become itinerant [82]. Furthermore, the experimentally observed $\alpha_{2,3}$, α_1, and β_1 branches lie far below those calculated for the itinerant case. In previous high-field dHvA measurements performed with magnetic field only along the c axis, the frequencies N and β_2' were interpreted as α_2 and α_1 of the f-itinerant model [99]. However, their angular dependence is clearly different from that suggested by the calculations. Similarly, the experimentally observed branch X was interpreted as the β_1 branch of the itinerant scenario [99]. This frequency indeed agrees with calculated β_1 values at small angles close to the c axis. The positive curvature of this branch, however, is inconsistent with the negative curvature of the calculated β_1 branch. Finally, in Fig. 3.18(c), we compare the angular dependence of the experimentally observed dHvA frequencies in CeRhIn$_5$ and LaRhIn$_5$. The dHvA frequencies of the latter compound were also obtained from high-field ranges up to the available B_{max}. The excellent agreement of the experimentally measured dHvA frequencies observed in CeRhIn$_5$ and LaRhIn$_5$ over the whole angular range is especially strong confirmation that the f electrons, which are localized at low fields [78], remain so even in fields higher than B^*.

3.2.7 Comparison of the dHvA frequencies in CeRhIn$_5$ at high magnetic fields and under high pressure

Additional confirmation of localized f electrons in CeRhIn$_5$ at high fields comes from the comparison of dHvA frequencies observed in CeRhIn$_5$ at high fields to that above the critical pressure. One

---

[2] This range, mostly above B^*, was chosen to provide high-enough resolution to distinguish close dHvA frequencies. A small variation of this range does not alter the results.

[3] The average field, B_{avg}, of a field interval from B_{min} to B_{max} is defined as the reciprocal average, i.e., $1/B_{avg} = 1/2(1/B_{min} + 1/B_{max})$.

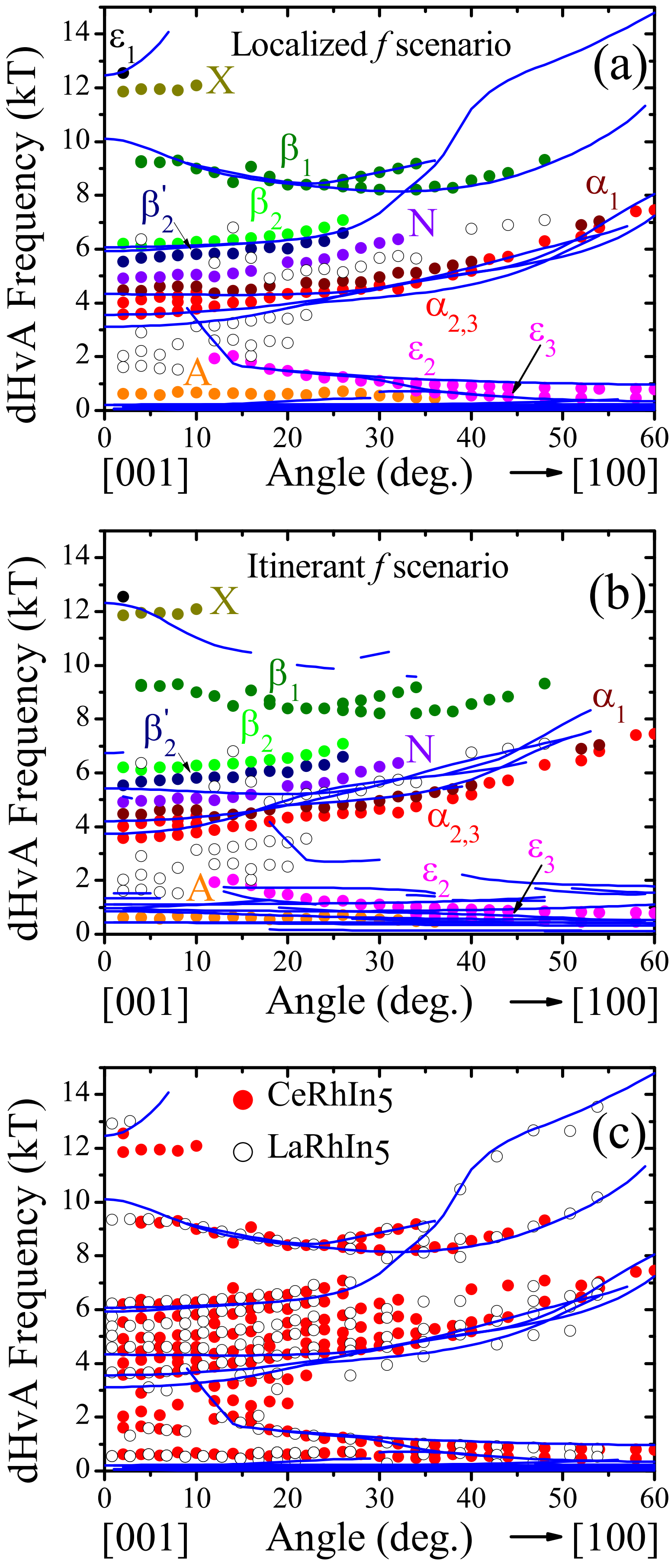

Figure 3.18: Angular dependance of the experimentally observed dHvA frequencies in CeRhIn$_5$ together with results of band-structure calculations (solid lines) within localized (a) and itinerant (b) scenarios, and with the experimentally observed dHvA frequencies in LaRhIn$_5$ (open circles) (c). In the latter case, the band-structure calculations for localized f electrons are also shown.

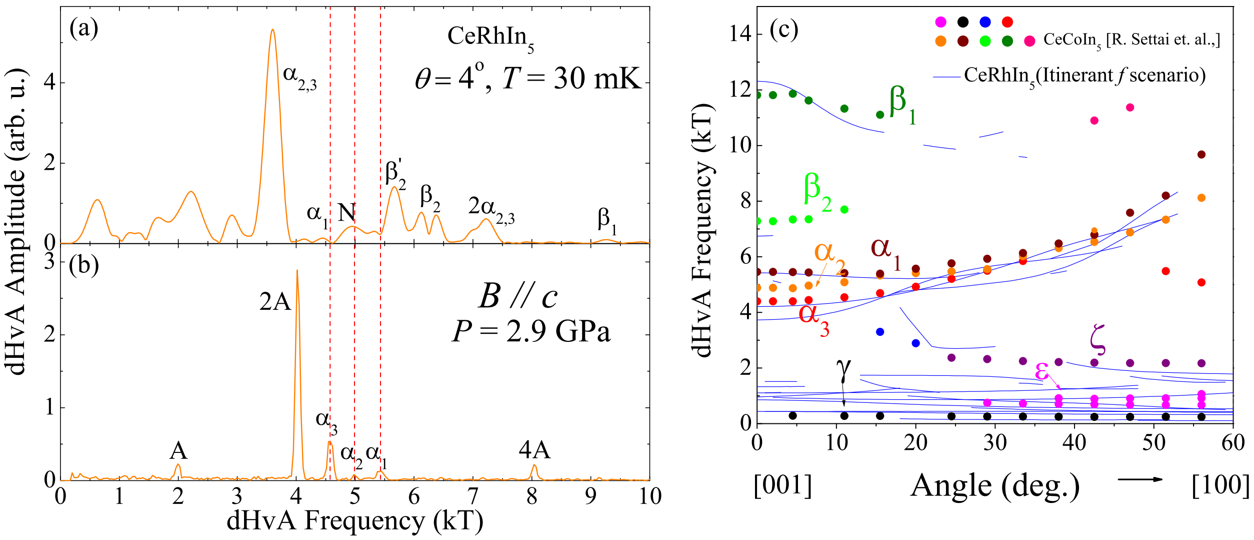

Figure 3.19: Comparison of the dHvA frequencies in CeRhIn$_5$ at high magnetic fields (a) and under high pressure (b). The results under pressure are from Ref. [82].(c) Angular dependance of the experimentally observed dHvA frequencies in CeCoIn$_5$ (from Ref. [119]) together with the results of f-itinerant band-structure calculations for CeRhIn$_5$ (solid lines).

of the appropriate ways to experimentally assess whether the f electrons of CeRhIn$_5$ are itinerant or localized under certain conditions is to compare the data with those obtained in CeRhIn$_5$ above the critical pressure, $P_c = 2.3$ GPa, where the f electrons are known to be itinerant [82]. In Fig. 3.19(a) and (b), we show a comparison of the dHvA frequencies in CeRhIn$_5$ over the field interval 29 - 36 T, mostly above B*, with those at $P = 2.9$ GPa, well above P_c [82]. This comparison is not straightforward, as the measurements under pressure were performed with field applied along the c axis, where dHvA oscillations can not be observed in torque measurements. We, therefore, use the data obtained at the lowest angle, 4°, at which all the additional frequencies were observed. Since all the dHvA frequencies almost don't change at small angles, the frequency difference between 0° and 4° can be neglected. The dHvA frequencies in CeRhIn$_5$ at high fields do not match those under high pressure. Only the α_2 frequency at high pressure roughly corresponds to the N frequency at high field. On the other hand, the α_1 and α_3 frequencies at $P = 2.9$ GPa do not match any high field frequencies. This comparison, therefore, argues in favor of the localized f electrons picture in CeRhIn$_5$ at high magnetic fields.

Furthermore, the FS of CeRhIn$_5$ is often compared to the FS of CeCoIn$_5$ to establish whether the f electrons of CeRhIn$_5$ are itinerant or localized under certain conditions, such as high pressure [82] or high magnetic fields [99, 102]. The heavy fermion compounds CeCoIn$_5$ is iso-structural to CeRhIn$_5$ and has an overall similar Fermi-surface topology. However, contrary to CeRhIn$_5$, CeCoIn$_5$ is non-magnetic with itinerant f electrons [119, 124, 78]. That is why the two cases are often compared. Strictly speaking, this approach is not correct as there are certain differences between the Fermi surfaces of CeCoIn$_5$ and CeRhIn$_5$ with itinerant f electrons, as shown in Fig. 3.19(c). Not only the sizes of the α_2 and α_3 orbits are slightly different, the β_2 orbit, present in CeCoIn$_5$, is absent in CeRhIn$_5$ with itinerant f electrons.

3.2.8 Field-dependence of the dHvA frequencies in CeRhIn$_5$ and LaRhIn$_5$

Figures 3.16 to 3.18 convincingly demonstrate that the Ce f-electrons are localized up to 36 T. That this situation persists up to still higher fields is evidenced by our pulsed-field measurements, shown in Fig. 3.20(a). The corresponding FFT spectra obtained over a moving $1/B$ window are shown in Fig. 3.20(b). Due to the much higher temperature, $T = 620$ mK, of the pulsed-field measurements, some of the additional dHvA frequencies, such as N, β_1 and X, emerge at higher fields as compared to our lower temperature static-field results, an example of which is shown in Fig. 3.20(c). Contrary to the previous report [99], some of these frequencies emerge well below B^*,

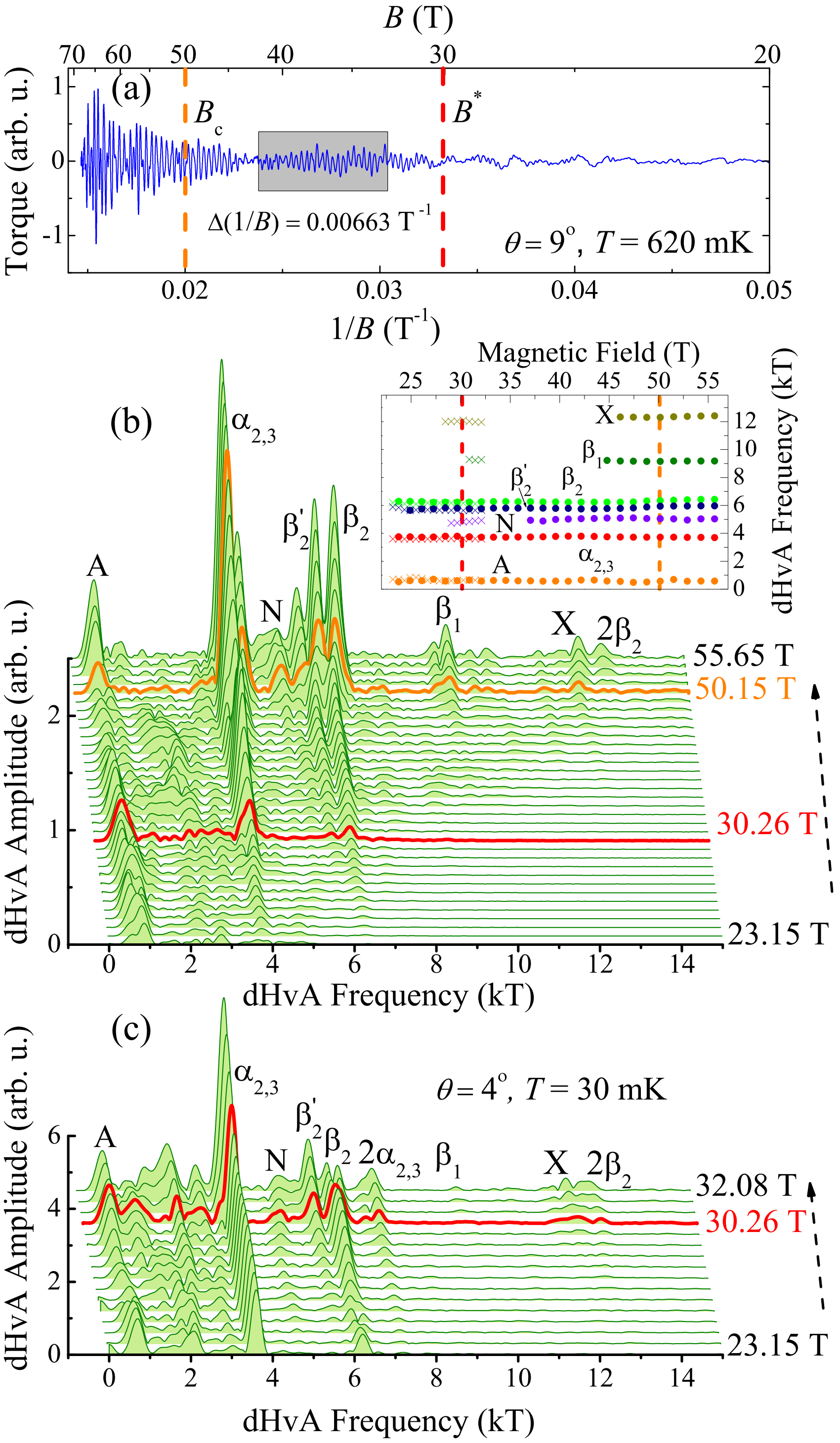

Figure 3.20: (a) dHvA oscillations in CeRhIn$_5$ in pulsed magnetic fields applied at 9° from the c axis. (b) FFT spectra of the oscillations from (a) obtained over the same $1/B$ range, shown by the rectangle in (a). For the bottom curve, the range is from $B_{min} = 21.5$ T to $B_{max} = 25.07$ T ($B_{avg} = 23.15$ T). For each successive curve, B_{min} is increased by 0.5 T up to 29 T, and by 1 T from there on. The inset shows the evolution of the dHvA frequencies with B obtained from pulsed (circles) and static (triangles) field measurements. (c) FFT spectra of the static-field dHvA oscillations, shown in Fig. 3.16, with B at 4° from the c axis. The $1/B$ range and the range for the bottom curve are the same as in (b). For each successive curve, B_{min} is increased by 0.5 T. The curves in (b) and (c) are shifted for clarity.

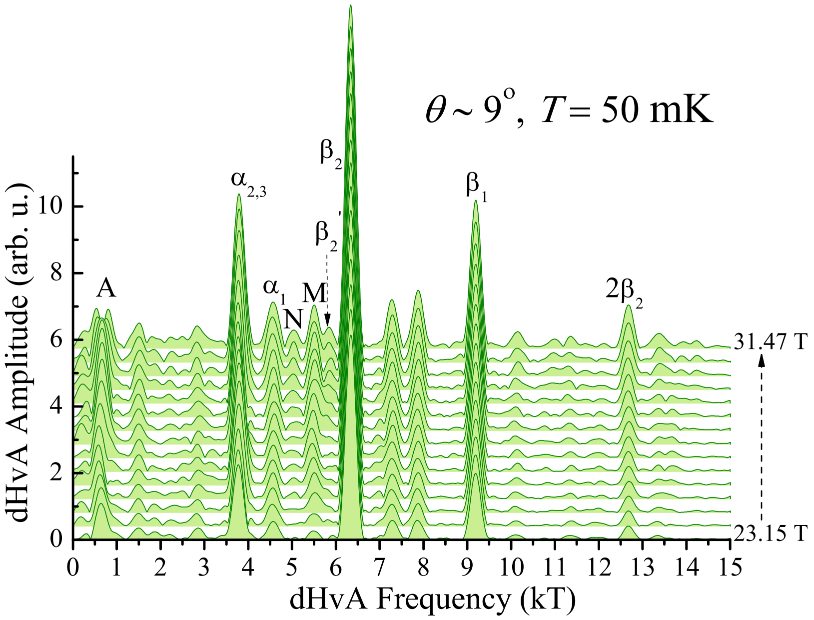

Figure 3.21: FFT spectra of the dHvA oscillations in LaRhIn$_5$ with magnetic field applied at 9° from the c axis at $T = 50$ mK. All the FFTs are obtained over the same $1/B$ range. For the bottom curve, the range is from $B_{min} = 21.5$ T to $B_{max} = 25.07$ T ($B_{avg} = 23.15$ T). For each successive curve, B_{min} is increased by 0.5 T. The curves are shifted vertically for clarity.

as can be seen in Fig. 3.20(b) and (c). We have not observed any frequency shift or the emergence of new frequencies at either B^* or B_c (inset of Fig. 3.20). Importantly, the β_2 frequency is still present above $B_c \simeq 50$ T. Furthermore, the effective masses remain finite in the immediate vicinity of B_c (as discussed in sec. 3.2.9). This suggests that the f electrons remain localized when the AFM order is suppressed by a magnetic field. The same conclusion was drawn for CeIn$_3$, for which the AFM order is also suppressed at a very high field of about 60 T [125].

We will now discuss the origin of the additional dHvA frequencies, such as β_2', N, β_1, and X, which emerge only at high fields. The frequency β_1 originates from the belly orbit of the electron band 14 (Fig. 3.14). Both the frequency itself and its angular dependence are in excellent agreement with the f-localized calculations [Fig. 3.18(a)]. This branch was not observed in any of the previous measurements. This is not surprising given that this orbit is strongly affected by the modification of the Brillouin zone in the AFM state (as discussed in sec. 3.2.3). In addition, the corresponding effective mass is strongly enhanced, $m^* \simeq 12\ m_0$ (sec. 3.2.9). The frequencies β_2' and N do not seem to correspond to any calculated branch within either the localized or itinerant model. It is, however, apparent that β_2' follows the angular variation of β_2 with a small and almost constant offset (Fig. 3.18). Remarkably, this offset ~ 0.6 kT, corresponds to the frequency A, which is almost angle independent. This suggests that β_2' originates from the magnetic breakdown between β_2 and A, i.e., $\beta_2' = \beta_2 - A$, assuming that A corresponds to a hole pocket. The exact origin of the frequencies N and X is unclear at present. Notably, the β_2' and N branches also emerge in LaRhIn$_5$ only at high fields [(see Fig. 3.21 and 3.18(c)], suggesting that they originate from magnetic-breakdown orbits. The frequency X is the only one that is not observed in LaRhIn$_5$. It is, therefore, less likely that this frequency originates from a magnetic breakdown as we discuss here. Figure 3.22(a) shows the field dependence of the oscillatory amplitude of the X and β_1 branches. The lines represent the field-dependent part of the Lifhitz-Kosevich formula. The effective masses were obtained from the mass plots (shown in sec. 3.2.9), and the Dingle temperatures were determined from the Dingle plots, as shown in Fig. 3.22(b). For both frequencies, the expected amplitude drops below the noise level just below the lowest field point. This implies that these oscillations gradually rise above the noise level with increasing magnetic field, rather than emerging all of a sudden at a given field value. Indeed, in the latter case, the oscillations are expected to emerge well above the noise level. The kink in the field-dependence of the X frequency amplitude is due to a drastic change of the Dingle

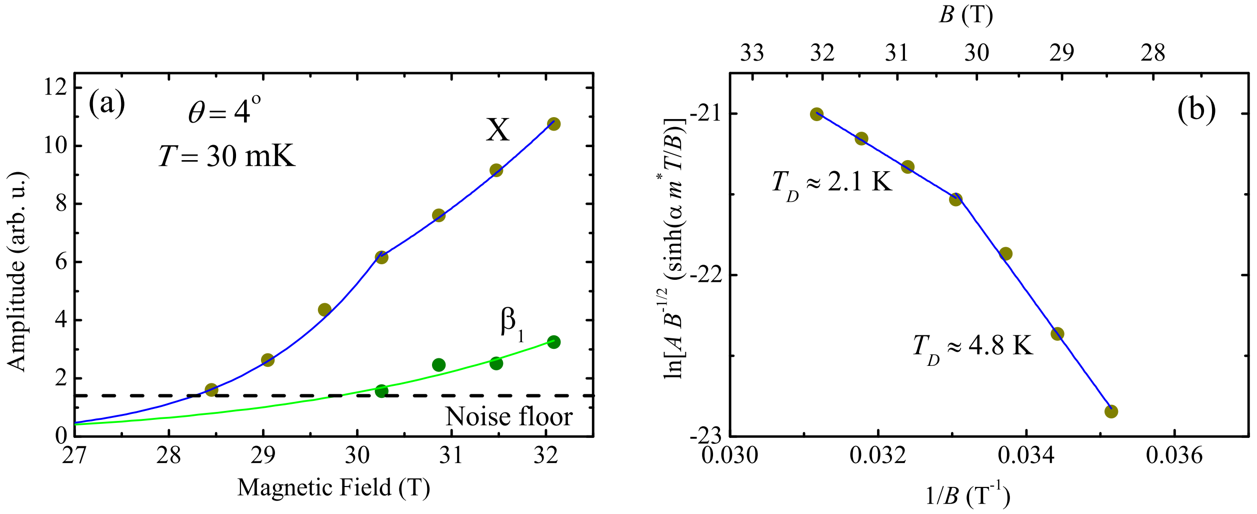

Figure 3.22: (a) dHvA amplitude of the X and β_1 branches as a function of magnetic field applied at 4° from the c axis at $T = 50$ mK. The lines correspond to the standard Lifshitz-Kosevich formula [54] with effective masses and Dingle temperatures determined from mass and Dingle plots, respectevely. (b) Dingle plot for the branch X. Note that the slope of the Dingle plot changes drastically at about 30 T.

temperature, as shown in Fig. 3.22(b). Remarkably, this change occurs at about 30 T. While it is not clear whether this change is directly related to B^*, it might explain why the X frequency was not observed below 30 T in the previous high field study [99].

Therefore, the emergence of X at high fields, although progressive as shown in Fig. 3.22, could be due to a minor FS reconstruction, such as a Lifshitz transition of a spin-split band, similar to what was observed in CeIrIn$_5$ [126] and YbRh$_2$Si$_2$ [127]. We emphasize that even if this is the case, the f electrons remain localised above 30 T as is evidenced by the presence of the β_1 and β_2 frequencies, and the very close match between the LaRhIn$_5$ and the CeRhIn$_5$ data.

3.2.9 Effective masses in CeRhIn$_5$

The effective masses, m^*, corresponding to the various dHvA orbits of CeRhIn$_5$ were determined by fitting the temperature dependence of the oscillatory amplitude with the standard Lifshitz-Kosevich formula [54] with $m^\star$ as fitting parameter. This was done deep inside the antiferromagnetic phase in the vicinity of B^* (Fig. 3.23) and in the field-induced polarized paramagnetic phase just above B_c (Fig. 3.24).

Inside the antiferromagnetic state, the effective masses were determined from the static-field data over the field range from 28 to 34.5 T ($B_{avg} = 30.86$ T) for two orientations of the magnetic field, at 4° and 8° from c towards the a axis, as shown in Fig. 3.23. The effective masses obtained for these two orientations are similar, indicating a rather weak angular dependence of the effective masses, at least close to the c axis. The effective masses corresponding to the dHvA frequencies observed at moderate magnetic fields, such as $\alpha_{2,3}$ and β_2, are in good agreement with previous reports [121, 78]. The effective masses corresponding to the additional frequencies observed only at high fields are much heavier, from $\sim 6m_0$ for the branch N, to $\sim 12m_0$ for the branch β_1 (where m_0 is the bare electron mass), indicating many-body mass enhancements. For comparison, the calculated band masses, m_b, for the β_1 branch are $0.85m_0$ and $0.81m_0$ at 4° and 8°, respectively.

In the field-induced polarized paramagnetic phase, the effective masses were extracted from the pulsed-field data over the field range from 50 to 68.18 T ($B_{avg} = 57.69$ T) with field applied at 9° from c towards the a axis, as shown in Fig. 3.24(a). Not only do the effective masses show no sign of divergence just above B_c, the effective masses of the β_2 and β_1 branches are strongly reduced with respect to the values at 30.86 T. Unfortunately, the amplitudes of these oscillations are not strong enough for a reliable determination of the effective masses in the intermediate field

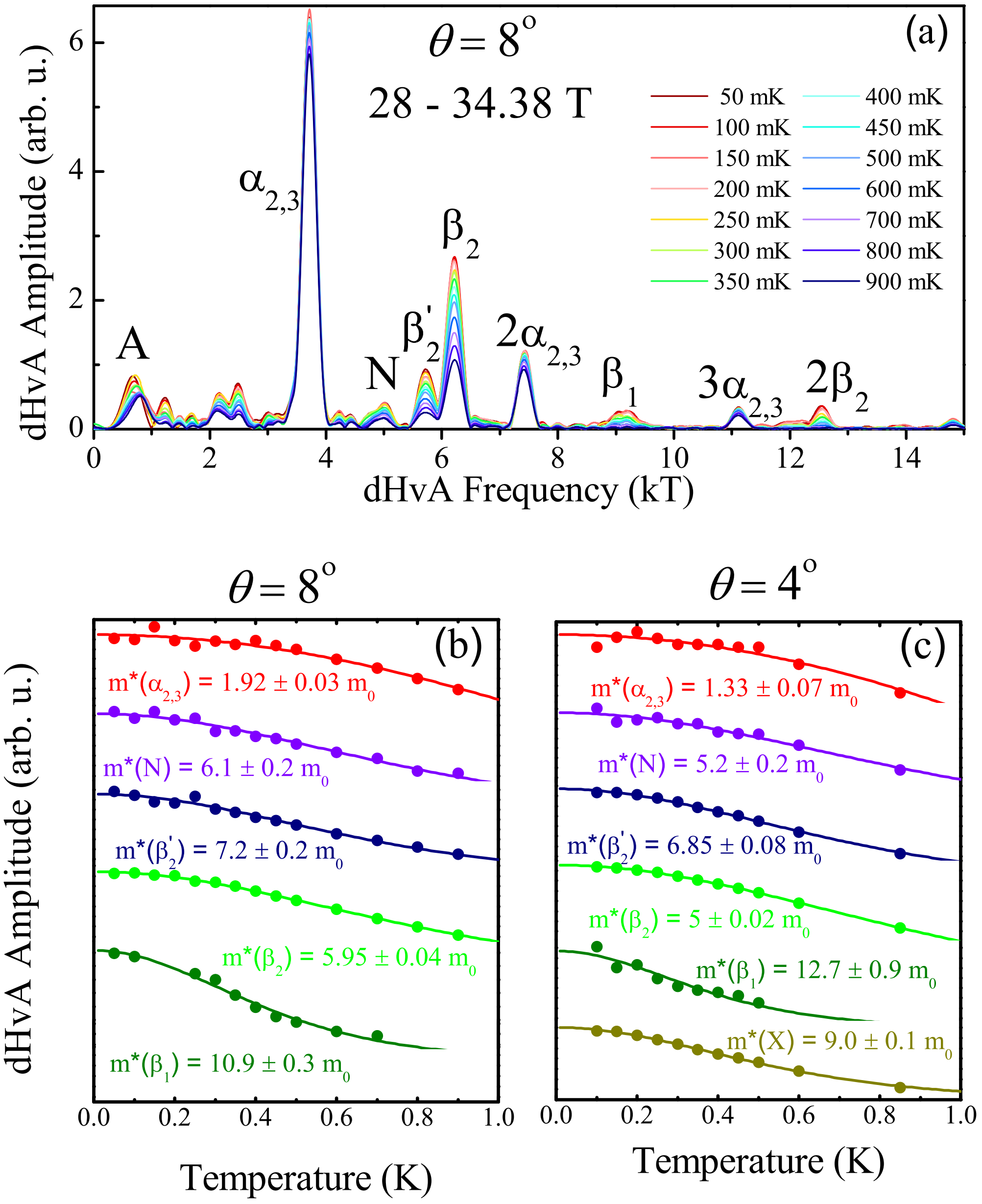

Figure 3.23: (a) Fourier spectra of the dHvA oscillations in $\mathrm{CeRhIn_5}$ for a field rotated by $\theta = 8°$ from c to the a axis over the field interval from 28 to 34.5 T at different temperatures. (b) and (c) Temperature dependence of the dHvA amplitudes at $\theta = 8°$ and $4°$, respectively. The lines are fits using the standard Lifshitz-Kosevich formula [54].

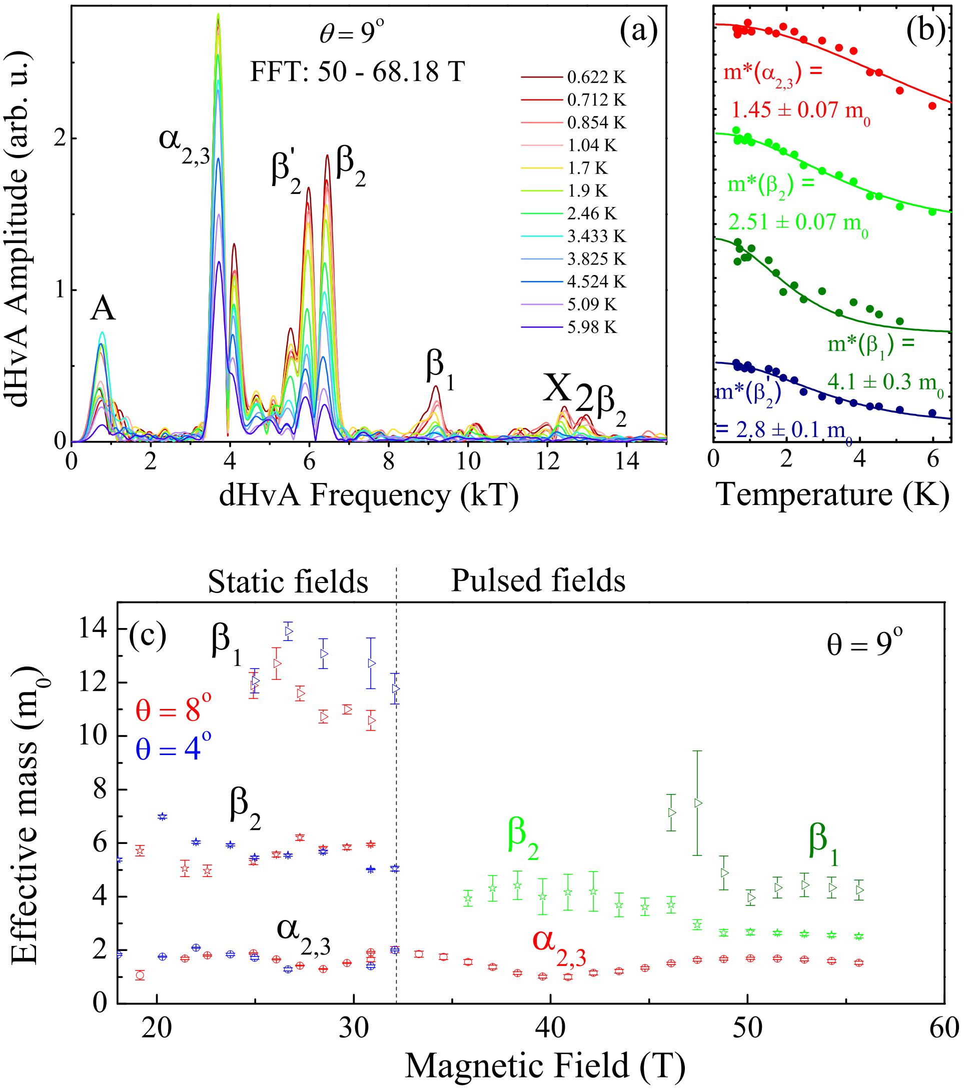

Figure 3.24: (a) FFT spectra of the dHvA oscillations in CeRhIn$_5$ for a field rotated by $\theta = 9°$ from c to the a axis over the field interval from 50 to 68.18 T at different temperatures. (b) Temperature dependence of the dHvA amplitudes from (a). The lines are fits using the standard Lifshitz-Kosevich formula [54]. (c) Field-dependance of effective masses of the dHvA frequencies $\alpha_{2,3}$, β_2, and β_2' obtained in static fields (such as shown in Fig. 3.23) and pulsed magnetic fields (such as shown in panel (b)

range as evident from the huge error bars in obtained effective masses shown in Fig. 3.24(b). The apparent reduction of the effective masses observed here is likely to be due to the field-induced polarization of the quasiparticle bands, which leads to the suppression of electronic correlations. A similarly strong suppression of the effective masses by magnetic fields was previously observed in CeB_6 [128, 129], $CeAl_2$ [130, 131], $CeRu_2Si_2$ [131], and $CeCoIn_5$ [119].

Such a field-induced polarization of the quasiparticle bands is also possibly apparent in the field evolution of FSs above B_c. At magnetic fields above 49 T, there is a small increase (of about 2%) in the size of the β_2 and β_2' FSs as shown in Fig. 3.25. Furthermore, there is also a splitting of the fermi surface orbit $\alpha_{2,3}$ and β_1 above 49 T. Also, the amplitudes of the dHvA frequencies abruptly increase at magnetic fields above 49 T, indicating an abrupt increase in the dingle temperature at 49 T.

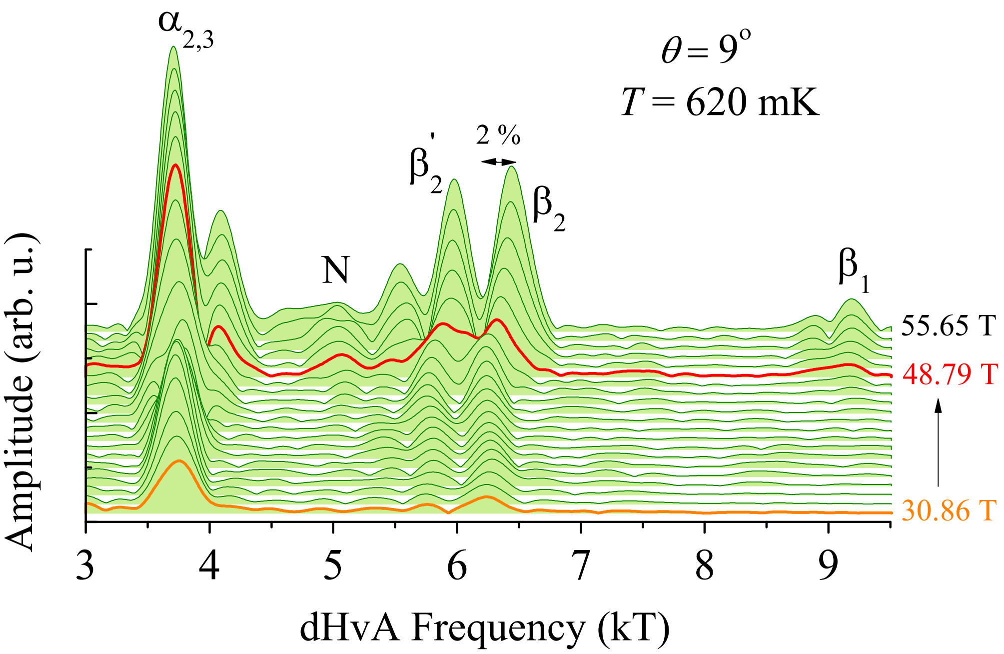

Figure 3.25: Evolution of the dHvA frequencies with B obtained in $CeRhIn_5$ in pulsed magnetic fields applied at 9° from the c axis obtained over the same $1/B$ range, shown by the rectangle in Fig. 3.20(a). For the bottom curve, the range is from $B_{min} = 28$ T to $B_{max} = 34.38$ T ($B_{avg} = 30.86$ T). For each successive curve, B_{min} is increased by 0.5 T up to 29 T, and by 1 T from there on. The curves are shifted for clarity.

All these changes observed above 49 T possibly are related to the suppression of the AFM state and emergence of a field-induced polarized paramagnetic phase above $B_c \approx 49\ T$.

3.2.10 Conclusions

In summary, we performed high-field dHvA measurements on $CeRhIn_5$ and $LaRhIn_5$. In $CeRhIn_5$, several additional dHvA frequencies emerge above certain threshold fields. In particular, we observed the previously undetected, thermodynamically important β_1 branch predicted by the f-localized band-structure calculations. Almost all of the dHvA frequencies observed in $CeRhIn_5$ are also present in $LaRhIn_5$. In addition, their angular dependence is identical in the two compounds. The presence and angle dependence of the observed dHvA frequencies are well accounted for by band-structure calculations with localized f electrons, indicating that the f electrons of $CeRhIn_5$ remain localized not only above $B^* \approx 30$ T, but also above $B_c \simeq 50$ T. We emphasize that delocalization of the Ce f-electron at high magnetic field would change the whole FS from the localized to the itinerant FS that we show in Fig. 3.14. Continued observation of the β_2 branch at the highest magnetic fields is clear evidence of that the Ce f-electron remains localized over the full magnetic field range that we have explored.

It was previously reported that the f electrons also remain localized in CeIn$_3$ above its critical field $B_c \simeq 60$ T [125]. Whereas CeIn$_3$ is an isotropic HF compound with an almost spheroidal FS, CeRhIn$_5$ is a prototypical example of a strongly anisotropic material with quasi-2D FSs. The continued localization of the f electrons well above B_c in both compounds is not consistent with either of the two existing theoretical models of AFM QCPs. This implies that magnetic field, which itself tends to localize f electrons, should be treated differently from such control parameters as pressure or chemical doping.

The identification of a ‘small/localized’ or a ‘large/itinerant’ Fermi surface is an important theoretical issue. In certain cases, the interpretation of dHvA results have been contentious. For example, in CeRu$_2$Si$_2$, a change of Fermi surface from itinerant to localized was reported, above a critical field H_m based on dHvA measurements [132, 133]. However, this interpretation is still under debate. An alternate interpretation of an itinerant Fermi surface above H_m through a Lifshitz transition was also put forward [134], which is more consistent with the premise that the f electrons are never truly localized as long as the system remains in the metallic state with an enhanced effective mass. There is always a finite hybridization in heavy fermion systems. Therefore, the true meaning of localized f electron and ‘small’ Fermi surface based on dHvA measurements is an important theoretical problem, as discussed in detail in ref [135]. Nonetheless, in CeRhIn$_5$, the low-field Fermi surface is ‘small/localized’, in the sense it is largely similar to that of LaRhIn$_5$, and is unanimously suggested by several dHvA studies. Our dHvA results establishes that this low-field small/localized Fermi surface does not abruptly change either across $B^* = 30$ T or $B_c \simeq 50$ T.

These results are published in [136].

3.3 Specific heat in high magnetic fields

3.3.1 Abstract

$CeRhIn_5$ is a prototypical antiferromagnetic heavy-fermion compound, whose behaviour in magnetic field is unique. Magnetic field applied in the basal plane of the tetragonal crystal structure induces two additional phase transitions. When the magnetic field is applied along, or close to, the c axis, a new phase characterized by a pronounced in-plane electronic anisotropy emerges at $B^* \approx 30$ T, well below the critical field, $B_c \simeq 50$ T, to suppress the antiferromagnetic order. The exact origin of this new phase, originally suggested to be an electronic-nematic state, remains elusive. Here we report low-temperature specific heat measurements in $CeRhIn_5$ in high static magnetic fields up to 36 T applied along both the a and c axis. For fields applied along the a axis, we confirmed previously suggested phase diagram, and extended it to higher fields. This allowed us to observe a triple point at ~ 30 T, where the first-order transition from incommensurate to commensurate magnetic structure merges into the onset of the second-order antiferromagnetic transition. For fields applied along the c axis, we observed a small but distinct anomaly at B^*, which we discuss in terms of a possible field-induced transition, probably weakly first-order. We further suggest that the transition corresponds to a change of magnetic structure. We revise magnetic phase diagrams of $CeRhIn_5$ for both principal orientations of the magnetic field based entirely on thermodynamic anomalies.

3.3.2 Introduction

At ambient pressure and zero magnetic field, $CeRhIn_5$ undergoes an antiferromagnetic (AFM) transition at $T_N = 3.8$ K, in which the Ce moments are antiferromagnetically aligned within the $CeIn_3$ planes. The moments spiral transversally along the c axis with a propagation vector $\mathbf{Q} = (0.5, 0.5, 0.297)$ incommensurate with the crystal lattice [76]. Magnetic field applied in the basal plane of $CeRhIn_5$ induces two additional transitions, observed in specific heat [73], thermal expansion, and magnetostriction measurements [95]. The lower temperature transition is first order. It occurs at $B_m \sim 2$ T at low temperatures, and corresponds to a change of magnetic structure from incommensurate to commensurate [96]. The higher temperature transition is second order. It corresponds to a change of the ordered moment, while the propagation vector, almost the same as in zero magnetic field [96], becomes temperature-dependent [97]. Both transitions were traced up to 18 T in static field measurements [95]. More recently, specific heat measurements in pulsed fields applied along the a axis revealed a non-monotonic field dependence of T_N [99]. The AFM transition temperature initially increases up to about 12 T, and then decreases monotonically all the way up to the critical field $B_c \sim 50\ T$. In these measurements, however, the two field-induced phases were not observed. Therefore, the complete phase diagram for fields along the a axis remains elusive.

When a magnetic field is applied along the c axis, T_N monotonically decreases until it is completely suppressed at $B_c \sim 50\ T$ [99, 100]. Surprisingly, the critical field for this orientation is approximately the same as along the a axis in spite of a considerable crystallographic and magnetic anisotropy of $CeRhIn_5$. On the other hand, the critical field was extrapolated from specific heat measurements in pulsed magnetic fields, while there is a difference between the results obtained in pulsed [99, 100] and static [72] fields.

The most interesting feature was observed in various measurements at $B^* \simeq 30$ T for field applied either along or slightly tilted from the c axis [99, 101, 43, 103, 104, 105, 137]. While it was interpreted as a transition into an electronic-nematic state [43], the exact origin and nature of this anomaly is still under debate. Surprisingly, specific heat measurements have so far failed showing a direct indication of this anomaly [72, 99, 100]. It is thus still unclear whether the anomaly corresponds to a real thermodynamic phase transition or a crossover.

The above mentioned inconsistencies and shortcomings demonstrate a clear need to perform specific heat measurements in high static fields to ascertain the quantum critical point, complete the phase diagram for fields along the a axis, verify the phase diagram along the c axis, and seek a direct evidence for the enigmatic novel state at B^*.

Here we report high-field low temperature specific heat measurements on a single crystal of CeRhIn$_5$. The measurements were performed in static fields up to 36 T for field orientations both along the a and c axes. For field applied along the a axis, we observed all the previously reported transitions, and traced them to higher fields. For field along the c axis, we observed the so far elusive anomaly at B^* in addition to the AFM transition. Based on these features observed in specific heat, we propose a revision of the magnetic phase diagram of CeRhIn$_5$ for both principal orientations of the magnetic field.

3.3.3 Experimental details

The high-quality single crystal of CeRhIn$_5$ used in the present study was grown by the In-self-flux technique, details of which can be found elsewhere [78]. The dimensions of the CeRhIn$_5$ crystal are $1.3\times0.8\times0.2$ mm^3 and the mass is 1.55 mg. The length of the sample is parallel to the c axis, as shown in Fig. 3.26.

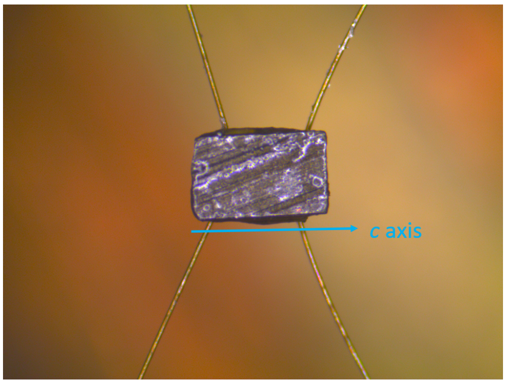

Figure 3.26: Single crystal of CeRhIn$_5$ used for the specific heat measurement.

Low-temperature specific heat measurements were performed in static magnetic fields up to 36 T by either a thermal relaxation technique at constant magnetic field or AC technique at constant temperature. Measurements at low fields using the thermal relaxation technique were performed in a ^{4}He cryostat equipped with a 12 T superconducting magnetic and a VTI providing the lowest thermal bath temperature of 1.5 K. While the measurements at high fields were performed in a 36 T resistive magnet equipped with a ^{4}He cryostat reaching the lowest thermal bath temperature of 1.3 K by directly pumping on the Helium bath. The measurements using AC calorimetric technique were entirely performed in the 36 T resistive magnet and ^{4}He cryostat reaching the lowest thermal bath temperature of 1.3 K. A Cernox thermometer, calibrated from 1.3 K to 40 K in magnetic fields up to 36 T, was used as a reference thermometer for the thermal bath.

In the thermal relaxation technique, the specific heat C of CeRhIn$_5$ is obtained by subtracting the addenda contribution from the total heat capacity of the system as shown in Fig. 3.27(a). It is evident that the addenda contribution to the total specific heat is negligibly small at low temperatures compared to the sample.

Specific heat measured using the AC calorimetric technique is consistent with that using the relaxation technique, as shown in Fig. 3.27(b). For the AC calorimetric technique, we plot $\tan\theta$ which is proportional to the specific heat of the sample, i.e., $\tan(\theta) = C\omega/\kappa$. Given that $\kappa \propto T$, and the temperature oscillation frequency ω (twice of heater excitation frequency) is constant, we have $\tan\theta \propto C/T$. Further, in AC technique C is the total heat capacity of the system including the addenda. However, as verified through the thermal-relaxation technique, the addenda contribution to the heat capacity of the system is negligibly small over the temperatures range of Fig. 3.27(b) and therefore, there is an excellent agreement between the results obtained by the two different techniques.

For the AC specific heat data, the sample temperature is determined by removing the self heating effect, i.e., T_{DC}, using the heater calibration described in the previous chapter on experimental techniques.

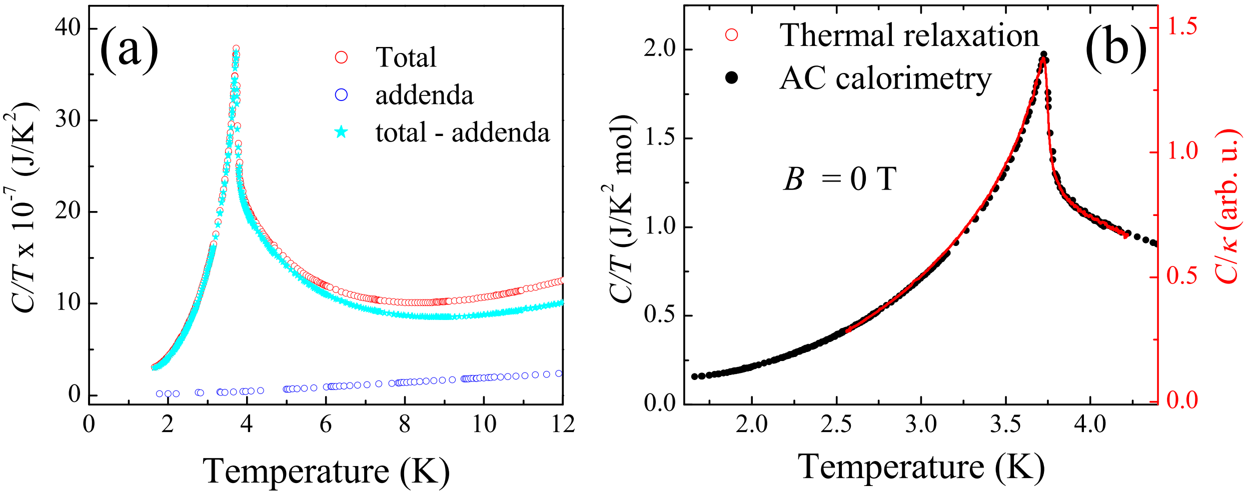

Figure 3.27: Total specific heat (red open circles) of $CeRhIn_5$ and addenda (blue open circles) obtained using thermal relaxation technique. (b) Comparison of the specific heat of $CeRhIn_5$ at zero field obtained using thermal relaxation (closed circles) and AC calorimetric (solid line) techniques. For the latter, $\tan\theta$ proportional to C/T is plotted.

3.3.4 Specific heat of $CeRhIn_5$ for field applied along the a axis

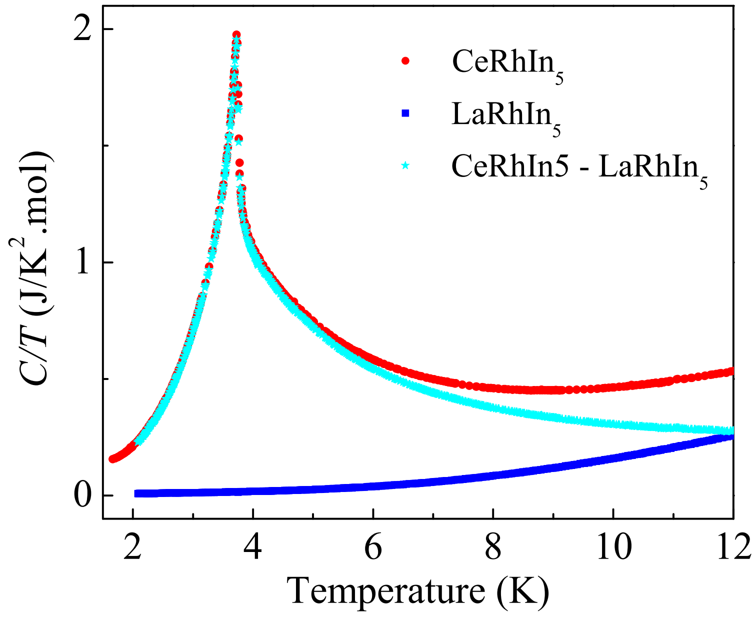

Figure 3.28: Specific heat of $CeRhIn_5$ and $LaRhIn_5$ at zero field obtained using the thermal relaxation technique.

The specific heat C/T as a function of temperature for $CeRhIn_5$ and $LaRhIn_5$ obtained using the thermal relaxation technique is shown in figure 3.28. The specific heat C/T decreases upon cooling before reaching a minimum at 9 K with a value $C/T \approx 0.45$ J/K^{2}mol. On further lowering the temperature, the specific heat increases first, leading to a sharp lambda-like feature in the specific heat at $T = 3.76$ K and then decreases rapidly thereon. This feature corresponds to the onset of a long-range anti-ferromagnetic order in $CeRhIn_5$ through a second-order phase transition at $T_N \approx 3.8$ K. The compound $LaRhIn_5$ is a non-f reference compound for $CeRhIn_5$ and therefore only has phonoic contribution to specific heat. Conventionally, such a non-f material is used to subtract the phononic contribution (βT^3) to the total specific heat of its iso-structural f electron compound, i.e., $CeRhIn_5$ (see Fig. 3.28).

Significant changes in the specific heat occurs in applied magnetic fields. Figure 3.29(a) shows

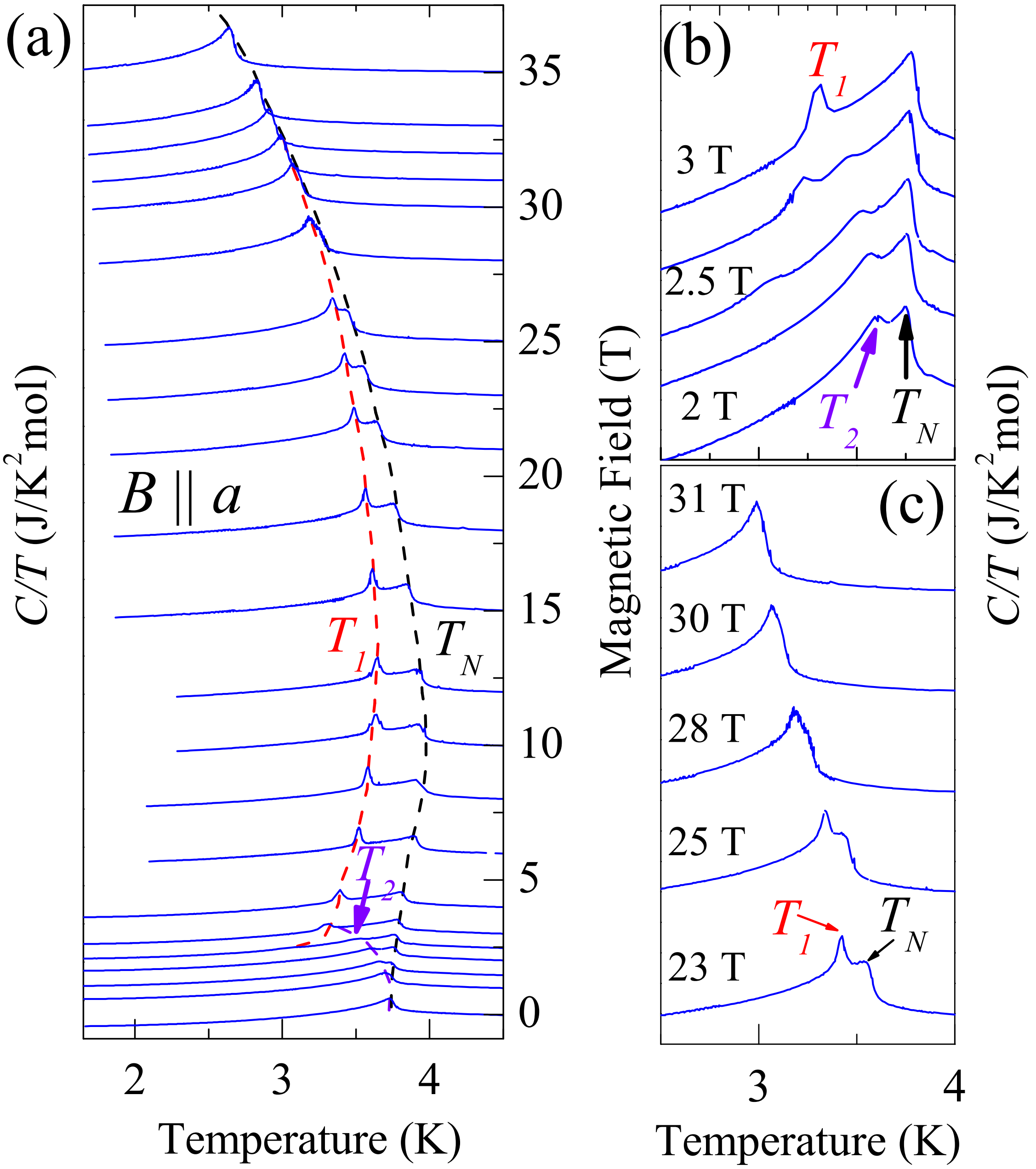

Figure 3.29: Specific heat divided by temperature, C/T, of CeRhIn$_5$ for magnetic field applied along the a axis. (a) C/T as a function of T obtained from relaxation technique for several values of magnetic field. Curves are vertically shifted according to the magnetic field scale shown in the right axis. A zoom at low and high fields is shown in (b) and (c) respectively. (d) Total specific heat, C, obtained from field sweeps using the AC technique.

specific heat divided by temperature, C/T, obtained from relaxation measurements for magnetic field applied along the a axis. For this field orientation, apart from the AFM transition at T_N, there are two additional field-induced transitions at T_1 and T_2, as shown in Fig. 3.29(b). The transition at T_1 manifests itself by a sharp δ-like peak characteristic of a first-order transition. The transition at T_2 appears as a λ-type anomaly typical for a second-order transition. This transition is observed only at low fields, as shown in Fig. 3.29(b). In agreement with previous reports, T_N initially increases up to about 10 T, and then decreases monotonically up to the highest field of our measurements. The transition temperature T_1 shows a similar trend. Above 3 T, T_1 increases up to about 12 T, and then starts to decrease. Its suppression rate, however, is slower than that of T_N. With increasing field, the two transitions approach each other. At 28 T, the two transitions are barely distinguishable, and at 30 T only the transition at T_N remains, as shown in Fig. 3.29(c).

All the transitions are also observed in measurements by AC technique, as shown in Fig. 3.30. In particular, the curve obtained at 3.4 K, shows four phase transitions. Interestingly, while the low-field transition at B_1^L manifests itself as a sharp peak, its high-field counterpart at B_1^H appears as a rather smeared anomaly, although it is also a first-order transition. This is not surprising considering that standard AC calorimetry models are based on steady-state measurements, which is not the case for a first-order phase transition due to the involvement of latent heat. Therefore, a first-order transition does not always manifest itself as the canonical δ-like feature. The shape, and even the presence, of an anomaly depends on the latent heat associated with the transition. On the other hand, a second-order transition always manifest itself as a distinct λ-like anomaly, which is, indeed, the case for the two known second-order transitions at B_2 and B_N.

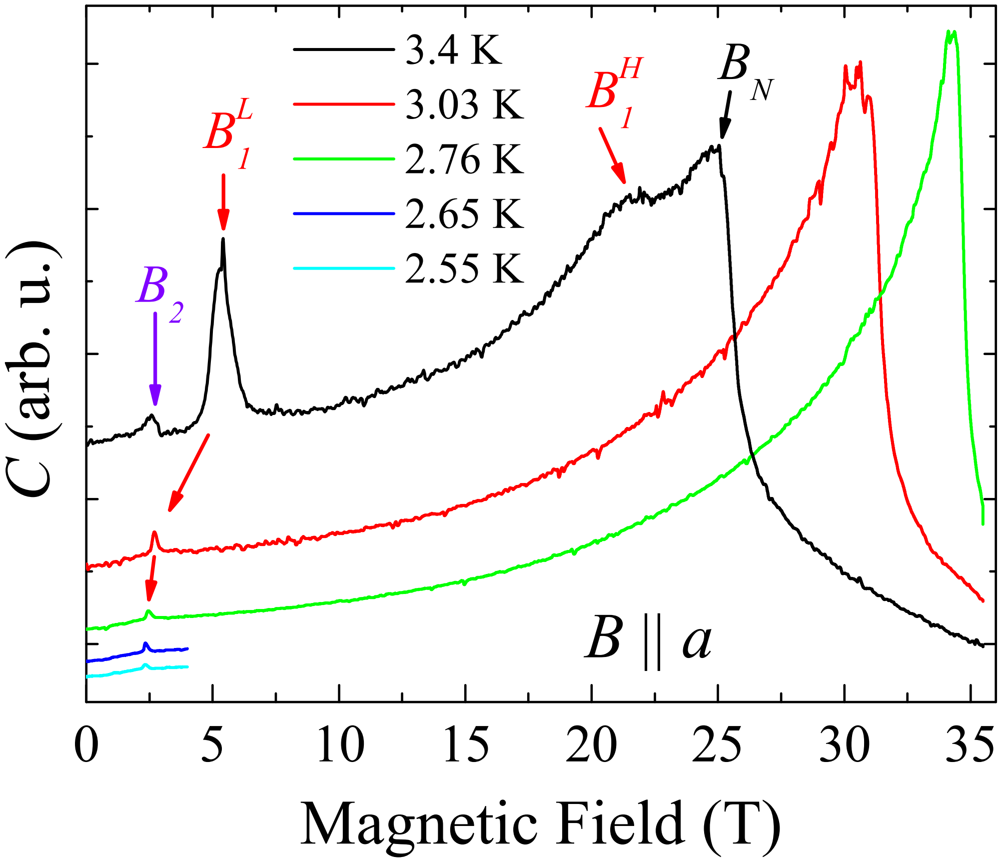

Figure 3.30: Specific heat divided by temperature, C/T, of CeRhIn$_5$ for magnetic field applied along the a axis. (a) C/T as a function of T obtained from relaxation technique for several values of magnetic field. Curves are vertically shifted according to the magnetic field scale shown in the right axis. A zoom at low and high fields is shown in (b) and (c) respectively. (d) Total specific heat, C, obtained from field sweeps using the AC technique.

The resulting magnetic field-temperature, $B-T$, phase diagram for field along the a axis is shown in Fig. 3.31. It contains three different antiferromagnetic phases labeled AFM1, AFM2, and AFM3. The magnetic structure of all three phases was previously determined by neutron diffraction [96, 97]. The zero-field phase AFM1 corresponds to an incommensurate antiferromagnetic spin helix with a propagation vector $\mathbf{Q} = (0.5, 0.5, 0.297)$. The AFM2 phase is an incommensurate elliptical helix with strongly modulated magnetic moments and a temperature-dependent propagation vector. The AFM3 phase is a commensurate collinear square-wave ('up-up-down-down' configuration) with a propagation vector $\mathbf{Q} = (1/2, 1/2, 1/4)$. All three phases meet at a triple point inside the AFM phase at (3 T, 3.4 K). The AFM2 phase exists only in a narrow temperature range close to T_N. This range shrinks with increasing magnetic field until the AFM2 phase is completely suppressed at $\sim$ 30 T, giving rise to yet another triple point. Remarkably, this field is about the same as B^*, at which the putative electronic-nematic phase emerges for fields close to the c axis. Above 30 T, only the commensurate phase AFM3 exists up to the complete suppression of the AFM order. A naive quadratic fit of T_N vs B reveals a critical field $B_c \simeq 54$ T, in agreement with previous pulsed field results [99].

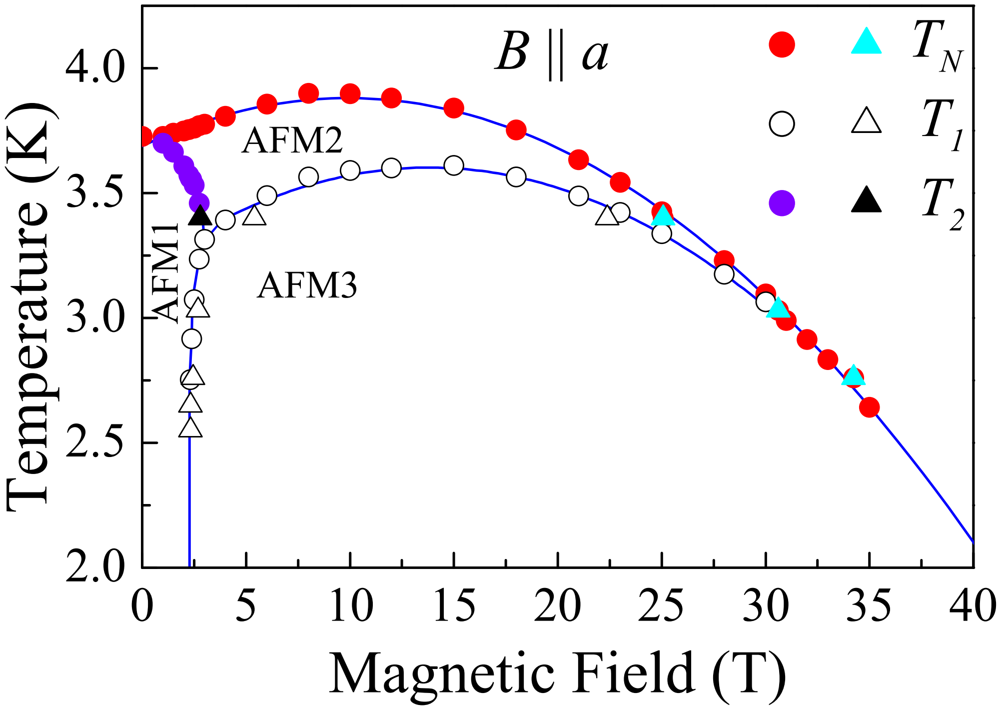

Figure 3.31: Magnetic phase diagram of CeRhIn$_5$ obtained from relaxation (circles) and AC (triangles) specific heat measurements for field applied along the a axis. Closed and open symbols correspond to second- and first-order transitions respectively.

3.3.5 Specific heat of CeRhIn$_5$ for field applied along the c axis

Figure 3.32 shows the temperature dependence of the specific heat divided by temperature, C/T, obtained using relaxation technique at different magnetic fields applied along the c axis. For this orientation of the magnetic field, T_N is gradually suppressed, consistent with previous reports [72, 99, 100]. This is the usual behaviour observed in AFM heavy-fermion compounds. However, we observed a non-monotonic behaviour of the specific heat jump at the AFM transition. With increasing field, the jump size gradually increases up to 27 T, above which there is a small abrupt drop. The jump size then remains almost constant between 29 and 35 T, the highest field of our measurements. A similar behaviour was also observed in the previous studies [100, 73]. This unusual behaviour indicates that there might be a change in the AFM state between 27 and 29 T.

The most remarkable result is obtained using the AC technique with field applied along the c axis. For this orientation, we observed a weak but distinct anomaly at B^*, as shown in Fig. 3.33 and 3.34(a). The exact position of the anomaly is defined from the second derivative of the specific heat

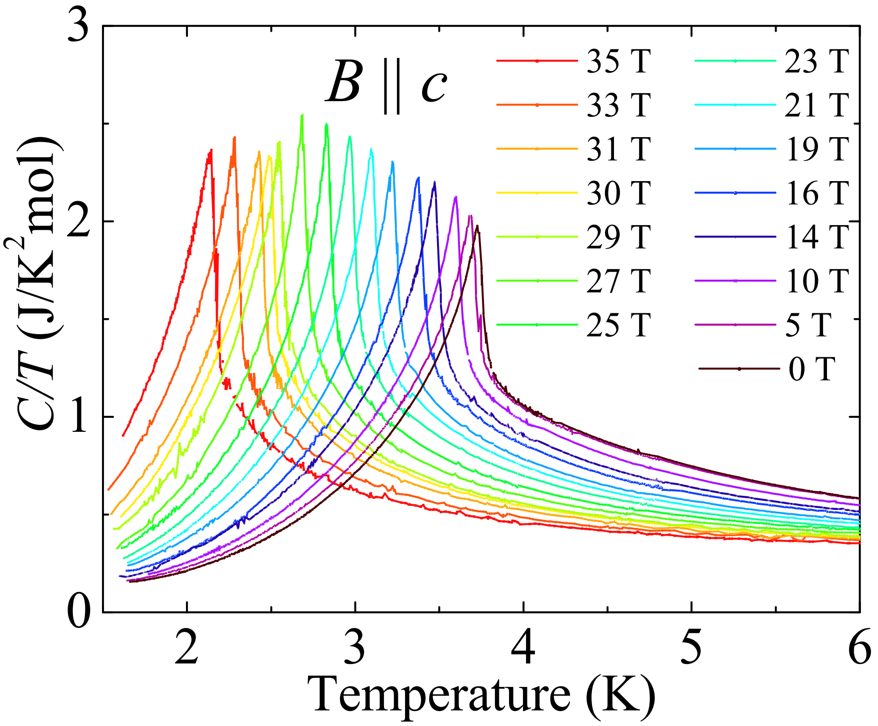

Figure 3.32: C/T of CeRhIn$_5$ for magnetic field applied along the c axis obtained from temperature sweeps using the relaxation technique.

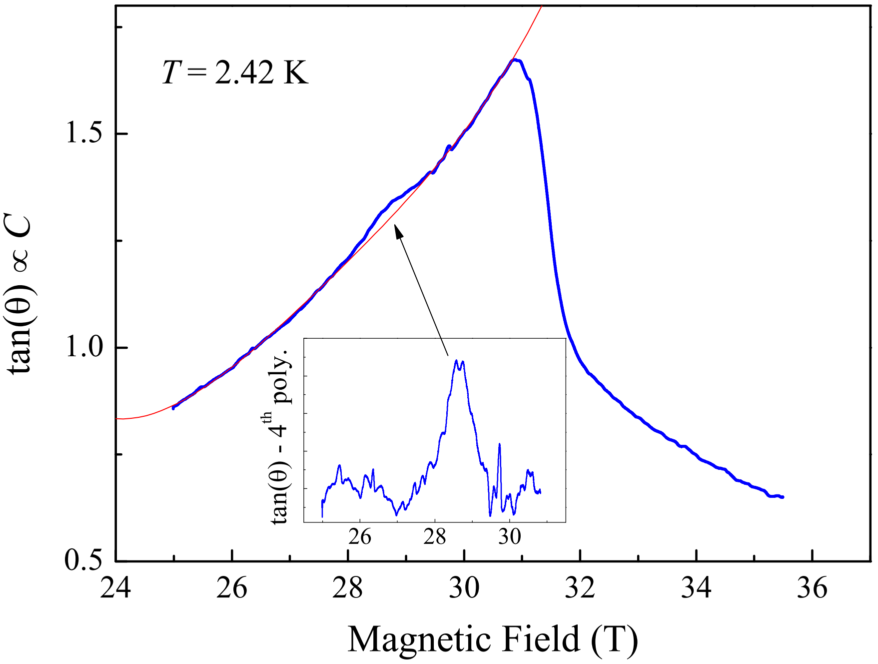

Figure 3.33: Specific heat of CeRhIn$_5$ for magnetic field applied along the c axis obtained from field sweeps using the AC technique at $T = 2.42$ K. Inset show the anomaly at B^* obtained after subtracting 4^{th} degree polynomial from C.

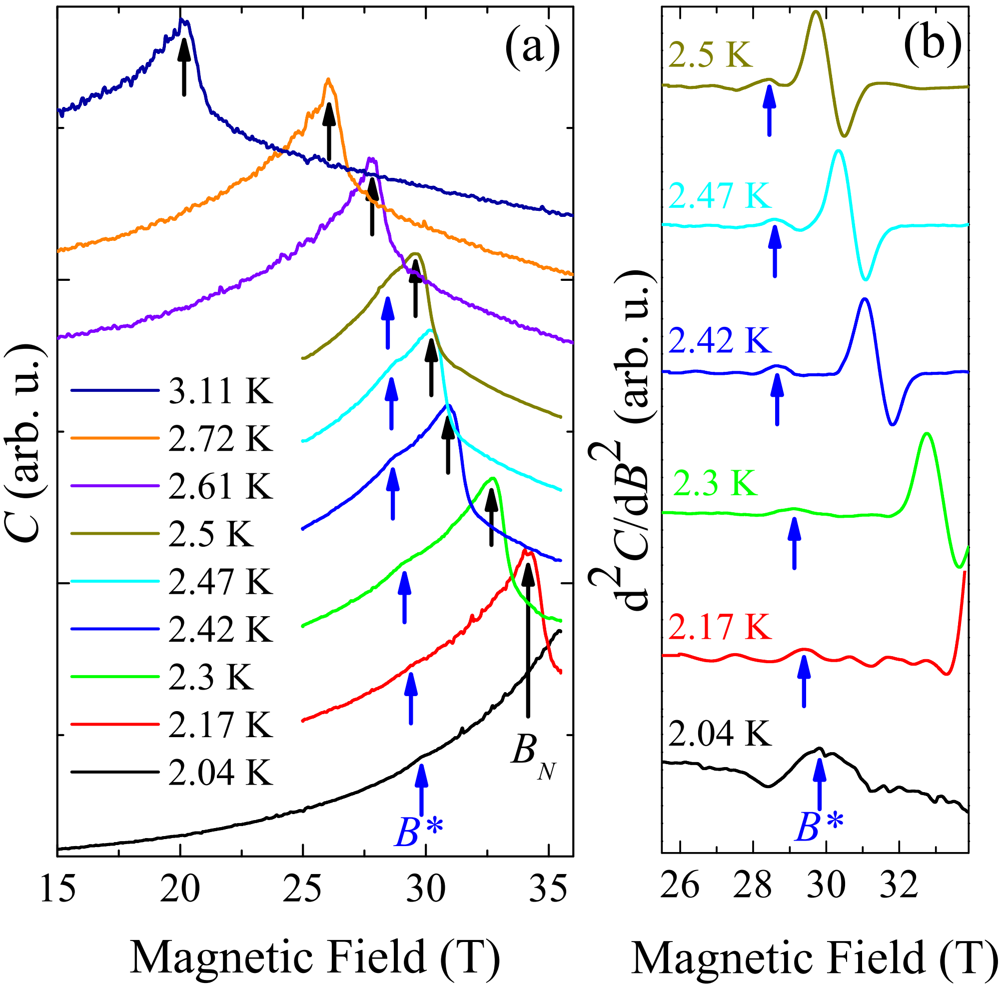

Figure 3.34: (a) Specific heat of CeRhIn$_5$ for magnetic field applied along the c axis obtained from field sweeps using the AC technique. Curves are vertically shifted for clarity. (b) Second derivatives of the heat capacity shown in (a) with respect to magnetic field. Arrows indicate the AFM transition and the anomaly at B^*.

with respect to magnetic field, where the anomaly manifests itself as a small maximum, as shown in Fig. 3.34(b). This anomaly was not observed in previous high-field specific heat measurements.

3.3.6 Discussion about the anomaly at B^*

We will now discuss a possible origin of the high-field state above B^* based on our findings. The presence of the specific heat anomaly at B^* implies that it is likely a real thermodynamic phase transition rather than a crossover, contrary to what was previously suggested [103]. The latter suggestion, however, was based on magnetostriction measurements performed in a magnetic field applied at 20° from the c axis. Furthermore, the anomaly we observe at B^* does not have the characteristic λ-like shape of a second-order phase transition contrary to those at B_2 and B_N in Fig. 3.30. Therefore, the anomaly observed at B^* most likely corresponds to a first-order phase transition. Moreover, it is thermodynamically forbidden that three second-order phase boundary lines meet at a triple point [138]. This further supports our hypothesis that B^* is a first-order phase transition. Finally, the anomaly at B^* is observed only within the AFM state, in agreement with previous reports [99, 101, 43, 103, 105]. Based on this, the most natural explanation of the phase transition at B^* is a change of magnetic structure. Previous high-field NMR measurements unambiguously suggest that the AFM phases both below and above B^* are incommensurate [104]. Therefore, B^* should correspond to a transition from one incommensurate phase, AFM1, to another phase incommensurate along the c axis, AFM4, with a propagation vector $\mathbf{Q} = (0.5, 0.5, l)$, where

l is different from 0.297 of the AFM1 phase.

This hypothesis is consistent with previous reports. Indeed, the previously observed resistivity jump at B^* [101, 43, 137] can be naturally accounted for by a metamagnetic spin-reorientation, as we suggest here. The only previously reported result, which is difficult to reconcile with our hypothesis, is that a Fermi surface reconstruction corresponding to the delocalization of the f electrons occurs at B^* [99, 102]. This conclusion, however, was challenged by recent angular-dependent de Haas-van Alphen effect measurements, which suggest that the f electrons in CeRhIn$_5$ remain localized up to fields higher even than B_c [139].

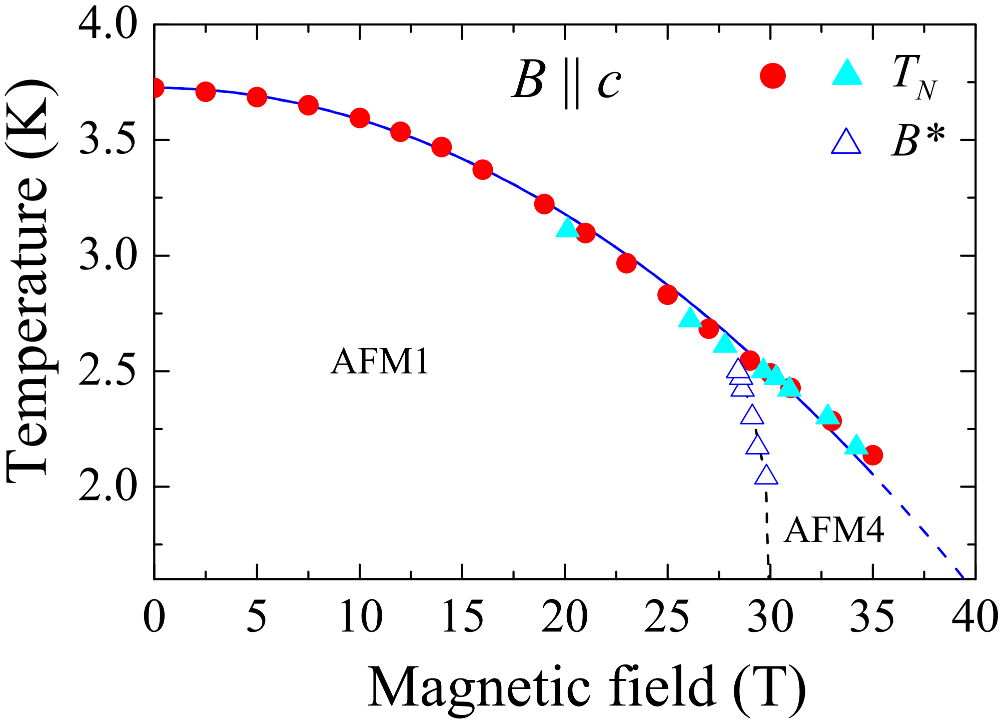

Figure 3.35: Magnetic phase diagram of CeRhIn$_5$ obtained from relaxation (circles) and AC (triangles) specific heat measurements. Closed symbols correspond to second-order transitions from AFM to PM phase. Open symbols indicate the anomaly at B^*, which presumably corresponds to a weakly first-order transition.

Figure 3.35 shows the revised magnetic phase diagram of CeRhIn$_5$ for field applied along the c axis. The field dependence of T_N obtained from our static-field measurements is consistent with that previously reported, based on the pulsed-field data [100]. A fit of the data to the $T_N(B) = T_{N0}[1 - (B/B_c)^2]$ expression, where T_{N0} is T_N at zero field, reveals a critical field $B_c \simeq$ 52 T. This value is in agreement with that previously reported [99]. The transition at B^* is weakly temperature-dependent in agreement with previous measurements [99, 101, 43, 103, 105]. As was already discussed above, we suggest that this first-order transition separates two different incommensurate magnetic phases.

We note that the situation is entirely different when a magnetic field is tilted from the c axis. First, a finite component of a magnetic field in the basal plane explicitly breaks the C_4 rotational symmetry. Even more important is that at angles bigger than 2°, the transition from incommensurate AFM1 phase into the commensurate phase AFM3 occurs below 30 T [139]. Therefore, the transition at B^* is from the commensurate phase AFM3 to the incommensurate phase AFM4. This is likely what was observed in recent ultrasound velocity measurements [105]. In these measurements, the anomaly observed at 20 T at the AFM1-AFM3 transition is very similar to that observed at $B^* \simeq 30$ T. Furthermore, the magnetostriction anomaly observed at B^* in a magnetic field tilted by about 20° from the c axis is similar to that observed at 7.5 T, where it corresponds to the AFM1-AFM3 transition.

3.3.7 Miscellaneous

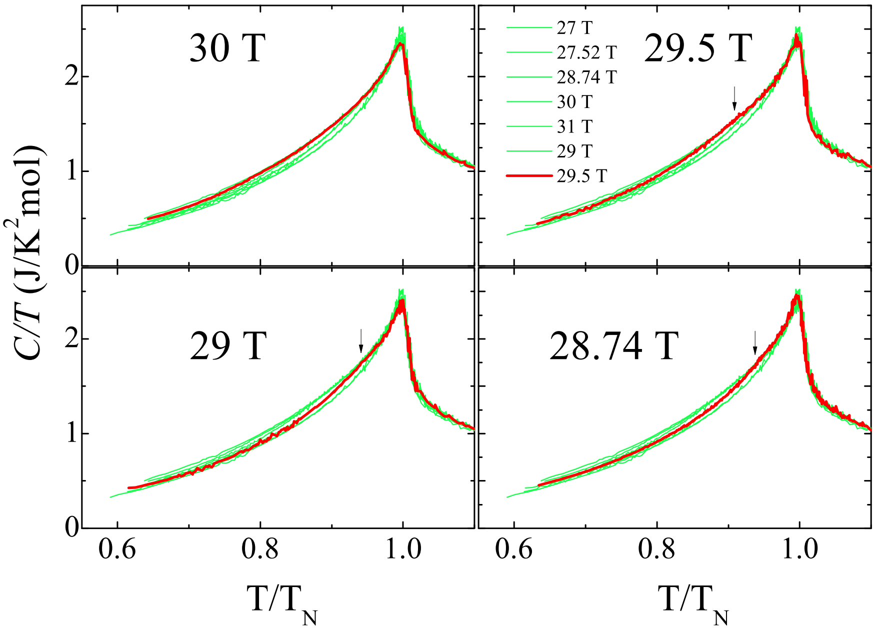

Figure 3.36: Specific heat in CeRhIn$_5$ using temperature sweep (relaxation technique) for magnetic fields close to B^*, applied along the c axis. The plots in green are for C/T at the remaining fields listed in the legend.

As shown in the $B-T$ phase diagram in Fig. 3.35, the B^* transition is weakly temperature dependent. It is, therefore, difficult to detect this transition in temperature sweeps in the relaxation technique. However, close to the AFM boundary, this transition has a relatively larger temperature dependence and shifts to slightly lower fields. We, therefore, performed specific heat measurements using thermal relaxation technique at few different fields slightly below 30 T, as shown in Fig. 3.36. Indeed, at magnetic fields close to 29 T, there is a weak anomaly observed in the specific heat just below the AFM transition (indicated by arrows on the red plots in each panel of Fig. 3.36 at $B = 29.5$ T, $B = 29$ T, and $B = 28.74$ T).

Scaling the temperature dependence of C/T with respect to T_N provide an easier template to understand the field-evolution of the specific heat, especially at low temperatures, such as in the AFM state. Such a plot for CeRhIn$_5$ for fields along the c axis is shown in figure 3.37. Contrary to the previous report [100], the specific heat in the AFM state (below T_N) evolves gradually starting from low fields and up to 35 T, the highest field of our measurement [see Fig. 3.37]. In Figure Fig. 3.37(b) we plot the value of C/T at 0.8 T_N as a function of field. For this value of scaled temperature, i.e., 0.8 T_N, there is a small jump at 29 T, in the otherwise smooth evolution of the convex-shaped specific heat in the AFM state with field. This small jump is due to the presence of the B^* transition in C/T at 29 T as shown in Fig. 3.36. Furthermore, another interesting observation is the abrupt change in the slope of C/T at 0.8 T_N vs B. The slope, which depict the evolution of specific heat with field, is almost doubled at fields above 29 T in comparison to the slope below 29 T. This indicates that above 29 T, the evolution of AFM state and possibly the AFM state itself is different from the low field state, i.e., below 29 T. This interpretation is consistent with our hypothesis of change of AFM structure at B^* (see Fig. 3.35).

Next we try to extract the magnetic field dependence of the electronic contribution to the total specific heat in CeRhIn$_5$. Usually for a metallic system, the total specific heat has electronic γ and phononic β contributions whose temperature dependance can be written as

$$C/T = \gamma + \beta T^2 \tag{3.1}$$

Experimentally, the electronic contribution or the Sommerfeld coefficient can be obtained as the intercept of the C/T vs T^2 plot. Figure 3.38 shows such plots for CeRhIn$_5$ in magnetic fields

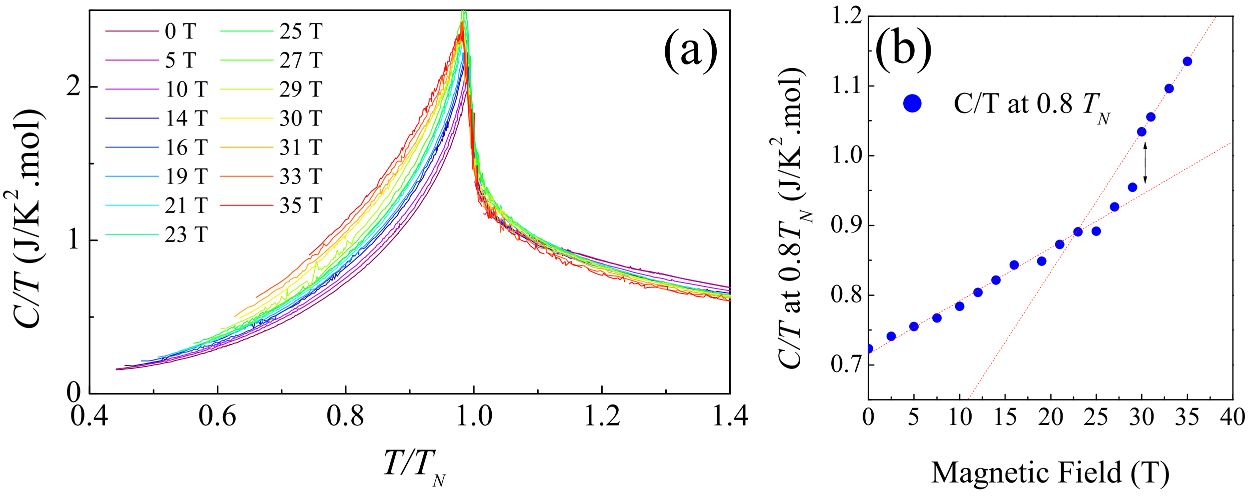

Figure 3.37: Evolution of specific heat in CeRhIn$_5$ with magnetic field obtained using the relaxation technique. All the plots at different magnetic fields are scaled with respect to T_N for the corresponding field. (b) C/T taken at $0.8T_N$ at different magnetic fields. The red dashed lines are linear fit to the evolution of C/T at low and high fields.

up to 35 T. In the paramagnetic phase (which is equivalent of metallic state), C/T is essentially a straight line (at $T \geq 10$ K). The lines at different fields are parallel to each other, i.e. equal slope β, indicating the phononic contribution is field independent. The y-intercept of this line give the electronic contribution γ. It decreases with increasing magnetic fields as is typically expected for heavy fermions due to suppression of correlation effects. At high fields (> 20 T), it is more or less constant.

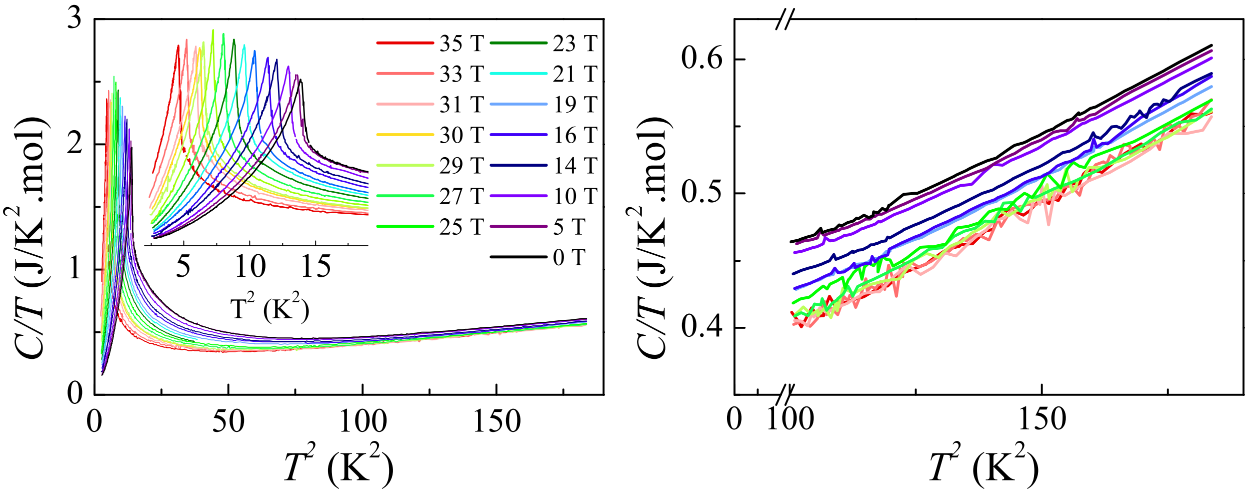

Figure 3.38: Evolution of the specific heat C/T in CeRhIn$_5$ plotted against T^2. The inset shows a zoomed-in view of C/T vs T^2 in the low temperature range (antiferromagnetic state). The panel on the right shows C/T vs T^2 in the high temperature range (paramagnetic state).

Determining the electronic contribution in the antiferromagnetic phase is not as straight forward because a simple linear fit does not work and we are limited by the base temperature ≈ 1.6 K. A very naive extraction of something equivalent to the electronic contribution in the AFM state is shown in Fig. 3.39. Here the C/T at the lowest temperature, i.e., $T = 1.65$ K is plotted as a function of magnetic field [see Fig. 3.39(b)].

However, such an analysis is not much reliable or informative. The specific heat below T_N has very distinct nature because of the additional contributions due to the AFM ordering of moments. Therefore, in addition to the electronic and the phononic contribution, an antiferromagnetic magnon contribution (C_{mag}) to the total specific heat must also be taken into account as below

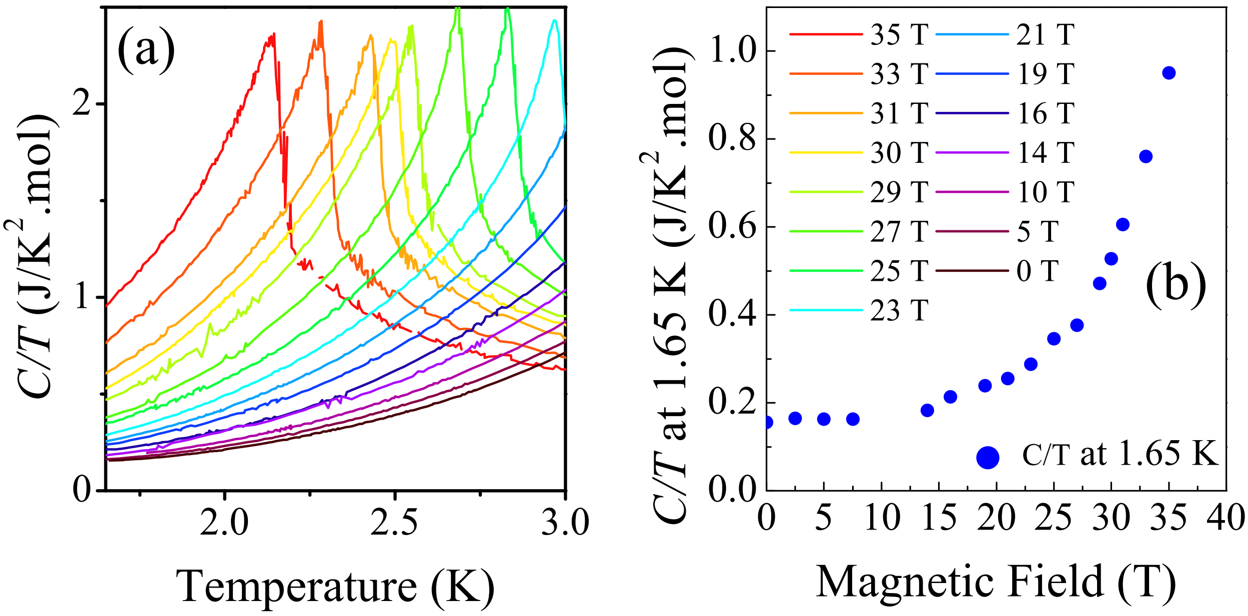

Figure 3.39: (a) Specific heat in CeRhIn$_5$ at different magnetic fields applied along the c axis. (b) Value of C/T taken at $T = 1.65$ K at different magnetic fields.

$$C_{Total} = C_{el} + C_{ph} + C_{mag}. \tag{3.2}$$

Now, the phononic contribution is very small at low temperatures, as can be seen in fig. 3.28 for LaRhIn$_5$, and therefore, can either be neglected or must be subtracted from the total specific heat before further analysis.

Next, to determine C_{mag}, appropriate models to fit the low temperature part of specific heat are used. Often, C_{mag} is approximated using the spin-wave theory. For antiferromagnets, spin wave theory gives a linear magnon dispersion relation i.e. $\omega \sim k$. The specific heat contribution due to spin wave formation comes out to be $C_M T^3$. Additionally, the magnetic anisotropy arising from molecular fields will introduce a finite gap in the magnon dispersion. This introduces a factor $e^{-\Delta/T}$, where Δ is the size of spin-gap.

For antiferromagnets, two models dealing with these details are generally used for fitting the specific heat in AFM state. The first one (eq. 3.3) comprises of an antiferromagnetic spin wave contribution with a dispersion relation in relativistic form $\omega = \sqrt{\Delta^2 + Dk^2}$, where Δ is the size of spin-gap, α is related to spin-wave stiffness D by $\alpha \propto D^{-1/3}$ [140].

$$C_{mag} = \gamma_0 T + \alpha \Delta^{7/2} T^{1/2} e^{-\Delta/T}(1 + (39/20)(T/\Delta) + (51/32)(T/\Delta)^2) \tag{3.3}$$

The linear contribution $\gamma_0 T$ is the electronic contribution in the AFM state. This model was previously used by Jiao et al. to extract the field-dependence of γ_0 in CeRhIn$_5$ [100]. The second one (eq. 3.4) is by Bredl [141] taking into account an activated term and is as follows

$$C/T = \gamma_0 + \beta_M T^2 + \beta'_M(\exp(-E_g/K_B T))T^2 \tag{3.4}$$

Here, $\gamma_0 T$ is again the electronic term in AFM state, $\beta_M T^3$ is AFM magnon term, $\beta'_M(\exp(-E_g/K_B T))T^3$ is activated term arising from an AFM SDW with a gap in the excitation spectrum due to anisotropy. This model was previously used by Cornelius et al. to extract γ_0 in CeRhIn$_5$ at zero field [77].

Using both these models, we tried to fit the magnetic contribution to the total specific heat in CeRhIn$_5$ at zero field (after subtracting the phonon contribution using LaRhIn$_5$) as shown in Fig. 3.40. The parameters extracted based on the fit using eq. 3.4 are ($\gamma_0 \approx 65$ mJ/K^2mol, $\beta_m \approx$ 23 mJ/K^2mol, $\beta'_m \approx 722$ mJ/K^2mol and $E_g/k_B \approx 8.2$ mJ/K^2mol) and are in good agreement with the previous report by Cornelius et al.[77] ($\gamma_0 \approx 56$ mJ/K^2mol, $\beta_m \approx 24.1$ mJ/K^2mol, $\beta'_m \approx$ 706 mJ/K^2mol and $E_g/k_B \approx 8.2$ mJ/K^2mol).

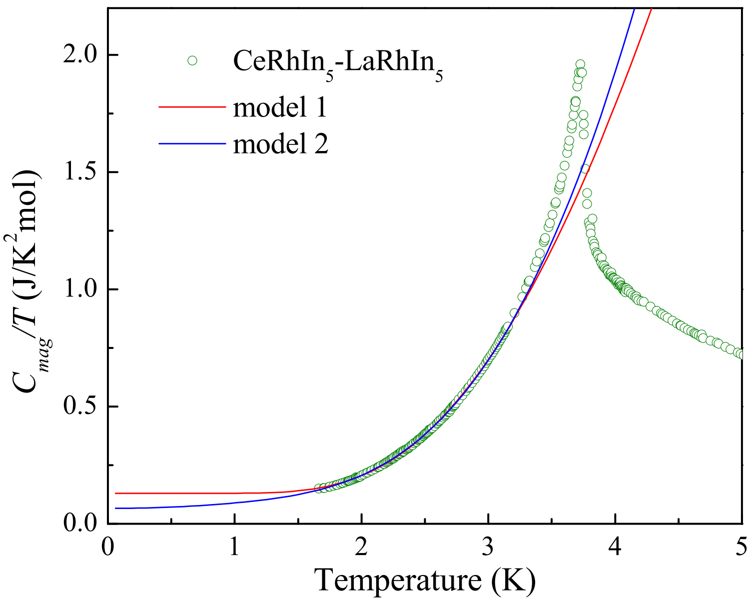

Figure 3.40: Fits of the magnetic contribution to the total specific heat in CeRhIn$_5$ at zero field using model 1 (eq. 3.3) (red line) and model 2 (eq. 3.4) (blue line) as discussed in the text.

Similarly, the extracted parameters based on the fit using eq. 3.3 are $\gamma_0 \approx 130$ mJ/K^2mol, $\alpha \approx 1.46 \times 10^{-6}$ mJ/K^2mol and $\Delta \approx 11.6$ mJ/K^2mol. These parameters are not in much agreement with the previous report by Jiao et al. [100] ($\gamma_0 \approx 82$ mJ/K^2mol, $\alpha \approx 6.5 \times 10^{-6}$ mJ/K^2mol and $\Delta \approx 11.2$ mJ/K^2mol.) However, these extracted parameters also vary depending upon the temperature range selected for fitting.

It is evident that fits based on eq. 3.3 and eq. 3.4 to the magnetic specific heat at low temperature fails at temperature close to T_N. The fit based on eq. 3.3 shows a larger deviation from the experimental data close to T_N. Furthermore, the variation of the extracted parameters with the data range used suggests that such an analysis might lead to misleading conclusions, especially when three to four free fitting parameters are involved. Therefore, a field dependence of the extracted parameter, such as shown for γ_0 in [100], must be considered cautiously.

3.3.8 Conclusions

In summary, we performed specific heat measurements in CeRhIn$_5$ in static fields up to 36 T applied both along the a and the c axis. For field along the a axis, we confirmed previously established rich phase diagram, and extended it to higher fields. For field along the c axis, we observed a distinct anomaly at $B^* \simeq 30$ T, suggesting that a real thermodynamic phase transition, probably weakly first-order, is likely to take place at this field. We suggest that this transition is from the low-field incommensurate magnetic structure to another incommensurate phase, characterized by a different propagation vector. High field inelastic neutron scattering measurements are required to definitely confirm this hypotheses. Such measurements, although very challenging, are now possible due to the recent experimental breakthrough [142].

These results are published in [139].

3.4 Ultrasound velocity and attenuation in high magnetic fields

3.4.1 Abstract

Here we report a comprehensive high-field ultrasound velocity study on bulk single crystals of CeRhIn$_5$. For a field applied at 2° from the c axis, we observed two sharp anomalies, at 20 T and 30 T, in all the symmetry-breaking modes (C_{11}, C_{44}, C_{66} and C_T) at low temperatures, suggesting additional broken symmetries of the underlying order parameter rather than just the four-fold rotational symmetry previously suggested. The former anomaly corresponds to the well-known first-order metamagnetic transition, where the magnetic structure changes from incommensurate to commensurate. The higher field anomaly takes place at $B^* \approx 30$ T, where an electronic nematic transition was previously suggested to occur. Both anomalies are of similar shape, but the corresponding changes of the ultrasound velocity have the opposite signs. Furthermore, both anomalies are observed within the antiferromagnetic state only. Based on these experimental results, we suggest that the anomaly at B^* also corresponds to a field-induced transition, this time from a commensurate to a different incommensurate antiferromagnetic state. With increasing the field angle from the c axis, the anomaly at B^* slowly shifts to higher fields, broadens and becomes smaller in magnitude. Therefore, the angle-dependent behaviour of the anomaly at B^* is found to be inconsistent with the microscopic picture of electronic-nematics, in which the anisotropy arising due to the directional alignment of nematic domains is proportional to the strength of the in-plane field component. The anomaly, traced up to 30° from the c axis, is no longer observed at 40° up to 36 T. These observations are in contrast with the previously reported results of transport studies performed on microfabricated samples of CeRhIn$_5$. Apart from the anomalies at 20 and 30 T in the symmetry breaking modes, we also observed clear features around 30 T at temperatures below 1.9 K in the C_{33} mode, which is symmetry preserving. These anomalies, however, are observed only when the magnetic field is applied very close to the c axis. With decreasing temperature, these features form a dome-like phase centered at 30 T within the AFM state. However, no feature was observed around 20 T in the C_{33} mode. Therefore, our results indicate that a rather exotic phenomena occur around 30 T. Based on the observations in the C_{33} mode, we suggest that the change of the magnetic structure, at least at small field angles, is either accompanied or driven by an additional transition probably due to an inter-layer exchange along the c direction.

3.4.2 Introduction

Classical complex fluids often exhibit a phase, in which their rod-shaped micro-structured molecules align in an orientational order in such a way that the rotational invariance is spontaneously broken. Such a phase is known as a nematic state.

Strongly correlated electron systems, such as the high temperature superconductors, iron-based superconductors, and heavy-fermion compounds, are essentially quantum fluids comprising of strongly interacting constituents, i.e., electrons. Due to the strong electronic correlations, these systems exhibit many exotic phases, such as unconventional-superconductivity, a strange metallic state, a non-Fermi-liquid state, pseudogap phase and hidden-order.

In an analogy to the nematic state in the classical fluids (liquid crystals), SCES are conjectured to host a similar symmetry broken nematic phase. Indeed, this was experimentally found in many strongly correlated electron systems such as high-temperature superconductors [39, 40, 41] , strontium ruthenate [42], and, more recently, in heavy-fermion systems [43]. In applied magnetic fields, above a certain critical field, an unusually large transport anisotropy was observed in the rather isotropic conducting planes of these 2D electronic systems. This strong electronic anisotropy was interpreted as an electronic-nematic (EN) state. Microscopically, it is understood that above a critical out-of-plane field, a new state is prepared, in which the electron fluid is replaced by nanosized electronic structures or ‘domains’, which can be aligned in a preferential direction by an arbitrary small in-plane field component thereby leading to an anisotropic electronic transport along the two orthogonal directions in the 2D conducting planes. Such a transport anisotropy increases with increasing the in-plane field component. However, in the absence of an in-plane field component (in other words fields perpendicular to the conducting planes), the transport anisotropy disappears but the domain formation may still exist. Only the presence of a finite in-plane field component aligns these domains and reveals the full effect of the symmetry breaking.

The apparent relation of this nematic phase to unconventional superconductivity is still under debate. It is an active area of research to understand if the nematic phase competes, coexists or enhances superconductivity, or simply appears accidentally. In this regard, the heavy-fermion compound $CeRhIn_5$ can play a crucial role to study the possible relation of unconventional superconductivity and an electronic nematic phase. In this system, a pressure-induced unconventional superconducting state [70] emerges in the vicinity of a pressure-induced QCP, while a state of enhanced in-plane electronic anisotropy, interpreted as an electronic-nematic phase, [43] emerges in the vicinity of the field-induced QCP. While the unconventional superconducting state in $CeRhIn_5$ is well established, a comprehensive understanding of the electronic anisotropic state is still elusive. The electronic-nematic interpretation of the enhanced in-plane electronic anisotropy above B^* comes from the magnetoresistance study on FIB fabricated devices [43]. There is always a finite strain on FIB-devices arising due to the difference in the thermal expansion coefficients of the sample and the substrate or the contacts by which the sample is held. Another member of Ce-115 family, $CeIrIn_5$, shows a drastic change of its properties due to strain [143]. In $CeRhIn_5$ too, a change of magnetic structure was observed in powdered samples [144] suggesting a strong impact of the strain on its physics. The role of strain for the electronic-nematic transition, therefore, cannot be ruled out.

While an anomaly around $B^* \sim 30$ T applied close to c axis has been observed in several other measurements on bulk samples such as specific heat, magnetostriction [103], ultrasound velocity [105] and NMR [104], torque and magnetization have so far failed to show a detectable feature corresponding to this transition. These measurements, however, cannot directly confirm the electronic-nematic character of the high-field state, while transport measurements can. Some of these measurements do conform with the rationale of a symmetry-broken electronic nematic state. For example, magnetostriction measurements indicated a small lattice response at 30 T in both the a and c directions. The lattice distortion along the a direction was interpreted as a signature of an enhanced hybridization of cerium f electrons with the in-plane $5p$ electrons of indium. Similarly, previous NMR and ultrasound reports also indicated an enhanced in-plane $c - f$ hybridization. However, our dHvA study confirms that the f electrons remain localized above 30 T in the high-field phase of enhanced anisotropy. Therefore, the origin of the electronic nematic state cannot be due to an enhanced $c - f$ hybridization and Kondo effect. The detection of an anomaly at 30 T in our specific-heat study suggests that a real phase transition occurs at this field. We discussed the transition at 30 T in terms of as a change of the magnetic structure. Fluctuations associated with a magnetic instability close to the QCP can be a candidate for the origin of a correlated state, in this case, an electronic-nematic state. Indeed, the pressure-induced and cobalt substitution-induced superconducting states in $CeRhIn_5$ are enhanced by a change of the antiferromagnetic structure. Anyway, the true origin of the 30 T transition remains elusive.

The order parameter associated with the transition holds vital information about its microscopic origin and must be studied an using an appropriate probe. In this regard, the elastic response is an extremely useful probe, not to only detect thermodynamic phase transitions but also to determine the symmetries of the associated order parameter through the strain-order parameter coupling. Ultrasound waves readily couple with electronic, magnetic, and structural degrees of freedom. Elastic constants (C) are a second-derivative of the free energy (F) with respect to the applied strain (ϵ), i.e., $C = d^2F/d\epsilon$. Experimentally, the elastic constants can be deduced from the ultrasonic velocity v in a crystal lattice of the mass density ρ as $C = \rho v^2$.

For a tetragonal crystal lattice, such as $CeRhIn_5$, there are six independent elastic constants (C_{11}, C_{12}, C_{13}, C_{33}, C_{44}, C_{66}). Except for C_{13}, the other five can be probed experimentally through ultrasound velocity measurements along the symmetry directions [100], [110] and [001]. The longitudinal (L) and transverse (T) ultrasonic modes along these symmetry directions and the corresponding elastic constants are listed in Table 3.1. Redundant ultrasonic modes are left out of this table.

Different ultrasound modes, obtained by different directions of the ultrasound propagation and

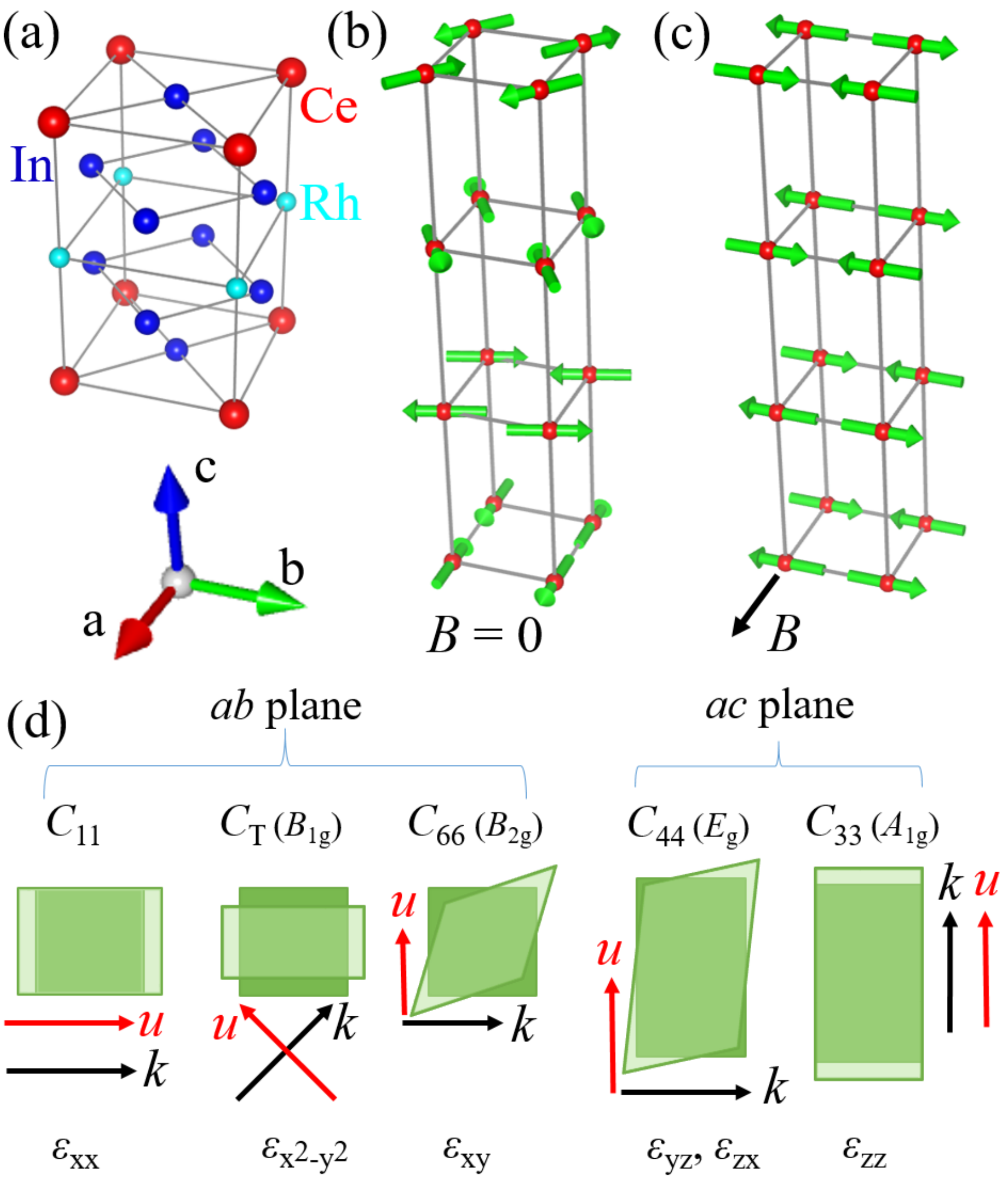

Figure 3.41: (a) Crystal structure of CeRhIn$_5$. Magnetic structure of CeRhIn$_5$ (b) in zero magnetic field and (c) in a magnetic field higher than 2 T applied along the [100] direction. Arrows indicate the orientation of the magnetic moments. Only Ce atoms are shown in (b) and (c) for clarity. (d) Schematic illustration of the symmetry strains induced by different ultrasound modes for a tetragonal crystal structure. For each mode, the propagation (k) and polarization (u) directions are shown by arrows. The associated irreducible representations are shown in brackets.

Ultrasound modes and the elastic constants for a tetragonal lattice			
Ultrasonic Mode	$\vec{k}$	$\vec{u}$	C_{ij}
$L_{[100]}$	[100]	[100]	C_{11}
$T_{[100]}$	[100]	[010]	C_{66}
$T_{[100]}$	[100]	[001]	C_{44}
$T_{[110]}$	[110]	[1-10]	$C_T = (C_{11}\text{-}C_{12})/2$
$L_{[001]}$	[001]	[001]	C_{33}

Table 3.1: The various ultrasounic modes for a tertragonal lattice and the corresponding elastic constants. The first column list the ultrasonic mode, here L: longitudinal and T: transverse and the subscript corresponds to the direction of propagation. The second and third columns depicts the directions of propagation and polarization, receptively. The corresponding elastic constant are listed in the fourth column.

polarization, induce different symmetry-breaking strains in the crystal, as schematically shown in Fig. 3.41(d) for a tetragonal crystal structure. This, in turn, allows for the determination of the symmetry of a phase order parameter as well as identification of the broken symmetries at a phase transition.

Recent ultrasound velocity study [105] on $CeRhIn_5$ detected an anomaly at 30 T in the transverse elastic constant C_T, while it was absent in the other four elastic constants. This was interpreted in terms of a quadrupolar ordering of the $O_{x^2-y^2}$ orbital due to the $\epsilon_{x^2-y^2}$ strain conforming with the previous interpretation of the broken $C_4^{\pm}$ tetragonal symmetry.

Here we report ultrasound velocity measurements in $CeRhIn_5$ in static magnetic fields up to 36 T and pulsed fields up to 65 T. The measurements in pulsed magnetic fields were performed using a phase-sensitive detection of the ultrasound signal across the sample using piezo-electric transducers in a ^{4}He cryostat. The measurements in static fields were performed using a frequency-sensitive detection of the signal in a ^{3}He cryostat equipped with an in-situ rotator.

3.4.3 Signature of AFM transition in elastic constants and attenuation

Similar to the heat capacity, the elastic modulus being a thermodynamic probe also detects the second-order anitferromagnetic phase transition in $CeRhIn_5$ as a distinct λ-like feature at 3.8 K, as shown in Fig. 3.42.

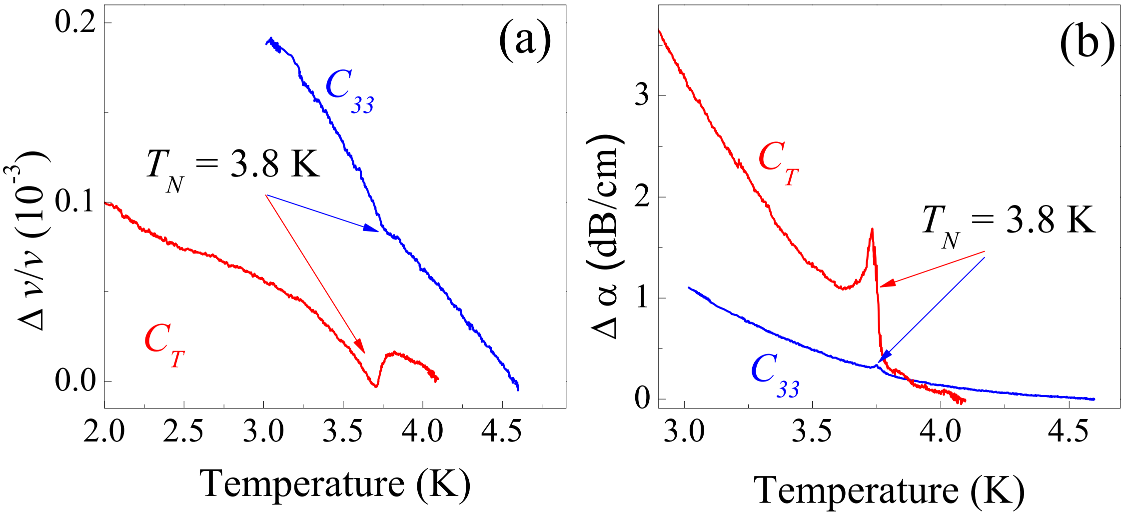

Figure 3.42: (a) Relative ultrasound velocity and (b) ultrasound attenuation in $CeRhIn_5$ across the antiferromangetic transition for the ultrasonic modes C_T and C_{33}.

The AFM transition is detectable in both the ultrasound velocities and attenuations marking the high sensitivity of our measurements. Here, the arrow points to the AFM transition observed in the elastic constants C_{33} and C_T and their corresponding elastic attenuations. The anomaly in the C_{33} mode is much smaller than that in the C_T mode.

3.4.4 Field-dependence of the relative ultrasound velocity variation $\Delta v/v$

Fig. 3.43 shows the relative ultrasound velocity variation with magnetic field applied close to the c axis in CeRhIn$_5$ for the five ultrasound modes described in Table 3.1.

The elastic constants C_{11}, C_{44}, C_{66} and C_T corresponds to the tetragonal symmetry breaking strains, as schematically depicted in the Fig 3.41(d). In addition to the symmetry breaking, C_{11} is also sensitive to the volume change. The elastic constants C_{11}, C_{44}, and C_{66} show an overall softening (decrease of the relative ultrasound velocity) with magnetic field up to B_p. The elastic constant C_T shows a hardening (increase of the relative ultrasound velocity) with magnetic field between B_m and B^* followed by a softening at higher fields. The C_{33} elastic constant shows an overall hardening with magnetic field up to the highest field of our measurement, i.e., 65 T. Contrary to the previous report [105], we observed clear features around $B^* \approx 30$ T in all the elastic constants, i.e., C_{11}, C_{44}, C_{66}, C_T and C_{33}. Similarly, the feature at $B_p \approx 45$ T is present in all the elastic constants, while it is most pronounced in C_{11}. However, in the C_T mode $B_{N(u)}$ appears instead of B_p, when the field is applied very close to the c axis. In the C_{11} mode, the feature at B_p is marked by a rapid hardening as depicted in Fig. 3.43(a). The rapid hardening might be due to the sensitivity of the C_{11} mode to volume changes. The feature at B_m is present in all the elastic constants except for C_{33}.

The feature at B_m corresponds to the well-known metamagnetic transition related to the change of the antiferromagnetic structure from the ambient-pressure, zero-field incommensurate helical structure (AFM1) [Fig. 3.41(b)] to a commensurate co-linear 'up-up-down-down' structure (AFM3), shown in Fig. 3.41(c). The transition occurs at $B_m = 2$ T for a field applied along the a axis. When the magnetic field is oriented away (by an angle α) from the basal plane towards the c axis, B_m initially varies as $1/\cos(\alpha)$, but deviates from dependence towards smaller values closer to the c axis. For a field orientation $\theta \approx 2^\circ$ from the c axis (or $\alpha = 88^\circ$), $B_m \approx 20$ T. For a field alignment better than 2° from the c axis, B_m has not been observed so far. To exclude a field alignment better than 2° as the origin of the absence of B_m in the C_{33} elastic constant, we performed field-dependent ultrasound velocity measurements at several orientations of the magnetic field (see Fig. 3.51). We did not observe B_m even at angles larger than 2° from the c axis where B_m should appear below 20 T. Therefore, the absence of B_m in the C$_{33}$ elastic constant implies that this mode does not couple to the in-plane electronic or magnetic changes.

The presence of the features in ultrasound velocity can understood from the symmetry considerations of the two antiferromagnetic structures, AFM1 and AFM3. AFM1 is an incommensurate spiral helical structure [Fig. 3.41(b)]. A spiral helical magnetic structure has a C_∞ rotational symmetry about the axis of the helix, while the tetragonal crystal structure has a C_4 rotational symmetry about the c axis. Therefore, a combination of the two, which is the case for the AFM1 phase in CeRhIn$_5$, should have the lower of the two rotational symmetries, i.e., a C_4 symmetry about the c axis. Now, in the up-up-down-down AFM2 structure [Fig. 3.41(c)], the magnetic moments are aligned in the tetragonal plane perpendicular to the magnetic field, i.e., in a preferential antiferromangetic arrangement. Therefore, the symmetry of the magnetic structure is lowered from C_4 to C_2 at the transition from incommensurate to commensurate at B_m. All the symmetry breaking strains that explicitly breaks the C_4 symmetry should then be able to detect such a transition. This is indeed the case, as B_m is detected in the C_T, C_{11} and C_{66} modes. However, the presence of B_m in the C_{44} mode suggests that additional symmetries are also broken across the IC-C transition, which are still to be identified. Nonetheless, experimentally, the most crucial point is the observation of the features at B_m and B^* in all the symmetry breaking modes. The transitions at B_m and B^* manifest themselves by similar anomalies, but the corresponding changes of $\Delta v/v$ have the opposite signs. This implies, that all the symmetries broken at B_m, including the C_4 rotational symmetry, are restored at B^*. It is, therefore, natural to conclude that both transitions are of the same origin, i.e., that the transition at B^* corresponds to another field-induced change of the magnetic structure, this time from the commensurate AFM3 to an incommensurate AFM4 phase

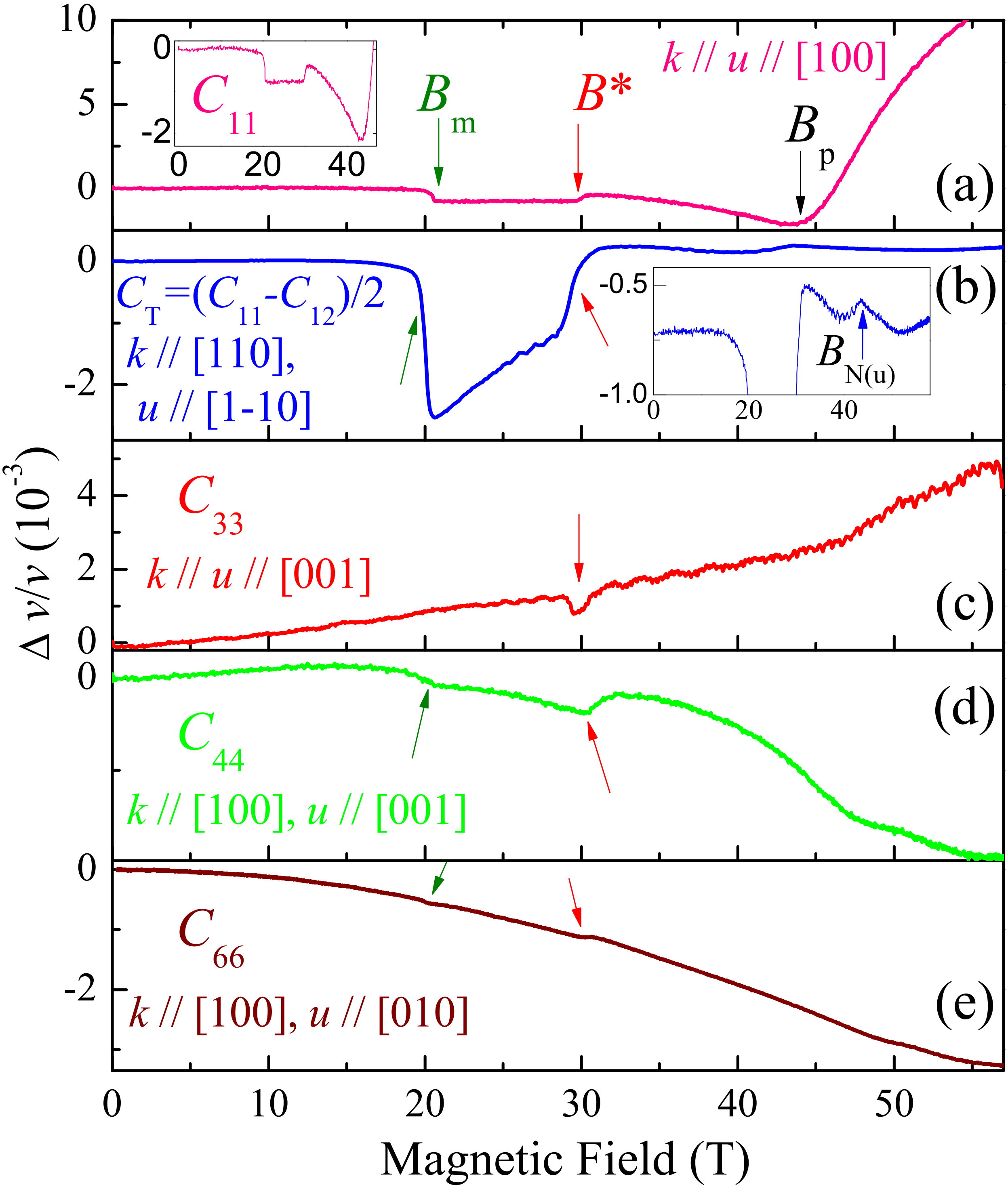

Figure 3.43: Field dependence of the relative ultrasound velocity variation, $\Delta v/v$, for the C_{11} (a), $C_T = (C_{11} - C_{12})/2$ (b), C_{33} (c), C_{44} (d), and C_{66} (e) modes at $T \simeq 1.4$ K. The field was applied at 2° from the c axis for all the modes. Arrows indicate the anomalies at B_m, B^*, $B_{N(u)}$ and B_p discussed in the text. For all the modes, the ultrasound propagation, k, and polarization, u, directions are indicated.

in the basal plane.

Moving further, we notice that in the C_{44} and C_{66} modes, the feature at B^* is larger than that at B_m. On the contrary, in the C_{11} and C_T modes, the anomaly at B^* is smaller than that at B_m. It is not clear why this is the case. Further, in the C_{33} mode, the feature at B^* has as a 'dip-like' shape, completely different from the 'step-like' shape in all the other modes. The unique shape of feature at B^* will be discussed later.

The absence of the well-established, purely in-plane transition at B_m as well as the presence of features around B^* and B_p in the C_{33} mode suggests that the transitions at B^* and B_p have out-of-plane characteristics in addition to the in-plane character. This implies that the feature at B^* might also correspond to the onset of a state of a 3-D electronic nature.

3.4.5 Temperature-dependence of $\Delta v/v$ and ultrasound attenuation

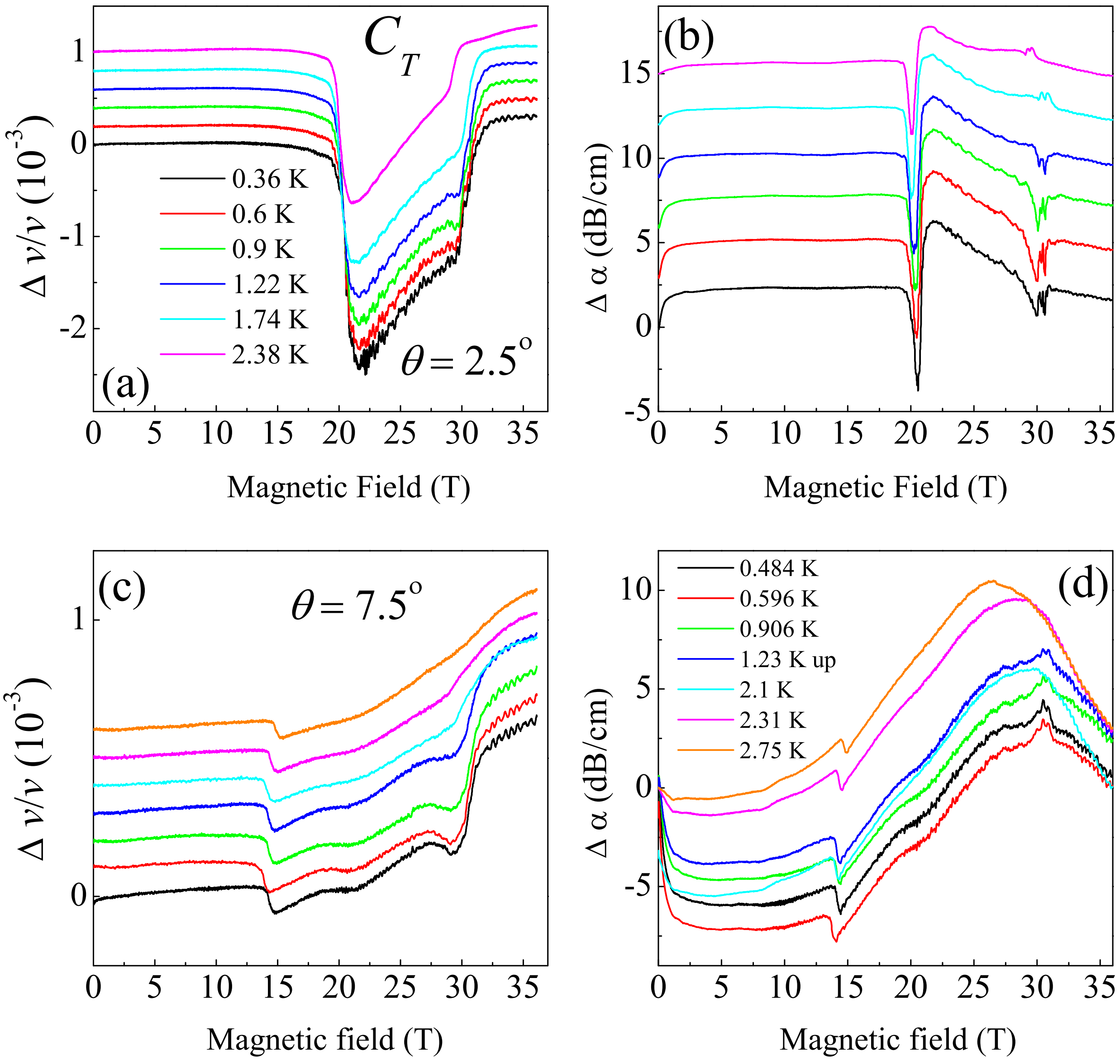

Figure 3.44: Temperature-dependence of the field-dependence of the relative ultrasound velocity (a),(c) and the corresponding attenuation (b),(d) for the C_T mode in CeRhIn$_5$ for two different field angles $\theta = 2.5^\circ$ (a),(b) and $\theta = 7.5^\circ$ (c),(d) from the c axis. Curves are shifted vertically for clarity.

Fig. 3.44 shows the temperature dependence of the field-dependent ultrasound velocity and elastic attenuation for the elastic constant C_T at two different orientations of the magnetic field,

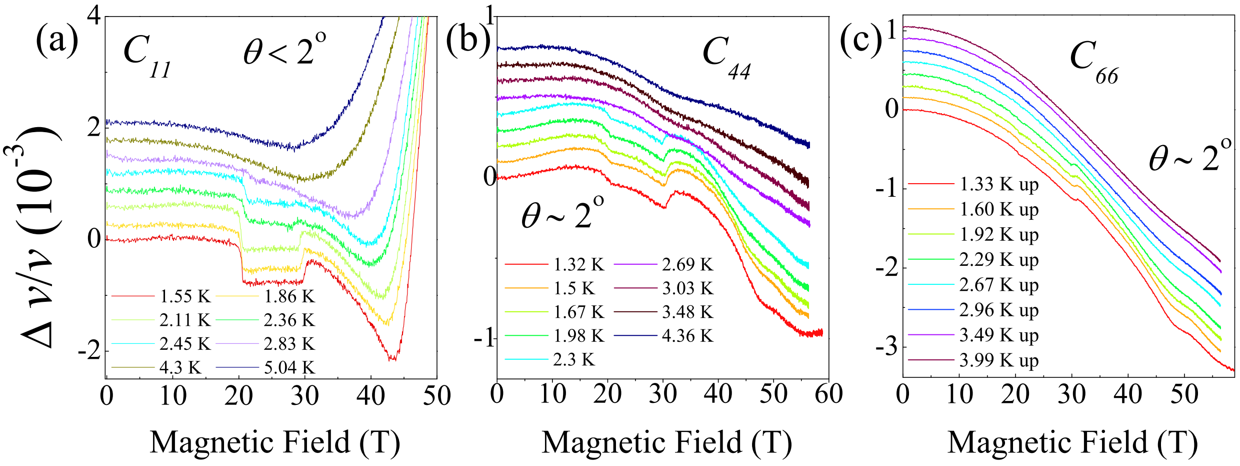

Figure 3.45: Temperature-dependence of field-dependence of relative ultrasound velocity for the (a) C_{11}, (b) C_{44} and (c) C_{66} modes in CeRhIn$_5$ for field applied at $\theta \approx 2°$ from the c axis. Curves are shifted vertically for clarity.

$\theta \approx 2.5°$ and $\theta \approx 7.5°$. Fig. 3.45 shows the temperature dependence of the elastic constants C_{11}, C_{44} and C_{66}. In all the modes, the transitions at B_m and B^*, are almost temperature independent. The transition at B_m moves to slightly higher fields at higher temperatures close to the AFM boundary. On the contrary, B^* moves to slightly lower fields when approaching the AFM boundary. The transitions are only slightly diminished in size with temperatures well below the AFM boundary and are drastically reduced only close to it. Both transitions exists strictly within the antiferromagnetic state [see Fig. 3.45(a)].

Based on the temperature dependence of field-dependent ultrasonic velocity in the C_{11}, C_{44}, C_{66}, and C_T modes, the temperature-magnetic field phase diagram is constructed, as shown in Fig. 3.46(a). All the points in the phase diagram corresponding to the various transitions are marked in Figs. 3.43, 3.44, 3.52 and 3.53 and are explained in the text. The points corresponding to the AFM boundary are from our specific heat study.

As mentioned previously, both the transitions at B_m and B^* exist strictly within the AFM state only. This suggests that the transition at B^* is also related to the magnetic properties of CeRhIn$_5$. This further supports our hypothesis that the transition at B^* corresponds to the change of the magnetic structure.

The transitions at B_m and B^* form a broad dome in the magnetic phase diagram [see fig. 3.46(a)], indicating that these two transitions binds a thermodynamic phase, AFM3, which has a commensurate AFM structure. The transition at B_p traces a PPM state boundary, as was previously suggested [105].

The features observed around B^* in the C_{33} mode show a peculiar temperature-dependence, different from the symmetry breaking modes. First of all, the features disappear above 2 K, about 0.5 K below the AFM phase boundary, as shown in Fig. 3.47. At low temperatures, there are two distinct features, one at a field slightly lower than 30 T and another one at a field slightly higher than 30 T. Furthermore, the two features show an asymmetric temperature dependence. higher field feature is almost temperature-independent at low temperatures. It moves to slightly lower fields on approaching 2 K. The lower field feature moves to lower fields with decreasing temperature. The features form an asymmetric dome centered at 30 T within the antiferromagnetic state [see fig. 3.46(b)]. The absence of a similar dome around the metamagnetic transition at 20 T argues for a rather exotic situation at B^*. Since the C_{33} mode is symmetry preserving and is sensitive to changes along the c direction of the tetragonal system such as interlayer exchange, an expansion or a compression, the feature are probably related to the emergence of the out-of-plane fluctuations or a 3D order around B^*, accompanying the suggested change of the magnetic structure. Another possibility is that these two features around B^* are real thermodynamic transitions. If this is the case, there are three different transitions within a small field range around B^*. Their absence in

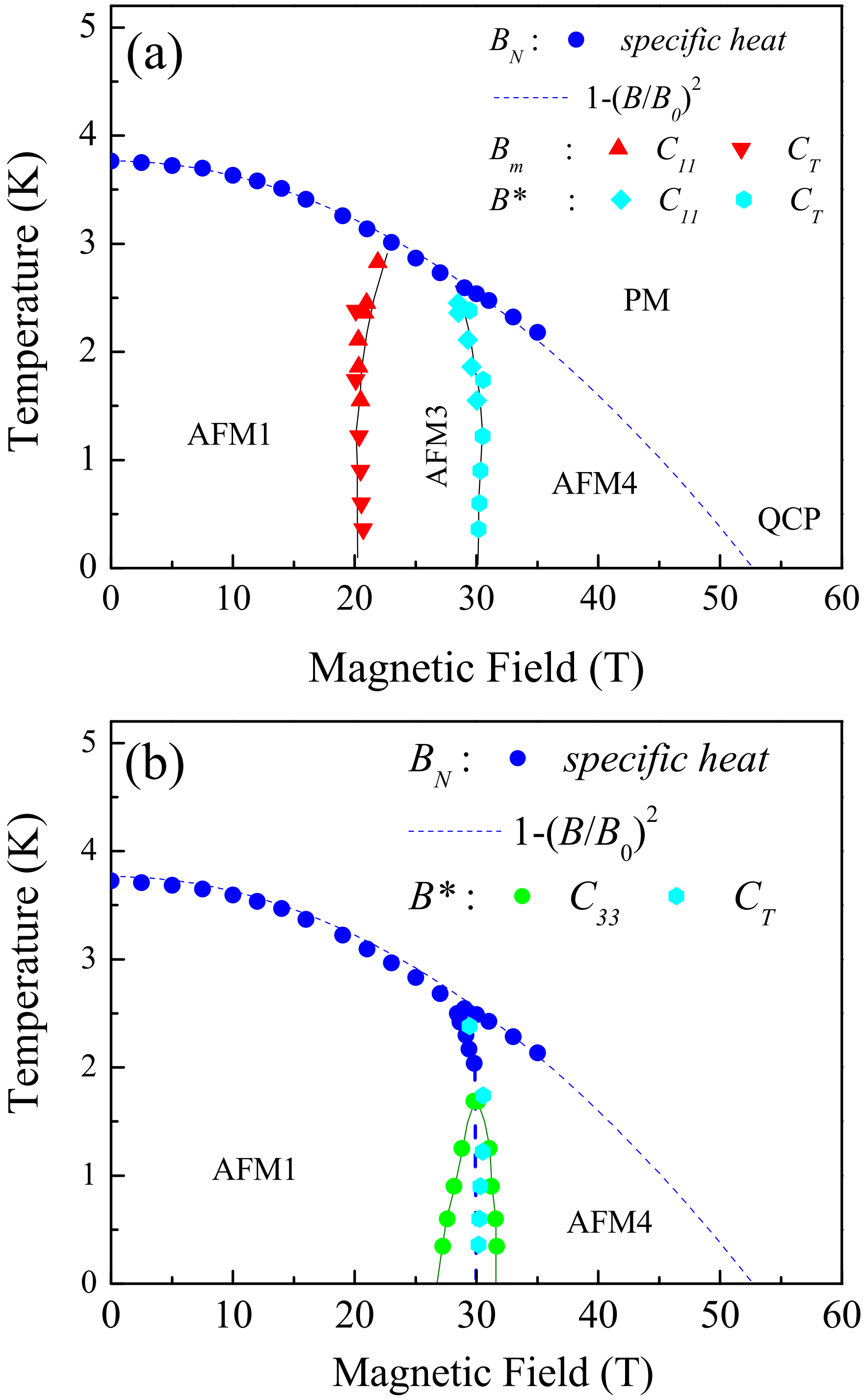

Figure 3.46: Temperature-magnetic field ($B-T$) phase diagram for CeRhIn$_5$ based on the field-induced transitions at B_m and B^* for (a) the symmetry breaking ultrasonic modes C_T and C_{11} and (b) for the symmetry preserving ultrasonic mode C_{33}. The blue closed circles corresponding to B_N with a $1-(B/B_0)^2$ fitting (dashed line) are from on our specific heat study. The solid and dashed lines separating the phases AFM1, AFM3, AFM4 are guides for the eye.

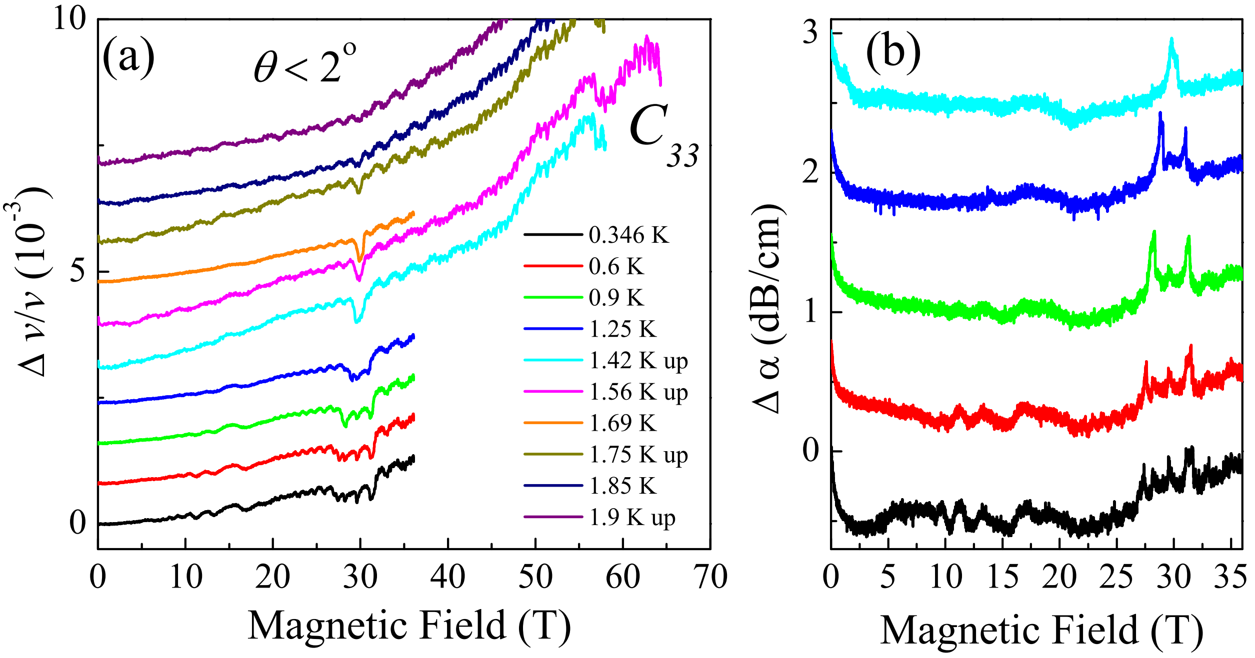

Figure 3.47: Temperature dependence of the field-dependence of the relative ultrasound velocity in CeRhIn$_5$ in the C_{33} mode (a) and the corresponding ultrasound attenuation (b) for a field applied at $\theta \sim 2^\circ$ from the c axis. Curves are shifted vertically for clarity.

the other modes can then be understood through a simple consideration. Since features in C_{33} correspond to the out-of-plane dynamics, C_{11}, C_T, C_{66} should not couple to them and, therefore, we do not observe them in these modes. However, in C_{44} mode, these features can possibly be detected at temperatures lower than 1.3 K. Measurements in the C_{44} mode at lower temperatures are required to confirm this hypothesis.

3.4.6 Angle-dependence of $\Delta v/v$ and ultrasound attenuation

Fig. 3.48 shows the field dependence of $\Delta v/v$ (a) and corresponding ultrasound attenuation (b) for various angles, θ, of the field from the c toward the a axis for the elastic constant C_T.

In the magnetoresistance study performed on FIB-fabricated devices of CeRhIn$_5$, the resistivity step observed at 30 T gradually increased for fields tilted away from the c axis up to $\theta = 20^\circ$, before decreasing again and fading away at $\theta \approx 60^\circ$ [43].

The angle-dependent behavior of the feature at B^* in ultrasound velocity is strikingly different in ultrasound velocity in a bulk single crystal of CeRhIn$_5$. As shown in Fig. 3.48, it is the strongest for field orientations closer to the c axis. Initially, for small inclinations of the field away from the c axis, it rapidly diminishes in size. For example, it diminishes by a factor of about 6 from $\theta \approx 2^\circ$ to $\theta = 5^\circ$ [Fig. 3.48(c)]. For still larger field angles from the c axis, it decreases in size rather slowly [Fig. 3.48(a)]. Similarly, the anomaly at B_m also decreases with increasing θ with an initial abrupt decrease by a factor of about 5 from $\theta \approx 2^\circ$ to $\theta = 5^\circ$. Therefore, the angle-dependence of the feature size at B^* is similar to that of the MMT transition at B_m. However, unlike the invariably sharp MMT transition, it gradually broadens with increasing θ until it is no longer distinguishable above $\theta = 30^\circ$. At $\theta = 40^\circ$, the transition at B^* is either not present up to 36 T or is dominated by the huge magnetoacoustic quantum oscillations corresponding to a small Fermi-surface pocket ϵ_2 [Fig. 3.48(d)]. This behavior of the B^* feature implies probably that it changes from a transition at low angles to a crossover at higher angles. This interpretation is also supported by our specific-heat measurements [139] very close to the c axis, which suggest B^* to be a real thermodynamic phase transition, and the magnetostriction measurements at $\theta \approx 17^\circ$ from the c axis, which suggest it to be a crossover [103].

Moving further, the feature at B^* slowly moves to higher fields with increasing θ [see fig.

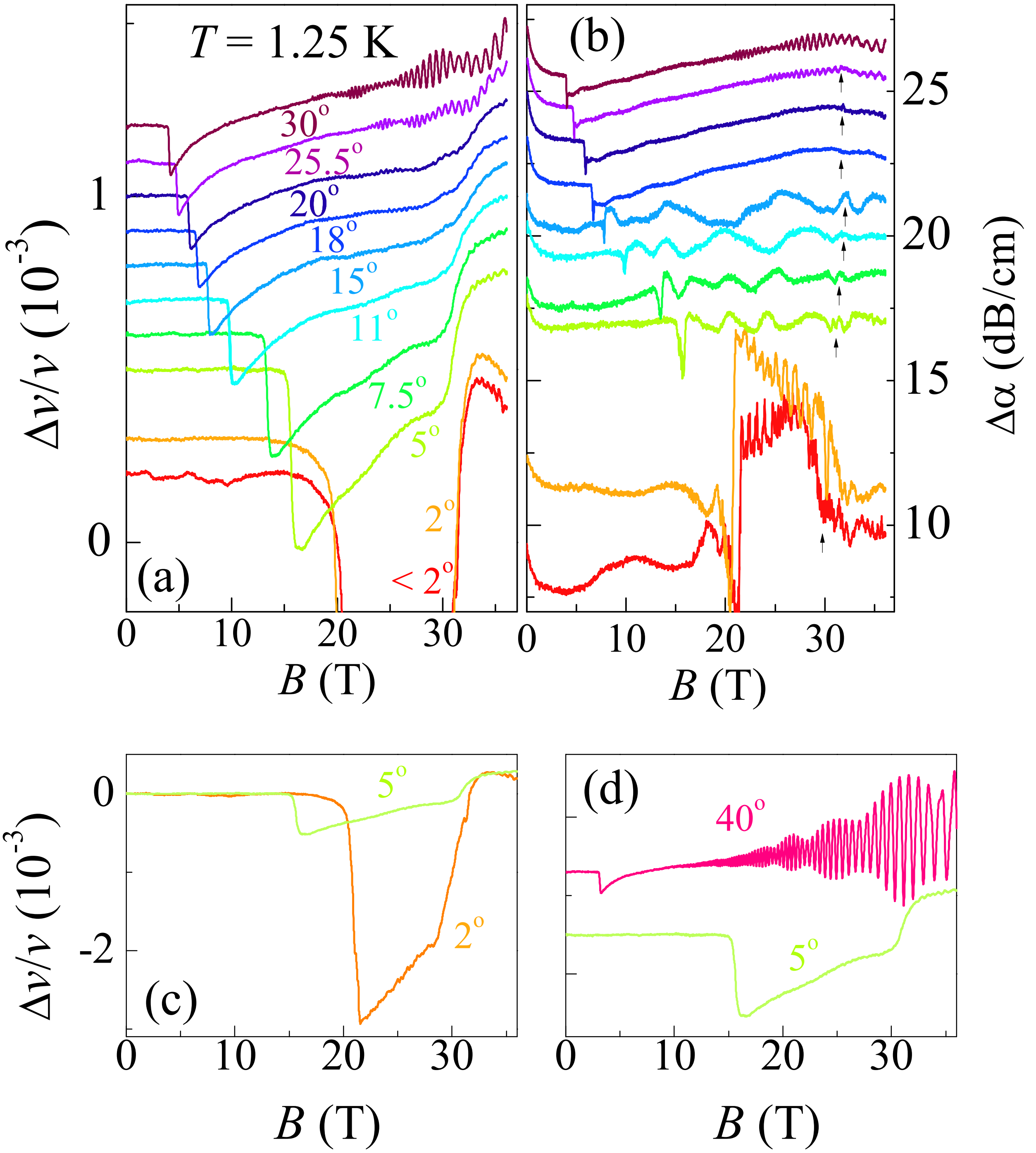

Figure 3.48: Angle-dependence of the field-dependent relative ultrasound velocity in CeRhIn$_5$ (a) and the corresponding ultrasound attenuation (b) for the ultrasonic mode C_T at various angles θ of the field from the c axis at $T \approx 1.25$ K. Bottom panels show a comparison of relative ultrasonic velocity at $\theta = 2°$ and $\theta = 5°$ (c) and $\theta = 5°$ and $\theta = 40°$ (d). Curves are shifted vertically for clarity.

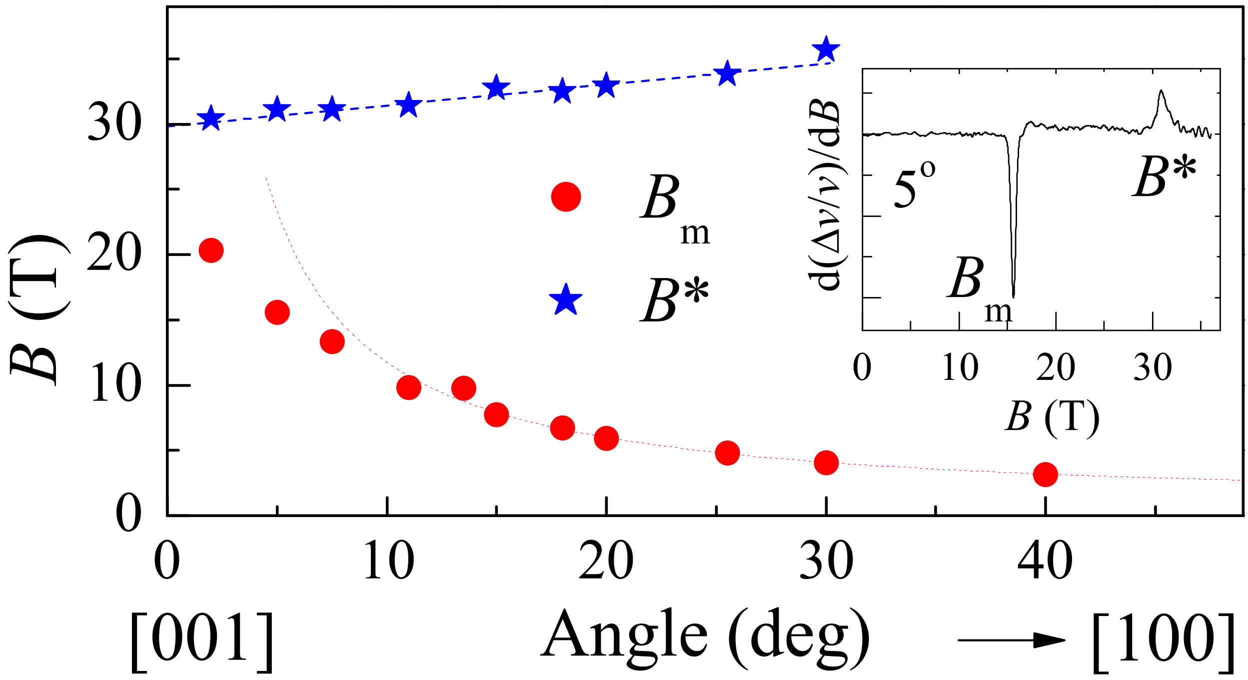

Figure 3.49: Angular variation of the field-induced transitions at B_m and B^* shown in Fig. 3.48. The position of each transition is determined from the peak in the first derivatives of $\Delta v/v$, as shown in the inset. The red dashed line is $2/cos(90-\theta)$ fit to B_m for $\theta \geq 10°$. The blue dashed line guide for the eye.

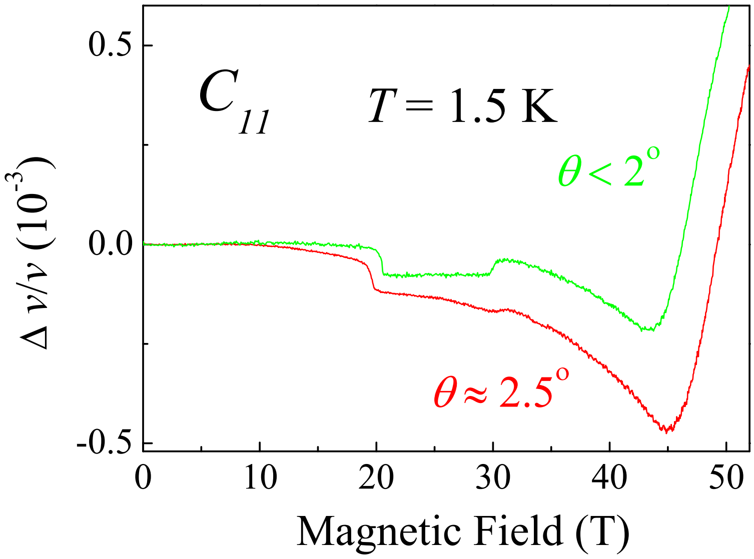

Figure 3.50: Field-dependence of the relative ultrasound velocity in the ultrasonic mode C_{11} in CeRhIn$_5$ for two different angles $\theta \approx 2.5°$ and $\theta \leq 2°$ from the c axis at $T \approx 1.5$ K.

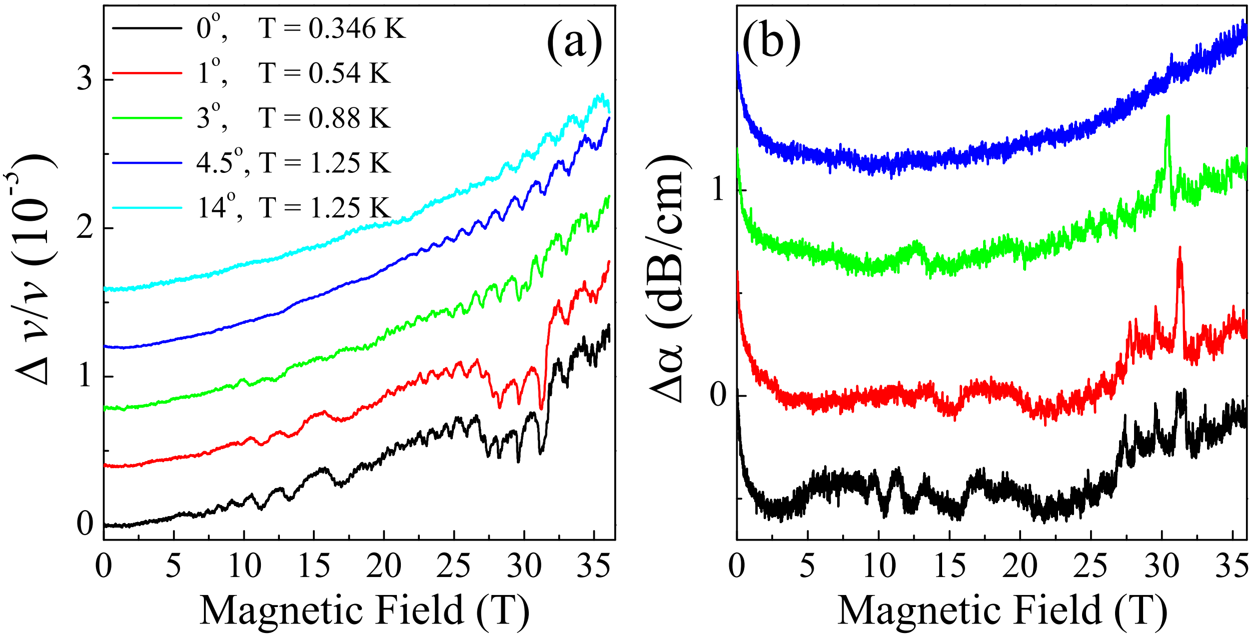

Figure 3.51: Field-dependence of the the relative ultrasound velocity in CeRhIn$_5$ (a) and the corresponding elastic attenuation (b) in the ultrasonic mode C_{33} for several orientations of the magnetic field in the vicinity of the c axis. Curves are shifted vertically for clarity.

3.49] in agreement with the previous reports [101, 43]. This suggests that unlike the metagenetic transition at B_m tuned by the in-plane field component, the suggested metamagnetic transition at B^* is not driven by the in-plane field component, but by an alternative route, such as a magnetic-structure modulation by an inter-layer exchange, a compression or an elongation. Such an inter-layer exchange is experimentally supported by the features observed around B^* in the C_{33} mode.

Similar to the C$_T$ mode, the feature at B^* and B_m become stronger for field orientations closer to the c axis in the C$_{11}$ mode [see Fig. 3.50]. In the C$_T$ mode, the feature at B^* is considerably bigger for fields applied very close to the c axis, i.e., $\theta \approx 2°$. Also, the behavior of $\Delta v/v$ above B^* for $\theta \approx 2°$ is different from that for $\theta > 2°$. For orientations close to 2°, $\Delta v/v$ shows a down-turn, which is absent for $\theta > 2°$.

Remarkably, it is only for these small orientations ($\theta \approx 2°$) that features around B^* exist in the C_{33} mode [see Fig. 3.51]. It is, therefore, evident that the transition at B^* and features around it are prominent only for fields very close to the c axis. This clearly establishes the importance of the out-of-plane field component for the B^* transition.

3.4.7 More about the transition at B^*

Based on the observations and results shown in the previous sections, we suggest the transition at B^* to be a metamagnetic transition corresponding to change of the magnetic structure from commensurate AFM3 to incommensurate AFM4, which restores all the symmetries broken at B_m. In all the modes, overall behavior of $\Delta v/v$ for fields below B_m and above B^* is similar. This indicates that the low-field and high-field phases are of the same nature implying similar incommensurate magnetic structures within AFM1 and AFM4. This behavior further supports a metamagnetic transition from commensurate to incommensurate at B* as a likely possibility.

The angle-dependence of the anomaly size at B^* is different from that observed in magnetoresistence, since decreasing the in-plane field component increases the size of the feature at least down to 2° from the c axis. The remarkable difference between angular-dependent behaviors of the B^* transition in bulk samples and microfabricated devices is likely to be due to the uniaxial strains usually present in the latter. CeRhIn$_5$ is known to be very sensitive to uniaxial strains. For instance, previously reported NQR measurements on bulk and powder samples of CeRhIn$_5$ suggest that even small strains (or stresses) change the zero-field magnetic structure from incommensurate to commensurate [144]. Additional measurements under uniaxial stress (or strain) at high magnetic fields on bulk samples are required to elucidate the role of the uniaxial stress in previous transport measurements on $\mathrm{CeRhIn_5}$ microstructures [101, 43].

It is already known that the change of magnetic structure at B_m is driven by an in-plane magnetic field component atleast down to 10° to 15° from the c axis, which is also beautifully captured by its initial $1/cos\theta$ dependence [see Fig. 3.49]. However, unlike the $1/cos\theta$ angular dependence of the B_m transition, the weak angular dependence of the B^* transition suggests that the change of AFM structure at B^* is not driven by the in-plane field component but a different mechanism.

Here, very naively, I will try to suggest such an alternative mechanism based on the features observed around B^* in the symmetry preserving C_{33} mode. In this mode, the asymmetric growing of the dome formed by these features around B^* with decreasing temperatures indicates the possibility of an exotic mechanism. One such possible mechanism is that at around $B^* = 30$ T, an inter-layer exchange between the $\mathrm{CeIn_3}$ layers occurs along the out-of-plane direction, which modulates the magnetic structure. The asymmetry of the dome can then be explained as a difference in the degree of the inter-layer exchange in two different AFM states, i.e., between the incommensurate AFM1 below 30 T and the incommensurate AFM4 phase above 30 T (for magnetic field very close to the c axis) or between the commensurate AFM3 below 30 T and the incommensurate AFM4 phase above 30 T (for magnetic field slightly tilted from the c axis, say 2°). Then within the dome region, the commensurate vector $(1/2, 1/2, 1/4)$ gradually changes to an incommensurate vector (1/2,1/2,$\delta(B)$) as a function of field, where $\delta(B)$ changes from 0.25 to probably about, 0.21. Nonetheless, the true origin of the features around B^* and the driving mechanism of the suggested change of the magnetic structure remain elusive.

It must be noted that so far magnetoresistence, magnetization, torque failed to show any detectable feature in the longitudinal or c direction. However, magnetostriction revealed an anomaly along the c direction, in addition to the a direction, for a field applied at $\theta \approx 17°$, but its presence was understood in terms of the Poisson's ratio.

3.4.8 Hysteresis in $\Delta v/v$ at high fields

Generally, in case of first order transitions, a hysteresis is observed in the measured quantity as a function of temperature or magnetic field. The first-order transition at B_m indeed shows a hysteresis between up and down field-sweeps [see Fig. 3.52(a),(b)]. This is consistent with the previous report [105]. There is a small but clear hysteresis at B^* in the C_{44} and C_{11} modes [see Fig. 3.53(a),(b)] suggesting that B^* is also likely a first-order transition. Further, in the C_T mode, there are hysteretic features both below and above B^*, as shown in Fig. 3.52. The inset in Fig. 3.52(a) shows a zoomed-in view of the hysteresis above B^*. The features marked by $B_{N(u)}$ in the up field-sweep and $B_{N(d)}$ in the down field-sweep seems to correspond to the antiferromagnetic transition. The average of these two fields, $(B_{N(u)}+B_{N(d)})/2$, fits well nicely to the AFM phase boundary in the temperature-field phase diagram (see violet closed circles in Fig. 3.54). This hysteresis at the AFM transition is surprising as the antiferromagnetic phase transition is a second-order. The λ-like shape of the specific-heat anomaly at the AFM transition confirms its second-order nature. Therefore, it is not clear if this hysteresis at the AFM transition can be explained by a field-induced change of the AFM structure. One plausible explanation is that there might be some very slow relaxation timescales involved in the high field phase. Or it might be simply an artifact of the pulsed-field measurements.

The temperature-dependence of the hysteresis observed at high fields is shown in Fig. 3.52(c) for $\theta = 2°$, and (d) for $\theta = 15°$ in the C_T mode. A similar temperature dependence is shown in Fig. 3.53(a) and (b) for the C_{11} and C_{44} modes, respectively. In Fig. 3.53, the field, at which the hysteresis closes (indicated by black arrows and corresponds to B_p in Fig. 3.43), corresponds to the transition to the polarized paramagnetic state (PPM), suggested previously [105], and fits well the PPM boundary in the phase diagram shown in Fig. 3.54.

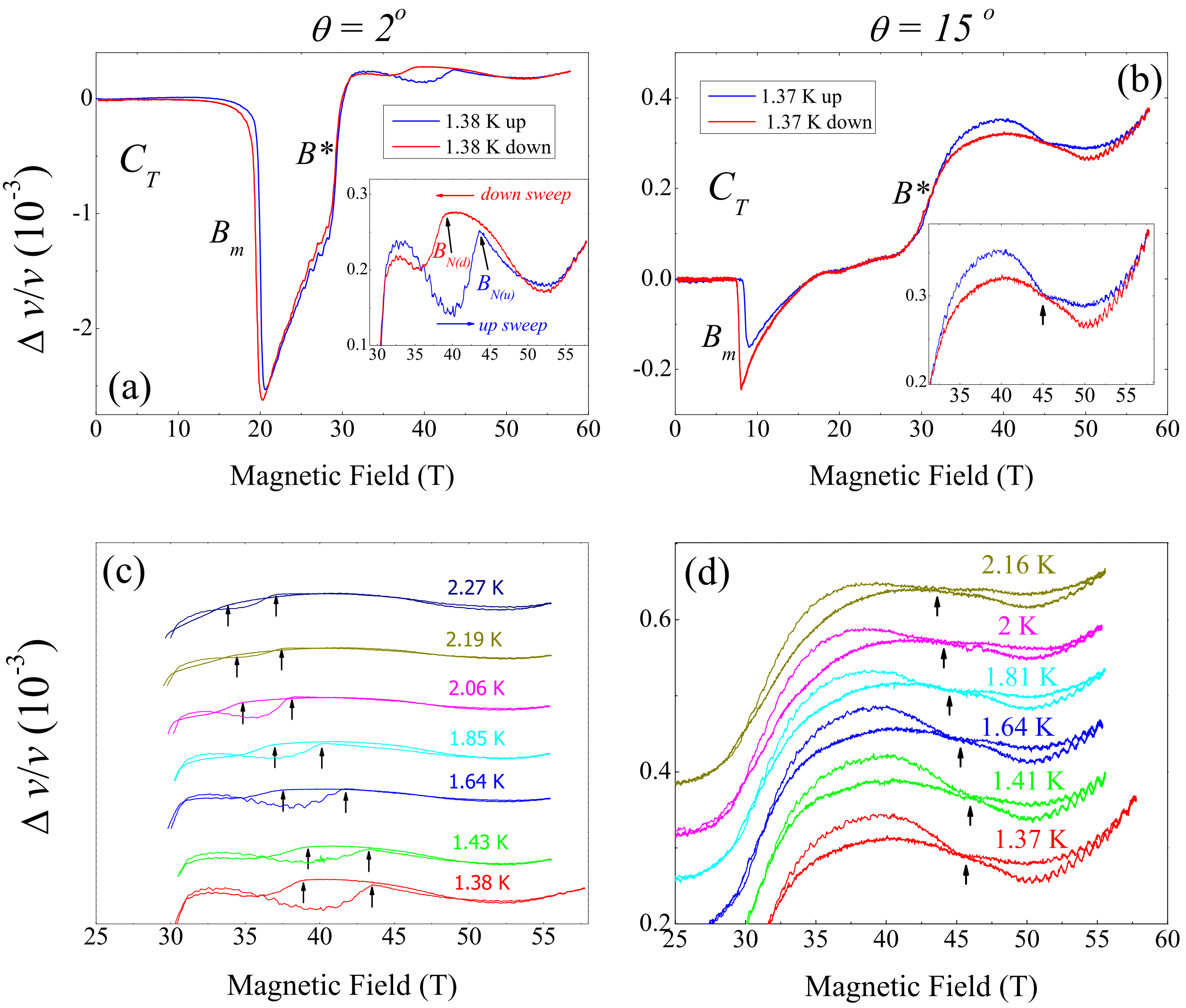

Figure 3.52: Field-dependence of the relative ultrasound velocity for the ultrasonic mode C_T corresponding to the up (blue) and down (red) sweeps of the magnetic field pulse for (a) $\theta = 2°$ and (b) $\theta = 15°$. Insets shows a zoomed-in view of the hysteresis observed at high fields. Temperature-dependence of hysteresis observed at high fields. Arrows indicates the positions of $B_{N(d)}$ and $B_{N(u)}$ for $\theta = 2°$ (c) and B_p for $\theta = 15°$ (d). Curves are shifted vertically for clarity.

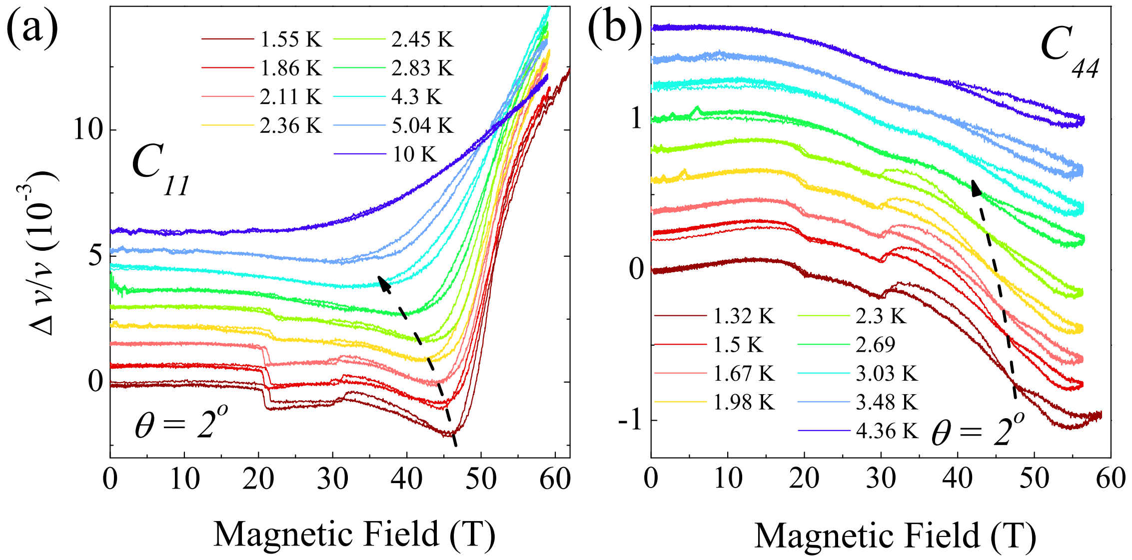

Figure 3.53: Temperature-dependence of the field-dependent relative ultrasound velocity for the up and down field sweeps of the magnetic field pulse in the ultrasonic modes (a) C_{11} and (b) C_{44}. The arrows indicate the field, at which the hysteresis between the up and down field sweeps closes and correspond to B_p. Curves are shifted vertically for clarity.

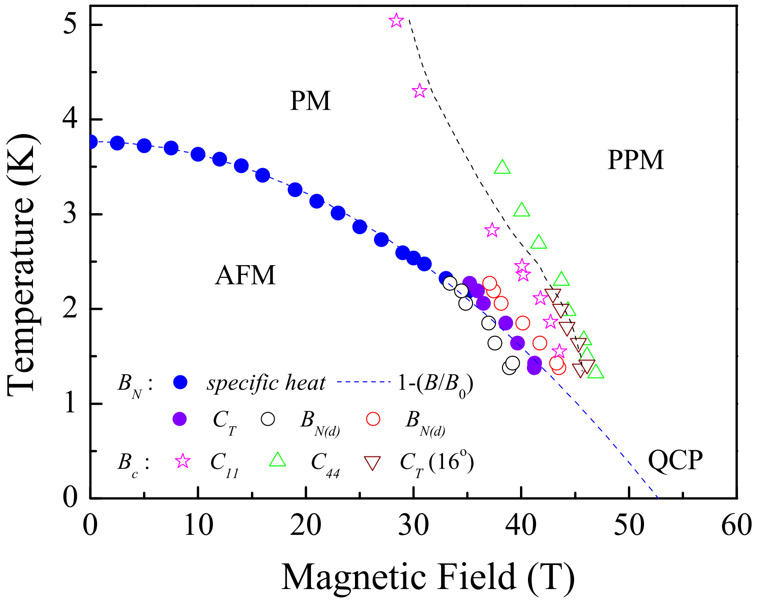

Figure 3.54: Temperature-magnetic field (($T - B$)) phase diagram of CeRhIn$_5$ based on the anomalies at B_p, $B_{N(u)}$ and $B_{N(d)}$ observed in the ultrasound modes C_{11}, C_{44} and C_T. The blue closed circles corresponding to T_N with a $1-(B/B_0)^2$ fitting (dashed line) are from our specific heat data. The dashed lines separating the PM and PPM phases are guides for the eye.

3.4.9 Magnetoacoustic quantum oscillations

We observed clear magnetoacoustic quantum oscillations (MAQOs) in the ultrasound velocity in all the modes measured both in static and pulsed fields. While the oscillations are stronger in certain modes, they are weak in others. The oscillations are the strongest in the C_{33} mode. For example, in the C_{33} mode, huge MAQOs are directly visible in the ultrasound velocity measured at the ^{3}He base temperature (T = 0.346 K), as shown in Fig. 3.55. The inset shows quantum oscillations corresponding to large Fermi-surface orbits obtained by subtracting a smooth background from the raw $\Delta v/v$ signal, essentially comprising of low frequencies $\leq$ 1 kT.

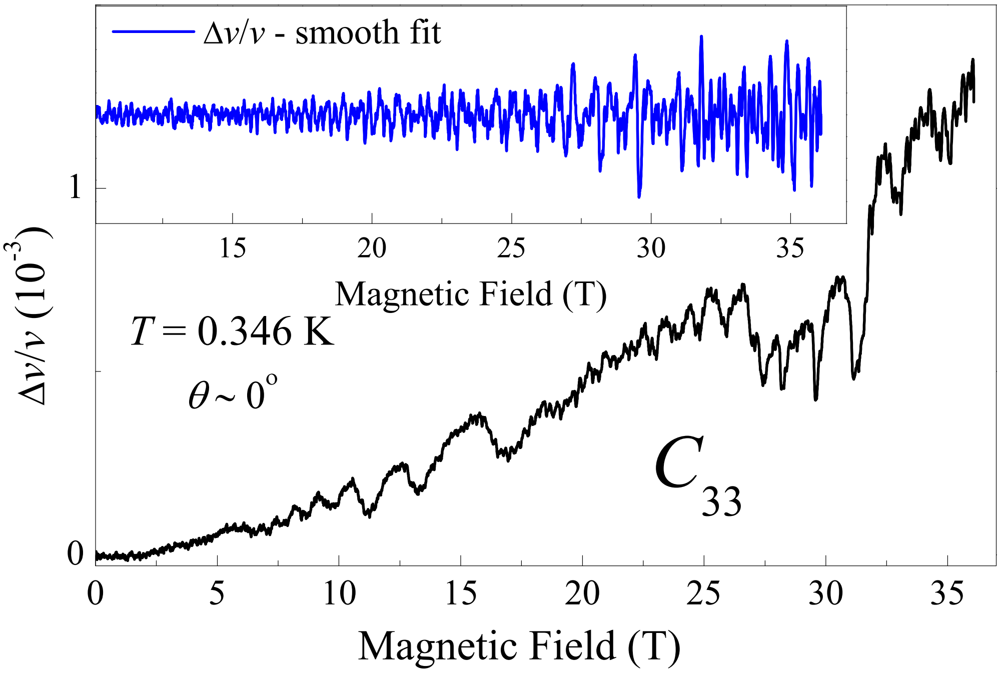

Figure 3.55: Magnetoacoustic quantum oscillations in CeRhIn$_5$ in relative ultrasound velocity in the C_{33} mode. The inset shows the high-frequency oscillations obtained by subtracting a smooth background.

In agreement with the results of the previous high-field ultrasound study on CeRhIn$_5$ [105], we observed strong low-frequency magnetoacoustic quantum oscillations in the C_T mode between B_m and B^*, as shown in the inset of Fig. 3.56. These oscillations with the frequency denoted A ($F_A \simeq 0.6$ kT) disappear above B^*, as shown in Fig. 3.56, also in agreement with the previous study. This experimental result was interpreted as an evidence of a possible Fermi-surface reconstruction at B^* in the previous work [105]. However, in that work, quantum oscillations were observed in the C_T mode only.

In our measurements, the magnetoacoustic quantum oscillations from other modes clearly reveal this frequency. For example, in the C_{33} mode, shown in Fig. 3.55, where the MAQO are the strongest, this frequency is present both below and above B^*. The corresponding FFT spectra for fields below (6-20 T) and above B^* (31.8 - 36 T) are shown in Fig. 3.57(a). The oscillations with the frequency A are clearly present both below [the inset of Fig. 3.57(a)] and above B^* [Fig. 3.57(a)].

In addition to the frequency A, our static-field data in the C_{33} mode reveals most of the previously observed dHvA frequencies in CeRhIn$_5$, such as $\alpha_{2,3}$, α_1 and β_2. Further, quantum oscillations below 20 T reveal a previously undetected small-Fermi surface orbit of the frequency S_1 = 70 T [inset of Fig. 3.57(a)] with the effective mass m^* = 1.8 m$_0$ [Fig. 3.57(b)]. This orbit seems to disappear above 20 T, coincidentally close to the IC-C transition at B_m observed in other modes for a field orientation $\theta \approx 2°$. This small change of the Fermi surface is possibly associated with the change of the magnetic structure.

Finally, in Figs. 3.58 (a) and (b), we show the field dependence of the MAQOs frequencies in the C_{33} mode at the ^{3}He base temperature for two different orientations $\theta \simeq 0°$ and $\theta \simeq 4.5°$

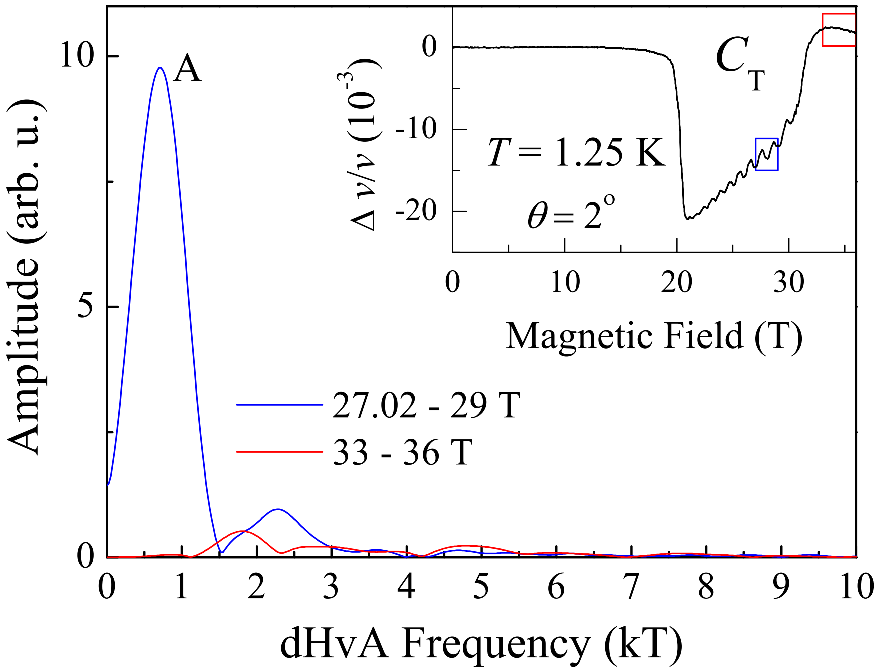

Figure 3.56: Fast Fourier transform (FFT) spectra of the magnetoacoustic quantum oscillations in the ultrasonic mode C_T (shown in the inset) obtained over the field ranges below and above B^*. A non-oscillating background was subtracted prior to performing the FFTs. The FFTs were perform over equivalent $1/B$ ranges indicated by rectangles in the inset.

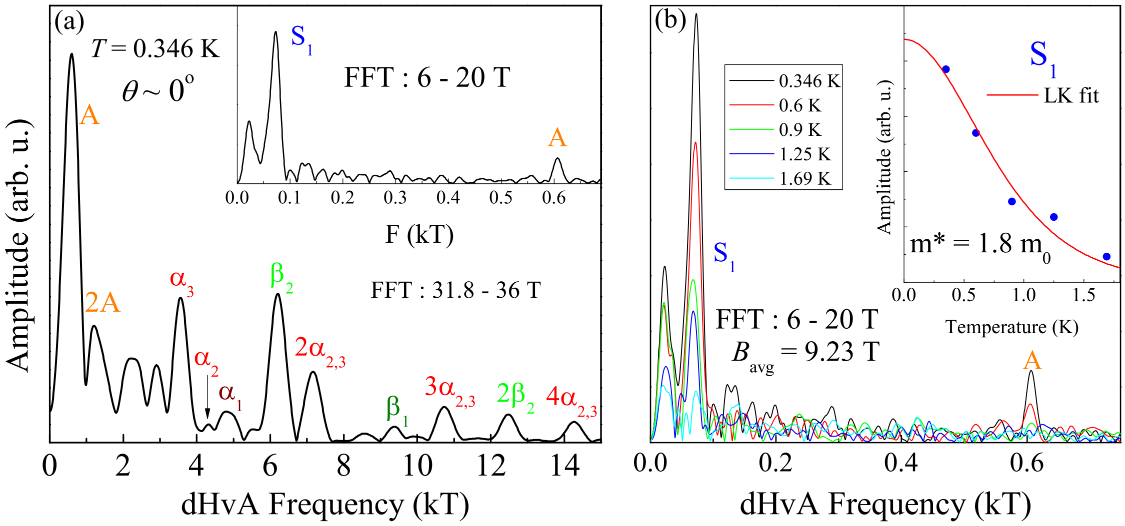

Figure 3.57: (a) FFT of MAQO shown in Fig. 3.55 for magnetic fields above B^*. The inset shows the FFT at fields below 20 T. (b) Temperature-dependence of the MAQO amplitudes from the inset of (a). The inset shows a LK-fit of the temperature-dependence of the amplitudes of the S_1 orbit.

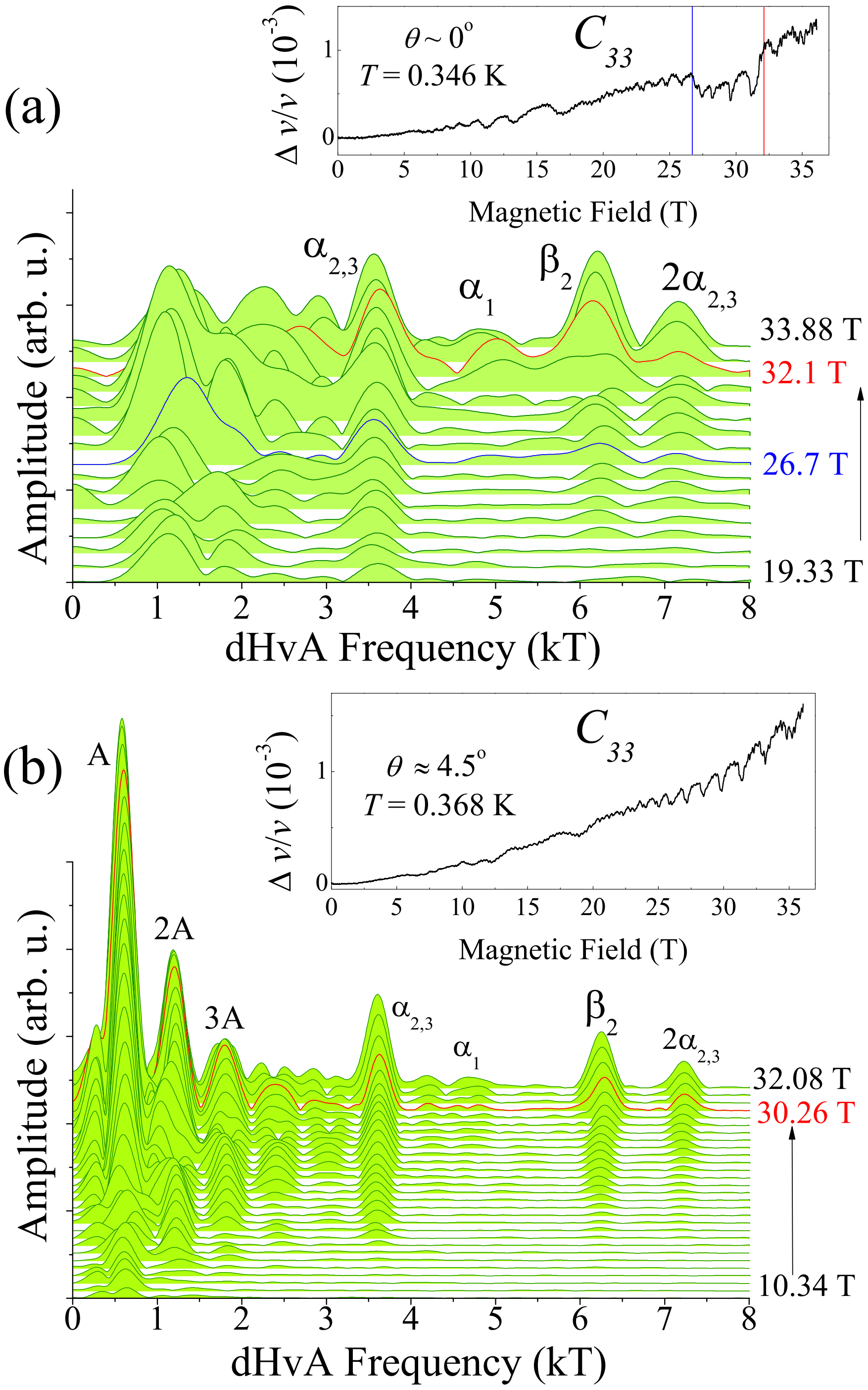

Figure 3.58: Field dependence of the MAQOs FFT spectra in CeRhIn$_5$ obtained in the longitudinal elastic constant C_{33} at $T \approx 0.35$ K for (a) $\theta = 0^\circ$ (b) $\theta = 4.5^\circ$. The insets show the corresponding MAQOs in the ultrasonic velocity. The FFT spectra are obtained over the same $1/B$ ranges. In the panel (a), for the top curve, the field range is from $B_{min} = 31.8$ T to $B_{max} = 36$ T ($B_{avg} = 33.88$ T). For each successive curve, B_{max} is decreased by 1 T down to 20 T. In the panel (b), for the bottom curve, the range is from $B_{min} = 10$ T to $B_{max} = 10.71$ T ($B_{avg} = 10.34$ T). For each successive curve, B_{min} is increased by 1 T up to 20 T, and by 0.5 T from there on. Curves are vertically shifted for clarity.

of field from the c axis. To study the field evolution of the Fermi-surface across the two features observed in the C_{33} mode at 26.7 T and 32 T for $\theta \simeq 0°$, the field range is divided into three intervals (1) above 32.1 T, (2) between 26.7 T and 32.1 T, (3) below 26.7 T. The red and blue lines separate these field intervals in Fig. 3.58 (a) as well as in the inset. Since the FFTs are performed over equal $1/B$ intervals, the frequency A cannot be resolved due to the very small field interval chosen for the FFTs. However, when a larger interval (equal to the one used in the dHvA analysis) is chosen to perform the FFTs, such as done for $\theta \simeq 4.5°$ [see Fig. 3.58(b)], the frequency A as well as its harmonics are clearly resolved. In both Figs. 3.58(a) and (b), the orbits $\alpha_{2,3}$ and β_2 are present in all the three intervals, while the spectral weight around the α_1 orbit develops progressively only at high fields. The α_1 frequency is a fundamental frequency corresponding to the localized f electrons in CeRhIn$_5$. Its presence at high fields in not an indication of an abrupt Fermi-surface reconstruction, but inherent to various limitations of this particular experiment, such as temperature and technique. For example, in our magnetization measurements [see Fig. 3.61(b)], the α_1 orbit is clearly seen to emerge out of the noise level at fields much lower than 30 T. Similar is the case for our dHvA measurements. Therefore, the MAQOs in the elastic constants C_T and C_{33} are in agreement with our dHvA results, and rule out a field-induced Fermi-surface reconstruction or an itineracy of the f electrons at B^*. However, some of the dHvA frequencies observed at high fields in our study are not observed here in the ultrasound velocity.

3.4.10 Conclusions

In summary, we performed high-field ultrasound velocity measurements on bulk single crystals of CeRhIn$_5$. For a magnetic field slightly tilted from the c axis, we observed distinct anomalies at both $B_m \simeq 20$ T and $B^* \simeq 30$ T at low temperatures in all the symmetry breaking modes, i.e., C_{11}, C_{44}, C_{66}, and C_T. In all these modes, the anomalies are of similar shape, but of the opposite sign. Both anomalies are absent in the symmetry preserving C_{33} mode. Furthermore, our temperature-dependent measurements reveal that both anomalies exist within the AFM state only. Given that the transition at B_m corresponds to a change of the magnetic structure from incommensurate below B_m to commensurate above B_m, we argue that the transition at B^* is of the same origin, i.e., from the commensurate phase below B^* to a new incommensurate phase above it. This makes CeRhIn$_5$ one of the rare compounds, in which the application of a high magnetic field induces a commensurate to incommensurate transition. High-field inelastic neutron diffraction measurements are desirable to definitely confirm our hypothesis. In the C_{33} mode, instead of the B^* transition, features around B^* are observed for a magnetic field applied very close to the c axis suggesting an exotic mechanism at B^*, such as an interlayer exchange, compression or elongation. Additional measurements are needed to understand their true origin.

When a magnetic field is tilted further away from the c axis, the anomaly at B^* slowly moves to higher fields, and progressively becomes smaller and broader. This behavior is in contrast with what was observed in the previous transport measurements on microfabricated samples, in which a sharp resistivity jump at B^* was observed to increase up to about 20° following by a decrease up to 60°, where it faded away. Different behaviors observed here on bulk samples and on the FIB-fabricated microstructures [101, 43] are likely to be due to uniaxial strains or stresses inevitably present in the latter [143]. CeRhIn$_5$ seems to be very sensitive to uniaxial strains. For instance, previously reported NQR measurements on bulk and powder samples of CeRhIn$_5$ suggest that even small strains (or stresses) change the zero-field magnetic structure from incommensurate to commensurate [144]. Additional measurements under uniaxial stress (or strain) at high magnetic fields on bulk samples are required to elucidate the role of the uniaxial stress in previous transport measurements on CeRhIn$_5$ microstructures [101, 43].

Parts of these results are published in [145].

3.5 Magnetization in high magnetic fields

Based on our specific heat and ultrasound results, we suggest that the transition at B^* corresponds to a change of the magnetic structure from the incommensurate AFM1 to another incommensurate AFM4 for fields along the c axis, and from the commensurate AFM3 to the incommensurate AFM4 for fields tilted by 2° or more from the c axis. So far, no anomaly was detected at B^* in either magnetic torque or magnetization. Similarly, no anomaly was detected in specific heat, before our AC calorimetric specific heat measurement shown in the previous section.

3.5.1 Longitudinal magnetization

The previous magnetization measurements were performed in pulsed magnetic fields at $T = 1.3$ K, in which no detectable anomaly was observed at B^* [71]. This might be due to several reasons. First of all, a first-order transition can be easily missed in pulsed-field measurements. Furthermore, there is a good chance that the anomaly was not observed because of eddy-currents heating. We observed the anomaly up to $T \approx 1.9$ K in the C_{33} ultrasound mode which probes the longitudinal direction. Another possible reason for the absence of an anomaly at B^* is field misalignment. Indeed, in the C_{33} ultrasound mode, the anomaly disappears already at $\theta = 4.5°$, as discussed in previous section [see Fig. 3.51].

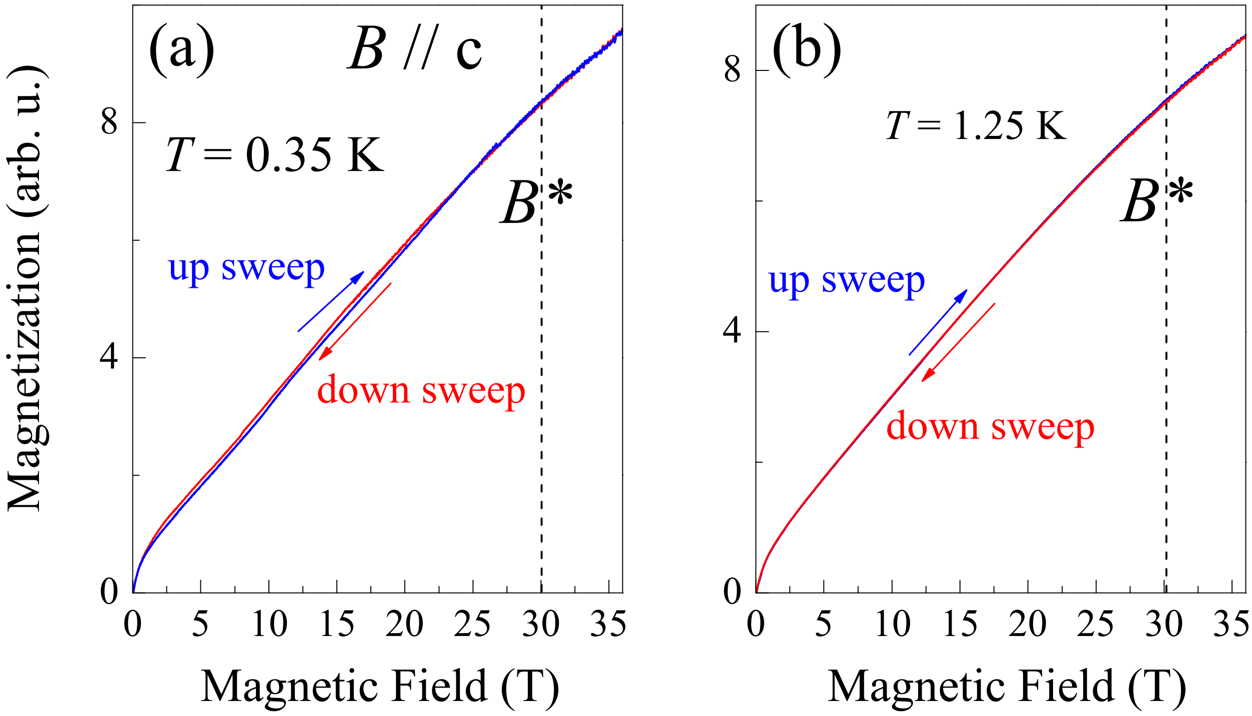

Figure 3.59: Longitudinal magnetization in CeRhIn$_5$ for field applied along the c axis at (a) T = 0.35 K and (b) 1.25 K. The blue (red) arrows indicate the up (down) field sweep curves.

Therefore, we performed magnetization measurements in a single crystal of CeRhIn$_5$ for field applied along the c axis in static magnetic fields up to 36 T in a ^{3}He cryostat. We used a technique based on the Faraday balance principle, discussed in chapter 2. This technique measures the longitudinal magnetization i.e. component of magnetization along the field direction (here parallel to the c axis).

Fig. 3.59 shows the longitudinal magnetization in CeRhIn$_5$ in magnetic fields up to 36 T along the c axis at $T = 0.35$ K (a) and $T = 1.25$ K (b). In accordance with the previous report [71], we do not observe any feature at B^* or at B_m. The most crucial result of this measurement is the absence of a detectable anomaly at or close to $B^* = 30$ T down to the lowest temperature measured i.e. $T = 0.35$ K. However, in accordance with the previous report [71], there seems to be a small change of slope of the magnetization across 30 T.

3.5.2 Perpendicular component of magnetization

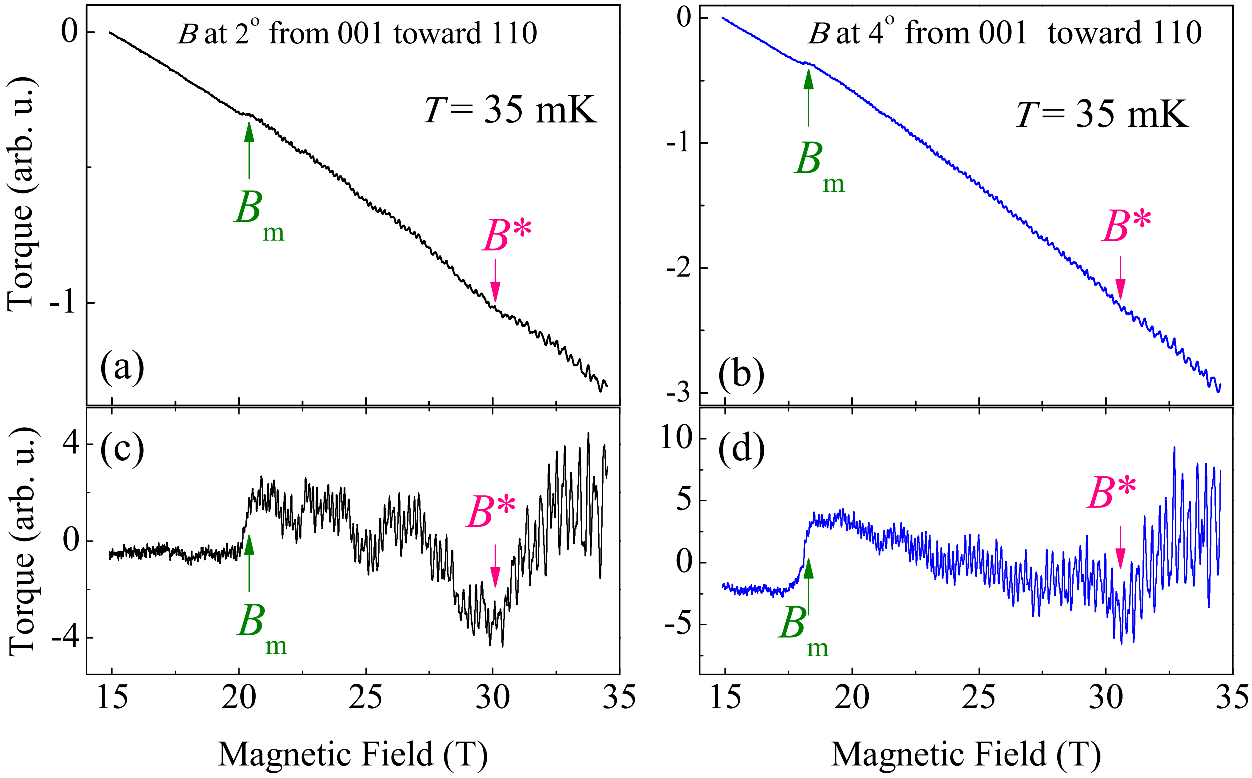

Figure 3.60: Possible signature of the transition at B^* in magnetic torque for magnetic field applied (a) at $\theta = 2°$ and (b) at $\theta = 4°$ from the c axis toward the ab direction. (c) and (d) shows the remaining torque signal after subtracting a second order polynomial from the magnetic torque in (a) and (b), respectively.

Since no detectable feature is present in the longitudinal magnetization, we go back to our magnetic torque data to see if a anomaly at B^* is preset in the component of magnetization perpendicular to the magnetic field. Figure 3.60 shows the magnetic torque in CeRhIn$_5$ for field applied at $\theta = 2°$ (a) and $\theta = 2°$ (b) from the c axis towards the [110] direction. In the raw torque signal, an anomaly corresponding to $B_m = 20.25$ T for $\theta = 2°$ and $B_m = 18.1$ T for $\theta = 4°$ is clearly observed, indicated by the green arrows in Fig. 3.60. For both the orientations of the field, a rather subtle feature is observed at $B \approx 30$ T. This feature becomes apparent on subtracting a quadratic polynomial from the magnetic torque, as shown in Fig. 3.60 (c) and (d). The pink arrows indicate the feature at $B \approx 30$ T.

In accordance with the angular-dependant behaviour of B^* in our ultrasound measurement, the feature at $B \approx 30$ is stronger at $\theta = 2°$ than that at $\theta = 4°$. Therefore, we suggest, this feature, probably corresponds to the suggested metamagnetic transition at B^*. The detection of a feature at B^*, although subtle, in magnetic torque, strongly supports our hypothesis of a change of the magnetic structure from commensurate to incommensurate. At angles higher than 4°, the quantum oscillations are much stronger and the feature becomes much less noticeable. In principle, we can measure torque at angles smaller than $\theta = 2°$, where this subtle feature should be more pronounced, but the signal becomes nosier at smaller angles as magnetic torque vanishes closer to the crystallographic axes. Therefore, performing alternate magnetic measurements that work for field applied along or close to the crystallographic axes, such AC susceptibly might be interesting.

3.5.3 Quantum oscillations in longitudinal magnetization

We observe clear quantum oscillations in the longitudinal magnetization, as shown in Fig. 3.61(a), obtained by subtracting a smooth non-oscillatory background from the magnetization curves in

Fig. 3.59. FFTs of the oscillation performed over equal $1/B$ intervals reveals the evolution of the dHvA frequencies with magnetic fields, as shown in Fig. 3.61(b).

Here, we observe many of the frequencies detected in our dHvA study, such as A, $\alpha_{2,3}$, α_1, and β_2. The evolution of frequencies with magnetic field clearly indicates that there is no discontinuous shift or emergence of new orbits at 30 T, thus ruling out a field-induced Fermi surface reconstruction at B^*, consistent with our dHvA study.

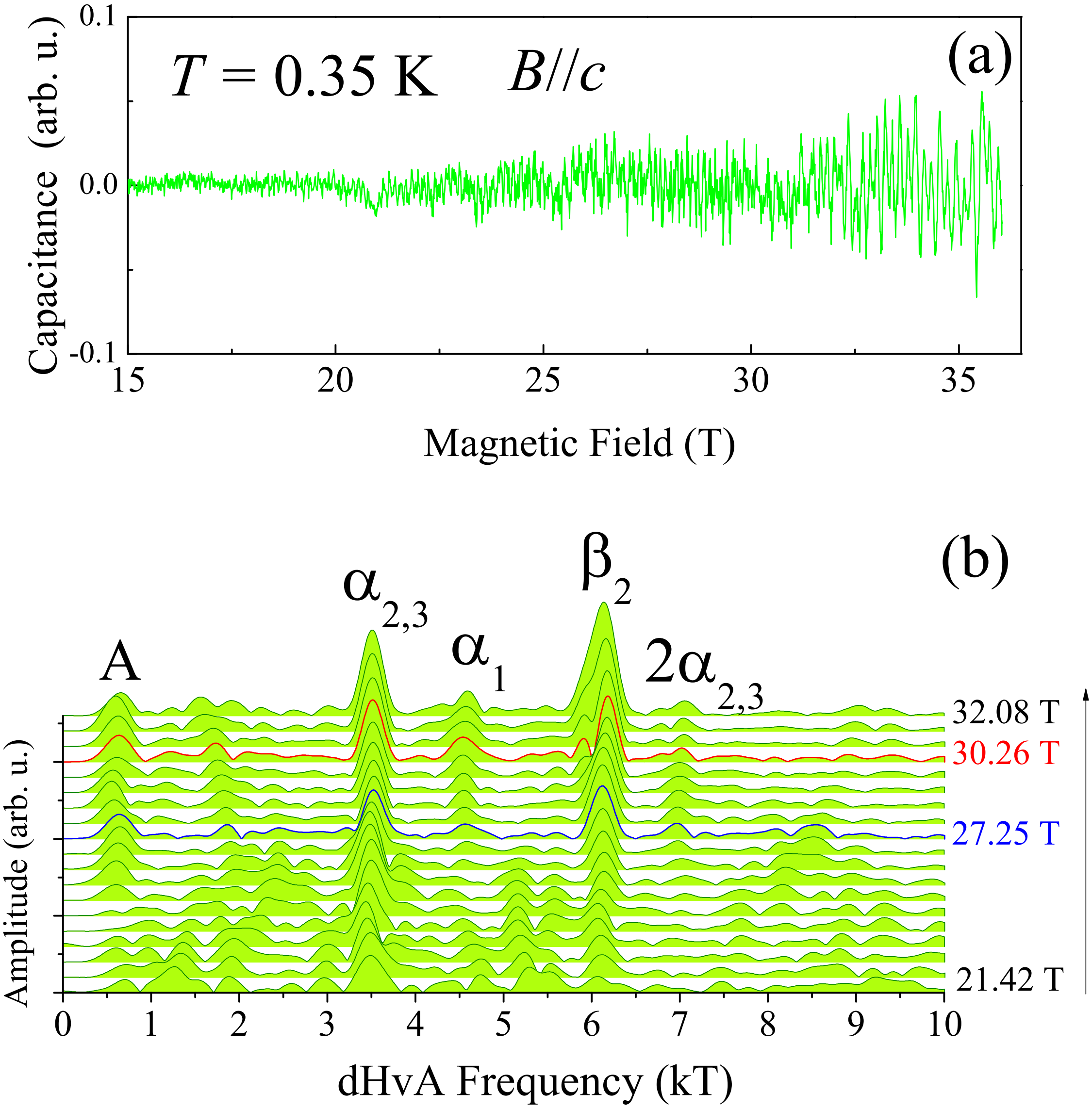

Figure 3.61: (a) Quantum oscillations in CeRhIn$_5$ observed in longitudinal magnetization at 0.35 K for field applied along the c axis. The quantum oscillations are obtained by subtracting a non-oscillatory smooth background from longitudinal magnetization shown in Fig. 3.61. (b) Field evolution of dHvA frequencies. All the FFTs are obtained over the same $\Delta(1/B)$ interval. The top curve corresponds to B_{min} =29 T, B_{max} =35.9 T and B_{avg} = 32.08 T. Each successive curves B_{min} is decreased in steps of 0.5 T and corresponding B_{max} is adjusted to keep $\Delta(1/B)$ constant. For the bottom most curve B_{min} = 20 T, B_{max} = 23.06 T and B_{max} = 21.42 T.

3.5.4 Conclusions

In conclusion, we performed magnetization measurements in CeRhIn$_5$ in high static magnetic fields. The component of magnetization parallel to field, i.e., longitudinal magnetization, does not show any detectable anomaly at B^* down to T = 350 mK. The component of magnetization perpendicular to magnetic field, measured through magnetic torque down to T = 35 mK, shows a distinct anomaly at B_m and a subtle anomaly at $B^* \approx 30$ T. This subtle anomaly around B^* supports our interpretation of B^* as a change of magnetic structure. Additional magnetic measurements, such as AC susceptibility can be helpful in detecting a more pronounced presence of B^* in magnetic properties of $\mathrm{CeRhIn_5}$.

Chapter 4

CeCoIn$_5$

4.1 Introduction

CeCoIn$_5$ is an extremely heavy fermion material having an enhanced Sommerfield coefficient $\gamma \sim 1$ J/K^{2}mol [146]. At ambient pressure and zero magnetic field, CeCoIn$_5$ exhibits a non-Fermi-liquid behaviour at low temperatures in the normal state just before becoming a superconductor below a critical temperature $T_c = 2.3$ K [146], signaled by a huge jump in specific heat [see Fig. 4.1]. The unconventional Cooper pairing in CeCoIn$_5$ is considered to be mediated by antiferromagnetic quantum fluctuations [146, 147, 148, 149].

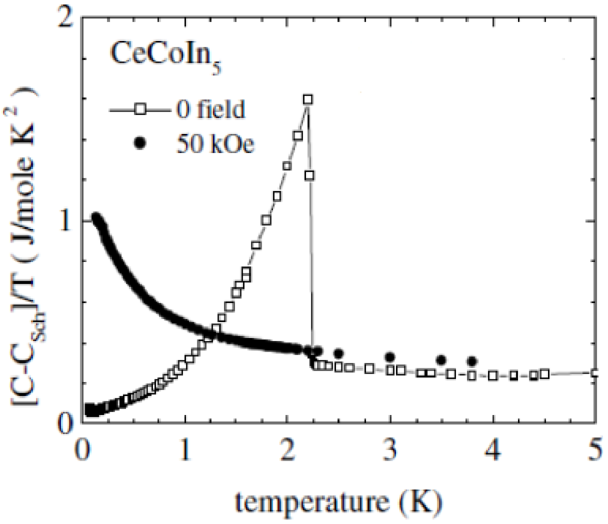

Figure 4.1: A strong signature of the superconducting transition in CeCoIn$_5$ at 2.3 K in the specific heat. Adapted from Ref [146].

The SC state is entirely suppressed by a pressure of about 3.6 GPa, above which a Fermi-liquid state was observed. The presence of an antiferromagnetic QCP at a negative pressure in CeCoIn$_5$ was proposed [150] in an analogy to the Cuprates, in which at negative chemical pressures, close to the suppression of the AFM state, several novel phases, such as the pseudogap phase, non-Fermi liquid, and the SC state were observed [151, 152]. The temperature-pressure phase diagram for CeCoIn$_5$ is shown in Fig. 4.2.

In an applied magnetic field, the superconducting state in CeCoIn$_5$ is suppressed at the upper critical field $H_{c2} = 5$ T along the c axis and $H_{c2} = 12$ T along the a axis. The temperature-field phase diagram for the two orthogonal orientations of fields, i.e, along [110] and [001] is shown in Fig. 4.3(a) and (b), respectively.

At $T \leq 1$ K, the superconducting phase transition near the $H_{c2} = 5$ T becomes first order [147]. Furthermore, a new phase, different from the main d-wave superconducting phase, appears close to H$_{c2}$ at low temperatures [155]. This new phase was interpreted as a Q-phase with a field-induced

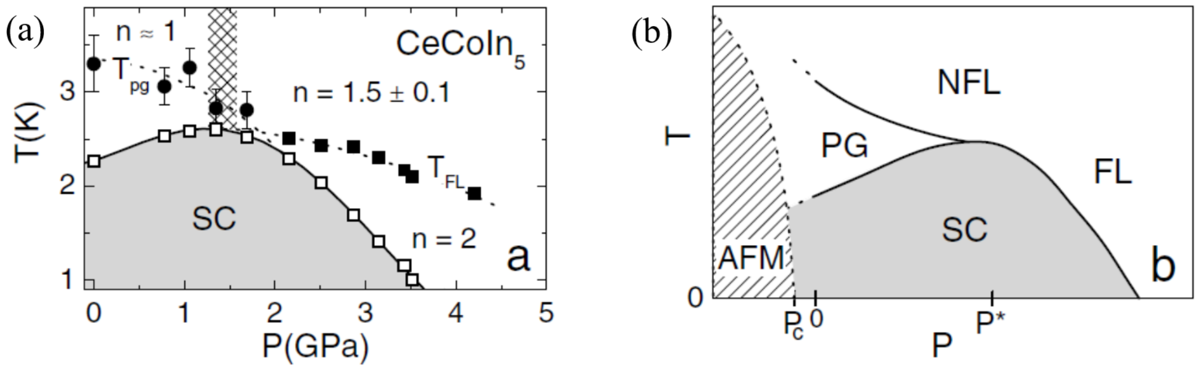

Figure 4.2: (a) Temperature-pressure phase diagram of CeCoIn$_5$. (b) Schematic T-P phase diagram of CeCoIn$_5$ in an analogy with Cuprates. Adapted from Ref. [150].

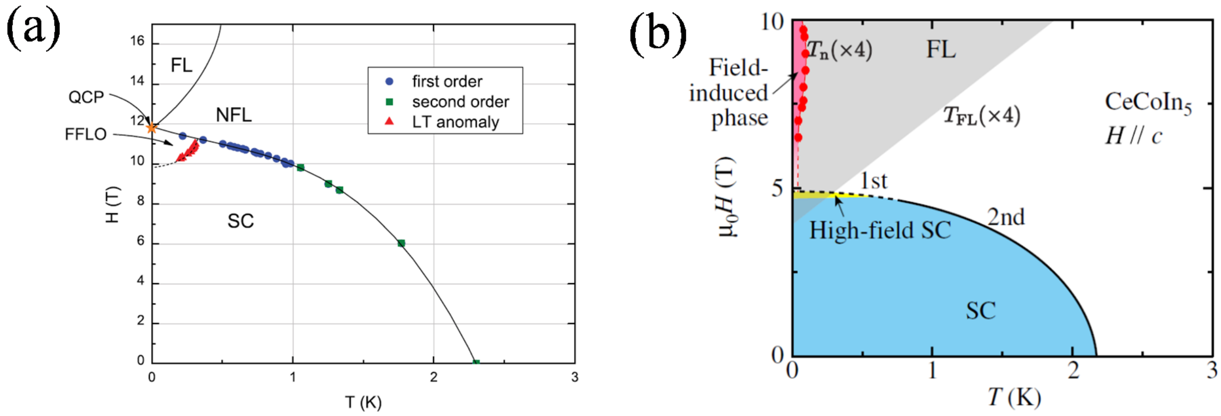

Figure 4.3: Temperature-magnetic field phase diagram of CeCoIn$_5$ for fields applied along (a) the [110] direction Ref. [153] and (c) the c axis Ref. [154].

SDW formation close to the nodes [156]. Alternative origins of this new phase have been argued to be the formation of a Cooper pair signet with a non-zero momentum [157, 153] (the elusive FFLO phase [158]), singlet and triplet SC pairing, and intertwined orders with p-wave pair-density-wave [159]. Specific heat and transport measurements suggested CeCoIn$_5$ to be in the proximity of a magnetic QCP at H_{c2} [155], where the SC is suppressed. Additional indications for the presence of a field-induced QCP at H_{c2} stem from the observed cross-over from non-Fermi-liquid state to Fermi-liquid state above the SC state and the emergence of a new intertwined state in the vicinity of H_{c2}. Further, a recent dHvA study revealed an emergence of a field-induced instability above H$_{c2}$ at a very low temperature $T_n = 20$ mK [154]. It was interpreted as a field-induced AFM state [see Fig. 4.3(b)]. How this instability evolves into the Fermi-liquid state remains an open question.

4.1.1 Fermi surface and effective masses of CeCoIn$_5$

The Fermi surfaces of CeCoIn$_5$ are quasi-two-dimensional consisting of an almost cylindrical band 15-electron Fermi surface and a highly corrugated cylindrical band 14-hole Fermi surface. The band 13-hole Fermi surface consists of two kinds of small closed pockets. Figure 4.4 shows the calculated Fermi surfaces in CeCoIn$_5$ obtained from the full potential linear augmented plane wave (FLAPW) band-structure calculations assuming itinerant f electrons [78]. Since CeCoIn$_5$ is a compensated metal, the volumes of the electron and the hole-Fermi surfaces are equal.

Previous dHvA studies [124, 119, 78, 161, 160, 154] detected most of the Fermi surface orbits predicted by the calculations, namely, α_3, α_2, α_1 corresponding to the nearly cylindrical band 15-electron FS and β_2, and β_1 corresponding to the corrugated cylindrical band 14-hole FS. The orbits ϵ and γ correspond to two small pockets of the 13-hole band FS. The angular dependence of the

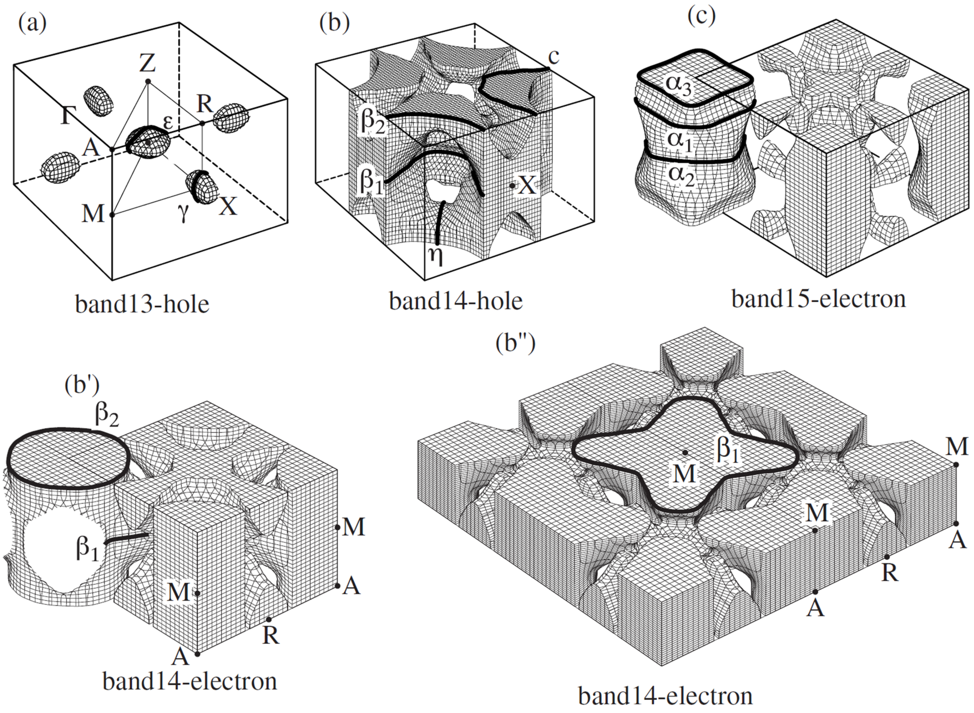

Figure 4.4: Calculated Fermi surfaces of CeCoIn$_5$ assuming itinerant f electrons. Adapted from Ref. [78]

experimentally observed dHvA frequencies in CeCoIn$_5$ in magnetic fields up to 17 T by R. Settai et al. [119] is shown in Fig. 4.5(c). Here the α branches follow approximately a $1/\cos\theta$ dependence, where θ is the field-angle from the [001] toward either [100] or [110] direction, indicating nearly cylindrical Fermi surfaces. The β_2 branch has a positive curvature, while β_1 has a negative curvature in agreement with the itinerant calculations. The outer large orbit c in the 14-hole band Fermi-surface has not been detected experimentally. The excellent agreement between the experimentally observed dHvA orbits and the itinerant band-structure calculations confirms the itineracy of the f electrons in CeCoIn$_5$.

A dHvA study at still higher fields up to 28 T detected an emergence of new dHvA frequencies F_a, F_c and F_d at fields above 23 T, as shown in Fig. 4.5(d) [160]. Further, a decrease of the Dingle temperature around 23 T was also observed for the frequency F_4, revealing a new magnetic field scale at $B \approx 23$ T. The change of Dingle temperature above 23 T suggests an important modification of the quasiparticle scattering, and, therefore, magnetoresistance of CeCoIn$_5$ must be probed for a direct signature of any scattering changes.

The cyclotron effective masses corresponding to the main dHvA branches are extremely enhanced. For instance, in the field range 15 - 16.9 T along the c axis,the observed cyclotron masses are about 50 m_0 for β_1 and β_2 branches, 15 m_0 for α_1, 8.4 m_0 for α_3 and 18 m_0 for α_2 [119]. However, the observed heavy masses do not completely account for the huge zero-field Sommerfield coefficient $\gamma \approx 1000$ mJ/K^{2}mol. The 'missing mass' was in part accounted for by the observation of a field-dependent effective masses on the majority of the Fermi surfaces as shown in Fig. 4.6 (a) and (b). The effective masses were observed to reduce with fields up to 18 T [119]. The reduction of the effective masses with magnetic field is common behavior in heavy fermions. Another reason for the 'missing mass' was uncovered by the observation of a spin-dependent mass enhancement for α_3 and β_2 orbits in fields up to 18 T without any non-linear splitting of these Fermi surfaces [161] as shown in Fig. 4.6(c). However, there are still undetected dHvA frequencies predicted by the calculations such as c in band-14 [see Fig. 4.4], which might have an enhanced mass.

Therefore, CeCoIn$_5$ needs to be explored at still higher fields to understand the field evolution of the Fermi-liquid state through the Fermi surface and the effective mass studies, as well as to understand the field-induced instabilities such as the one observed at 23 T [160].

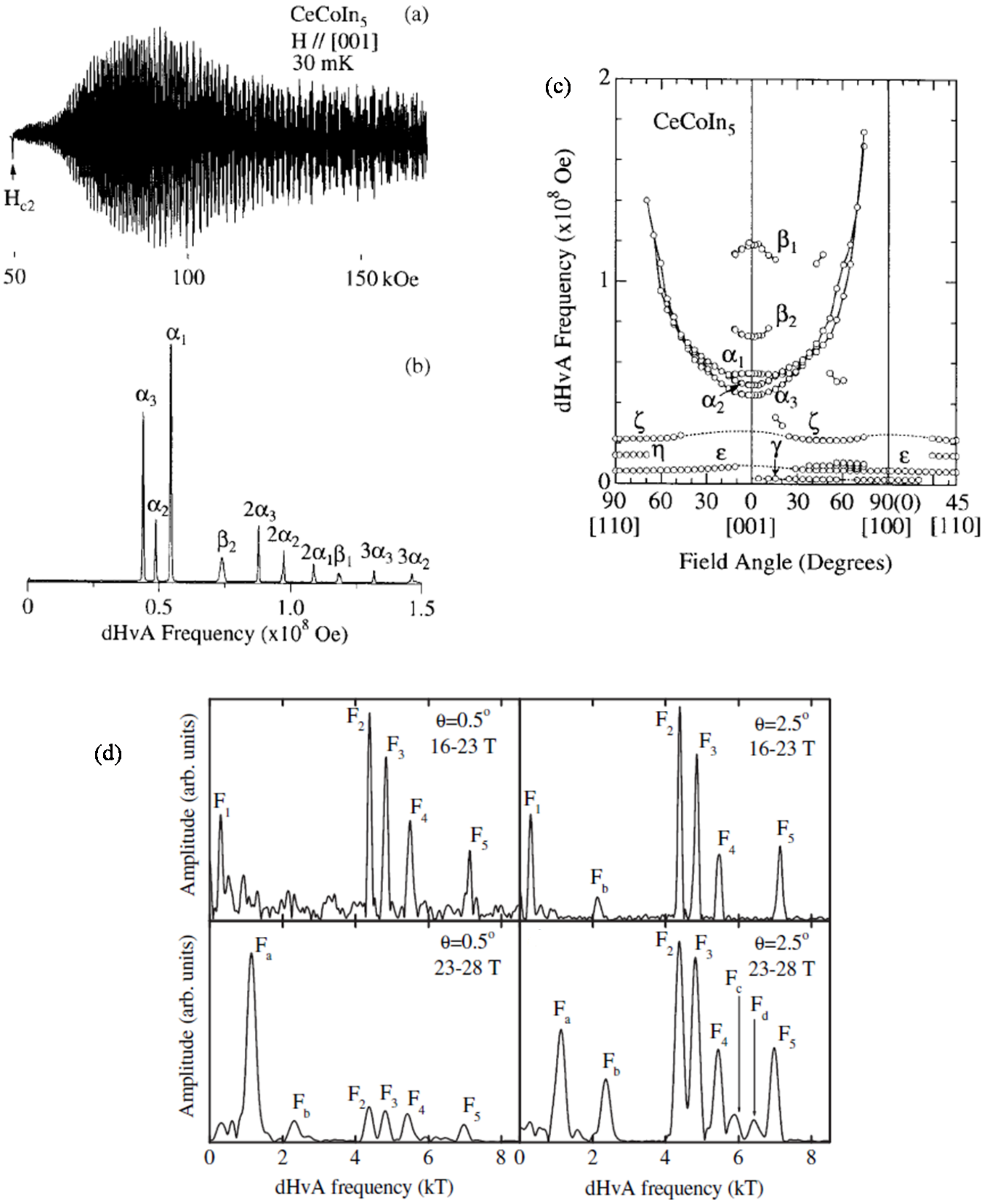

Figure 4.5: Low-fields quantum oscillations in CeCoIn$_5$. (a) As-measured quantum oscillations and (b) the corresponding FFT spectrum. (c) The angle-dependence of the dHvA frequencies reported by R. Settai et al. [119]. (d) FFT spectra of the high-field quantum oscillations reported by I. Sheikin et al. [160].

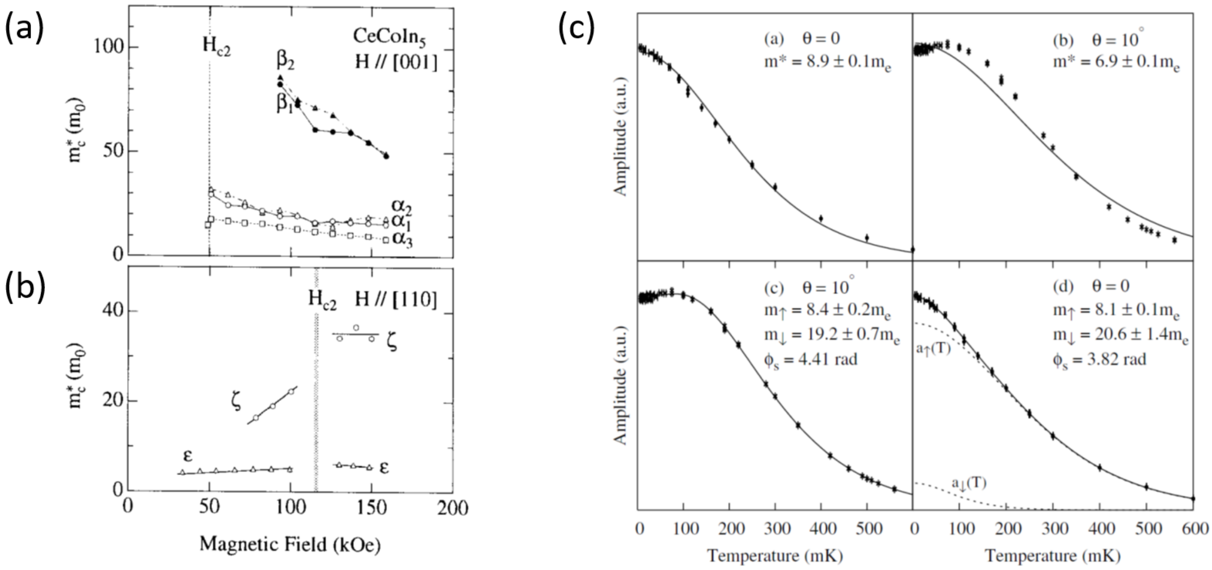

Figure 4.6: Effective masses in CeCoIn$_5$ (a) and (b) field-dependence of the effective masses by R. Settai et al. [119]. (c) Spin-dependent mass enhancement for α_3 orbit at orientation $\theta = 0°$ and $\theta = 10°$ by A. McCollam et al. [161].

4.2 Results

4.2.1 Abstract

We present high-resolution low-temperature dHvA effect and magnetoresistance measurements in CeCoIn$_5$ in static magnetic fields up to 36 T. In the dHvA effect, for a field applied close to the c axis, we observed a previously undetected high frequency $F_e = 10.24$ kT at high fields. This frequency has a strongly enhanced effective mass $m^* =$25-30 m_0. Furthermore, an anomalous behavior of the quantum oscillation amplitudes as well as the effective masses corresponding to the α orbits was observed around 23 T. The effective masses on the α Fermi surface rapidly decrease with magnetic field up to 23 T and then increase abruptly above this field. The large field interval of our dHvA measurements allowed us to observe a clear field-induced splitting of several dHvA frequencies. Our magnetoresistance measurements on FIB-fabricated microstructures of CeCoIn$_5$ revealed a distinct anomaly at 23 T in the in-plane transport, while the out-of-plane transport remains featureless. We interpret these field-induced changes at $B \approx 23$ T as a possible signature of the departure from the conventional Fermi-liquid state in high fields in CeCoIn$_5$.

4.2.2 dHvA effect in CeCoIn$_5$ in high fields

The dHvA effect measurements were performed in static magnetic fields up to 36 T in an dilution fridge equipped with a in-situ rotator. A single crystal of CeCoIn$_5$ was mounted on a 50 μm thick metallic cantilever with a 100 μm spacer separating it from the ground plate, as shown in the inset of Fig. 4.7.

4.2.3 Angle-dependence of the dHvA oscillations

Using the rotator, the c axis of the sample was carefully aligned along the magnetic field where the magnetic torque vanishes. Using the rotator, we measured the dHvA effect at several different orientations θ of the magnetic field from the c toward the a axis, as shown in Fig. 4.7.

As shown in Fig. 4.7, on increasing the field angle θ the background torque becomes larger. There is a distinct signature of the superconducting transition at $H_{c2} = 5$ T in the magnetic torque. Further, quantum oscillations start appearing at fields below 10 T and are strongly enhanced at high fields [see Fig. 4.7(b)].

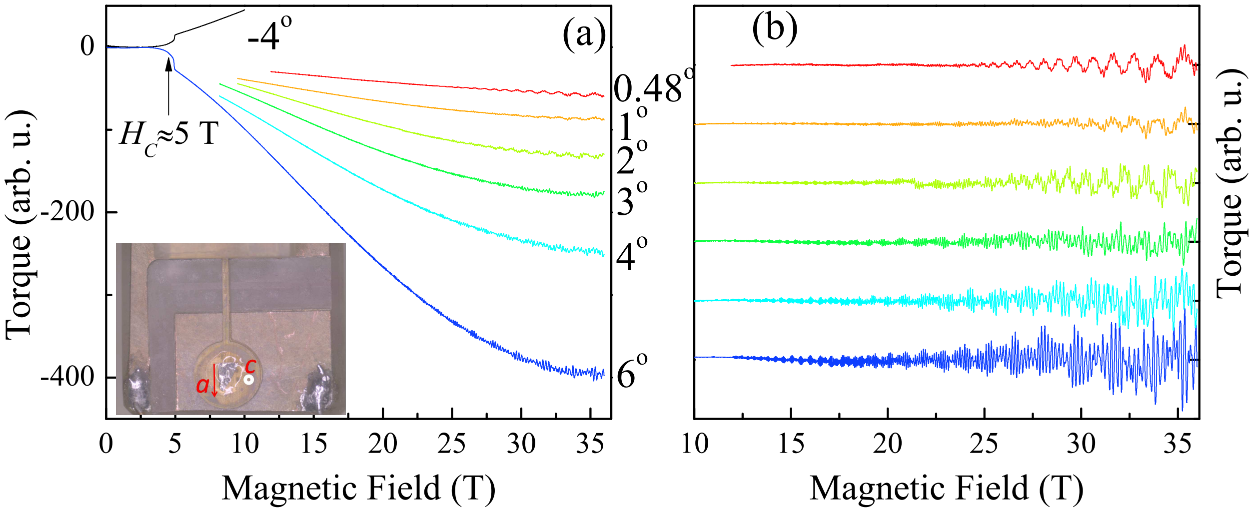

Figure 4.7: (a) As-measured magnetic torque in $CeCoIn_5$ for fields applied at several field angles θ from the c towards the a axis at $T = 30$ mK. (b) Quantum oscillations obtained by subtracting a smooth polynomial background from the raw torque signal in (a).

Fig. 4.8 shows the FFTs corresponding to the quantum oscillations in Fig. 4.7(b). The FFTs are performed over the high-field intervals 25 - 36 T to study the Fermi-surface of $CeCoIn_5$ at fields entirely above 23 T and with a high enough resolution to well resolve close dHvA frequencies.

We observed all the previously detected dHvA frequencies [124, 119, 78, 161, 160, 154], as shown in Fig. 4.8. In addition, we detected a new frequency $F_e = 10.24$ kT, which was not observed in any of the previous studies. F_e appears at $\theta = 6°$ between the second harmonics of α_2 and α_1. Either it corresponds to the so far undetected fundamental frequency c in the hole band-14, or it is new frequency not accounted for in the band-structure calculations. Another possible origin of F_e, although unlikely, is the spin-split of α_2, which is clearly resolved only in the second harmonic. The α_2 peak is indeed asymmetric. However, the spin-splitting of α_2 cannot be directly resolved in this field range. Further, the frequency F_c and β_2 also seem to be split into two peak for $\theta = 6°$.

4.2.4 Field-dependence of quantum oscillations in $CeCoIn_5$

The evolution of the dHvA frequencies with magnetic field at three different orientations is shown in Fig. 4.9. It is evident that the frequencies F_a, F_c and F_d appear only at fields above 23 T. This observation is consistent with the previous report [160].

Further, the new frequency F_e also seems to appear only at fields above 23 T, as is evident from Fig. 4.9(c). Its presence at high fields might also be related to the field-induced instability at 23 T, like F_a, F_c and F_d, or indeed it is only observed only at high fields due to its strongly enhanced effective mass.

The dHvA frequencies F_a, F_b and β_2 are strongly field dependent [see Fig. 4.9(d)]. F_a and β_2 decrease with magnetic field. For example, β_2 changes from 7.2 kT at 15 T to 6.8 kT at 32 T, i.e., it decreases by about 5%. The frequency F_b increases with field. Such a strong field dependence of these dHvA frequencies, probably, results from a field-induced non-linear splitting of these orbits, where the heavier split peak is not detected due to extremely heavy quasiparticle mass, and only the lighter split peak is observed.

Figure 4.10 shows the evolution of the dHvA amplitudes of the α_3, α_2 and α_1 orbits with magnetic field. An anomalous behavior of their amplitudes is observed over the field range 20-24 T. This anomalous behavior of the dHvA amplitudes is more pronounced for α_2 and α_1 and at field orientations closer to the c axis. The amplitude of α_1 gradually increases with field following a pronounced suppression close to 22 T before a new increase at higher fields. The amplitude of the α_3 frequency gradually increases at fields above 23 T signaling an abrupt increase of the Dingle temperature, which is almost doubled. At fields above 23 T, the amplitude of α_2 is almost

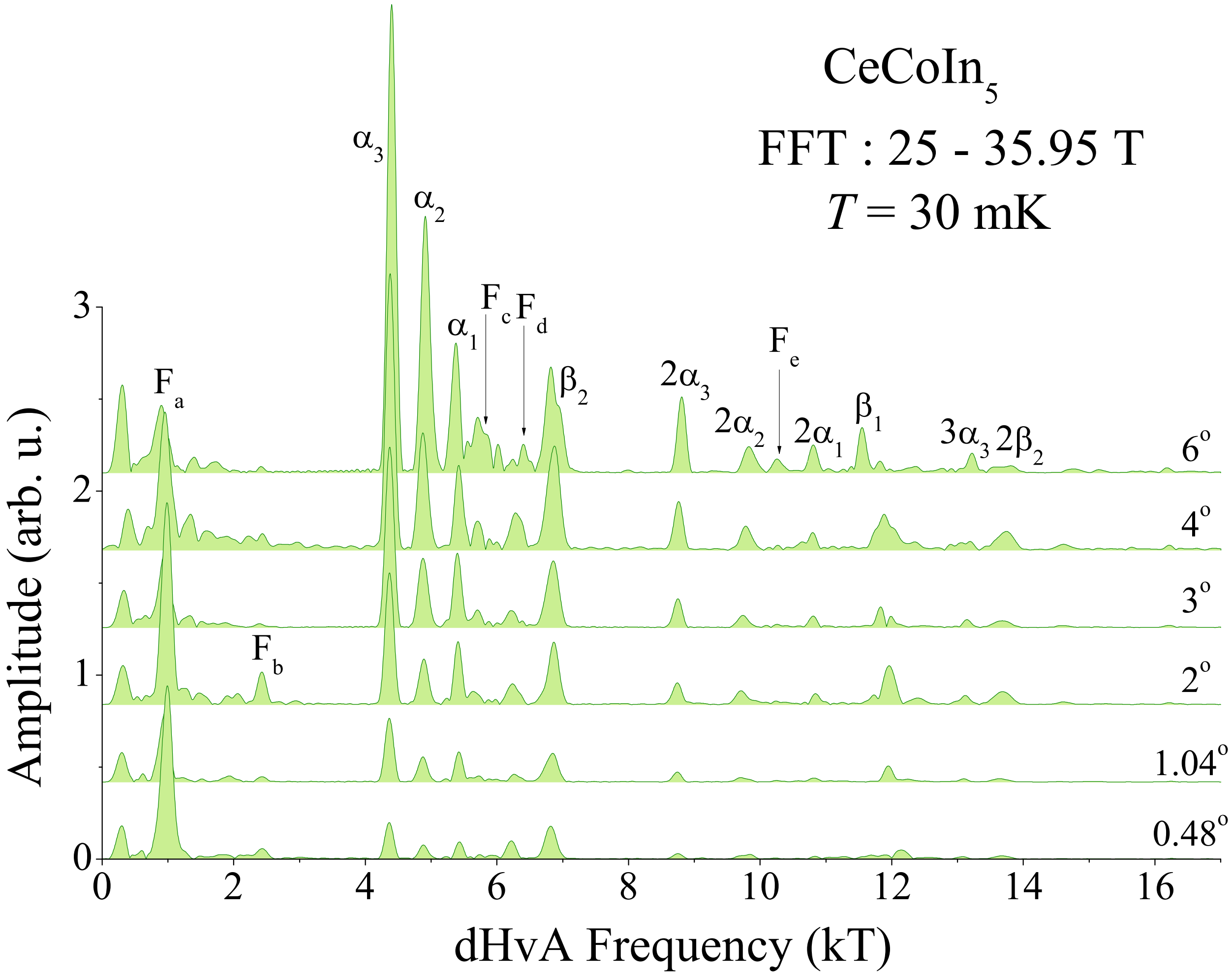

Figure 4.8: FFTs of the quantum oscillations in CeCoIn$_5$ (shown in Fig. 4.7) at several field angles θ from the c towards the a axis in the FFT range 25 - 35.95 T.

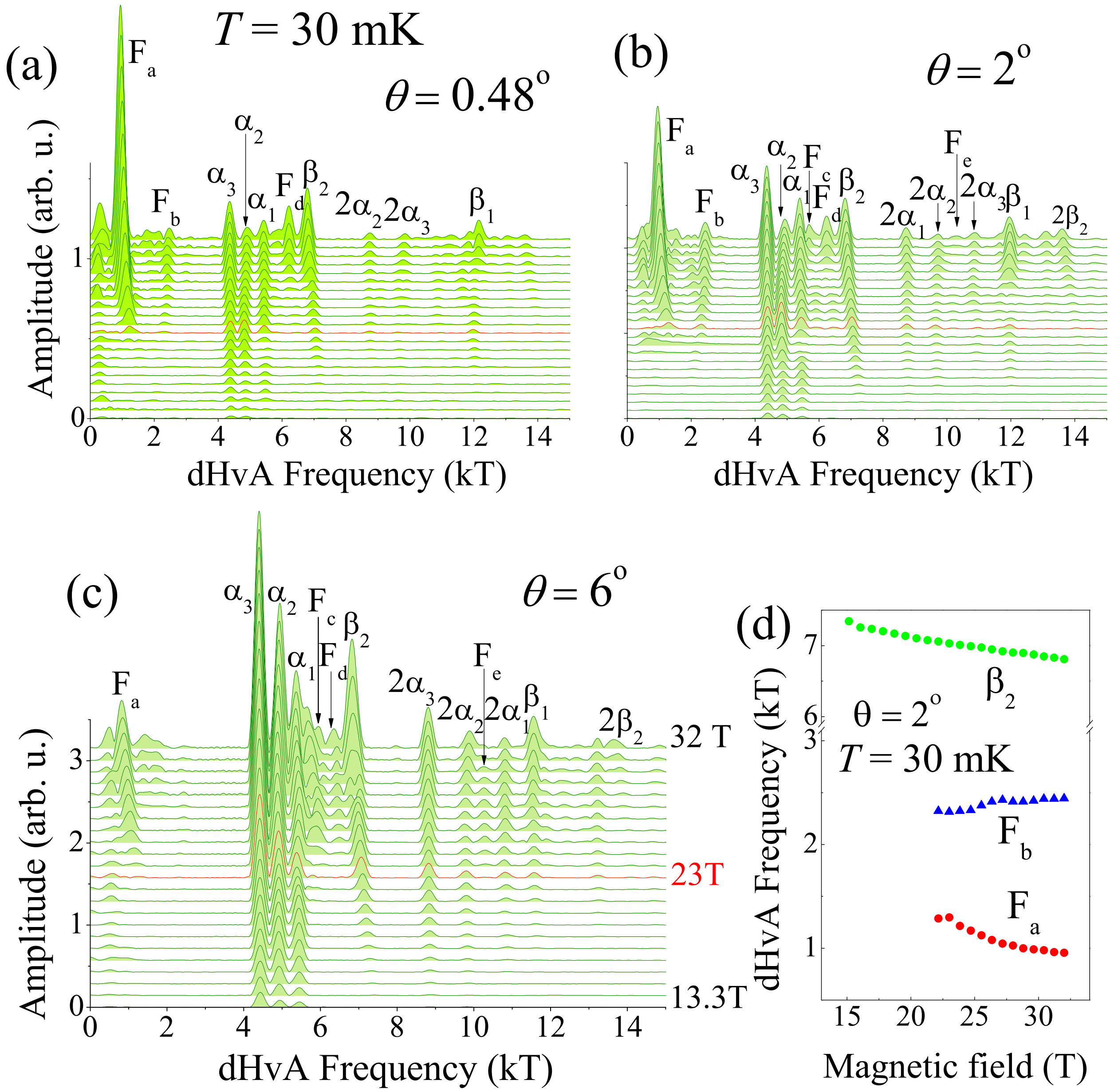

Figure 4.9: Evolution of the dHvA frequencies in CeCoIn$_5$ as a function of magnetic field at T = 30 mK and for three different orientations of the magnetic field (a) $\theta = 0.48°$, (b) $\theta = 2°$, and (c) $\theta = 6°$. For the top curve in each panel B_{min} = 28.8 T, B_{max} = 36 T and B_{avg} = 32 T. For each successive curves, B_{max} is decreased in steps of 1 T with the B_{min} adjusted accordingly keeping the $\Delta(1/B) = 0.00694\text{T}^{-1}$. The curves are shifted vertically for clarity. (d) shows the field dependence of the frequencies β_2, F_a and F_b at $\theta = 2°$.

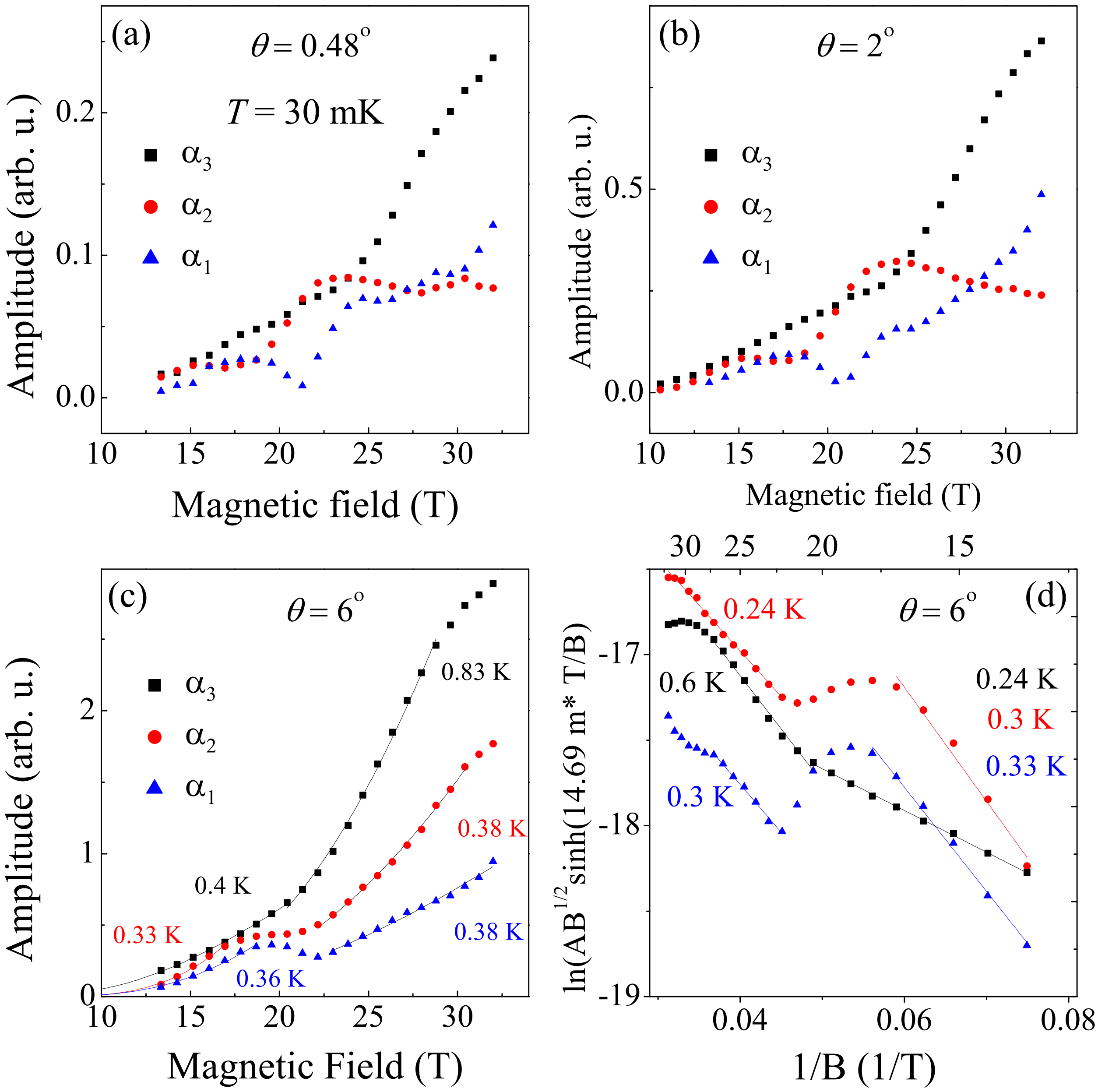

Figure 4.10: Evolution of the dHvA amplitudes of the α orbits in CeCoIn$_5$ with magnetic field at T = 30 mK and for several orientations (a) $\theta = 0.48°$, (b) $\theta = 2°$, and (c) $\theta = 6°$ of the magnetic field from the c toward the a axis. (d) Dingle plot of the dHvA frequencies α_3, α_2 and α_1 at T =30 mK and $\theta = 6°$. The effective masses used in the Dingle fit are shown in Fig. 4.13. The Dingle temperatures obtained from the fit both below and above 23 T are also shown.

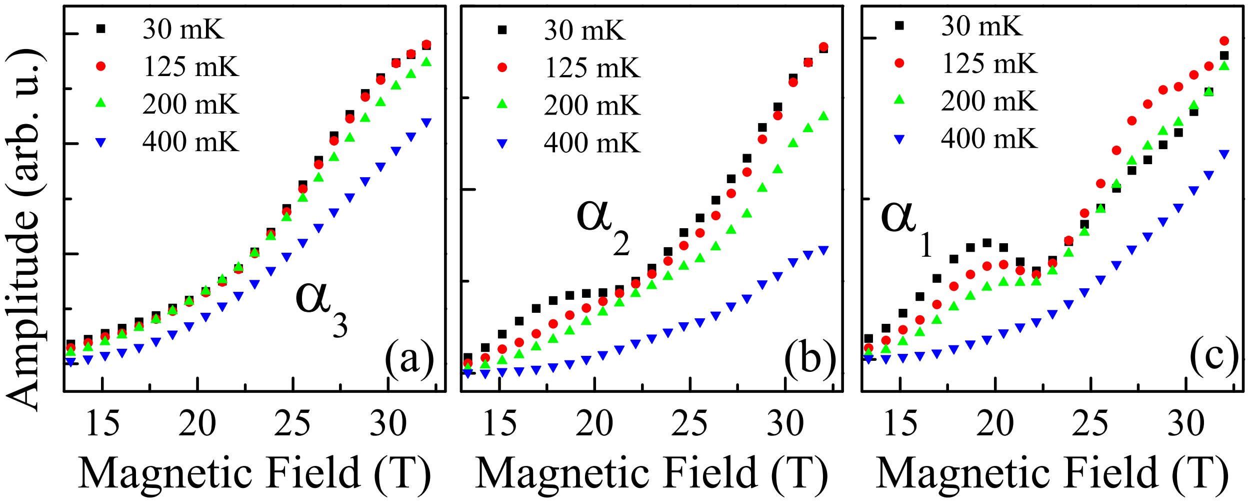

Figure 4.11: Evolution of the dHvA amplitudes in CeCoIn$_5$ with magnetic field applied at $\theta = 6°$ at several temperatures for (a) the α_3, (b) α_2, and (c) α_1 orbits.

unchanged for field orientations close to the c axis, i.e., at $\theta = 0.48°$ and $\theta = 2°$ [see fig. 4.10(a) and (b)]. At a larger field angle of $\theta = 6°$, the dHvA amplitudes of α_3, α_2 and α_1 all show a similar behavior, i.e., a gradual increase with field with an anomalous decrease between 20 and 23 T. The observed decrease of the Dingle temperature suggests a modification of the quasiparticle scattering for the α orbits. Therefore, the field-induced instability at 23 T seems to be related to the quasi-2D band-15 Fermi-surface.

Finally, in Fig. 4.11 we show the field evolution of the dHvA amplitudes of the α_3, α_2, and α_1 orbits at different temperatures. The anomalous decrease of the dHvA amplitudes, which is most pronounced for α_1, around 23 T becomes less prominent at higher temperatures, and is no longer observed at 400 mK [see Fig. 4.11(c)]. For α_2 and α_3 [see Fig. 4.11(a) and (b)], the anomalous behavior already become less noticeable already at 200 mK.

The disappearance of the anomalous behavior of the dHvA amplitudes at higher temperatures provides an important insights into the field-induced instability. It suggests the quasiparticle scattering in the vicinity of 23 T is strongly affected at low temperatures only.

4.2.5 Effective masses in CeCoIn$_5$

Figure. 4.12 shows the temperature evolution of the dHvA amplitudes in two different field ranges (equal intervals in $\Delta(1/B)$) with the reciprocal average B_{avg} (a) 25.28 T and (b) 31.51 T. The corresponding mass plots are shown in Figs. 4.12 (c) and (d).

The effective masses for both field interval are listed in Table 4.1. In accordance with previous reports, some of the effective masses are found to be strongly enhanced. The effective mass of the new frequency F_e is also strongly enhanced, i.e., 29.6 m_0 at 25.28 T, and 24.7 m_0 at 24.7 T. The effective masses of the frequencies appearing above 23 T are also quite high.

Further, some of the effective masses are strongly field dependent, as shown in Fig. 4.13. The effective mass of β_1 is more than halved from $\approx 60\ m_0$ at $B \approx 15\ T$ to $\approx 25\ m_0$ at $B \approx 32$ T. The effective masses of β_1 and β_2 rapidly decrease with field up to about 25 T following by a slow decrease up to about 28 T, above which they do not change any longer. The effective masses of the α orbits shows a peculiar field dependence. The masses of all the orbits decrease with field up to 23 T. Above 23 T, the effective masses no longer decrease, but rather increase with field. Such a field enhancement of the effective masses is quite rare. The increase of the effective mass is the strongest for the α_2 frequency, where it increases from $11 m_0$ at 23 T to 16 m_0 at 32 T. For α_3 and α_1, the masses increase with field only up to 28 T, and then start to decrease gradually at higher fields.

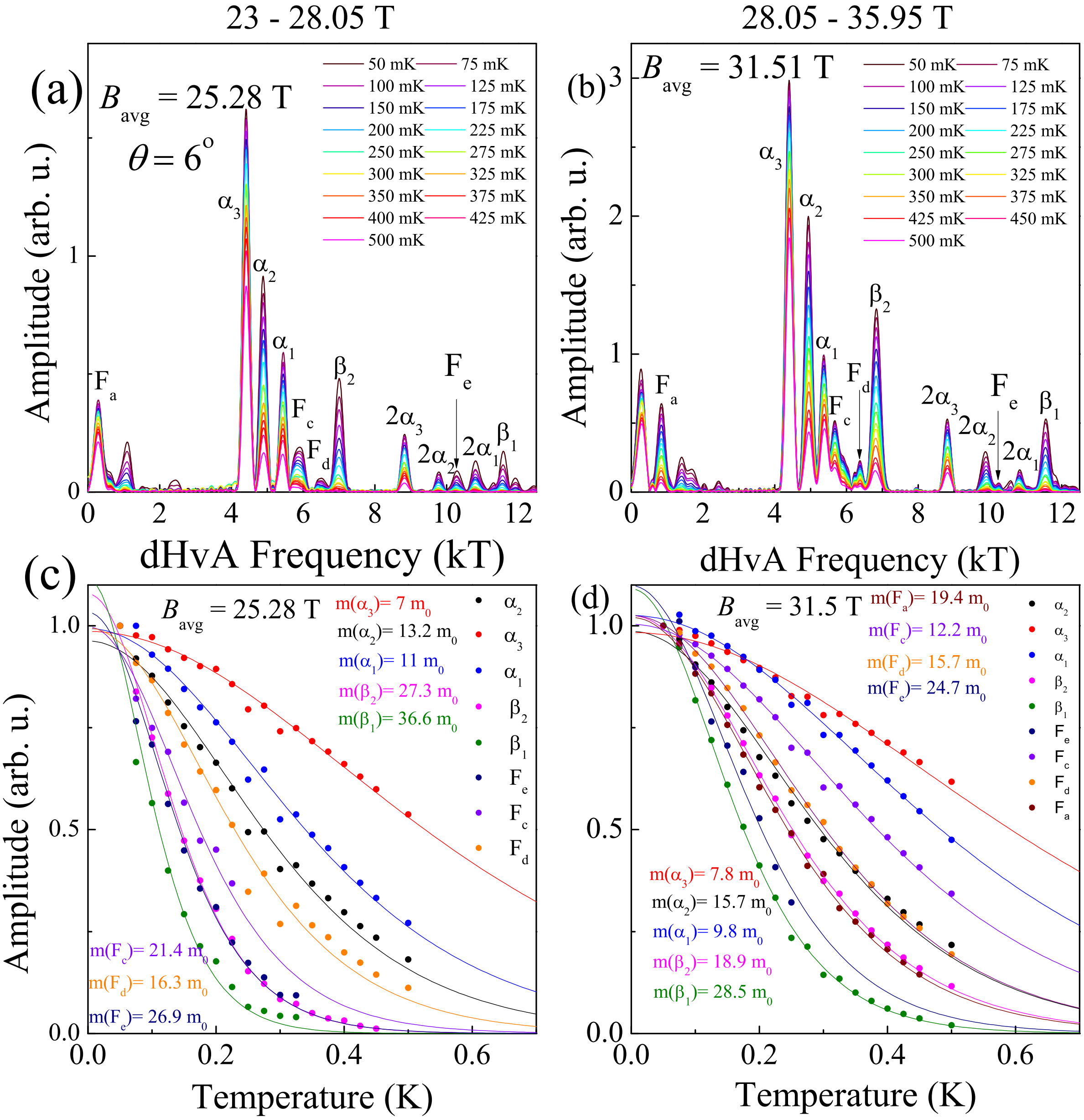

Figure 4.12: Temperature-dependence of the dHvA amplitudes in CeCoIn$_5$ over the field intervals with the reciprocal field average (a) B_{avg} =25.28 T and and (b) B_{avg} =31.51 T. The corresponding mass plots are shown in (c) and (d).

Effective masses in CeCoIn$_5$		
dHvA Frequency(kT)	m^* at 25.28 T (m_0)	m^* at 31.51 T (m_0)
α_3	7	7.8
α_2	13.2	15.7
α_1	11	9.8
β_2	27.3	18.9
α_1	36.6	28.5
F$_c$	21.4	12.2
F$_d$	16.3	15.7
F$_e$	29.6	24.7

Table 4.1: Effective masses (m^*) corresponding the various dHvA frequencies in CeCoIn$_5$.

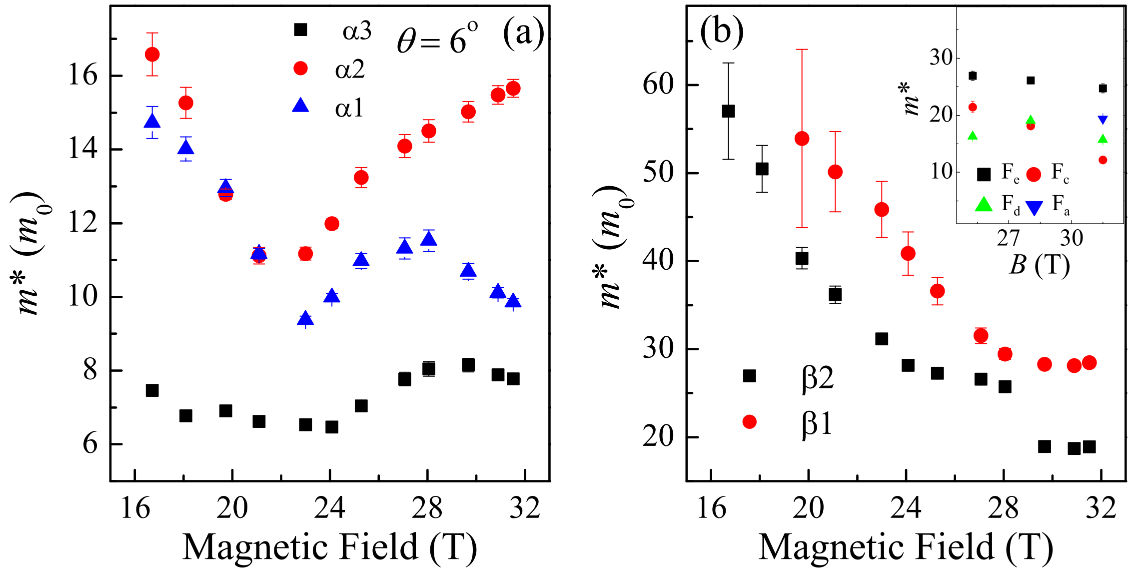

Figure 4.13: Field-dependence of the effective masses in CeCoIn$_5$ for (a) the α and (b) the β frequencies for the magnetic field orientation $\theta = 6°$.

4.2.6 Field-induced splitting of the Fermi surface

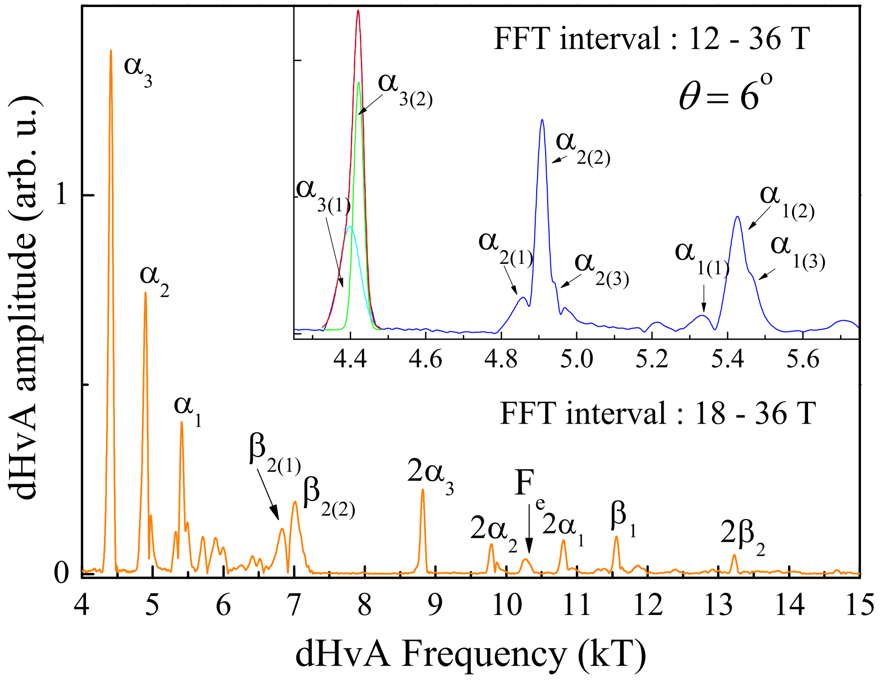

Figure 4.14: FFT of the dHvA oscillations in CeCoIn$_5$ obtained over a large field interval 18 - 36 T. The inset shows a still larger field interval to resolve the splitting of the α orbits.

The field-induced spin-splitting can be resolved by performing the FFT over a larger field range, such as shown in Figs. 4.14 and 4.15. The frequency α_3 has an asymmetric shape, in which the splitting can be resolved by a double-peak fit. Similarly, the shape of the α_1 and α_2 is asymmetric. Further, there are small split-peak-like features around the α_1 and α_2 orbits. The small peak $\alpha_{2(3)}$ close to main α_2 orbit has an effective mass similar to α_2, i.e., $m^* \approx 12\ m_0$. There are two small peaks, $\alpha_{1(1)}$ and $\alpha_{1(3)}$, close to the main α_1 orbit as well. Their effective masses are $m^* \approx 12\ m_0$ for $\alpha_{2(1)}$ and $m^* \approx 10\ m_0$ for $\alpha_{2(3)}$. The effective mass of $\alpha_{1(3)}$ was obtained by a double-peak fitting, as shown in Fig. 4.16(a). Further, the splitting of α_1 is clearly resolved in its second harmonic over the field range 15.4 - 29 T [see Fig. 4.16(b)].

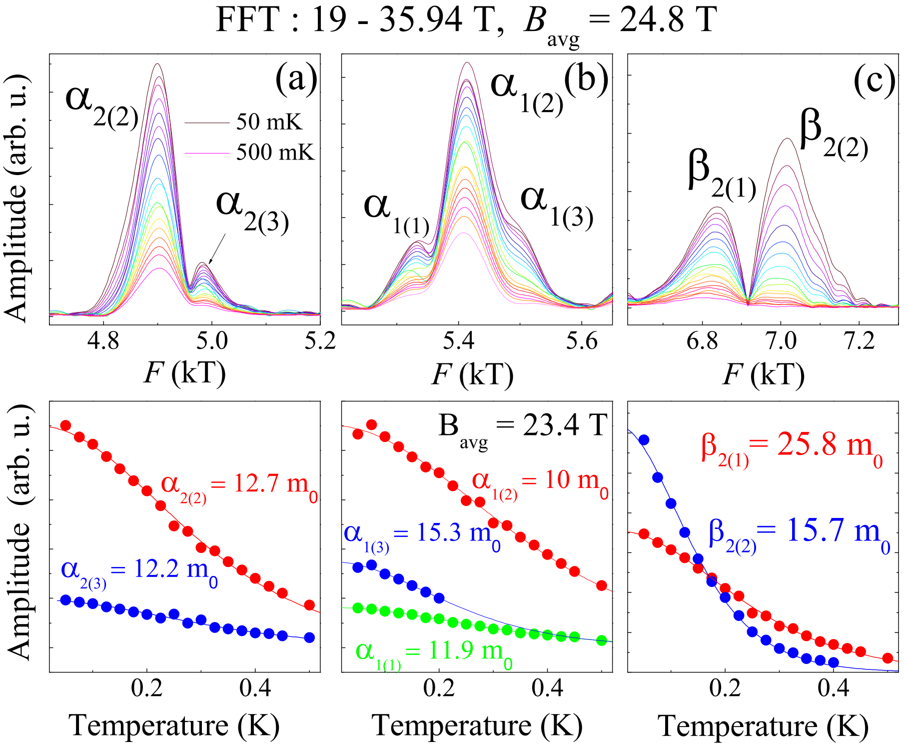

Figure 4.15: Temperature-dependence of the spin-splitting dHvA frequencies (a) α_3, (b) α_2, and (c) α_1 in CeCoIn$_5$ obtained by performing the FFT over a large field interval.

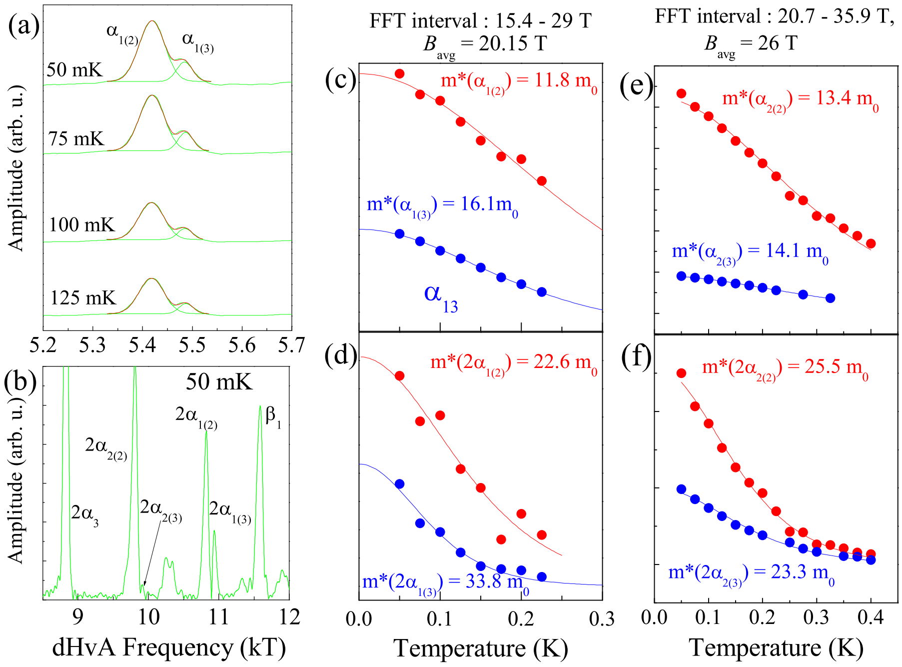

Figure 4.16: (a) A double-peak fit the α_1 orbit and the effective masses of (c) α_1 and (e) α_2. (b) The FFT spectrum showing the second harmonic of some dHvA frequencies. The corresponding effective masses are shown in (d) and (f).

The ratio of the effective masses of the split peaks $\alpha_{1(2)}$ and $\alpha_{1(3)}$ is almost the same as that for their second harmonic, i.e., $m^*(\alpha_{1(3)})/m^*(\alpha_{1(2)}) = m^*(2\alpha_{1(3)})/m^*(2\alpha_{1(2)}) \approx 1.4$. A still larger interval is required to extract the effective masses of the small split peak in the second harmonic of α_2 [Fig. 4.16(b) and (f)]. The effective mass ratio of the split peaks $\alpha_{2(2)}$ and $\alpha_{2(3)}$ as well as their second harmonics is also similar, i.e., $m^*(\alpha_{2(3)})/m^*(\alpha_{2(2)}) = m^*(2\alpha_{2(3)})/m^*(2\alpha_{2(2)}) \approx 1$. The splitting of α_3 cannot be resolved in its second harmonic $2\alpha_3$. A split peak $\beta_{2(1)}$ is observed close to main β_2 frequency labeled $\beta_2(2)$. However, no such splitting in seen in its second harmonic. Therefore, it is not clear if $\beta_{2(1)}$ is a result of field-induced spin-splitting, in which the main β_2 frequency should split into a heavier $\beta_{2(1)} = 6.8$ kT with $m^* = 25.8\ m_0$ and a lighter $\beta_{2(2)} = 7$ kT with $m^* = 15.7\ m_0$ (see Fig. 4.15).

4.2.7 Magnetoresistance in CeCoIn$_5$

The magnetoresistance measurements on a FIB-fabricated microstructure of CeCoIn$_5$ were performed in static fields up to 36 T in a dilution refrigerator equipped with an in-situ rotator.

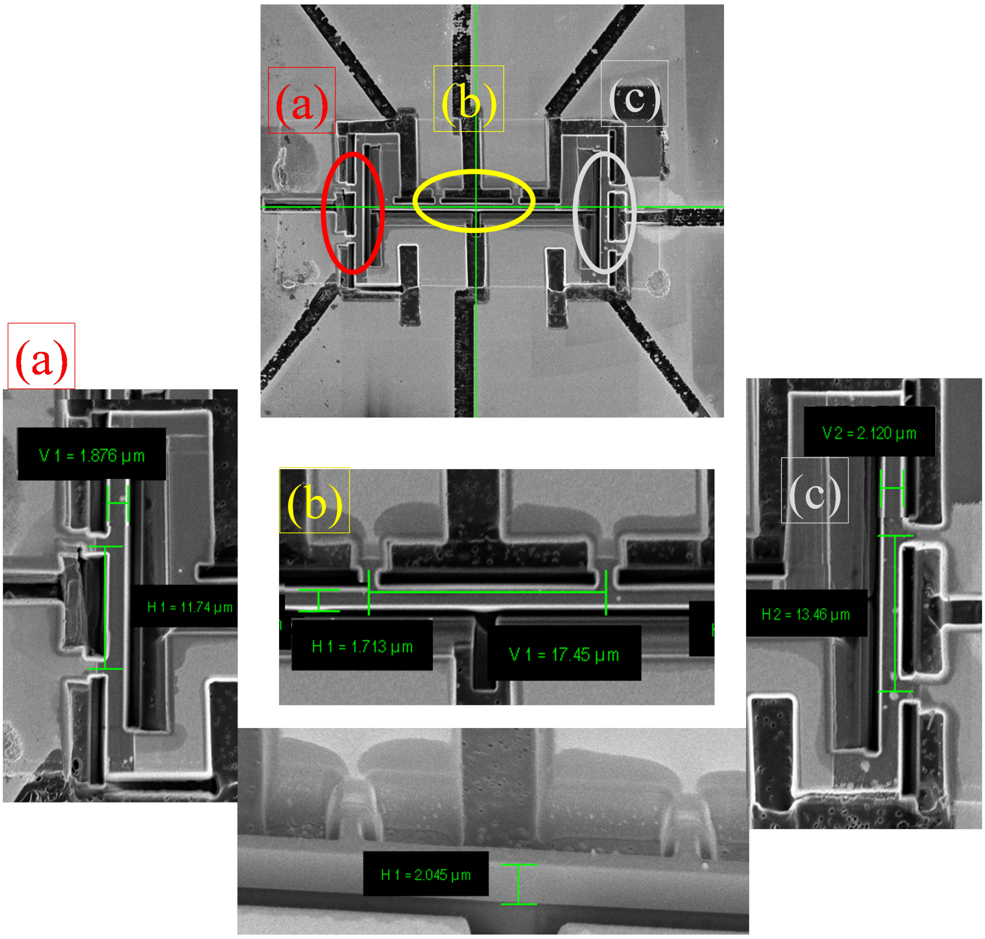

Figure 4.17: FIB-fabricated micro structured devices of CeCoIn$_5$. Devices labeled (a) and (c) are equivalent

The micro-structured devices of CeCoIn$_5$ were prepared by T. Helm at the MPI Dresden; the details of the process can be found elsewhere [162]. As shown in the Fig. 4.17, there are three different microstructured devices labeled (a), (b) and (c). The vertical devices labeled (a) and (c) are equivalent and their length is along the c axis. These devices were used to measure the out-of-plane transport, i.e., $I \parallel c$. The horizontal device labeled (b) has its length along the a axis and was used to measure the in-plane transport with $I \parallel c$. The dimensions of these devices are as following.

For the out-of-plane transport device labeled (a) : $l \times b \times h = 11.74\ \mu m \times 1.876\ \mu m \times 2.045\ \mu m$

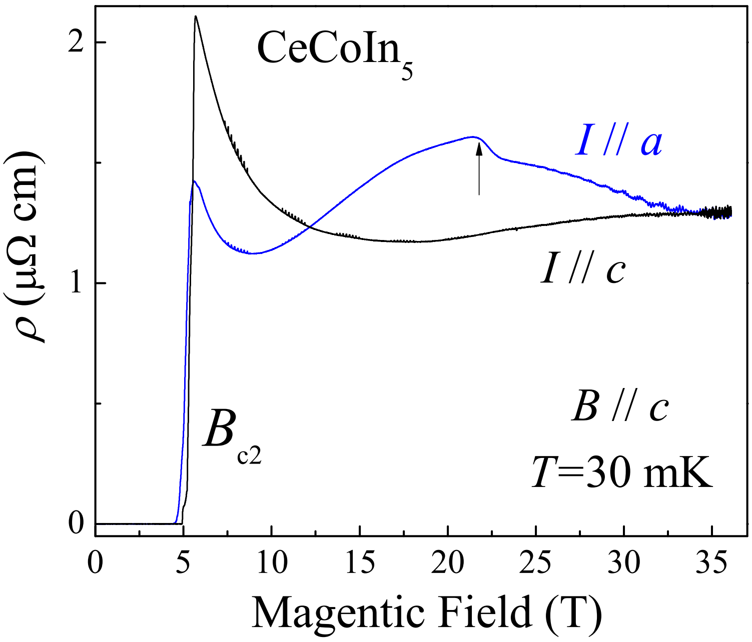

Figure 4.18: In-plane and out-of-plane transport in CeCoIn$_5$ for the field applied along the c axis at $T = 30$ mK. The arrow indicate the field-induced instability in the in-plane transport.

For the in-plane transport device labeled (b) : $l \times b \times h = 17.45\ \mu m \times 1.713\ \mu m \times 2.045\ \mu m$.

Figure 4.18 shows the in-plane and out-of-plane transport in the microstructured devices of CeCoIn$_5$ in fields up to 36 T applied along the c axis. Both configurations show the superconducting transition at $H_{c2} = 5$ T. The out-of-plane transport is featureless above H_{c2}. However, the in-plane transport shows an unusual behavior. It first increases with field up to 21 T followed by a step-like feature at 22 T and then decreases at higher fields.

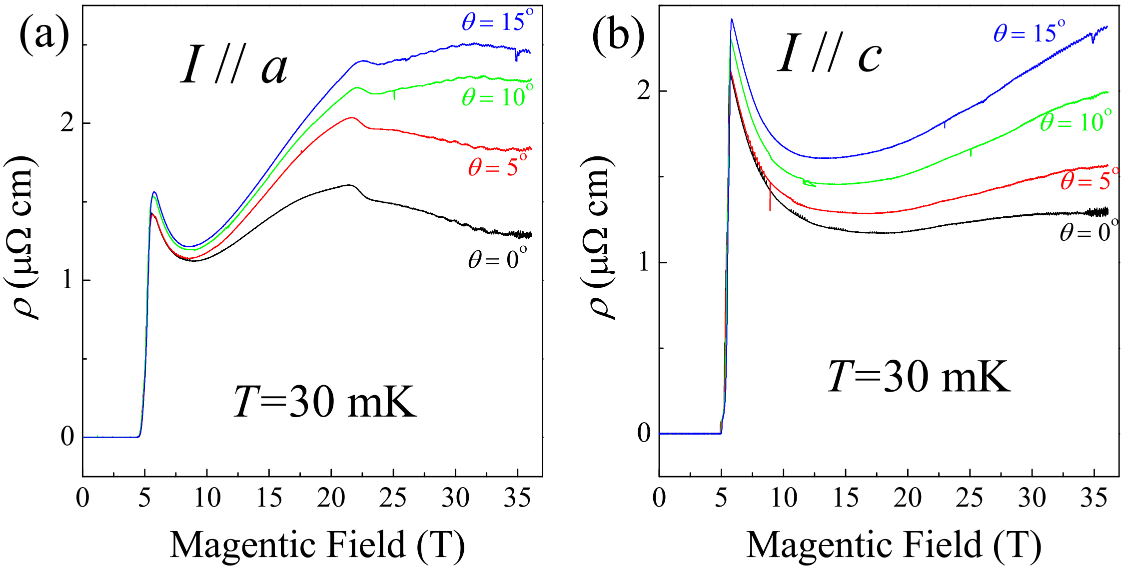

Figure 4.19: (a) In-plane and (b) out-of-plane transport in CeCoIn$_5$ for field applied at several angles θ from the c axis toward the a axis at $T = 30$ mK.

On increasing the angle θ of the magnetic field from the c toward the a axis, the high field magnetoresistance increases for both transport directions. The feature at 22 T becomes smaller with increasing θ. Also, the anomaly shifts to a slightly higher field with increasing the angle θ [see Fig. 4.19(a)].

Furthermore, we observed clear Shubnikov-de Haas oscillations at high fields for transport along both directions. The quantum oscillations in the in-plane transport after subtracting a non-oscillatory background for a field applied along the c axis are shown in the inset of Fig. 4.20. The FFT of the SdH oscillations reveals most of the frequencies detected in our dHvA measurements [see Fig. 4.20]. The relative amplitudes of the SdH oscillations are entirely different from those observed in the dHvA measurements. The field-induced splitting is clearly resolved for the α_1 orbit.

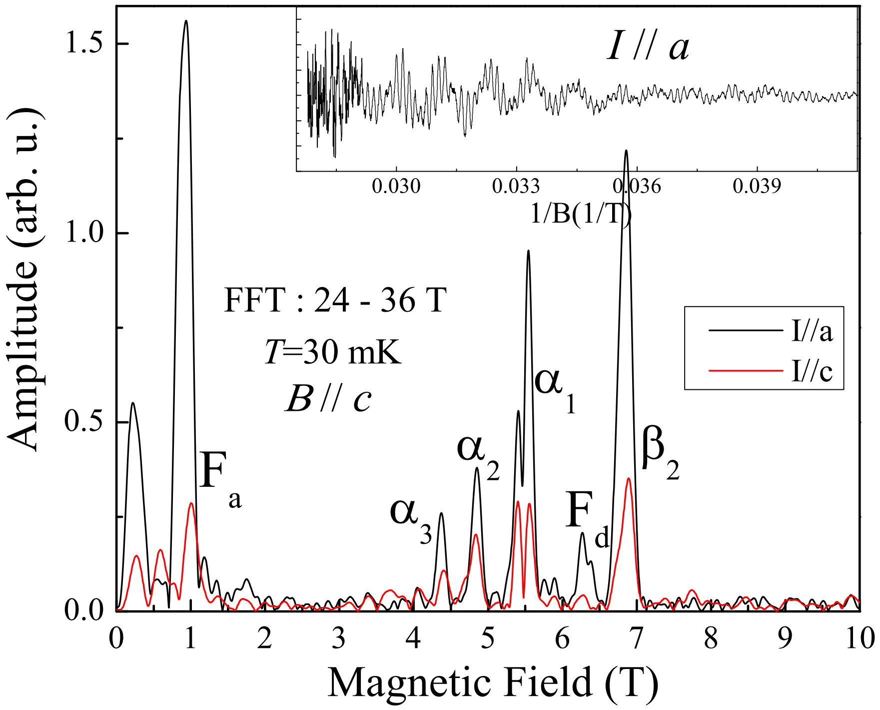

Figure 4.20: FFT spectra of Shubnikov de Haas quantum oscillations in CeCoIn$_5$ (shown in the inset) for a field applied along the c axis at T =30 mK.

4.3 Conclusions

In summary, we performed dHvA and mangetoresistance measurements in CeCoIn$_5$ at high fields close to the c axis. Our measurements revealed an anomalous quantum oscillation behavior at intermediate fields between 20 and 24 T, which is more pronounced at low temperatures and becomes unnoticeable at T = 400 mK. The effective masses also show an unusual field dependence. The effective masses of the α orbits show an abrupt increase above 23 T. Finally, magnetoresistance measurement revealed a clear anomaly at 22 T. Based on these observations, we suggest that a field-induced instability occurs in CeCoIn$_5$ at high fields. The enhancement of effective masses with magnetic fields suggests a departure from the standard Fermi-liquid behavior.

Chapter 5

Ce-218 heavy-fermion materials

5.1 Introduction

The Ce-115 family of heavy-fermion materials, comprising of members, such as $CeRhIn_5$, $CeCoIn_5$ and $CeIrIn_5$, has been extensively studied and revealed rich and exciting physics, as discussed in the preceding chapters. It is only natural to expect similar exotic physics to occur in their more 3D analogs, such as Ce_2RhIn_8, Ce_2CoIn_8 and Ce_2IrIn_8.

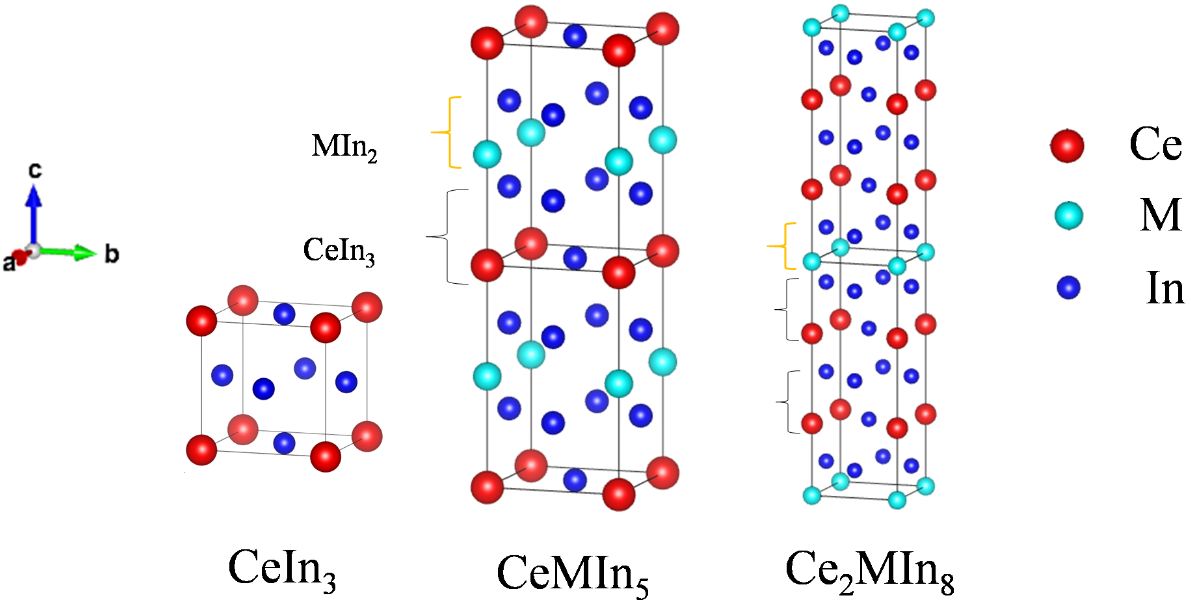

Figure 5.1: The crystal structure of (a) cubic $CeIn_3$, (b) tetragonal $CeMIn_5$ formed by stacking alternating layers of $CeIn_3$ and MIn_2 along the c axis and (c) tetragonal Ce_2MIn_8 formed by adding an extra $CeIn_3$ layer in between the alternating $CeIn_3$ and MIn_2 layers in $CeMIn_5$.

These compounds form the so-called Ce-218 family (Ce_2MIn_8, M = Rh, Co, Ir, Pt, Pd) of cerium-based heavy fermions. These compounds crystallize into a tetragonal Ho_2CoGa_8 type crystal structure. Unlike Ce-115s, where the crystal structure comprises of alternating layers of conducting $CeIn_3$ and insulating MIn_2, in Ce-218s, an additional conducting $CeIn_3$ layer is sandwiched in between two MIn_2 layers [see Fig. 5.1]. The stack so formed has two layers of $CeIn_3$ followed by a layer of MIn_2 alternating along the c axis. Therefore, the electronic structure becomes more 3D-like in comparison with the 2D-like electronic structure in $CeMIn_5$.

The physical properties of the 218 compounds are found to be qualitatively similar to their corresponding 115 analogs. For instance, similar to $CeRhIn_5$, Ce_2RhIn_8 is also an antiferromagnet, but with a lower $T_N = 2.8$ K [73]. Ce_2IrIn_8 shows a field-induced non-Fermi liquid behavior [163] just like its 115 analog $CeIrIn_5$. Similarly, Ce_2CoIn_8 also becomes superconducting at ambient pressure like $CeCoIn_5$, but with a lower $T_c \sim 0.45$ K [164].

Considering significant lowering of the superconducting ordering temperature T_c with the addition of an extra conducting $CeIn_3$ layer in Ce-218s, these compounds can be an ideal playground to understand the role of dimensionality in unconventional superconductivity. In this regard, information about their Fermi surfaces can play a crucial role. It is, therefore, important to check if the extra conducting layer drastically changes the Fermi-surface morphology in 218s in comparison with 115s or only the Fermi surfaces only grow bigger in size, but with a morphology similar to 115s. However, there are not many Fermi-surface studies on these compounds. To the best of my knowledge, dHvA oscillations have never been observed in Ce_2IrIn_8 and Ce_2CoIn_8 due to a poor sample quality, while in Ce_2RhIn_8 there is only one dHvA study in low fields, in which only two frequencies were detected [165]. Therefore, the Fermi surfaces of these compounds remain largely unexplored.

That is why, we tried to grow high-quality single crystals of these 218 compounds as well as their non-f lanthanum analogs to perform Fermi-surface studies. I grew these samples during my brief stay at the ICC-IMR, Tohoku university in Oarai, Japan.

5.2 Single crystals growth

The single crystals of Ce_2MIn_8's are grown using the self-flux method. The method is named as such because one of the starting materials, taken in excess amount, acts as the flux. In case of Ce_2MIn_8's, excess indium (In) acts as flux that helps in melting the starting elements (Ce, Co, Rh, Ir) well below their melting points. The single crystals grow as a result of precipitation when the molten homogenized supersaturated solution of the starting materials is slowly cooled down in a controlled manner. The following steps were perfomed for growing the single crystals.

1. Cleaning and baking the crucible The single crystals are grown in an alumina crucible. The crucible first has to be cleaned thoroughly to avoid unwanted impurities before placing the starting materials in it. To this end, the crucible is kept in acetone in a small flask, which is placed in an ultrasonic vibrator for about 10 minutes. The crucible is then taken out and placed in a baking furnace. In the baking furnace, the crucible is heated and simultaneously pumped using a turbo pump. The crucible baking is done for at least a few hours or overnight.

2. Starting materials The starting materials are commercially available elements of very high purity (more than 95%). The starting materials for growing single crystals of $Ce(La)_2MIn_8$'s were then placed in the cleaned alumina crucible in the stoichiometric ratio Ce(La): M (Co,Rh,Ir): In :: 2:1:20. Note, that indium (In), which acts as the flux, is taken in excess.

For growing Ce_2CoIn_8 and La_2CoIn_8, at first a stoichiometric ratio (Ce(La):Co :: 2:1) of the two starting materials, cerium (lanthanum) and cobalt was arc-melted to lower their melting points further and obtain a good homogeneous alloy of the two. After arc-melting a pellet of Ce_2Co (La_2Co) is formed, which is then placed in the crucible along with the excess indium. For the other two compounds, Ce_2RhIn_8 and Ce_2IrIn_8, the starting materials were placed in the crucibles in elemental forms without arc-melting.

3. Evacuation and encapsulation of the crucible Once the starting materials are placed in the alumina crucible, it is encapsulated in an evacuated quartz ampoule, which is then placed in the programmable heating furnace.

4. Crystal growth The stating materials in the sealed ampoules were put through the heating-cooling profile shown in Fig. 5.2 to grow single crystals. For growing Ce_2CoIn_8, the profile shown in Fig. 5.2(a) was used, while for growing Ce_2IrIn_8 and Ce_2RhIn_8 the profile shown in Fig. 5.2(b) was used. The mixture of starting materials was first heated up to about 1000°C. All the starting materials, even with a melting point much higher than 1000°C melt at this temperature because of the indium flux. The heating is kept constant at 1000°C for a few hours so that the melted

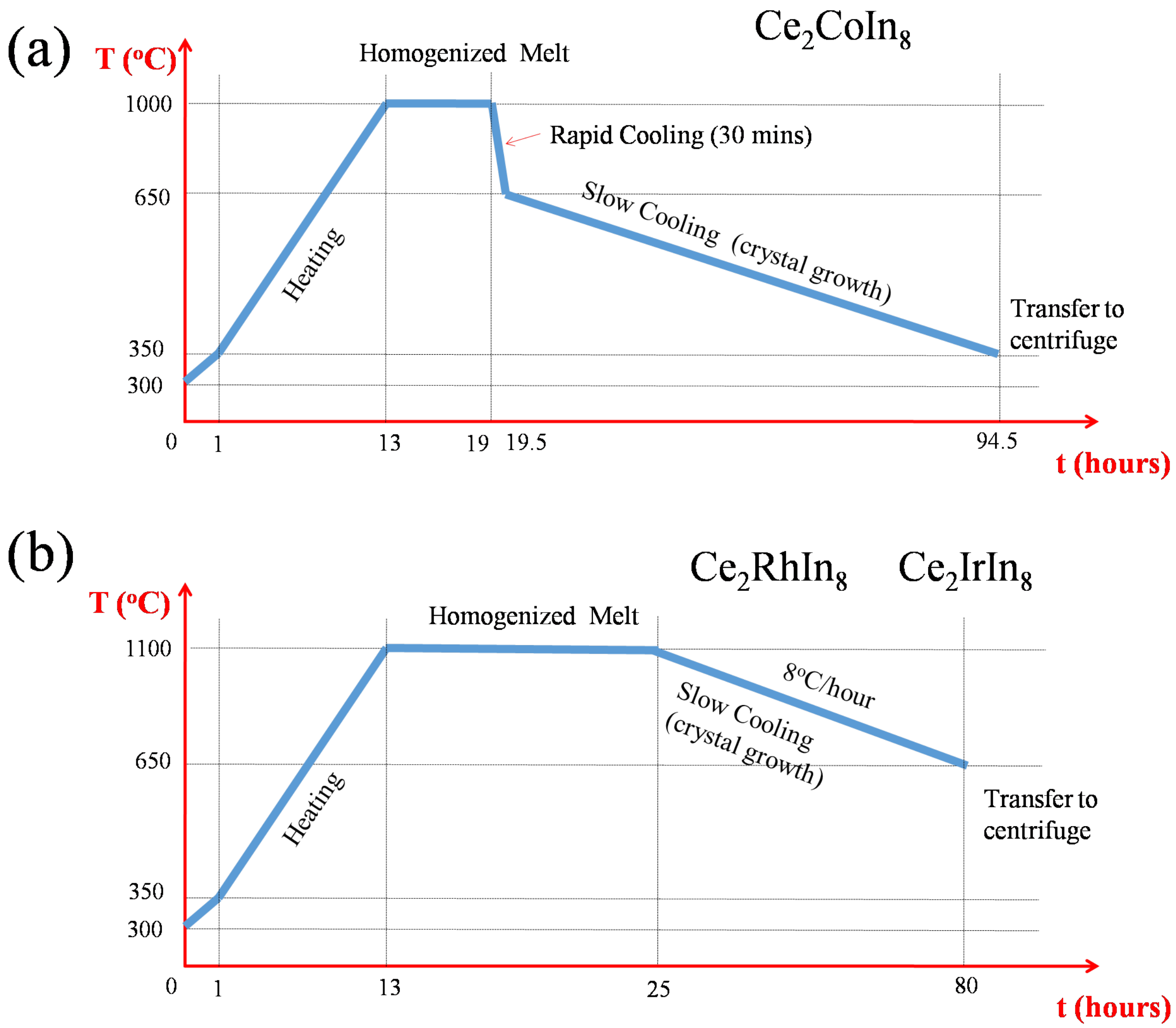

Figure 5.2: The heating-cooling profile used for growing single crystals of (a) Ce_2CoIn_8 and (b) Ce_2IrIn_8 and Ce_2RhIn_8.

materials form a homogenized solution. Then comes the most crucial step for the crystal growth, i.e., precipitation upon cooling.

The growth of crystals largely depends on the cooling profile followed. In order to grow Ce_2CoIn_8 single crystals, the heated melt is first cooled rapidly to 650°C in 30 minutes. From 650°C onwards, the mixture was cooled very slowly, at a rate of 4 °C/hour down to 350 °C, during which time the single crystals grow. To grow Ce_2RhIn_8 and Ce_2IrIn_8 single crystals, the molten homogenized solution at 1100°C is slowly cooled at a rate of 8°C/hour down to 650°C during which the single crystals grow.

The single crystals are still immersed in the molten excess of indium flux. This excess of indium can be removed by spinning it off in a centrifuge. Further, any residual indium flux can be removed by immersing the crystals in dilute Sulphuric acid for a short time.

Finally, after all these steps, we obtained nice faceted single crystals, such as shown in Fig. 5.3. The crystals grew in all sizes ranging from less a millimeter up to half a centimeter. The elemental characterization of these crystals was done using energy dispersive X-ray spectroscopy (EDS).

Ce_2IrIn_8 grew in a mixed phase with $CeIn_3$, i.e., single crystals of $CeIn_3$ also grew along with Ce_2IrIn_8. Similarly, Ce_2CoIn_8 grew in a mixed phase with $CeCoIn_5$. On the other hand, Ce_2RhIn_8 grew in pure single phase. Further, the lanthanum analogs of Ce_2IrIn_8 and Ce_2RhIn_8 were also successfully grown in single phase. However, instead of the intended La_2CoIn_8, crystals of $LaCoIn_5$ grew in a pure phase. Few nice looking single crystals were selected from among the lot to study.

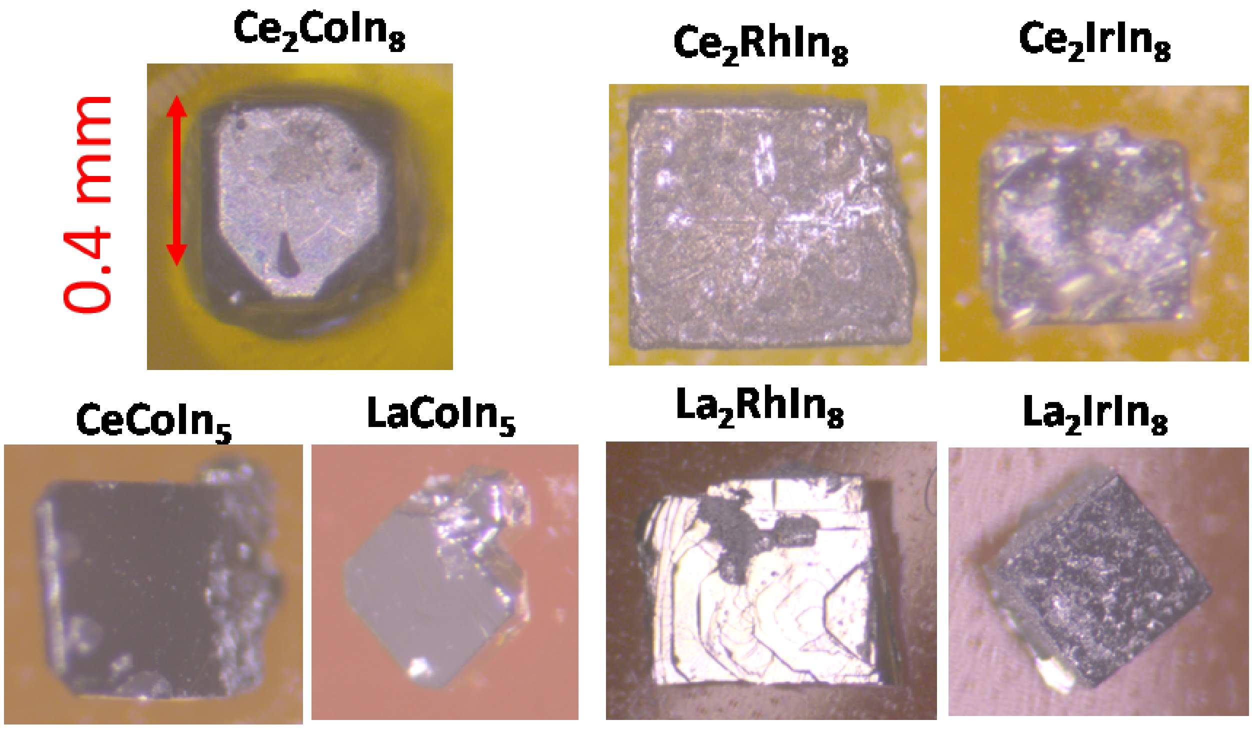

Figure 5.3: Single crystals of Ce-based 218 heavy fermions and their La analogs grown at the ICC-IMR.

5.3 Ce$_2$CoIn$_8$

As already mentioned, Ce$_2$CoIn$_8$ grew in a mixed phase along with CeCoIn$_5$. The single crystals of Ce$_2$CoIn$_8$ have a truncated hexahedron shape, while single crystals of CeCoIn$_5$ have a plate-like shape, as shown in Fig. 5.4.

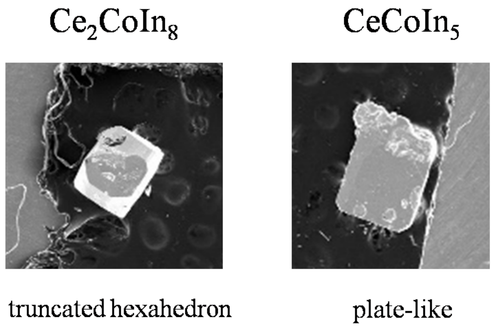

Figure 5.4: Single crystal of Ce$_2$CoIn$_8$ (left) and CeCoIn$_5$ (right)

Using single crystal diffraction, the lattice parameters of the Ce$_2$CoIn$_8$ single crystal are estimated as a = 4.4643 Å and c = 12.26 Å. The lattice constants are in agreement with previous reports [164, 166].

5.3.1 Resistivity and specific heat

We selected two crystals, a truncated hexahedron shaped crystal of Ce$_2$CoIn$_8$ (S2) and a plate shaped crystal of CeCoIn$_5$ for resistivity measurements using PPMS. The current was applied along the a axis in both cases. As expected, upon cooling down, both compounds showed a hump-like maximum corresponding to the onset of the Kondo coherence at intermediate temperature and a superconducting transition at lower temperatures [see Fig. 5.5]. For CeCoIn$_5$, the Kondo coherence occurs at $T_{coh} \approx 50$ K and the superconducting transition occurs at $T_c = 2.3$ K. For Ce_2CoIn_8, both $T_{coh} \approx 10$ K and $T_c = 0.4$ K are much lower.

Further, two additional step like features were observed in Ce_2CoIn_8 at $T_b = 0.9$ K and $T_a = 1.3$ K. These features were also detected in the previous studies as well [164, 167]. However, there is no detectable feature around 2.3 K, the superconducting transition temperature of $CeCoIn_5$, in Ce_2CoIn_8 suggesting the absence of any $CeCoIn_5$ impurity in this Ce_2CoIn_8 sample.

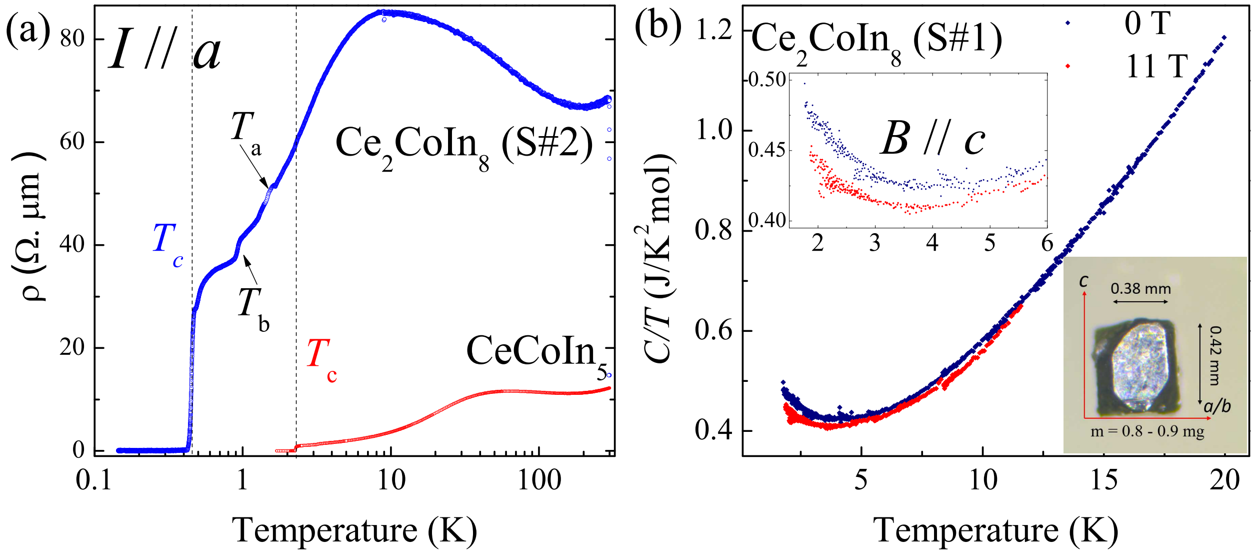

Figure 5.5: (a) Temperature dependence of resistivity in Ce_2CoIn_8 (blue) and $CeCoIn_5$ (red). (b) Low-temperature specific heat of Ce_2CoIn_8 obtained using the thermal relaxation technique at zero field (blue) and at 11 T (red). The upper inset shows a zoomed in view of specific heat at low temperatures. The lower inset shows the sample (S1) used for the specific heat measurement.

Next, we selected a smaller crystal of Ce_2CoIn_8 (S1) for specific heat and dHvA effect measurements. A picture of this crystal is shown in the lower inset of Fig. 5.5(b). The low-temperature specific heat measured using the thermal relaxation technique is shown in Fig. 5.5(b). The specific heat decreases upon cooling down to ≈3.5 K and then increases slightly at lower temperatures. There is no detectable trace of a $CeCoIn_5$ impurity in this single crystal (S1). Therefore, we selected this crystal to measure the dHvA effect as well.

5.3.2 dHvA effect

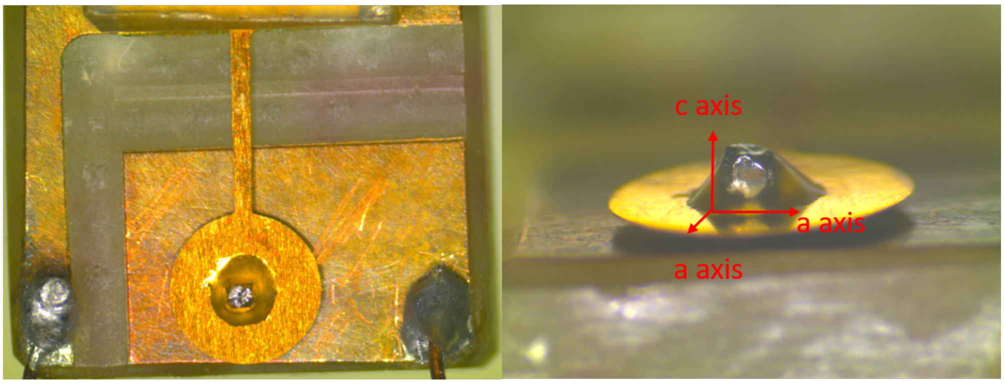

Figure 5.6: Single crystal of Ce_2CoIn_8 mounted on a 25 μm thick cantilever for dHvA effect measurements. The sample was rotated from the c towards the a axis.

To measure the dHvA effect in Ce_2CoIn_8, we used the most sensitive cantilever (25 μm thick). Figure 5.6 shows the single crystal S1 mounted on the cantilever. The dHvA effect in Ce_2CoIn_8

was measured in static magnetic fields up to 36 T in a dilution refrigerator equipped with an in-situ rotator.

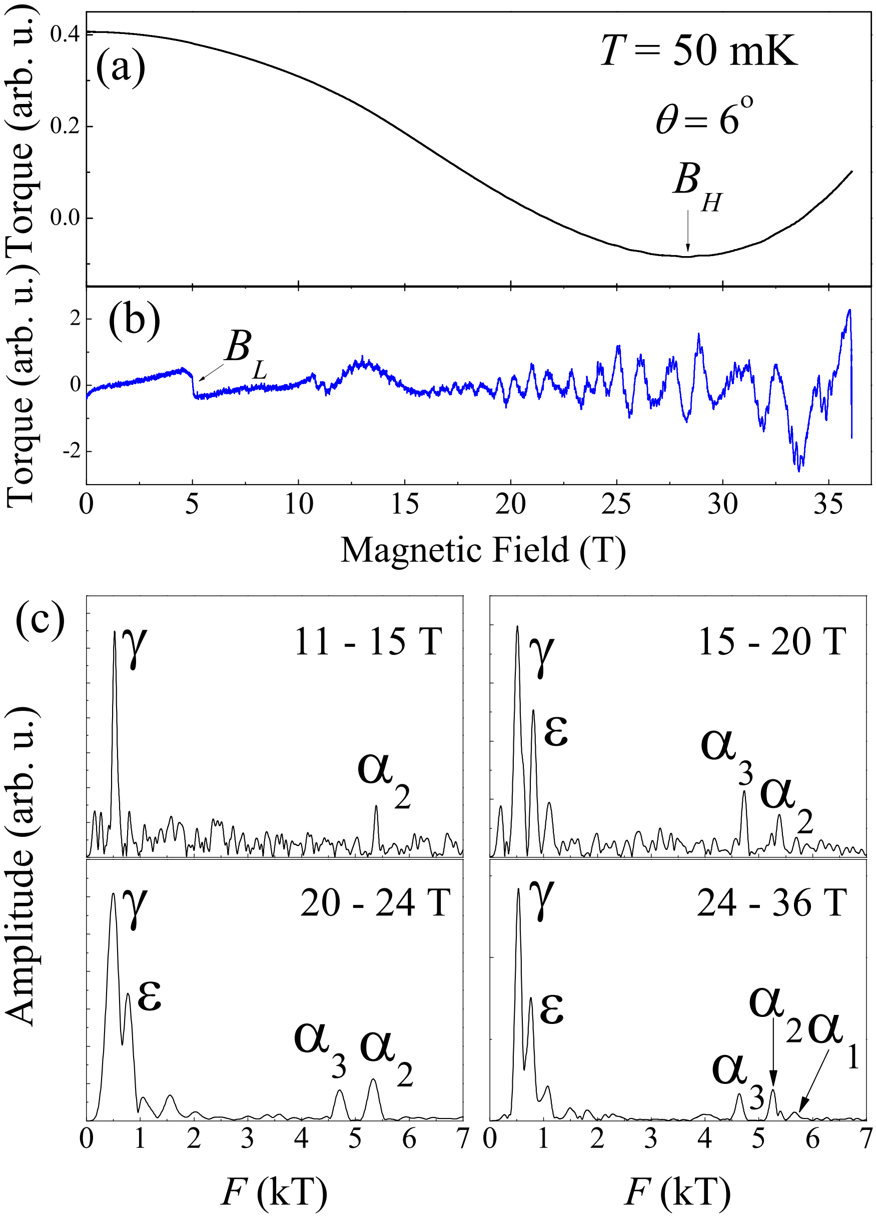

Figure 5.7: dHvA effect in Ce_2CoIn_8 at $T = 50$ mK in magnetic fields up to 36 T applied at $\theta = 6°$ from the c toward the a axis. (a) The as-measured magnetic torque in Ce_2CoIn_8. (b) Quantum oscillations in Ce_2CoIn_8 obtained by subtracting a smooth non-oscillatory background from the torque signal. (c) FFTs of quantum oscillations in (b) for different field ranges.

Figure 5.7(a) shows the magnetic torque acting on the Ce_2CoIn_8 single crystal in magnetic fields applied at $\theta = 6°$ from the c toward the a axis. The magnetic torque shows a peculiar broad minimum at $B_H \approx 28$ T. The origin of this minimum is not clear. Further, there is another small step-like feature at $B_L \approx 5$ T, which becomes clear on subtracting a smooth background, as shown in Fig. 5.7(b). The origin of this feature is also not clear. Coincidentally, B_L corresponds to the $H_c \parallel c$ in $CeCoIn_5$ and, therefore, might be due to a tiny amount of a $CeCoIn_5$ impurity. However, this would be surprising as specific heat showed no detectable trace of any $CeCoIn_5$ impurity in this crystal (S1) [see Fig. 5.5(b)].

Most importantly, we observed clear quantum oscillations in the heavy-fermion superconductor Ce_2CoIn_8 for the first time. To the best of our knowledge, quantum oscillations have not been so far observed in this compound. The oscillations appear already at about 10 T and grow stronger with field, such that the low-frequency oscillations become distinguishable on the magnetic torque

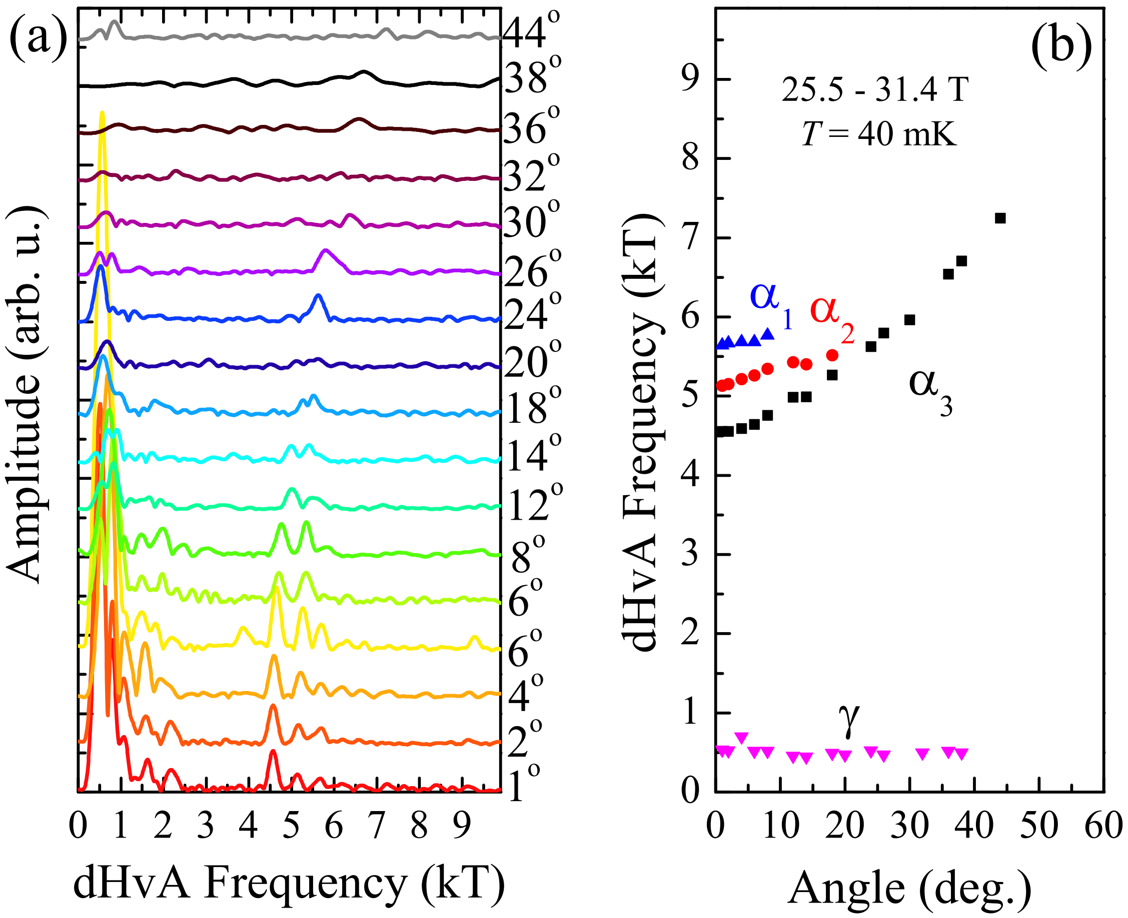

Figure 5.8: Angle dependence of the dHvA frequencies in Ce_2CoIn_8 at $T = 50$ mK obtained over the field range 25.5 - 31.4 T. (a) FFTs at various orientations of the magnetic field. The bottom four FFTs at $(1°, 2°, 4°$ and $6°)$ are obtained from torque measurements using a 25μm cantilever, for the rest ($6°$ to $44°$), a 50μm cantilever was used. Curves are shifted vertically for clarity. (b) dHvA frequencies plotted as a function of angle θ from the c toward the a axis.

signal itself.

The FFT of these quantum oscillations reveals several frequencies γ, ϵ, α_3, α_2 and α_1 shown in Fig. 5.7(c). While most of these frequencies are present already below 20 T, although their amplitudes are very small, the α_1 frequency with the smallest amplitude is visible only at high fields, above 24 T.

Next, we performed angle dependent measurements of these dHvA frequencies to map the Fermi surface of Ce_2CoIn_8. The angle dependence of all the observed frequencies is shown in Fig. 5.8(d). The frequency α_3 is observed up to large angles $\sim 44°$. The frequencies α_2 and α_1 persist up to smaller angles. α_3 roughly follows a $1/cos(\theta)$ dependence suggesting that it originates from a quasi-2D Fermi surface. The angle dependence of α_2 and α_1 is comparatively flatter suggesting a more distorted cylindrical Fermi-surface. The dHvA frequency γ is almost angle independent suggesting that it originates from a small isotropic Fermi-surface pocket.

To determine the nature of the f electrons, i.e., itinerant or localized, we compare the experimentally obtained dHvA frequencies in Ce_2CoIn_8 with those obtained from the LDA band-structure calculations[1]. The calculated Fermi-surfaces for La_2CoIn_8 assuming the f electrons to be localized and for Ce_2CoIn_8 assuming the f electrons to be itinerant are shown in Fig. 5.9.

The experimental dHvA frequencies are plotted against these band-structure calculations assuming the f electrons to itinerant [see Fig. 5.10(a)] and localized [see Fig. 5.10(b)]. The agreement with the localized calculations is extremely poor for the α frequencies. The agreement between the

---

[1] These calculations were performed by H. Harima, Kobe university, Japan.

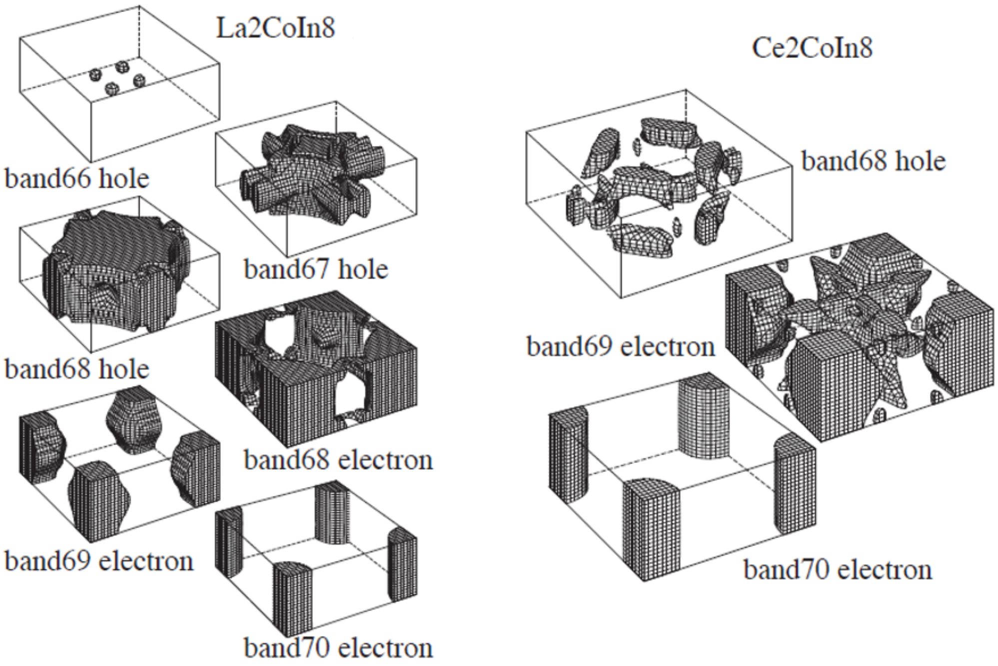

Figure 5.9: Theoretical Fermi surfaces of La_2CoIn_8 (left) and Ce_2CoIn_8 (right) obtained from band structure calculations.

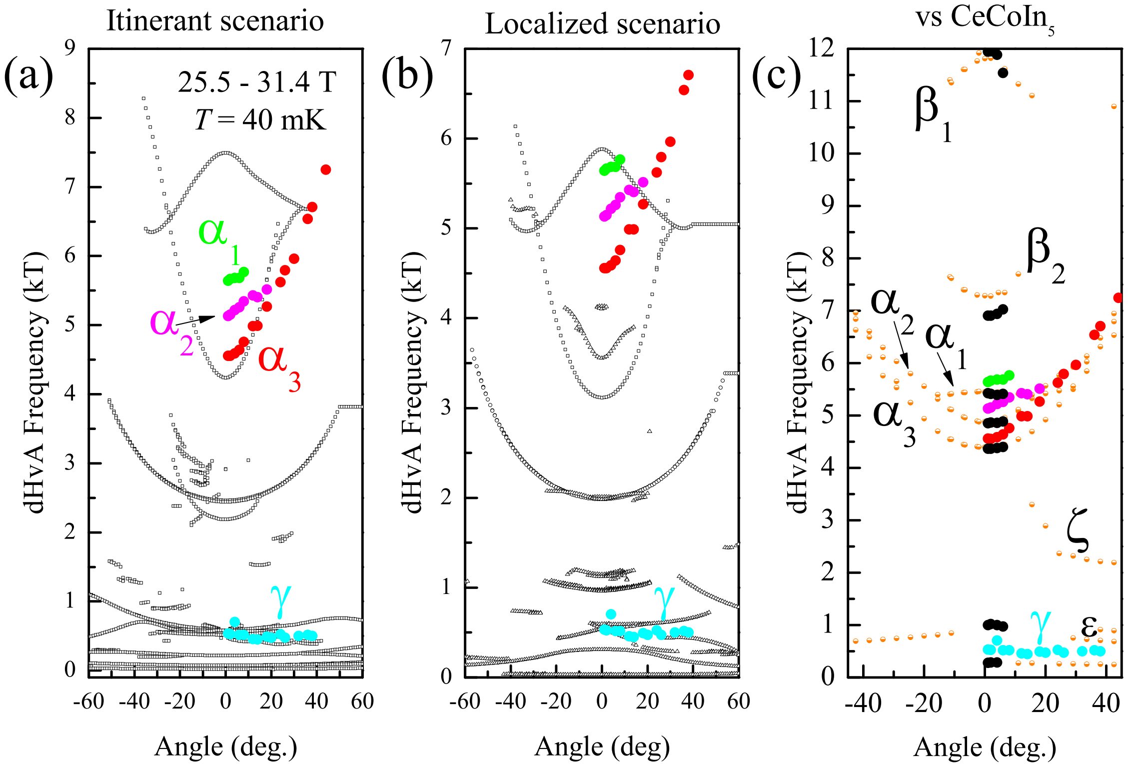

Figure 5.10: Comparison of experimentally obtained dHvA frequencies (coloured: red, green, cyan and magenta) in Ce_2CoIn_8 with (a) the theoretical band structure calculations assuming the f electrons to be itinerant and (b) localized (c) the experimentally obtained dHvA frequencies in $CeCoIn_5$ from ref [119] (open circles) and our work (closed black circles).

experimental frequencies and the itinerant calculations is not very good either. Although there is some resemblance of α_3 and γ with the calculations, α_2 and α_1 do not match any of the calculated branches.

Finally, in Fig. 5.10(c), we compare the dHvA frequencies in Ce_2CoIn_8 with the experimentally obtained dHvA frequencies in $CeCoIn_5$. Here, the open circles are dHvA frequencies in $CeCoIn_5$ obtained by R. Settai et al. in field up to 17 T, [119] at low fields and closed black circles represent the dHvA frequencies in $CeCoIn_5$ that we obtained in our high field (25.5 - 31.4 T) dHvA measurements discussed in the previous chapter.

There is a certain qualitative agreement between the experimentally obtained dHvA frequencies in Ce_2CoIn_8 and those in $CeCoIn_5$. However, compared to $CeCoIn_5$, the dHvA frequencies in Ce_2CoIn_8 are shifted upwards suggesting larger orbit sizes. Based on the qualitative agreement between the experimentally obtained dHvA frequencies in Ce_2CoIn_8 with those in $CeCoIn_5$, it appears that the Fermi surfaces of Ce_2CoIn_8 have a morphology qualitatively similar to $CeCoIn_5$, but with a larger volume. Another possibility for the qualitative agreement between the experimental frequencies in both compounds it that the frequencies observed in Ce_2CoIn_8 might be originating form a $CeCoIn_5$ impurity phase that is somewhat misaligned with the main Ce_2CoIn_8 phase. Although, this seems to be extremely unlikely, as no detectable trace of $CeCoIn_5$ was found in the specific heat measurements, further studies are needed to rule this out completely.

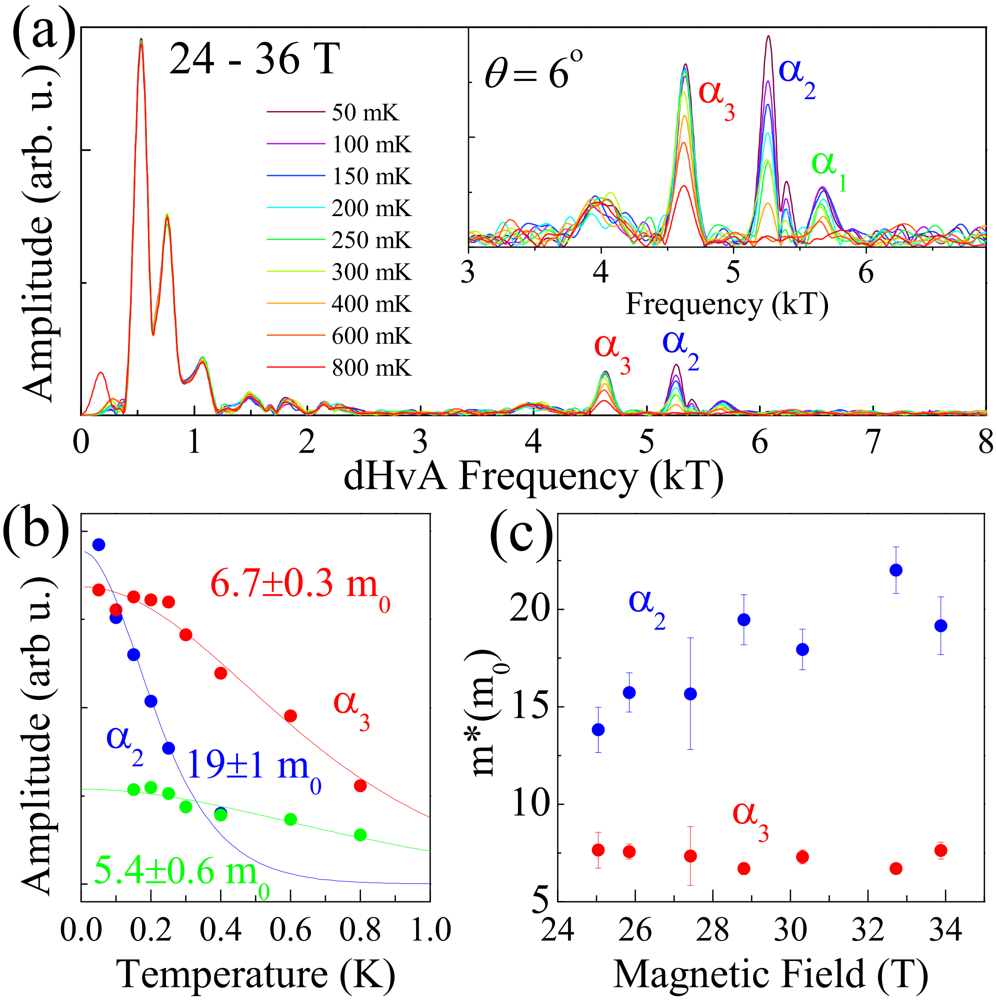

Figure 5.11: (a) Temperature-dependence of the dHvA amplitudes in Ce_2CoIn_8 obtained over the field range 24-36 T at $\theta = 6^\circ$ from the c toward the a axis. (b) Corresponding mass plots for α_3, α_2 and α_1. (c) Field-dependence of the effective masses for α_3 and α_2.

Next, we measured the temperature dependence of the dHvA amplitudes to determine the corresponding effective masses, as shown in Fig. 5.11(a) and (b). The effective masses deduced form the standard LK fit to the temperature dependence of the dHvA amplitudes are 6.7±0.3 m_0 for α_3, 19±1 m_0 for α_2 and 5.4±0.6 m_0 for α_1. The effective mass of α_2 in Ce$_2$CoIn$_8$ is higher than that in CeCoIn$_5$, while for α_1 it is lower. The effective mass of α_3 is almost field independent, while α_2 shows a mass enhancement with magnetic fields Fig. 5.11(c). The field-dependence of the effective masses could not be extracted at lower fields due to the very small amplitudes.

Moving further, in Fig. 5.12 we show the dHvA effect measurements in Ce$_2$CoIn$_8$ performed in a superconducting magnet for fields applied close to the a axis. Fig. 5.12(a) shows the magnetic torque (top) and the signal left after subtracting a smooth background (bottom). There are two features in the magnetic torque: a small one at $B_l \sim 5.5$ T and a bigger one at $B_h \sim 11$ T. It is not clear if the feature at B_l is the same as that observed for the field along the c axis also close to 5 T. The origin of the feature at 11 T is not clear either. At increasing orientation of the field away from the a toward the c axis, it becomes smaller and moves to higher fields. It becomes undetectable at $\approx 11°$ from a axis in field up to 18 T as shown in Fig. 5.12(b).

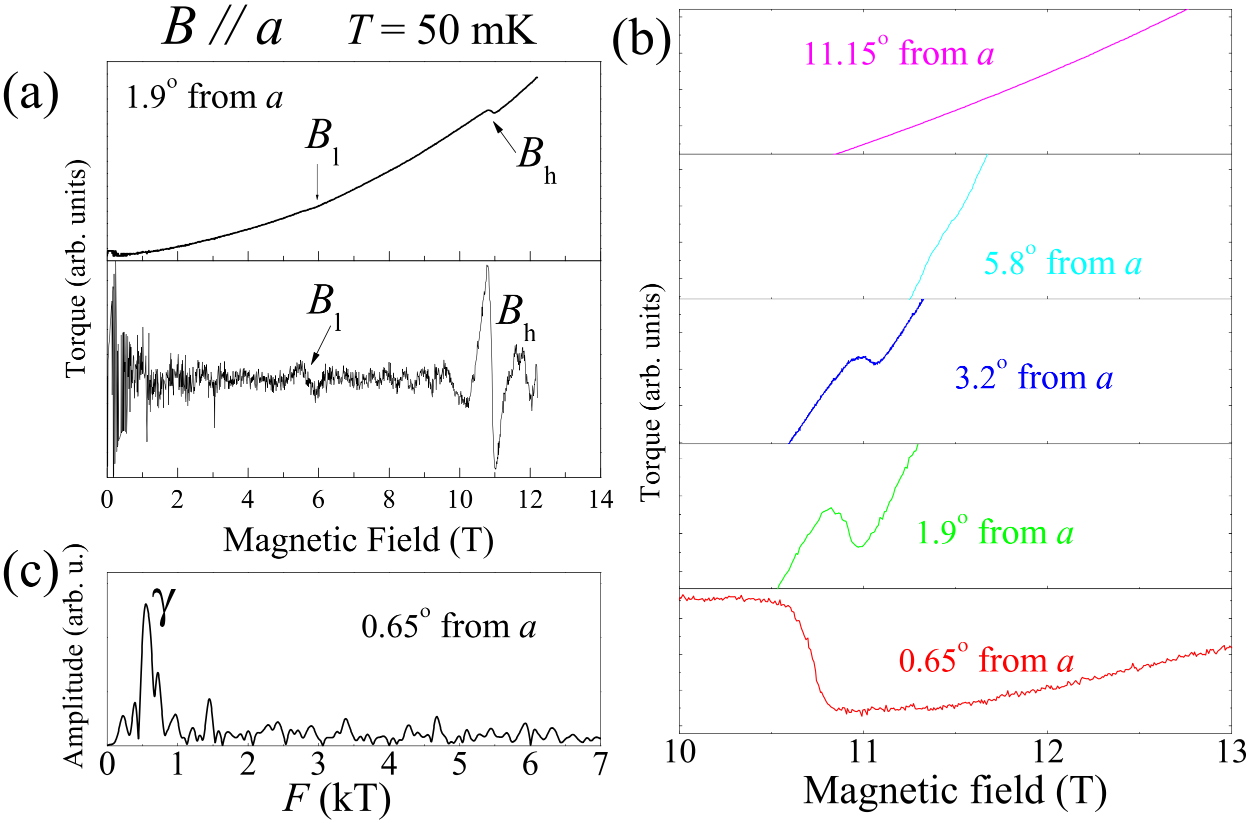

Figure 5.12: dHvA effect in Ce$_2$CoIn$_8$ at T =50 mK for a field applied close to the a axis. (a) Magnetic torque in Ce$_2$CoIn$_8$ (top) and the signal left after subtracting a smooth background (bottom). (b) Angle dependence of the feature at B_h at a few different orientations of field from the a toward the c axis. (c) The FFT of the magnetic torque after subtracting a polynomial background for a field applied at 0.65° from the $aaxis$.

The high frequency quantum oscillations are not present for fields close to the a axis suggesting that the large Fermi surfaces in Ce$_2$CoIn$_8$ are anisotropic and quasi-two-dimensional. The small isotropic Fermi-surface pocket γ is present, as shown in fig. 5.12(c).

5.4 Ce_2IrIn_8

We also tried to measure the dHvA effect on a small plate-like single crystal of Ce_2IrIn_8 in an 18 T superconducting magnet in a dilution refrigerator equipped with an in-situ rotator. Fig. 5.13(a) shows the magnetic torque in Ce_2IrIn_8 for magnetic fields applied in the vicinity tof the two principal crystallographic, i.e., close to c (left) and a axes (right).

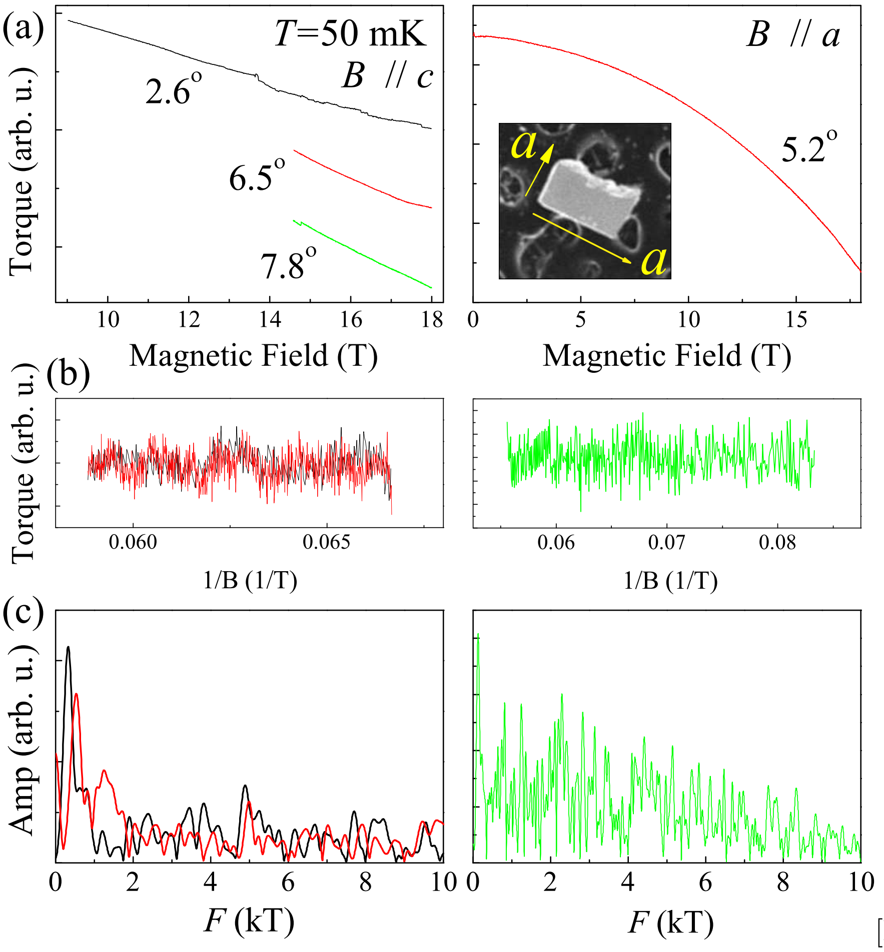

[htb]

Figure 5.13: Magnetic torque in Ce_2IrIn_8 in magnetic fields up to 18 T at 50 mK. (a) Magnetic torque in Ce_2IrIn_8 for fields applied close to the c (left) and the a (right) axes. (b) The corresponding torque signal after subtracting a polynomial background from the curves in (a). (c) FFT spectra of the torque signals in (b).

It is evident from Fig. 5.13(b) and (c) that there are no quantum oscillations for either orientation of the magnetic field up to 18 T. This suggest that the measured sample of Ce_2IrIn_8 is not of a high enough quality to observe quantum oscillations in intermediate fields. Measurements at still higher fields are needed to check if quantum oscillations can be observed in this sample of Ce_2IrIn_8.

5.5 Ce_2RhIn_8

Magnetic toque in Ce_2RhIn_8 was also measured on a small plate-like single crystal in the 18 T superconducting magnet in a dilution refrigerator. Fig. 5.14(a) shows the magnetic torque in Ce_2RhIn_8 for a magnetic field applied close to the c axis.

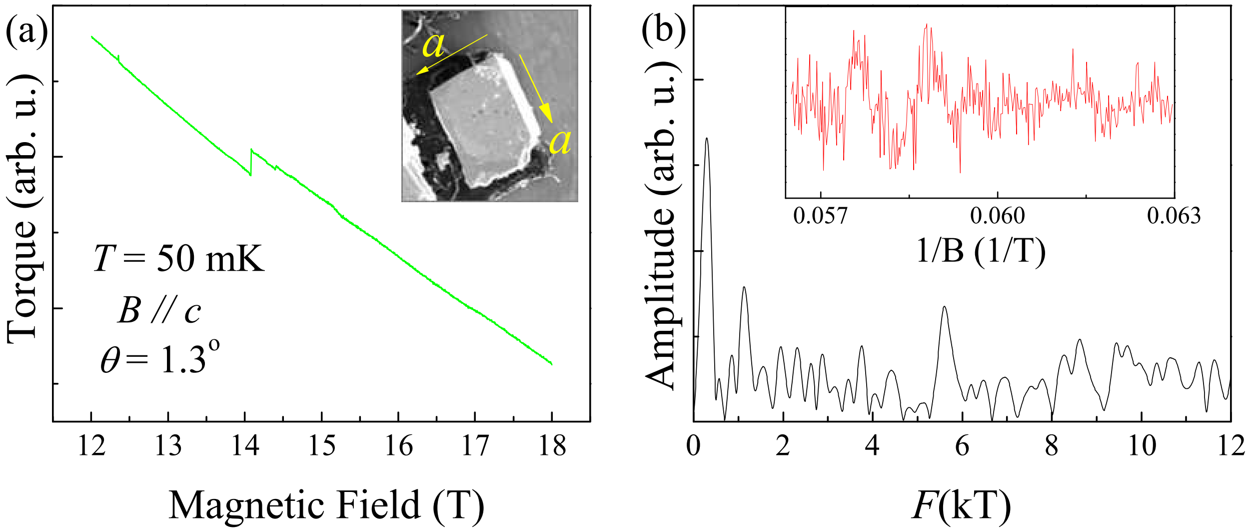

Figure 5.14: Magnetic torque in Ce_2RhIn_8 at 50 mK in magnetic fields up to 18 T close to the c axis (a). Magnetic torque in Ce_2IrIn_8 for fields close to the c axis. (b) The inset shows the torque signal after subtracting a polynomial background from (a). The main figures shows the FFT spectrum of the torque signal from the inset.

The inset of Fig. 5.14(b) shows the remaining magnetic torque after subtracting a smooth background. The FFT of this signal reveals a very low frequency, as shown in Fig. 5.14(b). In addition, there seem to be a at 5.6 kT barely above the noise level. Measurements at much higher fields are needed to check if it is a real dHvA frequency or not.

5.6 Conclusions

In summary, we were able to successfully grow single crystals of the Ce-218 family. The Ce_2CoIn_8 crystals are of high enough quality to show clear quantum oscillations. We performed angle- and temperature-dependent measurements of the dHvA frequencies in Ce_2CoIn_8. The Fermi-surface of Ce_2CoIn_8 is found to be qualitatively similar to $CeCoIn_5$ but with larger orbits. Some of the effective masses in Ce_2CoIn_8 are quite heavy, especially for the α_2 orbit. The samples of Ce_2RhIn_8 and Ce_2IrIn_8 do not show reliable quantum oscillations up to 18 T.

Chapter 6

Conclusions and perspectives

The results presented in the preceding chapters put forward a more evolved understanding of the Ce-115 and related compounds in high magnetic fields. In this final chapter, I list the conclusions of our results for the three compounds $CeRhIn_5$, $CeCoIn_5$ and Ce_2CoIn_8 one by one. While some of the conclusions and interpretations are supported in entirety by our results, for the others additional/complimentary measurements are needed either to definitely confirm our hypotheses or to further understand the physics that still remain unresolved even after this work. Therefore, right after the conclusions, I discuss some complimentary measurements that can be helpful in this regard.

$CeRhIn_5$

We performed high-field dHvA measurements on $CeRhIn_5$ and $LaRhIn_5$. In $CeRhIn_5$, several additional dHvA frequencies emerge above certain threshold fields. In particular, we observed the previously undetected, thermodynamically important β_1 branch predicted by the f-localized band-structure calculations. Almost all of the dHvA frequencies observed in $CeRhIn_5$ are also present in $LaRhIn_5$. In addition, their angular dependence is identical in the two compounds. The presence and angle dependence of the observed dHvA frequencies are well accounted for by band-structure calculations with localized f electrons, indicating that the f electrons of $CeRhIn_5$ remain localized not only above $B^* \approx 30$ T, but also above $B_c \simeq 50$ T. We emphasize that delocalization of the Ce f-electron at high magnetic field would change the whole FS from the localized to the itinerant FS. Continued observation of the β_2 branch at the highest magnetic fields is clear evidence of that the Ce f-electron remains localized over the full magnetic field range that we have explored. It was previously reported that the f electrons also remain localized in $CeIn_3$ above its critical field $B_c \simeq 60$ T [125]. Whereas $CeIn_3$ is an isotropic HF compound with an almost spheroidal FS, $CeRhIn_5$ is a prototypical example of a strongly anisotropic material with quasi-2D FSs. The continued localization of the f electrons well above B_c in both compounds is not consistent with either of the two existing theoretical models of AFM QCPs. This implies that magnetic field, which itself tends to localize f electrons, should be treated differently from such control parameters as pressure or chemical doping.

We also performed specific heat measurements in this compound in static fields up to 36 T applied both along the a and the c axis. For field along the a axis, we confirmed previously established rich phase diagram, and extended it to higher fields. For field along the c axis, we observed a distinct anomaly at $B^* \simeq 30$ T, suggesting that a real thermodynamic phase transition, probably weakly first-order, is likely to take place at this field.

Further, we also performed high-field ultrasound velocity measurements on bulk single crystals of $CeRhIn_5$. For a magnetic field slightly tilted from the c axis, we observed distinct anomalies at both $B_m \simeq 20$ T and $B^* \simeq 30$ T at low temperatures in all the symmetry breaking modes, i.e., C_{11}, C_{44}, C_{66}, and C_T. In all these modes, the anomalies are of similar shape, but of the opposite sign. Both anomalies are absent in the symmetry preserving C_{33} mode. Furthermore, our temperature-dependent measurements reveal that both anomalies exist within the AFM state only. Given that the transition at B_m corresponds to a change of magnetic structure from IC below B_m to C above B_m, we argue that the transition at B^* is of the same origin, i.e., from the C phase below B^* to a new IC phase above it. This makes $CeRhIn_5$ one of the rare compounds, in which the application of a high magnetic field induces a C to IC transition. When a magnetic field is tilted further away from the c axis, the anomaly at B^* slowly moves to higher fields, and progressively becomes smaller and broader. This behavior is in contrast with what was observed in the previous transport measurements on microfabricated samples, in which a sharp resistivity jump at B^* was observed to increase up to about 20° following by a decrease up to 60°, where it faded away. Different behaviors observed here on bulk samples and on the FIB-fabricated microstructures are likely to be due to uniaxial strains or stresses inevitably present in the latter. $CeRhIn_5$ seems to be very sensitive to uniaxial strains. For instance, previously reported NQR measurements on bulk and powder samples of $CeRhIn_5$ suggest that even small strains (or stresses) change the zero-field magnetic structure from incommensurate to commensurate. Finally, while both the anomalies at B_m and B^* are absent in the C_{33} clear distinct features are observed around B^* which are not observed in any other modes. These two features forms a done around B^* which seems to be expanding in field with decreasing temperatures.

Finally, our results on $CeRhIn_5$ opens up new perspectives for performing the following experiments in future

Neutron diffraction experiments in pulsed fields to determine the Q vector for the magnetic structure of $CeRhIn_5$ above B^*

Neutron diffraction experiments now possible in high fields above 30 T [142] is the most natural experiment perform to definitely confirm our hypothesis about the transition at B^* being a change of magnetic structure. The Q vector for the AFM4 state can be determined through this experiment.

High field NMR experiment at slightly tilted magnetic fields from the c axis

The high field NMR experiment for field precisely along the c axis revealed that the antiferromagnetic structure above B^* (AFM4) is incommensurate. For fields slightly tilted (say by 2°) from the c axis, similar NMR experiment should definitely be able to distinguish the three magnetic structures (AFM1, AFM3, and AFM4) in the B-T phase diagram. Therefore, an NMR experiment at slightly tilted magnetic fields can also be helpful in confirming our hypothesis.

AC specific heat at temperatures lower than 2 K.

If the two features above and below B^* are indeed real thermodynamic phase transition, then they can possibly be detected as small but distinct anomalies in the AC specific heat similar to the anomaly at B^*. Therefore, extending our AC specific heat measurements at lower temperatures is a natural experiment to perform.

High-field magnetostriction experiment for fields close to the c axis

If the features observed close to the transition at B^* in the C_{33} mode are related to the volume change, magnetostriction measurements for fields applied close to the c axis should be able to detect them as anomalies corresponding to an expansion or compression along the c direction of the tetrogonal lattice.

Transport measurements on bulk single crystals under uniaxial strain

The angular-dependent behaviour of the transition at B^* observed in our ultrasound velocity measurements performed on bulk single crystals is contradictory to the highly influential transport study performed on microstructured devices of $CeRhIn_5$ in which strains are inherently present. To the best of our knowledge, so far the enhanced in-plane anisotropic transport has not been observed in bulk single crystals. Therefore, to truly understand the enhanced in-plane anisotropy and the role of strains in its emergence in the FIB devices, such transport measurements must be performed on bulk single crystals under uniaxial strain.

Neutron diffraction experiments on bulk single crystal under uniaxial strain

To understand the change of magnetic structure from incommensurate at zero-field in bulk single crystals to commensurate in powered sample at zero-field, neutron diffraction experiments on bulk single crystal under uniaxial strain can be helpful.

Ultrasound velocity in the C_{33} mode in dilution refrigerator

While extending our ultrasound velocity measurements to dilution refrigerator temperatures is definitely desirable for all the modes to extend the T-B phase diagram to lower temperatures, the case for C_{33} mode is particulary interesting. The dome formed by the two feature in the T-B phase diagram, centered around B^*, is unique to this mode and seems to get broader in field at lower temperature. Therefore, extending the T-B phase diagram to lower temperatures is necessary to observe the full expanse of this dome.

High field AC susceptibility in CeRhIn$_5$

An anomaly at B^* is absent in longitudinal magnetization. However, a small feature is observed in magnetic torque near 30 T for field applied very close to the c axis (2° and 4°) which tends to become stronger for a better alignment of field from the c axis, i.e, it is stronger at 2° than 4°. But for fields closer to the crystallographic axis magnetic torque starts vanishing and therefore, the signal becomes noisy. This makes a strong case for AC susceptibly in CeRhIn$_5$ where unlike torque, measurements close to the crystallographic axis are not an issue. Also, sometimes metamagnetic transitions that weakly manifest in torque appear as pronounced anomalies in AC susceptibly.

Ultrasound velocity in the C_{44} mode using a in-situ rotator

The anomalies at B_m and B^* in the C_{44} modes have a kink like rather than sharp step like in C_T mode. Further, the anomaly at B^* is greater than the one at B_m. Based on these strange observations, it is possible that an angle-dependence of ultrasound velocity in the C_{44} at lower temperatures might also reveal features that were only observed in the C_{33} mode.

Ultrasound velocity in the C_T and C_{33} modes using a double axis in-situ rotator

For field applied precisely along the c axis, the metamagentic transition at B_m induced by an in-plane component of magnetic field ($B \geq 2$ T) moves to fields higher than 36 T. Therefore, it would be interesting to see if the transition at B^* also disappears or not for field precisely along the c axis. Such a measurement can elucidate the role of in-plane and out-of-plane field components on the transition at B^*.

CeCoIn$_5$

We performed dHvA and mangetoresistance measurement in CeCoIn$_5$ at high fields close to the c axis. Our measurements revealed anomalous quantum oscillation at intermediate fields between 20-24 T which is more pronounced at low temperatures and becomes unnoticeable at $T = 400$ mK. The effective masses also show a peculiar field dependence. The effective masses of the α orbits show an abrupt increase above 23 T. Finally, magnetoresistance measurement revealed a clear anomaly at 22 T. Based on these observations we suggest a field-induced instability occurs in CeCoIn$_5$ at high fields. The enhancement of effective masses with magnetic fields suggests a departure from the usual fermi liquid behavior.

Finally, our results on CeCoIn$_5$ opens up new perspectives for performing the following experiments in future

Extending the dHvA study in $CeCoIn_5$ to still higher fields

Our dHvA study in $CeCoIn_5$ should be extended to still higher fields in $CeCoIn_5$, to see if the field enhancement of effective mass of α_2 orbit continues, and if it diverges at still higher fields and resulting into another QCP.

Temperature-dependent magnetoresistance study

The magnetoresistance study also needs to extended further, especially a temperature dependence of the anomaly at 23 T transition to understand its origin.

High-field specific heat study

A high-field specific heat study is definitely needed to see if a field-induced phase transition occurs at 23 T.

High field AC susceptibility in $CeCoIn_5$

Certain transitions of magnetic origin are sometimes not observed in magnetic torque but may appear in AC susceptibly. Therefore, AC susceptibly measurement on $CeCoIn_5$ can be helpful in identifying if the 23 T anomaly has magnetic origins.

High field ultrasound velocity in $CeCoIn_5$

It is clear from our measurements on $CeRhIn_5$ that ultrasound technique is a powerful tool to understand unknown phase transitions. Therefore, ultrasound velocity measurement in $CeCoIn_5$ is a plausible experiment to perform to understand the 23 T anomaly.

Ce_2CoIn_8

In summary, we are able to successfully grow single crystal of the Ce-218 family. The Ce_2CoIn_8 crystals are of high quality and show nice quantum oscillation. We performed angle and temperature dependance of dHvA frequencies in Ce_2CoIn_8. The fermi surface in Ce_2CoIn_8 is found to be qualitatively similar to $CeCoIn_5$ but with larger orbit sizes. The effective masses in Ce_2CoIn_8 are quite heavy especially for the α_2 orbit. The compounds Ce_2RhIn_8 and Ce_2IrIn_8 do not show quantum oscillation up to 18 T.

Growing single crystals of still higher quality

The effective masses of the observed orbits do not fully account for the huge Sommerfield coefficient. Therefore, we expect heavier dHvA frequencies are still missing. Therefore, to fully map the fermi surface of Ce_2CoIn_8 single crystals of still higher quality are needed.

Specific heat study

The features observed at 5 T and 11 T in the magnetic torque are not fully understood and therefore warrant further studies. A specific heat study is needed to see these features corresponds to real phase transitions as well as to elucidate their origin.

Bibliography

[1] P. Drude, "Zur elektronentheorie der metalle," *Annalen der Physik*, vol. 306, pp. 566–613, 1900.

[2] P. Drude, "Zur elektronentheorie der metalle; ii. teil. galvanomagnetische und thermomagnetische effecte," *Annalen der Physik*, vol. 308, pp. 369–402, 1900.

[3] A. Sommerfeld, "Zur elektronentheorie der metalle auf grund der fermischen statistik," *Z. Physik*, vol. 47, pp. 43–60, 1928.

[4] J. Smith and E. Kmetko, "Magnetism or bonding: A nearly periodic table of transition elements," *Journal of the Less Common Metals*, vol. 90, pp. 83 – 88, 1983.

[5] T. Kasuya, O. Sakai, H. Harima, and M. Ikeda, "Consistent treatment of high and low frequency phenomena in Kondo and VF systems," *Journal of Magnetism and Magnetic Materials*, vol. 76-77, pp. 46 – 52, 1988.

[6] P. Fulde, J. Keller, and G. Zwicknagl, *Theory of Heavy Fermion Systems*, vol. 41 of *Solid State Physics*. Academic Press, 1988.

[7] P. A. Lee, T. M. Rice, J. Serene, L. J. Sham, and J. Wilkins, "Theories of heavy-electron systems," 1986.

[8] H. Ott, *Chapter 5: Characteristic Features of Heavy-Electron Materials*, vol. 11 of *Progress in Low Temperature Physics*. Elsevier, 1987.

[9] G. R. Stewart, "Heavy-fermion systems," *Rev. Mod. Phys.*, vol. 56, pp. 755–787, 1984.

[10] R. B. Lindsay, "On the atomic models of the alkali metals," *Journal of Mathematics and Physics*, vol. 3, pp. 191–236, 1924.

[11] D. R. Hartree, "The Wave Mechanics of an Atom with a Non-Coulomb Central Field. Part I. Theory and Methods," *Proceedings of the Cambridge Philosophical Society*, vol. 24, p. 89, 1928.

[12] J. C. Slater, "The self consistent field and the structure of atoms," *Phys. Rev.*, vol. 32, pp. 339–348, 1928.

[13] V. Fock, "Nherungsmethode zur lsung des quantenmechanischen mehrkrperproblems," *Z. Physik*, vol. 61, pp. 126–148, 1930.

[14] W. Metzner and D. Vollhardt, "Correlated lattice fermions in $d = \infty$ dimensions," *Phys. Rev. Lett.*, vol. 62, pp. 324–327, 1989.

[15] A. Georges and G. Kotliar, "Hubbard model in infinite dimensions," *Phys. Rev. B*, vol. 45, pp. 6479–6483, 1992.

[16] J. M. Luttinger, "Fermi surface and some simple equilibrium properties of a system of interacting fermions," *Phys. Rev.*, vol. 119, pp. 1153–1163, 1960.

[17] W. de Haas, J. de Boer, and G. van dën Berg, "The electrical resistance of gold, copper and lead at low temperatures," *Physica*, vol. 1, pp. 1115 – 1124, 1934.

[18] B. Knook, W. Star, H. Van Rongen, and G. Van den Berg, "The electrical resistance of some dilute alloys of the noble metals and Re at low temperatures," *Physica*, vol. 30, pp. 1124 – 1130, 1964.

[19] M. P. Sarachik, E. Corenzwit, and L. D. Longinotti, "Resistivity of Mo-Nb and Mo-Re alloys containing 1% Fe," *Phys. Rev.*, vol. 135, pp. A1041–A1045, Aug 1964.

[20] J. Kondo, "Resistance Minimum in Dilute Magnetic Alloys," *Progress of Theoretical Physics*, vol. 32, pp. 37–49, 1964.

[21] J. R. Schrieffer and P. A. Wolff, "Relation between the Anderson and Kondo hamiltonians," *Phys. Rev.*, vol. 149, pp. 491–492, 1966.

[22] P. Coleman, "Local moment physics in heavy electron systems," *AIP Conference Proceedings*, vol. 629, pp. 79–160, 2002.

[23] T. Kasuya, "A Theory of Metallic Ferro- and Antiferromagnetism on Zener's Model," *Progress of Theoretical Physics*, vol. 16, pp. 45–57, 1956.

[24] S. Doniach, "The Kondo lattice and weak antiferromagnetism," *Physica B+C*, vol. 91, pp. 231 – 234, 1977.

[25] R. M. Martin, "Fermi-Surfae Sum Rule and its Consequences for Periodic Kondo and Mixed-Valence Systems," *Phys. Rev. Lett.*, vol. 48, pp. 362–365, 1982.

[26] M. Oshikawa, "Topological approach to Luttinger's theorem and the fermi surface of a Kondo lattice," *Phys. Rev. Lett.*, vol. 84, pp. 3370–3373, 2000.

[27] M. A. Ruderman and C. Kittel, "Indirect exchange coupling of nuclear magnetic moments by conduction electrons," *Phys. Rev.*, vol. 96, pp. 99–102, 1954.

[28] A. P. Young, "Quantum effects in the renormalization group approach to phase transitions," *Journal of Physics C: Solid State Physics*, vol. 8, pp. L309–L313, aug 1975.

[29] J. A. Hertz, "Quantum critical phenomena," *Phys. Rev. B*, vol. 14, pp. 1165–1184, 1976.

[30] P. Coleman, C. Pépin, Q. Si, and R. Ramazashvili, "How do Fermi liquids get heavy and die?," *J. Phys.: Condens. Matter*, vol. 13, pp. R723–R738, 2001.

[31] H. v. Löhneysen, A. Rosch, M. Vojta, and P. Wölfle, "Fermi-liquid instabilities at magnetic quantum phase transitions," *Rev. Mod. Phys.*, vol. 79, pp. 1015–1075, 2007.

[32] E. Miranda and V. Dobrosavljević, "Disorder-driven non-fermi liquid behaviour of correlated electrons," *Reports on Progress in Physics*, vol. 68, pp. 2337–2408, 2005.

[33] G. R. Stewart, "Non-fermi-liquid behavior in d- and f-electron metals," *Rev. Mod. Phys.*, vol. 73, pp. 797–855, 2001.

[34] C. Varma, Z. Nussinov, and W. van Saarloos, "Singular or non-fermi liquids," *Physics Reports*, vol. 361, pp. 267 – 417, 2002.

[35] H. v. Löhneysen, T. Pietrus, G. Portisch, H. G. Schlager, A. Schröder, M. Sieck, and T. Trappmann, "Non-fermi-liquid behavior in a heavy-fermion alloy at a magnetic instability," *Phys. Rev. Lett.*, vol. 72, pp. 3262–3265, 1994.

[36] H. von Löhneysen, "Non-fermi-liquid behaviour in the heavy-fermion system," *Journal of Physics Condensed Matter*, vol. 8, pp. 9689–9706, 1996.

[37] N. D. Mathur, F. M. Grosche, S. R. Julian, I. R. Walker, D. M. Freye, R. K. W. Haselwimmer, and G. G. Lonzarich, “Magnetically mediated superconductivity in heavy fermion compounds,” *Nature*, vol. 394, pp. 39–43, 1998.

[38] N. J. Curro, T. Caldwell, E. D. Bauer, L. A. Morales, M. J. Graf, Y. Bang, A. V. Balatsky, J. D. Thompson, and J. L. Sarrao, “Unconventional superconductivity in $\mathrm{PuCoGa_5}$,” *Nature*, vol. 434, pp. 622–625, 2005.

[39] Y. Ando, K. Segawa, S. Komiya, and A. N. Lavrov, “Electrical resistivity anisotropy from self-organized one dimensionality in high-temperature superconductors,” *Phys. Rev. Lett.*, vol. 88, p. 137005, 2002.

[40] V. Hinkov, D. Haug, B. Fauqué, P. Bourges, Y. Sidis, A. Ivanov, C. Bernhard, C. T. Lin, and B. Keimer, “Electronic liquid crystal state in the high-temperature superconductor $\mathrm{YBa_2Cu_3O_{6.45}}$,” *Science*, vol. 319, pp. 597–600, 2008.

[41] J.-H. Chu, J. G. Analytis, K. De Greve, P. L. McMahon, Z. Islam, Y. Yamamoto, and I. R. Fisher, “In-plane resistivity anisotropy in an underdoped iron arsenide superconductor,” *Science*, vol. 329, pp. 824–826, 2010.

[42] R. A. Borzi, S. A. Grigera, J. Farrell, R. S. Perry, S. J. S. Lister, S. L. Lee, D. A. Tennant, Y. Maeno, and A. P. Mackenzie, “Formation of a nematic fluid at high fields in $\mathrm{Sr_3Ru_2O_7}$,” *Science*, vol. 315, pp. 214–217, 2007.

[43] F. Ronning, T. Helm, K. R. Shirer, M. D. Bachmann, L. Balicas, M. K. Chan, B. J. Ramshaw, R. D. McDonald, F. F. Balakirev, M. Jaime, E. D. Bauer, and P. J. W. Moll, “Electronic in-plane symmetry breaking at field-tuned quantum criticality in $\mathrm{CeRhIn_5}$,” *Nature*, vol. 548, pp. 313–317, 2017.

[44] Q. Si, S. Rabello, K. Ingersent, and J. L. Smith, “Locally critical quantum phase transitions in strongly correlated metals,” *Nature*, vol. 413, pp. 804–808, 2001.

[45] Q. Si, S. Rabello, K. Ingersent, and J. L. Smith, “Local fluctuations in quantum critical metals,” *Phys. Rev. B*, vol. 68, p. 115103, 2003.

[46] T. Senthil, M. Vojta, and S. Sachdev, “Weak magnetism and non-fermi liquids near heavy-fermion critical points,” *Phys. Rev. B*, vol. 69, p. 035111, 2004.

[47] M. Shimizu, “Effect of spin fluctuations in itinerant electron antiferromagnetism and coexistence with ferromagnetism,” *Journal of Magnetism and Magnetic Materials*, vol. 54-57, pp. 971 – 972, 1986.

[48] T. Moriya, *Spin Fluctuations in d-Electron Systems.* Berlin, Springer-Verlag., 1985.

[49] T. Moriya and T. Takimoto, “Anomalous properties around magnetic instability in heavy electron systems,” *Journal of the Physical Society of Japan*, vol. 64, pp. 960–969, 1995.

[50] A. J. Millis, “Effect of a nonzero temperature on quantum critical points in itinerant fermion systems,” *Phys. Rev. B*, vol. 48, pp. 7183–7196, 1993.

[51] P. H. P. Reinders, M. Springford, P. T. Coleridge, R. Boulet, and D. Ravot, “de Haas-van Alphen effect in the heavy-electron compound $\mathrm{CeCu_6}$,” *Phys. Rev. Lett.*, vol. 57, pp. 1631–1634, 1986.

[52] L. Taillefer and G. G. Lonzarich, “Heavy-fermion quasiparticles in $\mathrm{UPt_3}$,” *Phys. Rev. Lett.*, vol. 60, pp. 1570–1573, 1988.

[53] L. Taillefer, R. Newbury, G. Lonzarich, Z. Fisk, and J. Smith, “Direct observation of heavy quasiparticles in $\mathrm{UPt_3}$ via the dHvA effect,” *Journal of Magnetism and Magnetic Materials*, vol. 63-64, pp. 372 – 376, 1987.

[54] D. Shoenberg, *Magnetic Oscillations in Metals.* Cambridge Monographs on Physics, Cambridge University Press, 1984.

[55] A. Avella and F. Mancini, *Strongly Correlated Systems: Experimental Techniques*, vol. 180. Springer, 2014.

[56] I. M. Lifshitz and A. M. Kosevich, "On the calculation of the fermi surface and electronvelocities in a metal from magnetic susceptibility oscillations," *Doklady Akademii Nauk SSSR*, vol. 96, pp. 963–966, 1954.

[57] I. M. Lifshitz and A. M. Kosevich, "On the theory of magnetic susceptibility of metals at low temperatures," *Soviet Physics - JETP*, vol. 2, pp. 636–645, 1956.

[58] E. H. Sondheimer and A. H. Wilson, "The diamagnetism of free electrons," *Proceedings of the Royal Society of London. Series A, Mathematical and Physical Sciences*, vol. 210, pp. 173–190, 1951.

[59] E. Ohmichi and T. Osada, "Torque magnetometry in pulsed magnetic fields with use of a commercial microcantilever," *Review of Scientific Instruments*, vol. 73, pp. 3022–3026, 2002.

[60] J. Cooley and J. W. Tukey, "An algorithm for the machine calculation of complex fourier series," *Mathematics of Computation*, vol. 19, pp. 297–301, 1965.

[61] S. S. Courts and P. R. Swinehart, "Review of cernox$^{\mathrm{TM}}$ (zirconium oxy-nitride) thin-film resistance temperature sensors," *AIP Conference Proceedings*, vol. 684, pp. 393–398, 2003.

[62] M. Brando, "Development of a relaxation calorimeter for temperatures between 0.05 and 4 K," *Review of Scientific Instruments*, vol. 80, p. 095112, 2009.

[63] R. Lortz, Y. Wang, A. Demuer, P. H. M. Böttger, B. Bergk, G. Zwicknagl, Y. Nakazawa, and J. Wosnitza, "Calorimetric evidence for a fulde-ferrell-larkin-ovchinnikov superconducting state in the layered organic superconductor $\kappa-(\mathrm{BEDT-TTF})_2\mathrm{Cu(NCS)}_2$," *Phys. Rev. Lett.*, vol. 99, p. 187002, 2007.

[64] P. F. Sullivan and G. Seidel, "Steady-state, ac-temperature calorimetry," *Phys. Rev.*, vol. 173, pp. 679–685, 1968.

[65] J. D. Baloga and C. W. Garland, "ac calorimetry at high pressure," *Review of Scientific Instruments*, vol. 48, pp. 105–110, 1977.

[66] D. I. Gorbunov. Private communications.

[67] T. Sakon and M. Motokawa, "Electromechanical magnetization measurements at ultralow temperatures and high magnetic fields," *Review of Scientific Instruments*, vol. 71, pp. 3474–3477, 2000.

[68] P. Gegenwart, Q. Si, and F. Steglich, "Quantum criticality in heavy-fermion metals," *Nat. Phys.*, vol. 4, pp. 186–197, 2008.

[69] T. Senthil, "Deconfined Quantum Critical Points," *Science*, vol. 303, pp. 1490–1494, 2004.

[70] H. Hegger, C. Petrovic, E. G. Moshopoulou, M. F. Hundley, J. L. Sarrao, Z. Fisk, and J. D. Thompson, "Pressure-Induced Superconductivity in Quasi-2D $\mathrm{CeRhIn_5}$," *Phys. Rev. Lett.*, vol. 84, pp. 4986–4989, 2000.

[71] T. Takeuchi, T. Inoue, K. Sugiyama, D. Aoki, Y. Tokiwa, Y. Haga, K. Kindo, and Y. Ōnuki, "Magnetic and Thermal Properties of $\mathrm{CeIrIn_5}$ and $\mathrm{CeRhIn_5}$," *J. Phys. Soc. Jpn.*, vol. 70, pp. 877–883, 2001.

[72] J. S. Kim, J. Alwood, G. R. Stewart, J. L. Sarrao, and J. D. Thompson, "Specific heat in high magnetic fields and non-Fermi-liquid behavior in CeMIn$_5$ (M = Ir,Co)," *Phys. Rev. B*, vol. 64, 2001.

[73] A. L. Cornelius, P. G. Pagliuso, M. F. Hundley, and J. L. Sarrao, "Field-induced magnetic transitions in the quasi-two-dimensional heavy-fermion antiferromagnets Ce$_n$RhIn$_{3n+2}$ ($n = 1$ or 2)," *Phys. Rev. B*, vol. 64, p. 144411, 2001.

[74] E. Moshopoulou, Z. Fisk, J. Sarrao, and J. Thompson, "Crystal Growth and Intergrowth Structure of the New Heavy Fermion Materials CeIrIn$_5$ and CeRhIn$_5$," *J. Solid State Chem.*, vol. 158, pp. 25–33, 2001.

[75] N. J. Curro, P. C. Hammel, P. G. Pagliuso, J. L. Sarrao, J. D. Thompson, and Z. Fisk, "Evidence for spiral magnetic order in the heavy fermion material CeRhIn$_5$," *Phys. Rev. B*, vol. 62, pp. R6100–R6103, 2000.

[76] W. Bao, P. G. Pagliuso, J. L. Sarrao, J. D. Thompson, Z. Fisk, J. W. Lynn, and R. W. Erwin, "Incommensurate magnetic structure of CeRhIn$_5$," *Phys. Rev. B*, vol. 62, pp. R14621–R14624, 2000.

[77] A. L. Cornelius, A. J. Arko, J. L. Sarrao, M. F. Hundley, and Z. Fisk, "Anisotropic electronic and magnetic properties of the quasi-two-dimensional heavy-fermion antiferromagnet CeRhIn$_5$," *Phys. Rev. B*, vol. 62, pp. 14181–14185, 2000.

[78] H. Shishido, R. Settai, D. Aoki, S. Ikeda, H. Nakawaki, N. Nakamura, T. Iizuka, Y. Inada, K. Sugiyama, T. Takeuchi, K. Kindo, T. C. Kobayashi, Y. Haga, H. Harima, Y. Aoki, T. Namiki, H. Sato, and Y. Ōnuki, "Fermi surface, magnetic and superconducting properties of LaRhIn$_5$ and CeTIn$_5$ (T: Co, Rh and Ir)," *Journal of the Physical Society of Japan*, vol. 71, pp. 162–173, 2002.

[79] N. Harrison, U. Alver, R. G. Goodrich, I. Vekhter, J. L. Sarrao, P. G. Pagliuso, N. O. Moreno, L. Balicas, Z. Fisk, D. Hall, R. T. Macaluso, and J. Y. Chan, "4f-Electron Localization in Ce$_x$La$_{1-x}$MIn$_5$ with M = Co, Rh, or Ir," *Phys. Rev. Lett.*, vol. 93, p. 186405, 2004.

[80] A. Llobet, J. Gardner, E. Moshopoulou, J.-M. Mignot, M. Nicklas, W. Bao, N. Moreno, P. Pagliuso, I. Goncharenko, J. Sarrao, *et al.*, "Magnetic structure of CeRhIn$_5$ as a function of pressure and temperature," *Physical Review B*, vol. 69, p. 024403, 2004.

[81] H. Shishido, R. Settai, S. Araki, T. Ueda, Y. Inada, T. Kobayashi, T. Muramatsu, Y. Haga, and Y. Ōnuki, "Evolution of pressure-induced heavy fermion state and superconductivity in CeRhIn$_5$: A high-pressure fermi surface study," *Physical Review B*, vol. 66, p. 214510, 2002.

[82] H. Shishido, R. Settai, H. Harima, and Y. Ōnuki, "A Drastic Change of the Fermi Surface at a Critical Pressure in CeRhIn$_5$: dHvA Study under Pressure," *J. Phys. Soc. Jpn.*, vol. 74, pp. 1103–1106, 2005.

[83] G. Chen, K. Matsubayashi, S. Ban, K. Deguchi, and N. Sato, "Competitive coexistence of superconductivity with antiferromagnetism in CeRhIn$_5$," *Physical review letters*, vol. 97, p. 017005, 2006.

[84] S. Majumdar, G. Balakrishnan, M. Lees, D. M. Paul, and G. McIntyre, "Pressure-induced change in the magnetic modulation of CeRhIn$_5$," *Physical Review B*, vol. 66, p. 212502, 2002.

[85] S. Ohira-Kawamura, H. Shishido, A. Yoshida, R. Okazaki, H. Kawano-Furukawa, T. Shibauchi, H. Harima, and Y. Matsuda, "Competition between unconventional superconductivity and incommensurate antiferromagnetic order in CeRh$_{1-x}$Co$_x$In$_5$," *Phys. Rev. B*, vol. 76, p. 132507, 2007.

[86] M. Yokoyama, N. Oyama, H. Amitsuka, S. Oinuma, I. Kawasaki, K. Tenya, M. Matsuura, K. Hirota, and T. J. Sato, "Change of antiferromagnetic structure near a quantum critical point in $\mathrm{CeRh}_{1-x}\mathrm{Co}_x\mathrm{In}_5$," *Phys. Rev. B*, vol. 77, p. 224501, 2008.

[87] S. K. Goh, J. Paglione, M. Sutherland, E. C. T. O'Farrell, C. Bergemann, T. A. Sayles, and M. B. Maple, "Fermi-Surface Reconstruction in $\mathrm{CeRh}_{1-x}\mathrm{Co}_x\mathrm{In}_5$," *Phys. Rev. Lett.*, vol. 101, p. 056402, 2008.

[88] A. Llobet, A. D. Christianson, W. Bao, J. S. Gardner, I. P. Swainson, J. W. Lynn, J.-M. Mignot, K. Prokes, P. G. Pagliuso, N. O. Moreno, J. L. Sarrao, J. D. Thompson, and A. H. Lacerda, "Novel coexistence of superconductivity with two distinct magnetic orders," *Phys. Rev. Lett.*, vol. 95, p. 217002, Nov 2005.

[89] P. G. Pagliuso, C. Petrovic, R. Movshovich, D. Hall, M. F. Hundley, J. L. Sarrao, J. D. Thompson, and Z. Fisk, "Coexistence of magnetism and superconductivity in $\mathrm{CeRh}_{1-x}\mathrm{Ir}_x\mathrm{In}_5$," *Phys. Rev. B*, vol. 64, p. 100503(R), 2001.

[90] G. q. Zheng, N. Yamaguchi, H. Kan, Y. Kitaoka, J. L. Sarrao, P. G. Pagliuso, N. O. Moreno, and J. D. Thompson, "Coexistence of antiferromagnetic order and unconventional superconductivity in heavy-fermion $\mathrm{CeRh}_{1-x}\mathrm{Ir}_x\mathrm{In}_5$ compounds: Nuclear quadrupole resonance studies," *Phys. Rev. B*, vol. 70, p. 014511, 2004.

[91] M. Nicklas, V. A. Sidorov, H. A. Borges, P. G. Pagliuso, J. L. Sarrao, and J. D. Thompson, "Two superconducting phases in $\mathrm{CeRh}_{1-x}\mathrm{Ir}_x\mathrm{In}_5$," *Phys. Rev. B*, vol. 70, p. 020505, 2004.

[92] S. Kawasaki, M. Yashima, Y. Mugino, H. Mukuda, Y. Kitaoka, H. Shishido, and Y. Ōnuki, "Enhancing the superconducting transition temperature of $\mathrm{CeRh}_{1-x}\mathrm{Ir}_x\mathrm{In}_5$ due to the strong-coupling effects of antiferromagnetic spin fluctuations: An ^{115}In nuclear quadrupole resonance study," *Phys. Rev. Lett.*, vol. 96, p. 147001, 2006.

[93] L. Mendon ça Ferreira, T. Park, V. Sidorov, M. Nicklas, E. M. Bittar, R. Lora-Serrano, E. N. Hering, S. M. Ramos, M. B. Fontes, E. Baggio-Saitovich, H. Lee, J. L. Sarrao, J. D. Thompson, and P. G. Pagliuso, "Tuning the pressure-induced superconducting phase in doped CeRhIn_5," *Phys. Rev. Lett.*, vol. 101, p. 017005, 2008.

[94] W. Bao, A. Christianson, P. Pagliuso, J. Sarrao, J. Thompson, A. Lacerda, and J. Lynn, "Effect of la doping on magnetic structure in heavy fermion CeRhIn_5," *Physica B: Condensed Matter*, vol. 312-313, pp. 120 – 122, 2002.

[95] V. F. Correa, W. E. Okraku, J. B. Betts, A. Migliori, J. L. Sarrao, and A. H. Lacerda, "High-magnetic-field thermal expansion and elastic properties of CeRhIn_5," *Phys. Rev. B*, vol. 72, p. 012407, 2005.

[96] S. Raymond, E. Ressouche, G. Knebel, D. Aoki, and J. Flouquet, "Magnetic structure of CeRhIn_5 under magnetic field," *J. Phys.: Condens. Matter*, vol. 19, p. 242204, 2007.

[97] D. M. Fobes, S. Zhang, S.-Z. Lin, P. Das, N. J. Ghimire, E. D. Bauer, J. D. Thompson, L. W. Harriger, G. Ehlers, A. Podlesnyak, R. I. Bewley, A. Sazonov, V. Hutanu, F. Ronning, C. D. Batista, and M. Janoschek, "Tunable emergent heterostructures in a prototypical correlated metal," *Nat. Phys.*, vol. 14, pp. 456–460, 2018.

[98] T. Kanda, K. Arashima, Y. Hirose, R. Settai, K. Matsui, T. Nomura, Y. Kohama, and Y. Ihara, "Symmetry Lowering on the Field-Induced Commensurate Phase in CeRhIn_5," *J. Phys. Soc. Jpn.*, vol. 89, p. 094709, 2020.

[99] L. Jiao, Y. Chen, Y. Kohama, D. Graf, E. D. Bauer, J. Singleton, J.-X. Zhu, Z. Weng, G. Pang, T. Shang, J. Zhang, H.-O. Lee, T. Park, M. Jaime, J. D. Thompson, F. Steglich, Q. Si, and H. Q. Yuan, "Fermi surface reconstruction and multiple quantum phase transitions in the antiferromagnet CeRhIn_5," *Proc. Natl. Acad. Sci. USA*, vol. 112, pp. 673–678, 2015.

[100] L. Jiao, M. Smidman, Y. Kohama, Z. S. Wang, D. Graf, Z. F. Weng, Y. J. Zhang, A. Matsuo, E. D. Bauer, H. Lee, S. Kirchner, J. Singleton, K. Kindo, J. Wosnitza, F. Steglich, J. D. Thompson, and H. Q. Yuan, "Enhancement of the effective mass at high magnetic fields in $\mathrm{CeRhIn_5}$," *Phys. Rev. B*, vol. 99, p. 045127, 2019.

[101] P. J. W. Moll, B. Zeng, L. Balicas, S. Galeski, F. F. Balakirev, E. D. Bauer, and F. Ronning, "Field-induced density wave in the heavy-fermion compound $\mathrm{CeRhIn_5}$," *Nat. Commun.*, vol. 6, p. 6663, 2015.

[102] L. Jiao, Z. F. Weng, M. Smidman, D. Graf, J. Singleton, E. D. Bauer, J. D. Thompson, and H. Q. Yuan, "Magnetic field-induced Fermi surface reconstruction and quantum criticality in $\mathrm{CeRhIn_5}$," *Philos. Mag.*, vol. 97, pp. 3446–3459, 2017.

[103] P. Rosa, S. Thomas, F. Balakirev, E. Bauer, R. Fernandes, J. Thompson, F. Ronning, and M. Jaime, "Enhanced Hybridization Sets the Stage for Electronic Nematicity in $\mathrm{CeRhIn_5}$," *Phys. Rev. Lett.*, vol. 122, p. 016402, 2019.

[104] G. G. Lesseux, H. Sakai, T. Hattori, Y. Tokunaga, S. Kambe, P. L. Kuhns, A. P. Reyes, J. D. Thompson, P. G. Pagliuso, and R. R. Urbano, "Orbitally defined field-induced electronic state in a Kondo lattice," *Phys. Rev. B*, vol. 101, p. 165111, 2020.

[105] R. Kurihara, A. Miyake, M. Tokunaga, Y. Hirose, and R. Settai, "High-field ultrasonic study of quadrupole ordering and crystal symmetry breaking in $\mathrm{CeRhIn_5}$," *Phys. Rev. B*, vol. 101, p. 155125, 2020.

[106] S. Paschen, T. Lühmann, S. Wirth, P. Gegenwart, O. Trovarelli, C. Geibel, F. Steglich, P. Coleman, and Q. Si, "Hall-effect evolution across a heavy-fermion quantum critical point," *Nature*, vol. 432, pp. 881–885, 2004.

[107] P. Gegenwart, T. Westerkamp, C. Krellner, Y. Tokiwa, S. Paschen, C. Geibel, F. Steglich, E. Abrahams, and Q. Si, "Multiple Energy Scales at a Quantum Critical Point," *Science*, vol. 315, pp. 969–971, 2007.

[108] S. Friedemann, N. Oeschler, S. Wirth, C. Krellner, C. Geibel, F. Steglich, S. Paschen, S. Kirchner, and Q. Si, "Fermi-surface collapse and dynamical scaling near a quantum-critical point," *Proc. Natl. Acad. Sci. USA*, vol. 107, pp. 14547–14551, 2010.

[109] T. Mito, S. Kawasaki, Y. Kawasaki, G. q. Zheng, Y. Kitaoka, D. Aoki, Y. Haga, and Y. Ōnuki, "Coexistence of Antiferromagnetism and Superconductivity near the Quantum Criticality of the Heavy-Fermion Compound $\mathrm{CeRhIn_5}$," *Phys. Rev. Lett.*, vol. 90, p. 077004, 2003.

[110] G. Knebel, D. Aoki, D. Braithwaite, B. Salce, and J. Flouquet, "Coexistence of antiferromagnetism and superconductivity in $\mathrm{CeRhIn_5}$ under high pressure and magnetic field," *Phys. Rev. B*, vol. 74, p. 020501(R), 2006.

[111] T. Park, F. Ronning, H. Q. Yuan, M. B. Salamon, R. Movshovich, J. L. Sarrao, and J. D. Thompson, "Hidden magnetism and quantum criticality in the heavy fermion superconductor $\mathrm{CeRhIn_5}$," *Nature*, vol. 440, pp. 65–68, 2006.

[112] V. S. Zapf, E. J. Freeman, E. D. Bauer, J. Petricka, C. Sirvent, N. A. Frederick, R. P. Dickey, and M. B. Maple, "Coexistence of superconductivity and antiferromagnetism in $\mathrm{CeRh_{1-x}Co_xIn_5}$," *Phys. Rev. B*, vol. 65, p. 014506, 2001.

[113] E. Bauer, D. Mixson, F. Ronning, N. Hur, R. Movshovich, J. Thompson, J. Sarrao, M. Hundley, P. Tobash, and S. Bobev, "Antiferromagnetic quantum critical point in $\mathrm{CeRhIn_{5-x}Sn_x}$," *Physica B*, vol. 378-380, pp. 142–143, 2006.

[114] O. Gunnarsson and B. I. Lundqvist, "Exchange and correlation in atoms, molecules, and solids by the spin-density-functional formalism," *Phys. Rev. B*, vol. 13, pp. 4274–4298, 1976.

[115] Y. Haga. private communications.

[116] J. Thompson, R. Movshovich, Z. Fisk, F. Bouquet, N. Curro, R. Fisher, P. Hammel, H. Hegger, M. Hundley, M. Jaime, P. Pagliuso, C. Petrovic, N. Phillips, and J. Sarrao, "Superconductivity and magnetism in a new class of heavy-fermion materials," *J. Magn. Magn. Mater.*, vol. 226-230, pp. 5–10, 2001.

[117] E. Moshopoulou, J. Sarrao, P. Pagliuso, N. Moreno, J. Thompson, Z. Fisk, and R. Ibberson, "Comparison of the crystal structure of the heavy-fermion materials $CeCoIn_5$, $CeRhIn_5$ and $CeIrIn_5$," *Appl. Phys. A*, vol. 74, pp. s895–s897, 2002.

[118] D. D. Koelling and B. N. Harmon, "A technique for relativistic spin-polarised calculations," *J. Phys. C: Solid State Phys.*, vol. 10, p. 3107, 1977.

[119] R. Settai, H. Shishido, S. Ikeda, Y. Murakawa, M. Nakashima, D. Aoki, Y. Haga, H. Harima, and Y. Onuki, "Quasi-two-dimensional Fermi surfaces and the de Haas-van Alphen oscillation in both the normal and superconducting mixed states of $CeCoIn_5$," *J. Phys.: Condens. Matter*, vol. 13, pp. L627–L634, 2001.

[120] Y. Haga, Y. Inada, H. Harima, K. Oikawa, M. Murakawa, H. Nakawaki, Y. Tokiwa, D. Aoki, H. Shishido, S. Ikeda, N. Watanabe, and Y. Ōnuki, "Quasi-two-dimensional Fermi surfaces of the heavy fermion superconductor $CeIrIn_5$," *Phys. Rev. B*, vol. 63, p. 060503, 2001.

[121] D. Hall, E. C. Palm, T. P. Murphy, S. W. Tozer, C. Petrovic, E. Miller-Ricci, L. Peabody, C. Q. H. Li, U. Alver, R. G. Goodrich, J. L. Sarrao, P. G. Pagliuso, J. M. Wills, and Z. Fisk, "Electronic structure of $CeRhIn_5$: de Haas–van Alphen and energy band calculations," *Phys. Rev. B*, vol. 64, p. 064506, 2001.

[122] S. Elgazzar, I. Opahle, R. Hayn, and P. M. Oppeneer, "Calculated de Haas–van Alphen quantities of $CeMIn_5$ (M = Co, Rh, and Ir) compounds," *Phys. Rev. B*, vol. 69, p. 214510, 2004.

[123] D. M. Fobes, E. D. Bauer, J. D. Thompson, A. Sazonov, V. Hutanu, S. Zhang, F. Ronning, and M. Janoschek, "Low temperature magnetic structure of $CeRhIn_5$ by neutron diffraction on absorption-optimized samples," *J. Phys.: Condens. Matter*, vol. 29, p. 17LT01, 2017.

[124] D. Hall, E. C. Palm, T. P. Murphy, S. W. Tozer, Z. Fisk, U. Alver, R. G. Goodrich, J. L. Sarrao, P. G. Pagliuso, and T. Ebihara, "Fermi surface of the heavy-fermion superconductor $CeCoIn_5$: The de Haas–van Alphen effect in the normal state," *Phys. Rev. B*, vol. 64, p. 212508, 2001.

[125] N. Harrison, S. E. Sebastian, C. H. Mielke, A. Paris, M. J. Gordon, C. A. Swenson, D. G. Rickel, M. D. Pacheco, P. F. Ruminer, J. B. Schillig, J. R. Sims, A. H. Lacerda, M.-T. Suzuki, H. Harima, and T. Ebihara, "Fermi Surface of $CeIn_3$ above the Néel Critical Field," *Phys. Rev. Lett.*, vol. 99, p. 056401, 2007.

[126] D. Aoki, G. Seyfarth, A. Pourret, A. Gourgout, A. McCollam, J. A. N. Bruin, Y. Krupko, and I. Sheikin, "Field-Induced Lifshitz Transition without Metamagnetism in $CeIrIn_5$," *Phys. Rev. Lett.*, vol. 116, p. 037202, 2016.

[127] P. M. C. Rourke, A. McCollam, G. Lapertot, G. Knebel, J. Flouquet, and S. R. Julian, "Magnetic-Field Dependence of the $YbRh_2Si_2$ Fermi Surface," *Phys. Rev. Lett.*, vol. 101, p. 237205, 2008.

[128] W. Joss, J. M. van Ruitenbeek, G. W. Crabtree, J. L. Tholence, A. P. J. van Deursen, and Z. Fisk, "Observation of the magnetic field dependence of the cyclotron mass in the Kondo lattice CeB_6," *Phys. Rev. Lett.*, vol. 59, pp. 1609–1612, 1987.

[129] N. Harrison, P. Meeson, P. A. Probst, and M. Springford, "Quasiparticle and thermodynamic mass in the heavy-fermion system CeB_6," *J. Phys.: Condens. Matter*, vol. 5, pp. 7435–7450, 1993.

[130] E. Haanappel, L. Pricopi, A. Demuer, and P. Lejay, "Field-dependent cyclotron mass of CeAl_2," *Physica B*, vol. 259-261, pp. 1081 – 1082, 1999.

[131] L. Pricopi, E. Haanappel, S. Askénazy, N. Harrison, M. Bennett, P. Lejay, A. Demuer, and G. Lapertot, "de Haas–van Alphen studies of the heavy fermions CeAl_2 and $\mathrm{CeRu}_2\mathrm{Si}_2$," *Physica B*, vol. 294-295, pp. 276 – 279, 2001.

[132] H. Aoki, S. Uji, A. K. Albessard, and Y. Ōnuki, "dHvA effect study of metamagnetic transition in $\mathrm{CeRu}_2\mathrm{Si}_2$," *Journal of the Physical Society of Japan*, vol. 62, no. 9, pp. 3157–3171, 1993.

[133] H. Aoki, S. Uji, A. K. Albessard, and Y. Ōnuki, "Transition of f electron nature from itinerant to localized: Metamagnetic transition in $\mathrm{CeRu}_2\mathrm{Si}_2$ studied via the de Haas-van Alphen effect," *Phys. Rev. Lett.*, vol. 71, pp. 2110–2113, Sep 1993.

[134] R. Daou, C. Bergemann, and S. Julian, "Continuous evolution of the fermi surface of $\mathrm{CeRu}_2\mathrm{Si}_2$ across the metamagnetic transition," *Physical review letters*, vol. 96, no. 2, p. 026401, 2006.

[135] K. Miyake and H. Ikeda, "True meaning of "localized" f-electrons measured by dHvA experiments in Ce-based heavy fermion metals," vol. 75, p. 033704, 2006.

[136] S. Mishra, J. Hornung, M. Raba, J. Klotz, T. Förster, H. Harima, D. Aoki, J. Wosnitza, A. McCollam, and I. Sheikin, "Robust fermi-surface morphology of CeRhIn_5 across the putative field-induced quantum critical point," *Phys. Rev. Lett.*, vol. 126, p. 016403, 2021.

[137] T. Helm, A. D. Grockowiak, F. F. Balakirev, J. Singleton, J. B. Betts, K. R. Shirer, M. König, T. Förster, E. D. Bauer, F. Ronning, *et al.*, "Non-monotonic pressure dependence of high-field nematicity and magnetism in CeRhIn_5," *Nature communications*, vol. 11, pp. 1–10, 2020.

[138] S. Yip, T. Li, and P. Kumar, "Thermodynamic considerations and the phase diagram of superconducting UPt_3," *Physical Review B*, vol. 43, p. 2742, 1991.

[139] S. Mishra, A. Demuer, D. Aoki, and I. Sheikin, "Specific heat of CeRhIn_5 in high magnetic fields: Magnetic phase diagram revisited," *Phys. Rev. B*, vol. 103, p. 045110, 2021.

[140] S. de Medeiros, M. Continentino, M. Orlando, M. Fontes, E. Baggio-Saitovitch, A. Rosch, and A. Eichler, "Quantum critical point in $\mathrm{CeCo(Ge}_{1-x}\mathrm{Si}_x)_3$: Oral presentation," *Physica B: Condensed Matter*, vol. 281-282, pp. 340 – 342, 2000.

[141] C. Bredl, "Specific heat of heavy fermions in Ce-based Kondo-lattices at very low temperatures," *Journal of Magnetism and Magnetic Materials*, vol. 63-64, pp. 355 – 357, 1987.

[142] F. Duc, X. Tonon, J. Billette, B. Rollet, W. Knafo, F. Bourdarot, J. Béard, F. Mantegazza, B. Longuet, J. E. Lorenzo, E. Lelièvre-Berna, P. Frings, and L.-P. Regnault, "40-Tesla pulsed-field cryomagnet for single crystal neutron diffraction," *Rev. Sci. Instrum.*, vol. 89, p. 053905, 2018.

[143] M. D. Bachmann, G. M. Ferguson, F. Theuss, T. Meng, C. Putzke, T. Helm, K. R. Shirer, Y.-S. Li, K. A. Modic, M. Nicklas, M. König, D. Low, S. Ghosh, A. P. Mackenzie, F. Arnold, E. Hassinger, R. D. McDonald, L. E. Winter, E. D. Bauer, F. Ronning, B. J. Ramshaw, K. C. Nowack, and P. J. W. Moll, "Spatial control of heavy-fermion superconductivity in CeIrIn_5," *Science*, vol. 366, pp. 221–226, 2019.

[144] M. Yashima, R. Michizoe, H. Mukuda, H. Shishido, R. Settai, and Y. Ōnuki, "Incommensurate Antiferromagnetic Order under Pressure in CeRhIn_5 Studied by ^{115}In-NQR," *JPS Conf. Proc.*, vol. 29, p. 011010, 2020.

[145] S. Mishra, D. Gorbunov, D. J. Campbell, D. LeBoeuf, J. Hornung, J. Klotz, S. Zherlitsyn, H. Harima, J. Wosnitza, D. Aoki, A. McCollam, and I. Sheikin, "Origin of the 30 T transition in $\mathrm{CeRhIn_5}$ in tilted magnetic fields," *Phys. Rev. B*, vol. 103, p. 165124, Apr 2021.

[146] C. Petrovic, P. Pagliuso, M. Hundley, R. Movshovich, J. Sarrao, J. Thompson, Z. Fisk, and P. Monthoux, "Heavy-fermion superconductivity in $\mathrm{CeCoIn_5}$ at 2.3 K," *Journal of Physics: Condensed Matter*, vol. 13, p. L337, 2001.

[147] K. Izawa, H. Yamaguchi, Y. Matsuda, H. Shishido, R. Settai, and Y. Onuki, "Angular Position of Nodes in the Superconducting Gap of Quasi-2D Heavy-Fermion Superconductor $\mathrm{CeCoIn_5}$," *Phys. Rev. Lett.*, vol. 87, p. 057002, 2001.

[148] N. J. Curro, B. Simovic, P. C. Hammel, P. G. Pagliuso, J. L. Sarrao, J. D. Thompson, and G. B. Martins, "Anomalous NMR magnetic shifts in $\mathrm{CeCoIn_5}$," *Phys. Rev. B*, vol. 64, p. 180514, 2001.

[149] R. Movshovich, M. Jaime, J. D. Thompson, C. Petrovic, Z. Fisk, P. G. Pagliuso, and J. L. Sarrao, "Unconventional superconductivity in $\mathrm{CeIrIn_5}$ and $\mathrm{CeCoIn_5}$: Specific heat and thermal conductivity studies," *Phys. Rev. Lett.*, vol. 86, pp. 5152–5155, 2001.

[150] V. A. Sidorov, M. Nicklas, P. G. Pagliuso, J. L. Sarrao, Y. Bang, A. V. Balatsky, and J. D. Thompson, "Superconductivity and quantum criticality in $\mathrm{CeCoIn_5}$," *Phys. Rev. Lett.*, vol. 89, p. 157004, 2002.

[151] Y. Nakajima, H. Shishido, H. Nakai, T. Shibauchi, K. Behnia, K. Izawa, M. Hedo, Y. Uwatoko, T. Matsumoto, R. Settai, Y. Ōnuki, H. Kontani, and Y. Matsuda, "Non-Fermi Liquid Behavior in the Magnetotransport of $\mathrm{CeMIn_5}$ (M: Co and Rh): Striking Similarity between Quasi Two-Dimensional Heavy Fermion and High-Tc Cuprates," *Journal of the Physical Society of Japan*, vol. 76, p. 024703, 2007.

[152] K. Kumagai, M. Saitoh, T. Oyaizu, Y. Furukawa, S. Takashima, M. Nohara, H. Takagi, and Y. Matsuda, "Fulde-ferrell-larkin-ovchinnikov state in a perpendicular field of quasi-two-dimensional $\mathrm{CeCoIn_5}$," *Phys. Rev. Lett.*, vol. 97, p. 227002, 2006.

[153] A. Bianchi, R. Movshovich, C. Capan, P. G. Pagliuso, and J. L. Sarrao, "Possible fulde-ferrell-larkin-ovchinnikov superconducting state in $\mathrm{CeCoIn_5}$," *Phys. Rev. Lett.*, vol. 91, p. 187004, 2003.

[154] H. Shishido, S. Yamada, K. Sugii, M. Shimozawa, Y. Yanase, and M. Yamashita, "Anomalous change in the de Haas–van Alphen oscillations of $\mathrm{CeCoIn_5}$ at ultralow temperatures," *Phys. Rev. Lett.*, vol. 120, p. 177201, 2018.

[155] A. Bianchi, R. Movshovich, I. Vekhter, P. G. Pagliuso, and J. L. Sarrao, "Avoided antiferromagnetic order and quantum critical point in $\mathrm{CeCoIn_5}$," *Phys. Rev. Lett.*, vol. 91, p. 257001, 2003.

[156] M. Kenzelmann, T. Strässle, C. Niedermayer, M. Sigrist, B. Padmanabhan, M. Zolliker, A. D. Bianchi, R. Movshovich, E. D. Bauer, J. L. Sarrao, and J. D. Thompson, "Coupled superconducting and magnetic order in $\mathrm{CeCoIn_5}$," *Science*, vol. 321, pp. 1652–1654, 2008.

[157] H. A. Radovan, N. A. Fortune, T. P. Murphy, S. T. Hannahs, E. C. Palm, S. W. Tozer, and D. Hall, "Magnetic enhancement of superconductivity from electron spin domains," *Nature*, vol. 425, pp. 51–55, 2003.

[158] P. Fulde and R. A. Ferrell, "Superconductivity in a strong spin-exchange field," *Phys. Rev.*, vol. 135, pp. A550–A563, 1964.

[159] D. Y. Kim, S.-Z. Lin, F. Weickert, M. Kenzelmann, E. D. Bauer, F. Ronning, J. D. Thompson, and R. Movshovich, “Intertwined orders in heavy-fermion superconductor $\mathrm{CeCoIn_5}$,” *Phys. Rev. X*, vol. 6, p. 041059, 2016.

[160] I. Sheikin, H. Jin, R. Bel, K. Behnia, C. Proust, J. Flouquet, Y. Matsuda, D. Aoki, and Y. Ōnuki, “Evidence for a New Magnetic Field Scale in $\mathrm{CeCoIn_5}$,” *Phys. Rev. Lett.*, vol. 96, p. 077207, 2006.

[161] A. McCollam, S. R. Julian, P. M. C. Rourke, D. Aoki, and J. Flouquet, “Anomalous de Haas–van Alphen oscillations in $\mathrm{CeCoIn_5}$,” *Phys. Rev. Lett.*, vol. 94, p. 186401, 2005.

[162] P. J. Moll, “Focused ion beam microstructuring of quantum matter,” *Annual Review of Condensed Matter Physics*, vol. 9, pp. 147–162, 2018.

[163] J. S. Kim, N. O. Moreno, J. L. Sarrao, J. D. Thompson, and G. R. Stewart, “Field-induced non-fermi-liquid behavior in $\mathrm{Ce_2IrIn_8}$,” *Phys. Rev. B*, vol. 69, p. 024402, 2004.

[164] G. Chen, S. Ohara, M. Hedo, Y. Uwatoko, K. Saito, M. Sorai, and I. Sakamoto, “Observation of superconductivity in heavy-fermion compounds of $\mathrm{Ce_2CoIn_8}$,” *Journal of the Physical Society of Japan*, vol. 71, pp. 2836–2838, 2002.

[165] T. Ueda, H. Shishido, S. Hashimoto, T. Okubo, M. Yamada, Y. Inada, R. Settai, H. Harima, A. Galatanu, E. Yamamoto, N. Nakamura, K. Sugiyama, T. Takeuchi, K. Kindo, T. Namiki, Y. Aoki, H. Sato, and Y. Ōnuki, “Electronic, magnetic and superconducting properties of quasi-two dimensional compounds $\mathrm{Ce_2RhIn_8}$ and $\mathrm{Le_2RhIn_8}$,” *Journal of the Physical Society of Japan*, vol. 73, pp. 649–655, 2004.

[166] T. Yamashita, S. Ohara, Y. Aoki, R. Miyazaki, and I. Sakamoto, “Non-fermi-liquid behavior in electronic specific heat of heavy-fermion superconductor $\mathrm{Ce_2CoIn_8}$,” *Physica C: Superconductivity and its Applications*, vol. 470, pp. S556 – S557, 2010.

[167] M. Hedo, N. Kurita, Y. Uwatoko, G. Chen, S. Ohara, and I. Sakamoto, “Superconducting properties of new heavy fermion superconductor $\mathrm{Ce_2CoIn_8}$,” *Journal of Magnetism and Magnetic Materials*, vol. 272-276, pp. 146 – 147, 2004.